NBS SPECIAL PUBLICATION 574

U.S. DEPARTMENT OF COMMERCE / National Bureau of Standards

Basic Optical Properties of Materials Summaries of Papers

NATIONAL BUREAU OF STANDARDS

The National Bureau of Standards[1] was established by an act of Congress on March 3, 1901. The Bureau's overall goal is to strengthen and advance the Nation's science and technology and facilitate their effective application for public benefit. To this end, the Bureau conducts research and provides: (1) a basis for the Nation's physical measurement system, (2) scientific and technological services for industry and government, (3) a technical basis for equity in trade, and (4) technical services to promote public safety. The Bureau's technical work is performed by the National Measurement Laboratory, the National Engineering Laboratory, and the Institute for Computer Sciences and Technology.

THE NATIONAL MEASUREMENT LABORATORY provides the national system of physical and chemical and materials measurement; coordinates the system with measurement systems of other nations and furnishes essential services leading to accurate and uniform physical and chemical measurement throughout the Nation's scientific community, industry, and commerce; conducts materials research leading to improved methods of measurement, standards, and data on the properties of materials needed by industry, commerce, educational institutions, and Government; provides advisory and research services to other Government agencies; develops, produces, and distributes Standard Reference Materials; and provides calibration services. The Laboratory consists of the following centers:

Absolute Physical Quantities[2] — Radiation Research — Thermodynamics and Molecular Science — Analytical Chemistry — Materials Science.

THE NATIONAL ENGINEERING LABORATORY provides technology and technical services to the public and private sectors to address national needs and to solve national problems; conducts research in engineering and applied science in support of these efforts; builds and maintains competence in the necessary disciplines required to carry out this research and technical service; develops engineering data and measurement capabilities; provides engineering measurement traceability services; develops test methods and proposes engineering standards and code changes; develops and proposes new engineering practices; and develops and improves mechanisms to transfer results of its research to the ultimate user. The Laboratory consists of the following centers:

Applied Mathematics — Electronics and Electrical Engineering[2] — Mechanical Engineering and Process Technology[2] — Building Technology — Fire Research — Consumer Product Technology — Field Methods.

THE INSTITUTE FOR COMPUTER SCIENCES AND TECHNOLOGY conducts research and provides scientific and technical services to aid Federal agencies in the selection, acquisition, application, and use of computer technology to improve effectiveness and economy in Government operations in accordance with Public Law 89-306 (40 U.S.C. 759), relevant Executive Orders, and other directives; carries out this mission by managing the Federal Information Processing Standards Program, developing Federal ADP standards guidelines, and managing Federal participation in ADP voluntary standardization activities; provides scientific and technological advisory services and assistance to Federal agencies; and provides the technical foundation for computer-related policies of the Federal Government. The Institute consists of the following centers:

Programming Science and Technology — Computer Systems Engineering.

[1]Headquarters and Laboratories at Gaithersburg, MD, unless otherwise noted; mailing address Washington, DC 20234.
[2]Some divisions within the center are located at Boulder, CO 80303.

Basic Optical Properties of Materials Summaries of Papers

Presented at the Topical Conference
on Basic Optical Properties of Materials
Held at the National Bureau of Standards
Gaithersburg, Maryland, May 5-7, 1980

Edited by:

Albert Feldman

Center for Materials Science
National Measurement Laboratory
National Bureau of Standards
Washington, D.C. 20234

In cooperation with:

The Optical Society of America
1816 Jefferson Place, NW
Washington, DC 20036

U.S. DEPARTMENT OF COMMERCE, Philip M. Klutznick, Secretary

Luther H. Hodges, Jr., Deputy Secretary

Jordan J. Baruch, Assistant Secretary for Productivity, Technology, and Innovation

NATIONAL BUREAU OF STANDARDS, Ernest Ambler, Director

Issued May 1980

Library of Congress Catalog Card Number: 80-600038

National Bureau of Standards Special Publication 574
Nat. Bur. Stand. (U.S.), Spec. Publ. 574, 252 pages (May 1980)
CODEN: XNBSAV

U.S. GOVERNMENT PRINTING OFFICE
WASHINGTON: 1980

For sale by the Superintendent of Documents, U.S. Government Printing Office, Washington, D.C. 20402
Price $6.50
(Add 25 percent for other than U.S. mailing).

Foreword

This Special Publication contains summaries of papers to be presented at the Topical Conference on Basic Optical Properties of Materials to be held at the National Bureau of Standards in Gaithersburg, Maryland on May 5-7, 1980. The conference is sponsored by the National Bureau of Standards in cooperation with the Optical Society of America. This publication contains summaries of 62 papers which include 14 invited papers. The principal topical areas are:

Nonlinear Optical Properties
Ultraviolet Properties
Infrared Properties
Graded Index Materials
Inhomogeneous Materials
Properties of Thin Films
Optical Fibers
Planar Optical Waveguides
External Influences: Piezo-optics, Thermo-optics, Magneto-optics

The purpose of the conference is to discuss the state of the art in the measurement of the optical properties of optical materials. The emphasis is primarily on materials properties rather than on optical devices. The primary focus of the conference is on the measurement and theory of basic optical properties of materials in bulk, thin film,and fiber form.

The manuscripts for the conference have been prepared by the authors in camera-ready form, and any questions pertaining to their content should be addressed to those authors.

Albert Feldman
Chairperson

Acknowledgements

We wish to thank the following individuals for their invaluable assistance in preparing for the conference and this summary: Jeanmarie Bartlett, Marilyn Dodge, Barbara Hyde, Jo Ann Lorden, and Kathy Stang. Special thanks are due to Kimberly Morgan for organizing the mailings for the conference, and for editing and assembling the completed Summary of Papers. Thanks are due to the Word Processing Center of the National Measurement Laboratory for retyping several of the manuscripts.

Program and Editorial Committee

Albert Feldman - Chairperson
National Bureau of Standards

Edward Palik - Co-Chairman
Naval Research Laboratory

Michael I. Bell
National Bureau of Standards

Bernard Bendow
Rome Air Development Center

Harold E. Bennett
Michelson Laboratory
Naval Weapons Center

Arthur H. Guenther
Air Force Weapons Laboratory

Ivan P. Kaminow
Bell Telephone Laboratories

Robert V. Mohr
Catholic University

Alfred J. Thelen
Optical Coating Laboratory

Disclaimer

Certain commercial equipment, instruments, or materials may be identified in this publication in order to adequately specify the experimental procedure. In no case does such identification imply recommendation or endorsement by the National Bureau of Standards, nor does it imply that the material or equipment identified is necessarily the best available for the purpose.

CONTENTS

*Invited Speaker

POSTER PAPERS

GRADED INDEX AND INHOMOGENEOUS MATERIALS

PROPERTIES OF THIN FILMS I

Page

OPTICAL FIBERS

PROPERTIES OF THIN FILMS II

EXTERNAL INFLUENCES

PLANAR OPTICAL WAVEGUIDES

IMPORTANT AREAS OF OPTICAL MATERIALS RESEARCH

Harry V. Winsor
Maj., USAF
Defense Advanced Research Projects Agency
Arlington, VA 22209

This paper discusses the many areas of optical properties measurement improvement needed to develop the optical properties needed by advanced applications in energy, defense, communication, resources, surveillance, lasers, industrial processing, and optical system design and fabrication.

There are two central points to the talk:

- Optical systems are very special purpose, so each application may require information that is not apparent from the outset.
- The interaction of light with matter is very complex, leading to literally millions of measurable properties for each material.

In support of these two central points, several examples of critical optical properties will be discussed including, perhaps, topics from the following areas:

Solar energy systems properties
Thermal control coatings performance
High power laser windows and mirrors parametrics
Optical detector characterization
Fiber optics measurement
Non-linear conversion materials properties
Light emitting diodes and solid state lasers
Laser host materials behavior
Laser materials efficiency
Saturable absorber characterization
Photochemical reaction vessels design
Space environmental degradation
Radiation damage to optical materials
Temperature dependent optical properties
Acousto-optic coefficient
Electro-optic constants
Magneto-optic effects measurement
Stress-optic effects
Optical activity and its measurement
Chemical spectroscopy

Luminescence and fluorescence
Polarizers and polarization dependent phenomena

The examples (and others not discussed in detail) reveal an extraordinarily large optical measurements task which co-exists with a correspondingly large effort to optimize the relevant optical properties of optical materials. The talk will end with consideration of how these large problems can be systematically addressed by the optical research community.

PROPERTIES OF LOW-INDEX LASER MATERIALS

M. J. Weber
Lawrence Livermore Laboratory
University of California
Livermore, California 94550

The use of large, high-power lasers for inertial confinement fusion experiments has prompted the search for improved optical materials.[1] These include glasses and crystals for both passive components (lenses, windows, substrates) and active components (amplifiers, Faraday rotators). Neodymium-doped glass lasers, which operate at ≈ 1μm, have been the most widely used fusion lasers. Of major concern for these lasers are (1) the nonlinear optical properties, including intensity-dependent changes in the refractive index, multiphoton absorption, and damage processes, and (2) the spectroscopic properties of the active laser ion which affect energy storage and extraction and the overall lasing efficiency. To reduce self-focusing and beam breakup, materials for the amplifying medium and transmitting optics must have a small nonlinear refractive index n_2. This is characteristic of low-refractive-index materials. In the past few years, the optical properties and preparation of many low-index materials have been investigated. From this search, fluoride crystals and glasses have emerged as superior optical materials for short-pulse high-power lasers. Of these, fluorophosphate[2,3] and fluoroberyllate[4,5] glasses have received particular attention.

The large variety of inorganic glass forming systems[6] provides many opportunities to tailor materials for specific applications. Optical properties are generally most affected by the glass network former, however within a given glass type, further variations are possible by the selection of the network modifier cations. The optical properties of Nd^{3+} in hundreds of oxide, fluoride, and oxyfluoride glasses have been investigated to determine the range of variations possible by altering the host glass composition. Examples of the ranges of optical and spectroscopic properties observed for some common oxide and fluoride glasses are summarized in Table I. These represent values observed to date at the Lawrence Livermore Laboratory, but are not necessarily the extreme values possible. Depending upon the mode of operation and the environment of the laser, other physical and chemical properties may also be important. All of these properties are dependent, in varying degrees, on the chemical composition of the host.

Measurements of n_2 for a large class of oxide and fluoride crystals and glasses have been made using 100-ps, 1.06-μm laser pulses and time-resolved interferometry.[7] Values of n_2 for various glasses are summarized in Table I. These results established that low-index,

TABLE I. Observed variations of Nd laser glass properties. Spectroscopic properties are for the $^4F_{3/2} \rightarrow {}^4I_{11/12}$ transition.

Glass	NL Index $n_2(10^{-13}$ esu)	Cross Section $\sigma(pm^2)$	Linewidth $\Delta\lambda_{eff}$(nm)	Lifetime $\tau_R(\mu s)$
Silicate	$\geq$ 1.2	1.0-3.6	34-43	170-950
Phosphate	$\geq$ 1.0	1.8-4.7	23-34	320-560
Tellurite	> 10	3.0-5.1	26-31	140-240
Fluorophosphate	$\geq$ 0.5	2.2-4.3	27-34	350-600
Fluoroberyllate	$\geq$ 0.3	1.7-4.0	19-28	550-1000

low-dispersion materials have small n_2 values. These are materials having low atomic number anions and cations and small optical polarizabilities. Boling, Glass, and Owyoung[8] have discussed various empirical relationships that can be used to predict the nonlinear index based upon simple measurements of the linear index and dispersion. These relationships provide valuable guidance for screening materials.

For short pulse durations and large beam diameters, the principal refractive index nonlinearity arises from the optical Kerr effect. For longer pulses (> 1ns), electrostrictive effects may become important. These contributions have been found to be smaller for low-index materials.[9]

Most n_2 measurements in solids have been made at wavelengths far removed from the fundamental absorption edge. At shorter wavelengths, n_2 will increase due to resonant and nonresonant contributions to the wavelength dispersion of n_2.[10] This consideration is germane for fusion lasers such as KrF (248 nm) or the use of higher harmonics of Nd lasers (532, 355, 266 nm). At present, however, there is no data on the magnitude and functional dependence of the wavelength dependence of n_2.

Low-index materials are generally wide band gap materials.[11] Therefore materials selected to reduce self-focusing will probably also have small linear and nonlinear absorption. At ultraviolet wavelengths, most materials are subject to two-photon absorption (TPA). TPA coefficients at short wavelengths are known for only a few optical materials.[12] Measurements of TPA spectra of a variety of materials are needed to select laser materials with minimum losses at short wavelengths.

TABLE II. Comparison of Nd:fluoroberyllate laser glasses.

Composition (mol. %)	98 BeF_2 + 2 NdF_3	58 BeF_2 + 32 KF + 6 CdF_2 + 2NdF_3	47 BeF_2 + 27 KF + 14 CaF_2 + 10 AlF_3 + 2NdF_3
$^4F_{3/2} \rightarrow {}^4I_{11/12}$ Spectroscopic Properties:			
λ_p (nm)	1046	1048	1047
$\sigma(pm^2)$	2.0	3.8	3.2
$\Delta\lambda_{eff}$(nm)	27.7	20.1	23.2
$\tau_R(\mu s)$	920	600	610
Relative Small-Signal Gain Coefficient:[15]			
g (m^{-1})	7.8	17 (estimate)	14.8

Laser-induced damage thresholds of materials have also been found to vary with refractive index. Bettis, Guenther, and House[13] have measured damage thresholds for surfaces and thin films of many materials at 10.6 μm. They find a systematic increase in damage fluence with decreasing refractive index. Low-index fluoride materials have the highest damage thresholds. This behavior continued to hold at shorter wavelengths.[14]

Whereas low-index materials are clearly superior based on their nonlinear optical properties and laser-induced damage thresholds, for the amplifying medium, the effects of compositional changes on the spectroscopic properties must also be considered. From Table I we see that the Nd^{3+} stimulated emission cross section σ can be varied by more than a factor of 5. There are corresponding large changes in the radiative lifetime τ_R. For xenon flashlamp pumping, the population inversion obtainable in various glasses in a standard rest setup are comparable, but the small-signal gain coefficient varies because of the different σ values.[15] Therefore glasses having large cross sections, such as phosphates, have large gain coefficients. By varying the composition,

fluoroberyllate glasses having either small or large cross sections and gain coefficients are possible. Several examples are given in Table II and in Ref. 4. The spectroscopic variations achieved for Nd^{3+} should also be obtained for other rare-earth laser ions.

The absorption and emission spectra and gain profile of rare earths in glass are inhomogeneously broadened because of site-to-site differences in the local environment of the laser ion. This structural disorder is not evident in amplifiers operating under small-signal conditions, but under large-signal or saturated gain conditions, spectral hole burning may occur.[16] In addition, the energy extracted from an inhomogeneous system is always less than that obtainable from a homogeneous system having the same initial small-signal gain.

To minimize these effects, one seeks materials in which the ratio of the homogeneous to inhomogeneous linewidths is as large as possible. The effective fluorescence linewidth in Table I is a measure of a combination of the extent of the crystalline Stark splitting of the initial and final J manifolds and the inhomogeneous broadening. Of the glasses studied to date, fluoroberyllate glasses have the narrowest effective linewidths. Our knowledge of the effects of glass composition on the homogeneous linewidth, on the other hand, is still very limited. Laser-induced fluoroscence line narrowing techniques are used to measure the homogeneity of the spectroscopic properties in glass.[17] The homogeneous linewidths of oxide and fluoride glasses measured thus far do not differ greatly.[18] Therefore fluoroberyllate glasses should have good saturation properties. Additional studies of the homogeneous linewidths for a wider range of glasses are underway.[19]

Of the various low-index materials, fluoroberyllate glasses have the smallest refractive index nonlinearly and a large range of transparency. Inclusion-free materials have high damage thresholds.[20] Fluoroberyllate glasses have now been prepared by the Corning Glass Works[21] in sizes up to 20-cm diameter by 5-cm thick. The toxicity of beryllium necessitates special handling requirements for the melting and finishing of these glasses. The hygroscopicity of BeF_2 is well known, but by the addition of suitable modifier cations, the chemical durability can be greatly improved. Although the water solubility is still greater than for most commercial optical glasses, it is less than for many alkali halide optical crystals.[22]

Acknowledgements

Many colleagues at LLL have contributed to the results summarized in this paper. It is a pleasure to thank S. Brawer, C. Cline, D. Kingman, G. Linford, J. Lynch, D. Milam, R. Saroyan, W. L. Smith, and S. Stokowski for their contributions.

This work was performed under the auspices of the U.S. Dept. of Energy Office of Basic Energy Sciences and the Lawrence Livermore Laboratory under Contract No. W-7405-Eng-48.

References

[1]M. J. Weber, "Optical Materials for Neodymium Fusion Lasers," in *Critical Materials Problems in Energy Production*, ed. C. Stein (Academic Press, New York, 1976), p. 261.

[2]O. Deutschbein, M. Faulstich, W. Jahn, G. Krolla, and N. Neuroth, "Glass with a Large Laser Effect: Nd-Phosphate and Nd-Fluorophosphate," *Appl. Optics* 17, 2228 (1978).

[3]J. T. Wenzel, D. H. Blackburn, W. K. Haller, S. E. Stokowski, and M. J. Weber, "Development of Fluorophosphate Optical Glasses," SPIE Vol. 204, *Physical Properties of Optical Materials* (in press).

[4]C. F. Cline and M. J. Weber, "Beryllium Fluoride Optical Glasses: Preparation and Properties," *Wiss. Ztschr. Friedrich-Schiller-Univ. Jena, Math.-Nat. R.*, 28, Jg. H. 2/3, 351 (1979); also available as Lawrence Livermore Laboratory Rpt. UCRL-81168.

[5]K. H. Sun, "Fluoride Glasses," *Glass Technology* 20, 36 (1979).

[6]H. Rawson, *Inorganic Glass-Forming Systems* (Academic Press, London and New York, 1967).

[7]M. J. Weber, D. Milam, and W. L. Smith, "Nonlinear Refractive Index of Glasses and Crystals," *Opt. Engin.* 17, 463 (1978).

[8]N. L. Boling, A. J. Glass, and A. Owyoung, "Empirical Relationships Predicting Nonlinear Refractive Index Changes in Optical Solids," *IEEE J. Quantum Electron.* QE-14, 601 (1978).

[9]D. Heiman, R. W. Hellwarth, and D. S. Hamilton, "Raman Scattering and Nonlinear Refractive Index Measurements of Optical Glasses," *J. Non-Cryst. Solids* 34, 63 (1979).

[10]R. W. Hellwarth, "Third-Order Optical Susceptibilities of Liquids and Solids," in *Progress in Quantum Electronics*, Vol. 5 (Pergamon Press, London, 1977).

[11]S. H. Wemple, "Optical Oscillator Strengths and Excitation Energies in Solids, Liquids, and Molecules," *J. Chem. Phys.* 67, 2151 (1977).

[12]W. L. Smith, "Laser-Induced Breakdown in Optical Materials," *Opt. Engin.* 17, 489 (1978).

[13]J. R. Bettis, A. H. Guenther, and R. A. House II, "Refractive-Index Dependence of Pulsed-Laser-Induced Damage," *Optics Lett.* 4, 256 (1979).

[14]B. E. Newman and D. H. Gill, "Ultraviolet Damage Resistance of Laser Coatings," NBS Spec. Publ. 541, *Laser Induced Damage in Optical Materials: 1978*, p. 190.

[15]J. Linford, R. A. Saroyan, J. B. Trenholme, and M. J. Weber, "Measurements and Modeling of Gain Coefficients for Neodymium Laser Glasses," *IEEE J. Quantum Electron.* QE-15, 510-523 (1979).

[16]See, for example, V. I. Nikitin, M. S. Soskin, and A. I. Khizhnyak, "Influence of uncorrelated inhomogeneous broadening of the 1.06 μ band of the Nd^{3+} ions on laser properties of neodymium glasses," *Sov. J. Quantum Electron.* 8, 788 (1978).

[17]S. A. Brawer and M. J. Weber, "Observation of Fluorescence Line Narrowing, Hole Burning, and Ion-Ion Energy Transfer in Neodymium Laser Glass," *Appl. Phys. Lett.* 35, 31-33 (1979).

[18]J. Hegarty and W. M. Yen, "Optical Homogeneous Lindewidths of Pr^{3+} in BeF_2 and GeO_2 Glasses," *Phys. Rev. Lett.* 43 1126 (1979).

[19]J. M. Pellegrino, J. Hegarty, W. M. Yen, and M. J. Weber, "Composition Dependence of Nd^{3+} Homogeneous Linewidth in Glasses," *Bull. Amer. Phys. Soc.* (March, 1980) and to be published.

[20]W. H. Dumbaugh and D. W. Morgan (private communication).

[21]S. E. Stokowski, D. Milam, and M. J. Weber, "Laser Induced Damage in Fluoride Glasses: A Status Report," in NBS Spec. Publ. 541, *Laser Induced Damage in Optical Materials: 1978*, p. 99.

[22]C. F. Cline, D. D. Kingman, and M. J. Weber, "Durability of Beryllium Fluoride Glasses in Water: Comparison with other Glasses and Crystals, *J. Non-Cryst. Solids* 33, 417 (1979).

NONLINEAR OPTICAL SUSCEPTIBILITIES OF SEMICONDUCTORS AND OPTICAL BISTABILITY

H.M. Gibbs, S.L. McCall, T.N.C. Venkatesan,
A. Passner, A.C. Gossard, and W. Wiegmann
Bell Laboratories
Murray Hill, New Jersey 07974

The transmission of 500 ns pulses through GaAs-AlGaAs heterostructures has been studied as a function of light intensity and wavelength; see Fig. 1[1]. The intrinsic exciton absorption can be modeled by the sum of a small unsaturable background and a dominant term which saturates as a Bloch resonance; see Fig. 2. Corrections for the Gaussian transverse spatial profile and finite optical thickness lead to 150 W/cm^2 for the uniform-plane-wave saturation intensity for an optically thin GaAs exciton transition. The nearly Bloch-like saturation curve does not imply that the free exciton transition is a simple saturable two-level system, but does suggest that it saturates as a homogeneously broadened line.

A signal beam transmitted by a Fabry-Perot cavity can be modulated by a control beam which changes the refractive index of the intracavity medium. High finesse at the signal wavelength and strong absorption at the control wavelengths result in efficient optical gating and modulation. Such modulation has been observed using GaAs with detector-limited switch-on times of 1 ns and switch-off times of 2-20 ns and a physical length of only 5 μm; see Fig. 3.[2] In a succeeding paragraph, the refractive index extracted from these data is compared with that calculated from the nonlinear absorption measurements above.

Using these free exciton optical nonlinearities in GaAs, optical bistability has been observed in a semiconductor for the first time[1,3]; see Figs. 4 and 5. The bistability is primarily dispersive with the nonlinear refractive index arising from light-induced changes in exciton absorption. Using light of frequency just below the exciton peak, bistability was observed from 5 to 120°K with 40-ns turn-off and subnanosecond turn-on times with 1 mW/μm^2 holding intensity.

For many optical bistability applications, the larger the nonlinearity the better. If one calculates the change in refractive index $\Delta n \approx 10^{-2}$ for the intensity changes $\Delta I \approx 100$ kW/cm^2 used in the GaAs optical modulation and bistability experiments, one calculates $\Delta n/\Delta I \approx 10^{-4}$ cm^2/kW. This, of

course, is not n_2. Those experiments were performed at intensities far above the I_S=0.6 kW/cm^2 from Fig. 2. Presumably, this was necessary because the sample was ten times thicker and because the laser wavelength was 20 to 40 Å away from the exciton peak to reduce the unsaturable background absorption.

One may represent the contribution of the exciton resonance to the refractive index as

$$n_{EX}(\lambda) = \frac{(\alpha_{EX}\lambda/4\pi)\Delta\lambda/\delta\lambda}{1+\left(\frac{\Delta\lambda}{\delta\lambda}\right)^2+I/I_S}; \qquad (1)$$

the wavelength λ exceeds the wavelength of peak exciton absorption by $\Delta\lambda$, and $\delta\lambda$ is the width (HWHM) of the exciton resonance with peak absorption $\alpha_{EX}L$.

The nonlinear index n_2 can be calculated as dn_{EX}/dI for I=0:

$$n_2 = -\frac{\lambda\alpha_{EX}(\Delta\lambda/\delta\lambda)}{4\pi I_S(1+(\Delta\lambda/\delta\lambda)^2)^2}. \qquad (2)$$

This has extreme values for $\Delta\lambda=\pm\delta\lambda$: $|n_2|(\max)=\lambda\alpha_{EX}/16\pi I_S$; the value is 0.4 cm^2/kW for GaAs with α_{EX}=4/μm and I_S= 150 kW/cm^2 from Ref. 1. Values of α_{EX} as high as 6/μm have been seen.[1] There is considerable hope that thinner GaAs etalons can be constructed with sharper exciton features and less background absorption permitting bistable operation much closer to the exciton resonance and with much lower input intensities.

A subsequent observation of optical bistability in a semiconductor was reported recently by Miller, Smith, and Johnston using an uncoated 560-μm long etalon of InSb at 5°K.[4] They find n_2 is 10^{-2} to 10^{-1} cm^2/kW.

A large n_2 is desirable if one wants to reduce the holding intensity, but the time response of n_2 is crucial for fast devices. In GaAs, the saturation which turns on the bistability can be subpicosecond[5], but the recovery once the light is removed seems to be governed by the carrier lifetime which can be nanoseconds unless shortened by impurities or defects.[2] Switching times for the InSb bistability have not been reported.

[1] H. M. Gibbs, A. C. Gossard, S. L. McCall, A. Passner, W. Wiegmann, and T.N.C. Venkatesan, Solid State Commun. 30, 271 (1979).

[2] H.M. Gibbs, T.N.C. Venkatesan, S.L. McCall, A. Passner, A.C. Gossard, and W. Wiegmann, Appl. Phys. Lett. 34, 511 (1979).
[3] H.M. Gibbs, S.L. McCall, T.N.C. Venkatesan, A.C. Gossard, A. Passner, and W. Wiegmann, CLEA:IEEE J. Quantum. Electron. QE-15, 108D (1979) and Appl. Phys. Lett. 35, 451 (1979).
[4] D.A.B. Miller, S.D. Smith, and A. Johnston, Appl. Phys. Lett. 35, 658 (1979). D.A.B. Miller and S.D. Smith, Opt. Commun. 31, 101 (1979).
[5] C.V. Shank, R.L. Fork, R.F. Leheny, J. Shah, Phys. Rev. Lett. 42, 112 (1979).

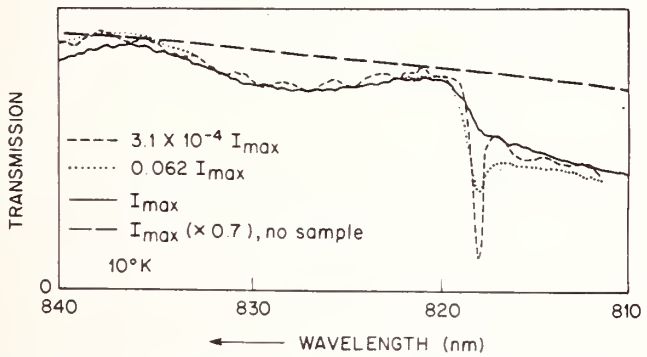

Fig. 1 Nonlinear transmission of 500 ns pulses through an antireflection-coated $Al_{0.24}Ga_{0.76}As$-GaAs-$Al_{0.24}Ga_{0.76}As$ heterostructure with layer thicknesses in μm of 2.38-0.42-3.33, respectively. $I_{max} \simeq 43$ kW/cm^2.

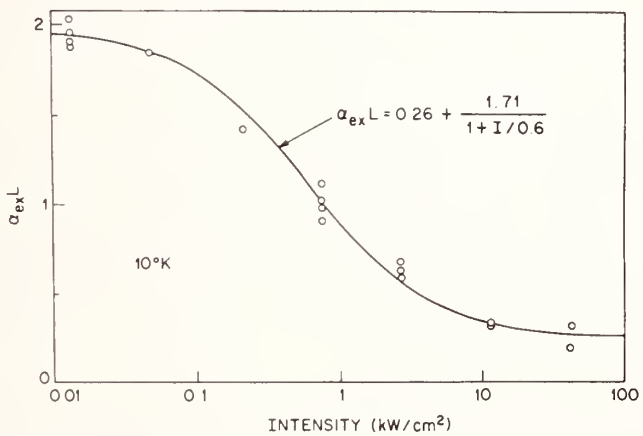

Fig. 2 Saturation of the free exciton resonance in GaAs with 500 ns pulses of wavelength equal to the wavelength of peak exciton absorption. The solid curve is a least squares fit of $\alpha L=A[1+B/(1+I/I_S)]$, which yielded $A=0.257\pm0.033$, $B=6.65\pm0.99$, and $I_S=0.605\pm0.064$ kW/cm^2.

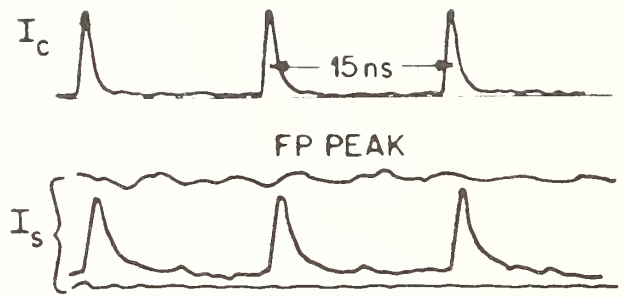

Fig. 3 Control of a 10-mW cw dye laser beam I_S (λ_S=821.3nm) by 2.5-W 200-ps modelocked Ar pulses I_C (λ_C=514.5 nm). The device consists of a molecular-beam, epitaxially-grown sandwich of 4.1 μm of GaAs between 0.21 μm thick $Al_{0.42}Ga_{0.58}As$ windows with reflectivities of 0.9 and 0.25 at λ_S and λ_C, respectively.

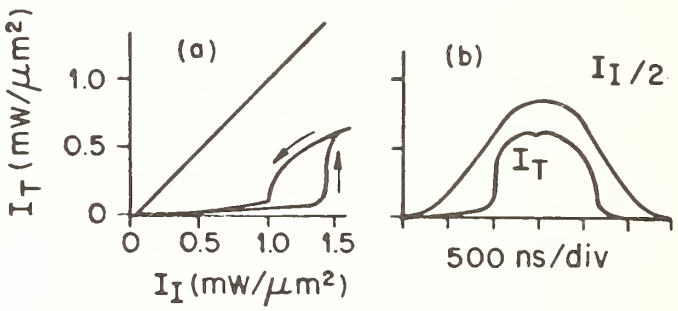

Fig. 4 Excitonic optical bistability in GaAs at 15°K and 819.9 nm laser wavelength. Bistability as seen in (a) x-y display and (b) time display. The 45° line in (a) shows etalon transmission at the next etalon peak (≈830 nm).

Fig. 5 Approximate GaAs absorption αL(a), roundtrip phase shift ϕ(b), and Fabry-Perot transmission under conditions of optical bistability (c) and Fig. 4. The solid curves are for zero input intensity where the exciton absorption is fully effective. The dashed curves are for intensities which are high enough to saturate the exciton feature, but low enough to leave the band-to-band contributions to α and ϕ unaffected. The peak absorption $\alpha_{EX}L$ at the exciton resonance was 10 in our sample.

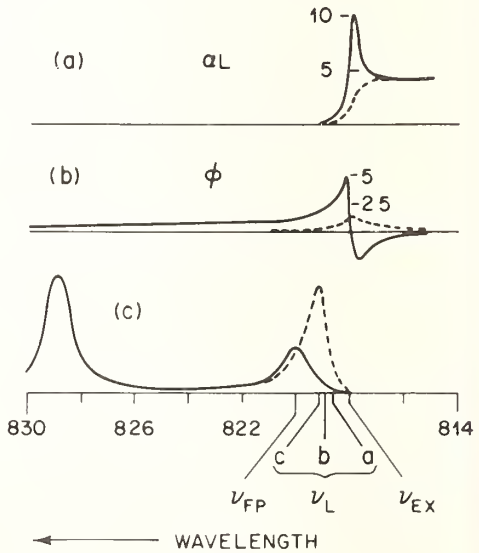

BAND STRUCTURE CALCULATIONS OF THE TWO-PHOTON ABSORPTION COEFFICIENTS OF InP AND CdTe

A. Vaidyanathan and A. H. Guenther
Air Force Weapons Laboratory
Kirtland AFB, NM 87117

and

S. S. Mitra
Department of Electrical Engineering
University of Rhode Island
Kingston, R. I. 02881

In the last two decades there have been numerous theoretical and experimental studies of two-photon absorption coefficients in crystalline solids. In spite of these extensive investigations, a generally accepted quantitative description of two-photon absorption has not been achieved even for the case of the simplest semiconductors, as is evidenced by the unacceptably large disparity between theoretical estimates and available experimental measurements. These differences stem in part from the simplifying models employed to describe the electronic band structures and oscillator strengths. In an attempt to improve this situation we have calculated the two-photon absorption coefficients of crystalline InP and CdTe by first computing their electronic band structures by means of the empirical pseudopotential method (EPM), followed by a numerical evaluation of the two-photon transition probability employing second-order perturbation theory.

We start with the following expression for the transition probability rate of an electron in a solid, with direct energy gap E_g, from an initial valence band state $|v\vec{k}\rangle$ to a final conduction band $|c\vec{k}\rangle$ by the simultaneous absorption of two photons whose frequency is such that $2\hbar\omega \geq E_g > \hbar\omega$

$$W = \frac{2\pi}{\hbar} \int \frac{d^3\vec{k}}{(2\pi)^3} \left| \sum_n \frac{H_{vn} H_{nc}}{E_{vn}(\vec{k}) - \hbar\omega} \right|^2 \delta\left(E_{vc}(\vec{k}) - 2\hbar\omega\right) . \qquad (1)$$

In eq. (1) E_{vi} (i = c,n) is the energy separation between bands v and i at wave vector $\vec{k}$, the summation n is over all intermediate states, and the $\vec{k}$ integral extends over the entire first Brillouin zone. The H_{ij}'s occurring in eq. (1) are the Hamiltonian matrix elements given by

$$H_{ij} = \frac{2\pi\hbar e^2 N |P_{ij}|^2}{m^2 \omega} , \qquad (2)$$

where N is the photon number density and the P_{ij}'s are appropriate momentum matrix elements.

It is obvious from eqs.(1) and (2) that to evaluate the two-photon transition probability, knowledge of the electronic energies and wave functions throughout the first Brillouin zone is needed. We obtain these by carrying out EPM calculations of the energy bands, using available pseudopotential form factors. In order to numerically integrate eq. (1) we convert the delta function in energy to a delta function in wave vector by use of the following relation:

$$\delta\left(E_{vc}(\vec{k}) - 2\hbar\omega\right) = \sum_{\ell} \frac{\delta(\vec{k}-\vec{k}_{\ell})}{\left|\vec{\nabla}_{\vec{k}} E_{vc}(\vec{k})\right|} , \qquad (3)$$

where $\vec{k}_{\ell}$ represents all values of $\vec{k}$ for which $E_{vc}(\vec{k}) = 2\hbar\omega$. The momentum matrix elements are obtained from the relation:

$$\left|\vec{P}_{ij}\right|^2 = \left| \langle j,\vec{k} \left| \frac{\hbar}{i} \vec{\nabla}_{\vec{r}} \right| i,\vec{k} \rangle \right|^2 , \qquad (4)$$

where $|i,\vec{k}\rangle$ and $|j,\vec{k}\rangle$ are the Bloch functions of the states i and j at wave vector $\vec{k}$. We then calculate the two-photon transition probabilities of InP and CdTe by including the transitions originating from the three highest valence bands (which are degenerate at $\vec{k} = 0$ in the absence of spin-orbit splitting), and ending in the lowest conduction band. The intermediate states in the highest 4 valence bands and lowest 31 conduction bands were included in the summation in equation (1), resulting in a convergency better than 0.01%. Finally, the two-photon absorption coefficient (β) is obtained from the two-photon transition probability rate by use of the following expression.

$$\beta = \frac{2 W 2\hbar\omega}{I^2}, \qquad (5)$$

where I is the intensity of the radiation.

The resulting values of β for InP and CdTe are reported in Table I, together with available experimental data and the results of earlier theoretical calculations.

Table I. Two-Photon Absorption Coefficients of CdTe and InP in units of (cm/MW)

Crystal	Wavelength (μm)	THEORETICAL					EXPERIMENTAL
		Keldysh[a]	Braunstein[b]	Basov[c]	Lee and Fan[d]	Present	
InP	1.064	0.026	0.008	0.0003	0.096	0.722	0.18-0.26[d]
CdTe	1.064	0.023	0.007	0.0005	---	0.201	0.02-0.3[e]

a. L. V. Keldysh, Sov. Phys. JETP 20, 1307 (1965).
b. R. Braunstein and N. Ockman, Phys. Rev. 134, A499 (1964); see also S. S. Mitra, L. M. Narducci, R. A. Shatas, Y. F. Tsay, and A. Vaidyanathan, Appl. Opt. 14, 3038 (1975).
c. N. G. Basov, A. Z. Grasyuk, I. G. Zubarev, V. A. Katulin, and O. N. Krokhin, Sov. Phys. JETP 23, 366 (1966). Also, A. Vaidyanathan, T. W. Walker, A. H. Guenther, S. S. Mitra, and L. M. Narducci, Phys. Rev. B (in press).
d. C. C. Lee and H. Y Fan, Phys. Rev. B 9, 3502 (1974).
e. J. M. Ralston and R. K. Chang, Opto-electronics 1, 182 (1969); J. H. Bechtel and W. L. Smith, Phys. Rev. B13, 3515 (1976); S. J. Bepko, Phys. Rev. B12, 669 (1975); and M. Bass, E. W. Van Stryland, and A. F. Stewart, Appl. Phys. Lett. 34, 142 (1979).

Acknowledgement

This research was supported in part by an Air Force Systems Command-National Research Council Postdoctoral Resident Research Associateship (A.V.).

MEASUREMENT AND INTERPRETATION OF ULTRAVIOLET OPTICAL PROPERTIES OF SOLIDS

David W. Lynch
Ames Laboratory-USDOE and Department of Physics
Iowa State University, Ames, Iowa 50011

This paper reviews methods of measuring the optical properties of solids in the energy range above 6eV and some of the experimental problems encountered. General interpretations are discussed with some examples. References prior to 1978 may be found in references 1 and 2.

Above 6eV, measurement techniques become somewhat limited compared with those used in the visible region because of the limited number of transparent materials. Special problems arise in making polarizers which are highly efficient over a large wavelength range, and transparent materials, other than unsupported thin films, are not available for use above 11eV as substrates for thin films. The advent of synchrotron radiation has ameliorated problems associated with sources above 6eV. It usually provides a known state of polarization as well. The problems associated with the samples themselves often become more severe above 6eV. Thin film samples may incorporate oxygen during their preparation, and the 2p electrons of oxygen absorb strongly from 6eV to very high energies, 75eV or more. Both thin film and bulk samples may have surface oxides as well, and the correction for such an overlayer is far less reliable when it is an absorbing oxide instead of a transparent one. Finally, surface roughness often has a more deleterious effect on reflectance data at shorter wavelengths. The ideal measurement has not yet been made, one in which the sample surface was shown to be clean, e.g., by Auger spectroscopy, unstrained, e.g., by LEED, and flat, e.g., by measuring scattered light, during the measurement of the optical properties.

Measurements of optical properties fall into three general classes.

1. Ellipsometry. Such methods appear to have been used only once in the vacuum ultraviolet.[3] Although synchrotron radiation is polarized, the need to analyze refelected radiation with a polarizer of low efficiency and limited spectral range makes ellipsometric methods unattractive.
2. Photometric reflectance. One either measures the reflectance at one angle over a wide energy range and Kramers-Kronig analyzes the reflectance (by far the most popular method) or fits it to a series of oscillators, or one measures the reflectance at several angles of incidence and uses the Fresnel equations to obtain the optical constants. One then must know the state of polarization of the incident radiation or treat it as a third unknown. In at least one case it has not been very constant during the course of the measurements.[4] In addition

to the effects of surface roughness and oxides mentioned above, additional errors can arise for insulators from luminescence. A detector which scans continuously over angle can detect luminescence and surface scattering. It can be eliminated in some cases by suitable choice of detectors, and in some cases by gating the detectors and using the pulsed nature of synchrotron radiation. At energies above about 30eV the reflectance of most materials falls to very low levels. To maintain accuracy the measurements must be made at large angles of incidence, necessitating larger samples.

3. Photometric transmission. Above 30eV the reflectance is usually so low that corrections for multiple reflections are negligible. Transmission measurements on samples of different thicknesses then give absorption coefficients which can be KK analyzed to get the refractive index.

There are other methods. Characteristic electron energy losses can be analyzed to get optical constants and this method is an excellent one for anisotropic materials, especially highly anisotropic layered materials [5] for which most of the above-mentioned methods give poor results for $\vec{E} \parallel \vec{c}$. The total yield of photoelectrons gives a spectrum generally proportional to the absorption coefficient spectrum, but in arbitrary units, above an energy of about 20eV. Finally, modulation spectroscopic methods can be used to at least 200eV to measure the dependence of optical properties on applied uniaxial stress, and electric and magnetic fields, and on temperature.

The accuracy of the resultant optical constants is difficult to determine, being so strongly dependent on the degree to which the actual sample approaches the ideal. Kramers-Kronig integrals and resultant sum rules and "super" sum rules can be very useful in determining consistency, but only when data believed to be reliable extend over a very wide energy range. Such consistency tests work rather well for Al, but not for Au, and they have been carried out for very few other materials.

Above 6 to 10eV the reflectance of most solids falls with increasing photon energy, and the anisotropy of the optical constants diminishes, then disappears. If there are core levels deep enough so that they do not exhibit band effects, deeper than about 10eV, the reflectance and absorption will increase at the threshold for the core level. The core levels are usually spin-orbit split so the measured spectra must be separated into two components before interpretation. The core levels have definite angular momenta and are localized on one atomic site. The selection rules for the excitation at their simplest make the spectrum resemble one component of the angular-momentum-and site-decomposition of the density of empty states. The strong localization also causes the oscillator strength to be spread over a very wide energy range. The localization of the transitions makes such core level studies promising for the stody of alloys, but the lack of satisfactory interpretation in the cases in which it has been employed makes future utility doubtful.

The core edges do however, offer some novel features. For both semiconductors and insulators, core excitons can form and the binding energy may be quite high because of the extreme localization of the exciton. In the case of semiconductors the binding energies are higher than can be understood at present [6]. Also for semiconductors the core excitons can be used to study the conduction band by itself, something not possible with conventional uv spectroscopy which uses the highly dispersed valence band for initial states. In metals many-body effects cause additional structure at the soft x-ray core edges in simple metals, while Coulomb-induced coupling of quasi-discrete and continuum transitions causes unusual line shapes for core edges of metals with incomplete d-shells. All these phenomena may be studied by modulation spectroscopy.[7,8]

Many soft x-ray core transitions exhibit extended x-ray absorption fine structure (EXAFS) similar to that seen above deep core x-ray edges, but the structure is usually overlapped by other nearby soft x-ray core edges.

If there are no core levels in the 5-30eV range the reflectance may still rise at some threshold. This is the case with most transition metals and with noble metals. Here there are bands lying 5-15eV above the Fermi level, bands which are not free-electron like. These bands are relatively flat and transitions to them cause an increase in the absorption. They begin at an energy which depends, to first order, primarily on the crystal structure. As far as is known, such flat bands do not form in a number of transition metal compounds, e.g., TiC, A-15-structured superconductors, and Na_xWO_3, but the reason is not always the greater spacing between the transition metal ions.

The falloff in reflectance often signifies a plasma edge as in the case of a free-electron gas. One can plot the loss function for the excitation of volume longitudinal excitations, $Im(-1/\tilde{\varepsilon})$, which is the zero wave-vector limit of a more general function best measured by the inelastic scattering of fast electrons. We have found that most transition metals have two distinct peaks in both the volume and the surface loss functions. The larger is always near the free electron plasmon energy, counting the d and the s-p electrons. The other is always lower in energy, lying in the absorption minimum just below the threshold energy for the excitation of electrons into the high-density bands mentioned above. This peak represents some sort of screened plasmon, the collective motion of a group of electrons whose mutual Coulomb interaction is screened by other electrons. For transition metals one cannot identify the groups of electrons from only data. They may be just the d- electrons, just the s,p- electrons or neither. In layered semiconductors a similar phenomenon occurs, but the groups of electrons there are better defined, being bonding and non-bonding valence electron-. The occurrence of two volume plasmons is easily seen from a macroscopic dielectric model, but a microscopic interpretation is still lacking. The optical data are of considerable aid in understanding the

electron energy loss data, for in reactive materials the energy loss measurements are usually made with reflected electrons.[9] The volume and surface losses cannot be separated easily, and their spectral features are known to overlap severely.

This work was supported by the U.S. Department of Energy, contract No. W-7405-Eng-82, Division of Materials Science budget code AK-01-02-02-2.

References

1. D. W. Lynch, J. de Physique 39, C4-125 (1978).

2. D. W. Lynch in C. Kunz, ed., Topics in Current Physics, Vol. 10, "Synchrotron Radiation, Techniques and Applications" (Springer-Verlag, Berlin, 1979), Chapter 7.

3. M. Schlederman and M. Skibowski, Appl. Opt. 10, 321 (1971).

4. D.Beaglehole, M. De Crecenzi, M. L. Thèye, and G. Vuye, Phys. Rev. B19, 6303 (1979).

5. C. H. Chen and J. Silcox, Phys. Rev. B20, 3605 (1979).

6. A. Quattropani, F. Bassani, G. Margaritondo, and G. Tinivella, Il Nuovo Cim. 51B, 335 (1979).

7. C. G. Olson and D. W. Lynch, Solid State Comm. 31, 601 (1979).

8. C. G. Olson and D. W. Lynch, to appear in Solid State Comm.

9. W. K. Schubert and E. L. Wolf, Phys. Rev. B20, 1855 (1979).

THE OPTICAL PROPERTIES OF KAPTON: MEASUREMENT AND APPLICATIONS*

L. R. Painter,† E. T. Arakawa, M. W. Williams, and J. C. Ashley
Health and Safety Research Division
Oak Ridge National Laboratory
Oak Ridge, Tennessee 37830

Kapton Type H polyimide film[1] is used extensively in situations demanding good electrical insulation, radiation resistance, and/or chemical resistance, particularly at high operating temperatures. At room temperature the physical properties of Kapton are similar to those of Mylar polyester film[1], but Kapton is less affected by temperature changes and is also ≈50 times more resistant to radiation damage than Mylar. In fact, Kapton has been found to retain its useful properties over the wide temperature range from -269°C to +400°C. In view of its extensive use, measurements of the optical properties of Kapton and calculations of the transport parameters for ionizing radiations, particularly low energy electrons, in Kapton are of interest.

We have found over the past decade that the most satisfactory way to obtain the absorption spectrum of an organic material over an extended wavelength region that includes essentially all of the oscillator strength of the valence electrons is by transmission measurements. Unfortunately methods developed for obtaining samples of organic materials suitable for transmission measurements at wavelengths below

---

*Research sponsored jointly by the Deputy for Electronic Technology, Air Force Systems Command, under Interagency Agreement DOE No. 40-226-70 and the Office of Health and Environmental Research, U.S. Department of Energy, under contract W-7405-eng-26 with the Union Carbide Corporation.

†Also Department of Physics and Astronomy, University of Tennessee, Knoxville, Tennessee 37916.

[1]Manufactured by E. I. du Pont de Nemours and Company.

the UV absorption edge (1-4), in which uniform thin films of an organic material have been obtained by vacuum evaporation or from a solution of the material in a suitable solvent, cannot easily be applied to Kapton. Kapton is available[1] as Type H film with nominal thicknesses from 7.6×10^{-6} m to 1.27×10^{-4} m. Such films are too thick for transmission measurements in the vacuum UV region. The optical properties of Kapton were thus obtained for wavelengths in the range of 16.3 nm to 2500 nm from reflectance measurements on Kapton films stretched over a sample holder. At each wavelength the measured reflectance as a function of the angle of incidence was least-squares fit to Fresnel's equations to yield the real and imaginary parts of the complex refractive index, $\tilde{n} = n + ik$, and of the complex dielectric function, $\tilde{\varepsilon} = \varepsilon_1 + i\varepsilon_2$. At photon wavelengths where the extinction coefficient k is zero, normal incidence reflectance and transmittance were measured and a direct calculation made of the refractive index n. Transmission measurements on the thinnest Kapton films in the wavelength region of the ultraviolet absorption edge were also used to calculate k values in the region of the edge. Measurements were made with a spectrophotometer (Cary Model 14) in the 2500 nm to 300 nm range, a Seya-Namioka monochromator (McPherson Model 235) in the 620 nm to 82.7 nm range and with a grazing-incidence monochromator (McPherson Model 247) in the 95.4 nm to 16.3 nm range. Below 165 nm, measurements were made using line sources (hydrogen discharge and a condensed air spark) while above 165 nm continuum sources were employed. The estimated uncertainties on the values obtained for n and k were everywhere $\lesssim \pm 6\%$.

As a test of the general validity of the data obtained, the measured k values for Kapton, which has a monomeric unit of $\{C_{22}H_{10}N_2O_4\}$, were combined with estimated values of k at shorter wavelengths to form a spectrum extending over the oscillator strength of both valence and core electrons. The values of k due to valence electrons were extrapolated to lower wavelengths and estimations (4) made of superimposed structure in k due to the C, N, and O K-shell electrons. A Kramers-Kronig analysis of this k-spectrum (3,4) yields n-values in the experimental

region which agree with the measured values within the estimated uncertainties associated with the measurements. As a further overall check on the values of k over the entire wavelength range, the "k sum-rule" (3,4) was performed on these data and yields a total number of electrons consistent with the known number of valence plus core electrons per monomeric unit of 188. Thus the optical constants over the whole wavelength range, arrived at by a combination of measurements and estimations, are internally self-consistent. These data were then used, as previously demonstrated for polystyrene (5,6) and polyethylene (4), to calculate values of the mean excitation energy of Kapton, electron mean free paths in Kapton, and the stopping power of Kapton for electrons.

Values of the mean free paths in Kapton for electrons of energies from $\approx 1.6\times10^{-17}$ J to $\approx 1.6\times10^{-15}$ J were calculated from the variation with photon wavelength of the energy loss function, $\mathrm{Im}[-1/\tilde{\varepsilon}]$, obtained from the measurements of $\tilde{\varepsilon}$. The values agreed with those predicted by a recently proposed (7) simple expression for calculating electron mean free paths, Λ, in solid organic insulators, i.e.,

$$\Lambda \frac{n\rho}{M} = f(E),$$

where n is the number of valence electrons per monomeric unit, ρ the density of the material, M the molecular weight of the monomeric unit, and E the energy of the incident electron. This expression was based on a theoretical formula for mean free path with input parameters derived from the experimental optical properties of six organic insulators -- the only data then available which extended over a sufficiently wide wavelength range. The agreement of the values of Λ obtained by calculations based on the optical properties, $\tilde{\varepsilon}$, of Kapton and from the simple expression for Λ given in Ref. 7 assuming a density of 1.42×10^{3} kg/m^3 for Kapton[2], increases our confidence both in the measured values

[2]Electrical Insulation Products Division Du Pont Film Department, Bulletin H-1D.

of the optical properties of Kapton which were difficult to obtain accurately and in the simple expression for electron mean free paths in solid organic insulators which was based on only six materials.

REFERENCES

1. T. Inagaki, R. N. Hamm, E. T. Arakawa, and L. R. Painter, Optical and dielectric properties of DNA in the extreme ultraviolet. *J. Chem. Phys.* 61, 4246-4250 (1974).

2. T. Inagaki, R. N. Hamm, E. T. Arakawa, and R. D. Birkhoff, Optical properties of bovine plasma albumin between 2 and 82 eV. *Biopolymers* 14, 839-847 (1975).

3. T. Inagaki, E. T. Arakawa, R. N. Hamm, and M. W. Williams, Optical properties of polystyrene from the near-infrared to the x-ray region and convergence of optical sum rules. *Phys. Rev. B* 15, 3243-3253 (1977).

4. L. R. Painter, E. T. Arakawa, M. W. Williams, and J. C. Ashley, Optical properties of polyethylene: measurement and applications. Accepted for publication by *Radiation Research*.

5. J. C. Ashley, Mean excitation energy of polystyrene. *Phys. Rev. B* 19, 5429-5430 (1979).

6. J. C. Ashley, C. J. Tung, and R. H. Ritchie, Inelastic interactions of electrons with polystyrene: calculations of mean free paths, stopping powers, and csda ranges. *IEEE Trans. Nucl. Sci.* NS-25, 1566-1570 (1978).

7. J. C. Ashley and M. W. Williams, Electron mean free paths in solid organic insulators. Accepted for publication by *Radiation Research*.

OPTICAL PROPERTIES OF TiC_x ($0.64 \leq x \leq 0.90$) FROM 0.1 TO 30eV

D. W. Lynch, C. G. Olson and D. J. Peterman
Ames Laboratory-USDOE and Department of Physics
Iowa State University, Ames, Iowa 50011
and
J. H. Weaver
Synchrotron Radiation Center, University of Wisconsin-Madison,
Stoughton, Wisconsin 53589

The absorptance of four bulk samples of TiC_x were measured in the 0.1-4.6eV energy range and the reflectances measured between 4 and 30eV. For x=0.64 the sample was polycrystalline, previously fused, while single crystals were used for x=0.833,0.90, and 0.97. All samples were electropolished before measurements. The samples for x=0.64 and 0.90 were large enough so that absolute data could be obtained for Kramers Kronig analysis. The reflectances and absorptances of the other two samples are in arbitrary units.

Our data are in poor agreement with earlier data on sintered samples[1] and with infrared and visible data on single crystals,[2] but in general agreement with vuv data on single crystals.[2] Figure 1 shows the reflectances of our samples while the optical conductivity obtained by KK analysis for two samples is shown in Fig. 2. From these figures one can see that there is a one-for-one correspondence of the structures in the reflectance and the conductivity so the trends with stoichiometry can be followed meaningfully in the reflectance spectra. The partial sum rule on ε_2 shows that about 4.3 electrons per molecule contribute to optical absorption between 0.4 and 30eV for x=0.90 vs 4.1 for x=0.64. Interband absorption occurs at very low energies, down to 0.1eV, so meaningful Drude parameters cannot be extracted.

Discussions of bonding in TiC and related compounds have a long history. We attempted to explain our data on the basis of two recent band calculations [3,4] and had more success with the latter of the two, which was self-consistent. The lowest curve in Fig. 2 shows the calculated joint density of states for TiC (x=1) calculated from parameterization of the bands of Ref. 4, which are shown in Fig. 3. The agreement is surprisingly good. The strong absorption in the 1-10.7eV region arises from transitions between bands based on Ti 3d and C 2p levels. Their exhaustion occurs at the minimum in the conductivity at 10.7eV. The rise at higher energy is due to transitions from the C 2s band, the lowest band in Fig. 3. The calculated structures appear too sharp, no lifetime broadening having been included. A detailed assignment to particular regions of reciprocal space is premature.

Most of the stoichiometry dependence occurs above 5eV. Above 10.7eV the transitions primarily originate on the C 2s levels and their conductivity should then fall as x decreases. This occurs, but the final states, which involve hydridized Ti 3d and C 2p levels should change as well. (Also the Fermi level should move, but there is no evidence in our data for the validity of the simple rigid band model.) The low energy peak at 1.3eV does not change as x changes. It appears to be a transition between parallel bands cut by the Fermi level, e.g., along Λ in Fig. 3.

Figure 4 shows the electron energy loss functions for volume and surface longitudinal excitations. (No electron energy loss spectra have been reported for TiC.) The high energy peak in the volume loss function is near the free electron plasmon energy, calculated with the 2s and 2p electrons of C as well as three electrons per Ti. The lower energy "plasmon" occurs at the minimum in the conductivity. The surface loss function peaks are at lower energies than those in the volume loss function, but are not related by a factor of $1/\sqrt{2}$ as for a free electron gas. The low energy peaks in the volume and surface loss functions overlap and would not be resolved in electron energy loss spectra measured in reflection.

This work was supported in part by the U.S. Department of Energy, contract No. W-7405-Eng-82, Division of Materials Sciences, budget code AK-01-02-02-2 and in part by the National Science Foundation under contract DMR 7821080.

The single crystals of TiC_x were kindly supplied by Wendell S. Williams of the University of Illinois. The polycrystalline sample was produced by F. A. Schmidt of the Ames Laboratory. The storage ring is operated by the Synchrotron Radiation Center, University of Wisconsin-Madison, under contract DMR 7721888 from the National Science Foundation. We thank K. H. Schwarz and A. C. Switendick for supplying us with a table of energy eigenvalues.

References

1. J. F. Alward, C. Y. Fong, M. El-Batanouny, and F. Wooten, Phys. Rev. B 12, 1105 (1975); Solid State Comm. 17, 1063 (1975).

2. R. G. Lye and E. M. Logothetis, Phys. Rev. 147, 622 (1966).

3. V. Ern and A. C. Switendick, Phys. Rev. 137, A1927 (1965).

4. A. Neckel, P. Rastle, R. Eibler, P. Weinberger, and K. Schwarz, J. Phys. C. 9, 579 (1976).

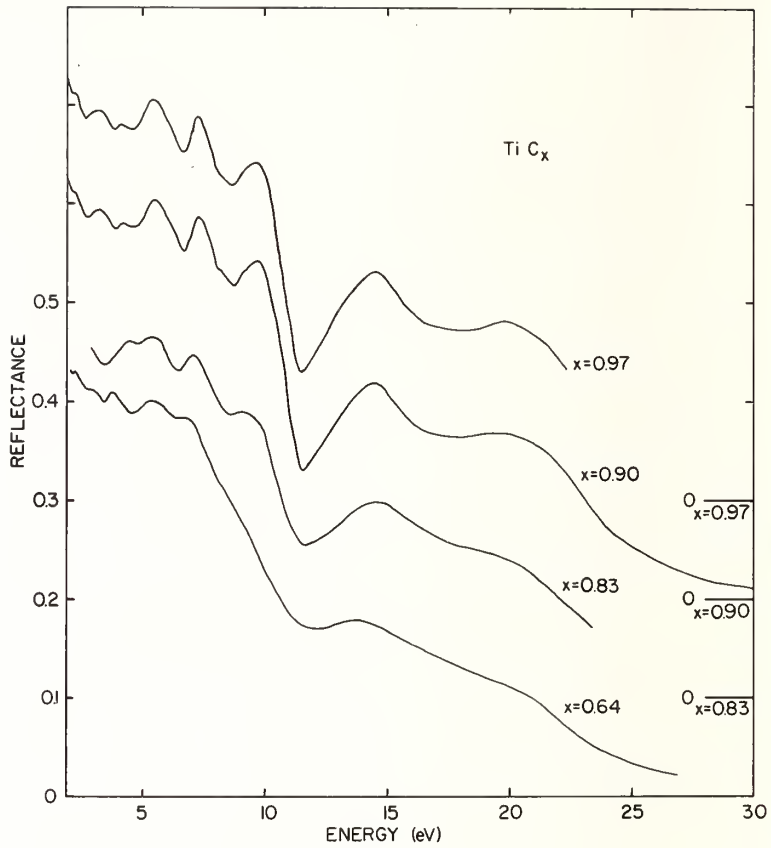

Figure 1.

Reflectance spectra of TiC for several stoichiometries. Reflectance scales for x=0.83 and 0.97 have been adjusted and are essentially arbitrary.

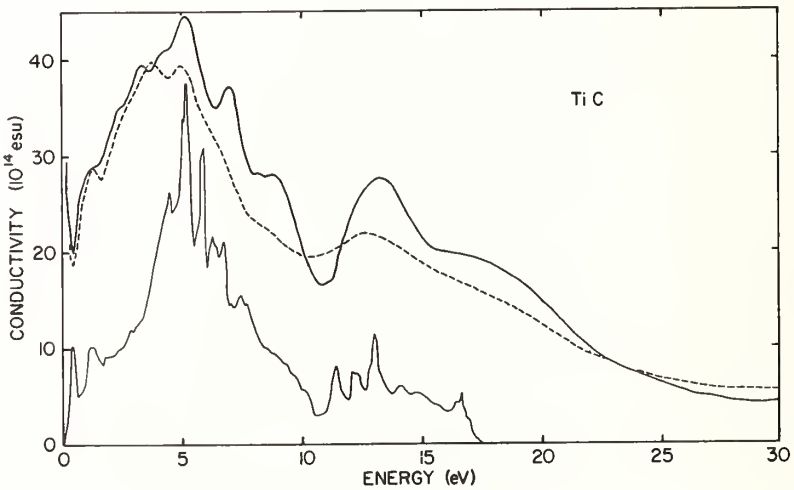

Fig. 2. Optical conductivity of TiC_x. Solid: x=0.90, dashed, x=0.64. Obtained from the date of Fig. 1 by Kramers-Kronig analysis. The lowest curve is the conductivity for x=1 calculated without dipole matrix elements from the bands of Ref. 4 (Fig. 3).

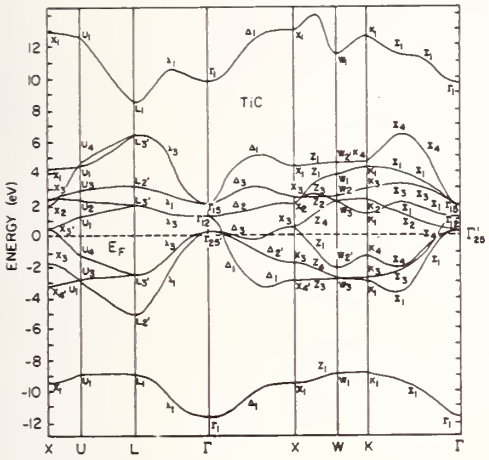

Figure 3.

Calculated electronic energy bands of stoichiometric TiC (Ref. 4).

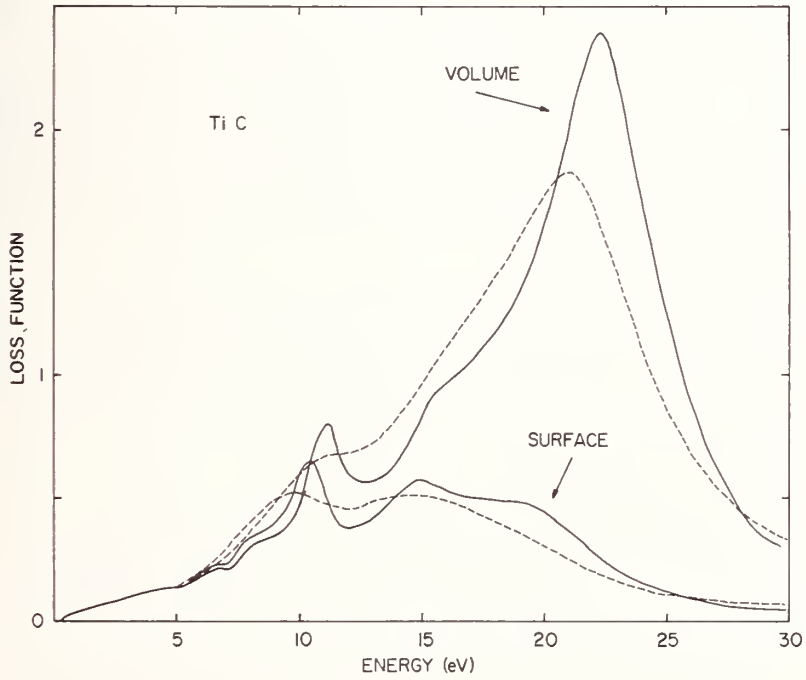

Figure 4. Electron energy loss functions, $Im(-1/\tilde{\varepsilon})$ (volume) and $Im(-1/(\tilde{\varepsilon}+1))$ (surface) for TiC_x. Solids, x=0.90; dashed, x=0.64.

SUPERCONVERGENCE RELATIONS AND THE ANALYSIS OF OPTICAL DATA*

D. Y. Smith§
Physikalisches Institut der Universität Stuttgart
7 Stuttgart 80, Germany
and
Argonne National Laboratory
Argonne, Illinois 60439, U. S. A.
and
E. Shiles
Virginia Commonwealth University
Richmond, Virginia 23284, U.S.A.

Recent studies have shown that the optical constants satisfy a large number of sum rules in addition to the well-known f sum rules. These provide tests of agreement with both theoretical constraints and independently measured quantities. They are particularly valuable in combining optical measurements obtained by different techniques to form composites of data covering a wide spectral range. In conjunction with an iterative self-consistent Kramers-Kronig procedure, optical sum rules have been used to analyze the optical properties of Al, Si and GaAs. This approach has made it possible to select the most probable values from the available optical measurements and has pinpointed a number of systematic experimental errors.

1. Sum Rules for the Optical Constants. It has been known for many years that the imaginary part of the complex dielectric function, $\varepsilon(\omega) = \varepsilon_1(\omega)+i\varepsilon_2(\omega)$, the imaginary part of the complex refractive index, $N(\omega) = n(\omega)+i\kappa(\omega)$, and the energy-loss function, $\mathrm{Im}\varepsilon(\omega)^{-1}$, satisfy f sum rules. For example

$$\int_0^\infty \omega\varepsilon_2(\omega)\, d\omega = \frac{\pi}{2}\omega_p^2, \tag{1}$$

where ω_p is the plasma frequency, $\omega_p=(4\pi\mathcal{N}e^2/m)^{1/2}$, with $\mathcal{N}$ the electron density.

By applying methods originally developed for dispersion analysis of scattering data in high-energy physics, it has recently been shown[1,2] that similar superconvergence relations or sum rules hold for the real parts of the optical functions. Some simple examples are

$$\int_0^\infty \{n(\omega) - 1\}\, d\omega = 0 \tag{2}$$

and

$$\int_0^\infty \{\varepsilon_1(\omega) - 1\}\, d\omega = -2\pi^2\sigma(0), \tag{3}$$

where $\sigma(0)$ is the d.c. conductivity. There are, infact, an infinite number of such relations[3] involving higher powers and products of ε_1, ε_2, n and κ. Generalizations[4] of all these rules exist for circularly- and elliptically-polarized light, and a number of finite-energy f sum rules[5] hold under special circumstances.

Mathematically the rules are a consequence of the analyticity of the optical functions and their asymptotic behavior at high frequencies. Physically they are a consequence of causality and the equations of motion[3]. For example, in classical linear response theory Eqs. 2 and 3 are just a restatement of the law of inertia while Eq. 1 is equivalent to Newton's equation of motion.

In addition to these superconvergence relations for the optical functions, the mean energy loss of a fast charged particle penetrating through matter, i.e. the stopping power, is related to the dielectric function through a sum rule[6]. This provides a useful test of the dielectric function particularly at higher energies.

2. Self-Consistent Kramers-Kronig Analysis. The Kramers-Kronig relations are widely used in the analysis of optical data. However, they require the knowledge of one optical function over the entire spectral range. Experimentally this requirement is never fulfilled, rather, optical measurements consist of a mixture of reflection, absorption, refractive index, and ellipsometric measurements in different, generally non-overlapping spectral regions.

Commonly the Kramers-Kronig relations are applied to a single optical quantity by using plausable extrapolations into the ranges for which measurements of this property are not available. However, superior results can be obtained by treating the mixture of all optical measurements by an iterative, self-consistent solution to the Kramers-Kronig relations. In practice this involves choosing one optical property, preferably available over a wide range of energies, as a starting function. To augment the measured values, provisional estimates of the function outside the range of measurements must be made from other data. The provisional solution is then improved iteratively using all available data until satisfactory convergence is achieved. Application of the constraints given by the various optical sum rules provides a systematic procedure for selecting the most probable values from the available optical measurements during the iterative process.

3. Application: The Bulk Optical Properties of Al, 0.04 to 10,000 eV. The self-consistent Kramers-Kronig procedure has been applied to elemental Al and Si, and to GaAs. The most detailed results[7] have been obtained for aluminium and these will be outlined here. Reflectance measurements on samples of aluminum prepared in ultrahigh vacuum are available from the far infrared to the near ultraviolet and formed the basis for the initial trial function. These data are probably the best available at present and are free from surface contamination and

surface-plasmon effects. At wavelengths shorter than the plasma edge the normal reflectance was calculated from a combination of measured absorption data and refractive index estimates from a preliminary calculation of Sasaki and Inokuti[8] based on model fits to reflectance and transmission measurements. On iteration it was found that the region near the plasma edge (15eV) was the most uncertain because of difficulties associated with both reflectance and transmission measurements in this transition region. Electron energy-loss measurements were therefore used as a guide by requiring that the dielectric function reproduce the energy-loss function.

The optical functions were tested at various stages in the iterative calculation with the optical sum rules. The d.c. conductivity sum rule provided a useful control on the conduction-electron portion of spectrum since it is insensitive to band-to-band transitions. Agreement of $\sigma(0)$ with direct measurement was always well within experimental error. From the beginning application of the f sum rule disclosed a significant systematic error: the electron density corresponding to the experimental spectrum was over 14 electrons/atom (e/a) rather than the known value of 13 e/a.

The spectral region responsible for this inconsistency could be located because the valence, K-shell and L-shell absorptions are well separated and finite-energy f sum rules[5] could be applied. It was found that the absorption measurements for several hundred volts above the L-edge (72eV) were systematically some 14 % too high. All reliable measurements in this region have been made in transmission on thin film samples. However, these samples have a high surface oxide-layer to bulk ratio and appear to be subject to spurious effects. A combination of ad hoc reduction of the extinction coefficient in this region and new data from Frascati yielded agreement with both the partial f sum rules and the total f sum as well as the average excitation energy for charged particle energy loss.

In addition to providing a more reliable composite of the optical constants, this analysis has disclosed two interesting physical processes: (a) the "shielding" of valence-electron processes by the polarizable core electrons and (b) the exchange of oscillator strength between core and valence electrons.

The first of these appears as a difference between the partial f sums for ε_2,κ and the energy-loss function for the conduction electron spectrum. Each quantity measures a somewhat different physical process and the "effective" number of electrons contributing to each process differs because of the polarizable ion cores. Denoting the dielectric constant of the fictitious medium made up of the ion cores alone by ε_b, the effective number of conduction electrons calculated from the sum rules for ε_2,κ and the energy-loss function are in the ratio[5]:

$$n_{eff}|_{\varepsilon_2} : n_{eff}|_{K} : n_{eff}|_{\varepsilon^{-1}} :: 1 : \varepsilon_b^{-1/2} : \varepsilon_b^{-2}. \quad (4)$$

In the case of aluminum ε_b is found to have a value of 1.03_5.[7]

The second effect, the exchange of oscillator strength, appears as a departure of the oscillator strength for a given shell of electrons from the occupation number (i.e. from the assumption of unit oscillator strength per electron). This is well known in atomic physics but does not appear to have been as generally demonstrated for solids heretofore. It is easily understood in the one-electron approximation as a result of the Pauli-principle prohibition of transitions to occupied states. Thus, electrons in the K-shell cannot make transitions to occupied states at higher energies and lose oscillator strength. Similarly, valence electrons cannot make downward transitions (which have negative oscillator strength) and hence have oscillator strengths greater than one. In the case of Al the three valence electrons contribute an oscillator strength of 3.1_1, the eight L-shell electrons have a strength of 8.2_7, while the two K-shell electrons have a strength of only 1.6_1. The oscillator strength lost by one shell is gained by the others so that the total remains 13.

FOOTNOTES AND REFERENCES

* Work supported by the Deutsche Forschungsgemeinschaft and the U.S. Department of Energy.

§ Permanent address: Solid State Science Division, Argonne National Laboratory, Argonne, Illinois 60439, U.S.A.

1. M. Altarelli, D.L. Dexter, H.M. Nussenzweig, and D.Y. Smith, Phys. Rev. B6, 4502 (1972).

2. W. M. Saslow, Phys. Lett. 33A, 157 (1970); A. Villani and A. H. Zimerman, Phys. Rev. B 8, 3914 (1973) and Phys. Lett. 44A, 295 (1973); K. Furuya, A. H. Zimerman and A. Villani, Phys. Rev. B 13, 1357 (1975); and F. W. King, J. Math. Phys. 17, 1509 (1976).

3. M. Altarelli and D.Y. Smith, Phys. Rev. B 9, 1290 (1974).

4. D.Y. Smith, Phys. Rev. B 13, 5303 (1976).

5. D.Y. Smith and E. Shiles, Phys. Rev. B 17, 4689 (1978).

6. U. Fano, Phys. Rev. 103, 1202 (1956).

7. E. Shiles, T. Sasaki, M. Inokuti, and D.Y. Smith (submitted for publication).

8. T. Sasaki and M. Inokuti, Conference Digest of the Third Internat. Conference on Vacuum Ultraviolet Radiation Physics, Y. Nakai, editor (The Physical Society of Japan, Tokyo 1971) page 2aC2-2.

MEASUREMENT OF THE FAR INFRARED OPTICAL CONSTANTS OF DISORDERED SOLIDS

U. Strom and P. C. Taylor
Naval Research Laboratory
Washington, D. C. 20375

The study of optical properties in the region from 0.1 to 100 cm^{-1} requires diverse experimental techniques depending on the specific material and frequency of interest. Traditionally, Fourier transform spectroscopy (FTS) has been the primary spectroscopic tool in the far infrared (FIR). This technique is fast and reliable, but suffers from weak radiation sources at the long wavelength end of the spectrum ($\lesssim$ 10 cm^{-1}). Furthermore, FTS is poorly suited to the measurement of the broad spectral features expected for disordered materials.

We briefly outline here recent developments in the far infrared spectroscopic study of disordered solids over a large range of discrete frequencies. The sources of radiation are optically pumped molecular gas lasers (5-150 cm^{-1}) and Klystrons (< 5 cm^{-1}). The primary optical constants obtained are the imaginary (ε'') and real (ε') parts of the dielectric constant and their dependences on temperature and frequency. These in turn are related to the index of refraction n and the conductivity σ by $\sigma = \omega\varepsilon''$, $n = \sqrt{\varepsilon'}$ and $n\alpha(cm^{-1}) = 120\ \pi\sigma(\Omega^{-1}cm^{-1})$.

The simplest experiment which can be performed is direct optical transmission. For a free-standing thin parallel-faced slab of material of thickness d and complex refractive index N = n-ik the transmission at normal incidence (for k = 0) is found to vary with a period of $(2nd)^{-1}$ in wavenumbers.[1] The transmission will be reduced for k > 0 (where $\alpha = 2\omega k/c$). In Fig. 1 we show the measured far-infrared transmission of a freestanding 10.4 μm thick film of amorphous Ge.[2] The solid line represents the expected transmission for an absorption-free film with n = 4.25. The difference between the two curves yields an absorption coefficient α which peaks near 105 cm^{-1}. This absorption is forbidden by selection rules in crystalline Ge but occurs in a-Ge because of the lack of long-range periodicity.

In Fig. 2 the absorption curve for Ge is extended below 50 cm^{-1} by microwave cavity measurements. Measurements of such small values of absorptions are made possible by the sensitivity increase over direct transmission by a factor which is comparable to cavity Q values ($\sim 10^3$ to 10^4).[3] Generally, a perturbative technique is used, in which small changes in cavity Q and resonance frequency f can be directly related to ε'' and ε', respectively. As seen in Fig. 2, the absorption falls off nearly quadratically with decreasing frequency ($\alpha \propto \omega^2$). This quadratic dependence of the FIR absorption coefficient is characteristic of many disordered solids, such as Se in Fig. 2, other chalcogenide and oxide glasses, as well as polymers.[3] It is attributed to the disorder-

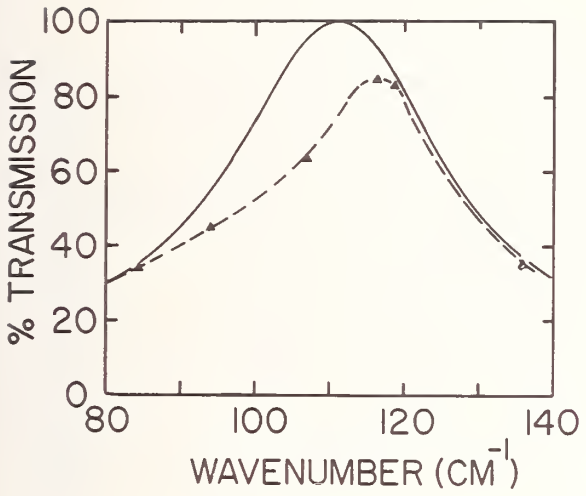

Fig. 1. Transmission at 300K of a 10.4 μm thick film of amorphous Ge evaporated at 2Å/sec. Dashed curve through measurement. Solid curve represents absorption free (k=0) transmission with n=4.25.

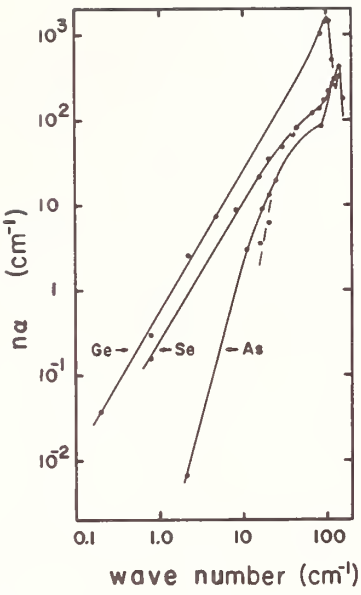

Fig. 2. Absorption of bulk (As, Se) and evaporated film (Ge) elemental amorphous semiconductors at 300K.

induced optical coupling to Debye-like lattice excitations which have a density of states proportional to ω^2. For a one-phonon process this absorption is predicted to be temperature independent, as is indeed observed above 10 cm^{-1}.

In a few amorphous and disordered solids the frequency dependence of α in the FIR is faster than quadratic; i.e., $\alpha \propto \omega^n$ with $n > 2$. Examples are amorphous As in Fig. 2 and the ionic conductor Na β-Alumina in Fig. 3. In the case of As the 3-fold coordination of the As-atom introduces structural rigidity[4] which inhibits optical coupling to long-wavelength lattice modes. Such reduced optical activity would also be expected for amorphous Ge (a-Ge) which is four-fold coordinated. However, the a-Ge structure is over-constrained to such an extent that sizeable voids, which are free of Ge, form within the evaporated film. There is evidence[2], from changes in the FIR absorption with evaporation conditions, that the FIR absorption is dominated by the presence of charged defects on the interior surfaces of the voids. Thus, the "intrinsic" absorption in "void-free" a-Ge is possibly lower than even that of As.

We contrast these results with Na β-Alumina, a crystalline material which exhibits certain properties of a disordered solid.[5] Na β-Alumina consists of spinel-like blocks of Al_2O_3 which are separated by highly disordered planes occupied by Na and O_3 ions. At $T \gtrsim 300K$ the Na cations diffuse rapidly within a conducting plane, resulting in an ionic conductivity which is typical of liquids. With cooling the

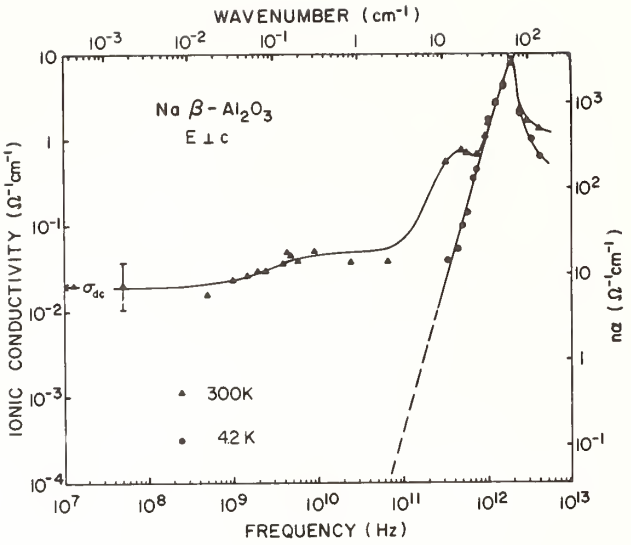

Fig. 3. Conductivity σ (where $n\alpha = 120\pi\sigma$) of Na β-Alumina with electric field parallel to conducting planes.

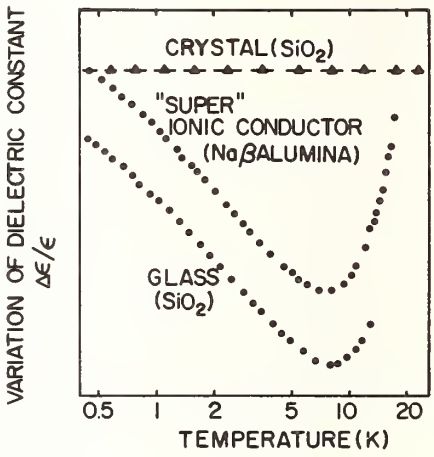

Fig. 4. Change in dielectric constant versus temperature at 10 GHz (0.33 cm^{-1}) for crystalline and glassy SiO_2 and the ionic conductor Na β-Alumina. Vertical full scale 10^{-2}.

cation layers remain disordered and exhibit dielectric, thermal and resonance properties similar to those of glasses. The low T dielectric response[6] is shown in Fig. 4, which illustrates the "glass-like" behavior of the ionic conductor. The local Na^+ vibrational motion leads to a strong FIR absorption peak near 65 cm^{-1}, as seen in Fig. 3. This motion is essentially decoupled from the considerably higher frequency vibrational modes of the $A\ell_2O_3$ structure. In addition, the coupling to long wavelength acoustic modes is also inhibited as evidenced by the rapid fall-off of the absorption at long wavelengths (measured at 4K to remove the effect of a temperature dependent vibrational peak near 12 cm^{-1}), i.e. $\alpha \sim \omega^n$ with $n \lesssim 4$.

The above examples are illustrative of the potential for careful measurements of the optical constants at discrete frequencies in the far infrared region. For disordered solids such measurements are particularly sensitive to the degree and nature of the disorder. Although the sensitivities of the measurements below 5 cm^{-1} are high ($\Delta\varepsilon'/\varepsilon' \sim 1$ part in 10^7 at 0.3 cm^{-1}) because of high Q cavities, the measurement accuracy above 5 cm^{-1} is much less precise. However, carefully designed confocal resonators for the region above 5 cm^{-1} can provide considerably improved sensitivity. Such improvements, coupled with the great number of far infrared lines available from optically pumped FIR lasers, promise an increasing wealth of optical information in a relatively unexplored spectral region.

References

1. O.S. Heavens, Optical Properties of Thin Films (Dover, New York, 1935), p. 20.
2. P.C. Taylor, U. Strom, J.R. Hendrickson and S.K. Bahl, Phys. Rev. B 13, 1711 (1976).
3. U. Strom and P.C. Taylor, Phys. Rev. B 16, 5512 (1977).
4. C.R. Pidgeon, G.D. Holah, F. Al-Bakdar, P.C. Taylor and U. Strom, Proc. 3rd International Conf. on Submillimeter Waves, Univ. of Surrey, England (1978).
5. U. Strom, P.C. Taylor, S.G. Bishop, T.L. Reinecke and K.L. Ngai, Phys. Rev. B 13, 3329 (1976).
6. U. Strom, M. von Schickfus and S. Hunklinger, Phys. Rev. Lett. 41, 910 (1978).

INFRARED IMPURITY ABSORPTION SPECTRA OF PREMIUM-Q QUARTZ

Herbert G. Lipson
Rome Air Development Center
Deputy for Electronic Technology
Hanscom AFB, MA 01731

Applications such as precision quartz oscillators and surface acoustic wave devices place stringent requirements on the purity and consistency of high grade synthetic quartz. The frequency stability of satellite-borne oscillators, particularly when operated in a ionizing radiation environment, may be affected through changes in impurity-related defects present in the quartz. In practice, it has been found that sweeping[1], or electrodiffusion, where an electric field is applied parallel to the z-axis while the material is heated to temperatures between 400 and 550C, markedly reduces frequency changes induced by ionizing radiation.

Characteristic impurity bands found in the low temperature infrared spectra provide more information for early evaluation of oscillator quartz than the usual quality control methods which rely on room temperature absorbance measurements at one specific wavenumber[2]. In this paper the impurity bands found in state-of-the-art Premium-Q and optical grade quartz are classified and changes in these bands introduced by sweeping and ionizing radiation, as well as their polarization dependence are discussed.

A comparison of absorption spectra of unswept and swept quartz measured at 300, 85 and 15K is shown in Figure 1[3].

At 300°K, only one impurity band at 3585cm^{-1} can be resolved above the broad peaks characteristic of the Si-O lattice mode overtone absorption at 3200, 3300 and 3400cm^{-1}. Since the frequency value 3500cm^{-1} widely used for quartz characterization at room temperature is on the side of the 3400cm^{-1} Si-O vibration and does not coincide with any specific band, this method is not sensitive enough to evaluate Premium-Q material. The impurity bands, which are well-resolved at 15K, can be distinguished above the Si-O background at 85K. Four principal bands designated S_1, S_2, S_3 and S_4 with peak positions at 3349, 3396, 3438, and 3581cm^{-1}, respectively,[4] at 85K are found in nearly all synthetic quartz. While the band positions do not shift appreciably between 85 and 15K, and vary only slightly ($\pm$ 1cm^{-1}) from sample to sample, wide variations have been observed in the intensities of these bands measured for different bars of the same autoclave run or even for adjacent regions of a bar. Thus the s-bands are sensitive indicators

SARP PREMIUM-Q QUARTZ
D14-45

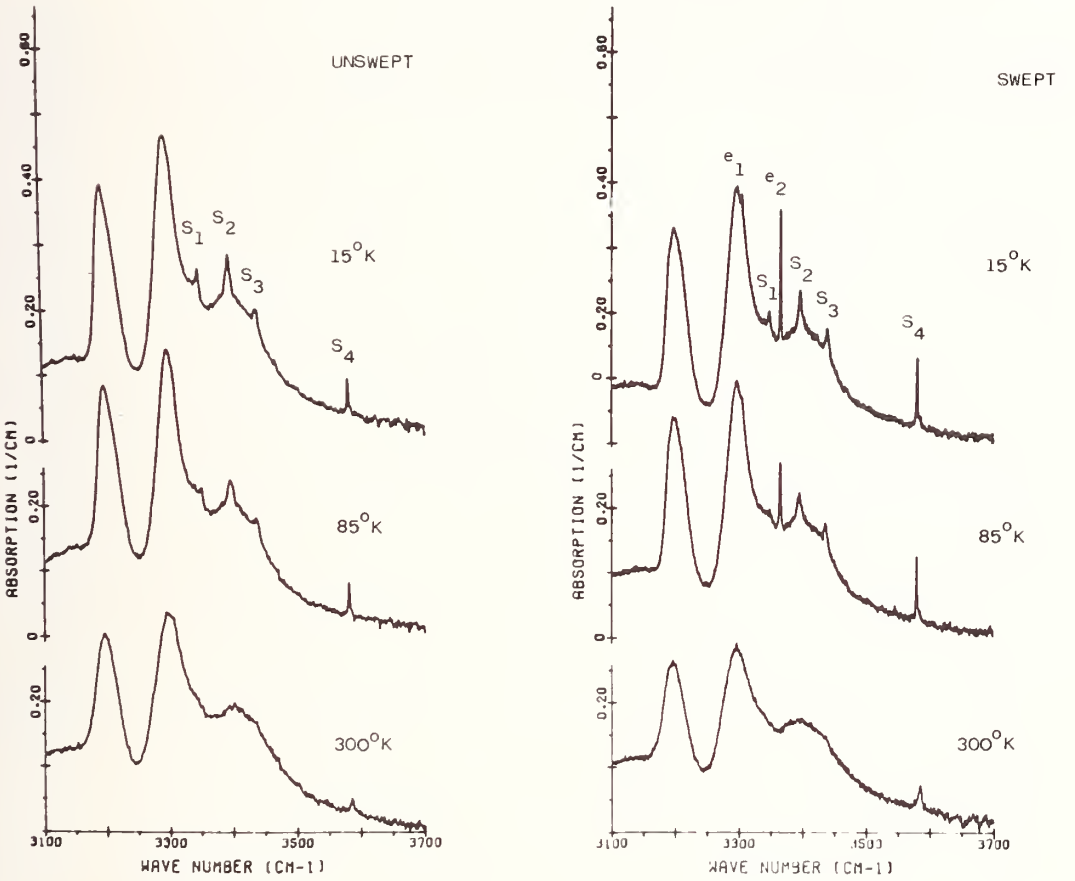

1. Absorption spectra taken at 300, 85 and 15K with E ⊥ Y for unswept and swept Premium-Q quartz from Sawyer Research Products autoclave run D14-45.

Note the labeled impurity bands appearing at low temperature S_1 - S_4, characteristic for synthetic quartz and e_1 and e_2 produced by electrodiffusion (sweeping).

of inhomogeneities resulting from the crystal growth process.

Sweeping (electrodiffusion) changes the s-band intensities very little, but introduces two additional bands with peaks at 3306 and 3366cm^{-1} which have been designated e_1 and e_2. These bands are also produced by electron or ^{60}Co irradiation[4,5] of unswept quartz.

The same impurity bands characteristically present in swept Premium-Q quartz are also found in selected material classified as optical grade as shown in Figure 2.

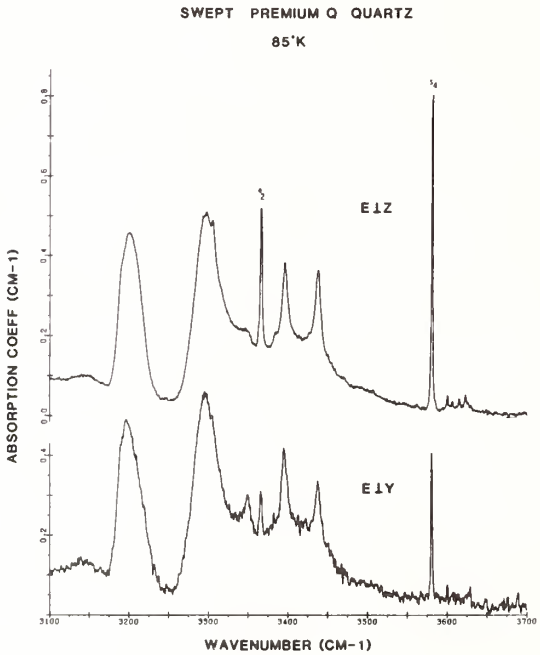

2. Absorption spectra for Premium-Q optical grade quartz taken at 85K indicating the effect of orientation of the sample with respect to the E-vector on the e_2 and s_4 bands.

As with other Premium-Q quartz, most of the band intensities depend on polarization. With E ⊥ Z, the s_3, s_4, e_1 and e_2 bands are stronger and s_1 is weaker than with E ⊥ Y, while s_2 is nearly unaffected. The s_4 and e_2 bands designated in the figure which have half-widths equal to or less than 1cm^{-1} (instrument resolution), respectively, show the strongest polarization. When the absorption of the same sample is measured with infrared radiation propagating in the Y-direction and a wire grid polarizer set for E ∥ C (E ∥ Z), the e_2 band can hardly be resolved above the background and the s_4 band is very weak. With E ⊥ C, strong absorption is observed for both bands.

The impurity absorption bands arise from interstitial H^+ ions which can associate with a non-bonding oxygen orbital in the form of OH^- molecules[6,7]. During the sweeping process charge-compensating alkali

ions such as Na^+ or Li^+, present or purposely introduced into the melt, are moved away from substitutional aluminum impurities by the electric field and are replaced by hydrogen present in the ambient gas. A similar movement of the alkali ions can also be produced by ionizing radiation at sufficiently high temperatures[5,8].

Widely different e_2 band intensities resulting for samples swept commercially by the same process[5] has led to the conclusion that the strength of this band is principally determined by the initial substitutional aluminum concentration in the quartz. The results of an investigation in progress on samples with identical initial infrared spectra and more uniform aluminum concentration to determine whether changes in e-band strength are sufficiently sensitive to monitor the sweeping process will be presented. Also the use of e-band intensity as a possible indicator of the extent of radiation hardening of oscillator quartz will be discussed.

References

1. D.B. Fraser, Physical Acoustics, Vol 5, W.P. Mason, Editor, Academic Press, New York, pp. 59-110; J.C. King, U.S. Patent 3,932,777 (1976)

2. B. Sawyer, IEEE Trans. Sonics and Ultrasonics SU-19, 41 (1972).

3. H.G. Lipson, F. Euler, and A. Armington, Proc. 32nd Annual Symposium on Frequency Control, 11(1978).

4. R.N. Brown and A. Kahan, J. Phys. Chem. Solids, 36, 467(1975).

5. H.G. Lipson, F. Euler and P.A. Ligor, to be published in Proc. 33rd Annual Symposium on Frequency Control (1979).

6. A. Kats, Phillips Research Reports, 17, 133(1962).

7. D.M. Dodd and D.B. Fraser, J. Phys. Chem. Solids, 26, 673(1965).

8. J.J. Martin, L.E. Halliburton, M. Markes, N. Koumuakalis, W.A. Sibley, R.N. Brown and A. Armington, to be published in Proc. 33rd Annual Symposium on Frequency Control(1979).

The author would like to thank Mr. F. Euler for helpful discussions.

FAR INFRARED STUDY OF THE REFLECTION SPECTRA OF SnS

D. G. Mead*
Nicolet Instrument Corporation, Madison, WI 53711

H. R. Chandrasekhar+
Dept. of Physics, University of Missouri-Columbia, Columbia, MO 65211

Tin sulphide SnS is a IV-VI semiconductor possessing an orthorhombic structure with eight atoms per unit cell forming double-layer planes normal to the c(longest) axis.[1] Thus, SnS cleaves very easily in a plane perpendicular to the c-axis, suggesting a weak inter-layer bonding. Unpolarized infrared transmission and power reflectivity spectra of SnS,[2,3] polarized infrared and Raman[4] have been reported and lattice dynamical calculations[5] investigated.

The reported polarized infrared power reflection spectra[4] were analysed by means of a Kramers-Kronig (KK) relation and the infrared active transverse-optic (TO), associated longitudinal phonon frequencies and the dielectric constants determined for all three principal directions. A similar analysis was also carried out for isomorphs SnSe[4], GeS[6] and GeSe[7]. For GeS[6] the widely used formula of the damped classical oscillator (see eq. 1, ref. 6) was fitted to the reflectivity data to yield the position, strength and damping constant of each oscillator. No such analysis was reported for SnS and SnSe[4] or GeSe[5]. It is evident from the oscillator fits to GeS[6] that only poor agreement between the calculated and experimentally observed spectra were obtained. The fit presented for the electric vector $\underline{E}||\underline{c}$ was found to be substantially worse than for $\underline{E}||\underline{a}$ and $\underline{E}||\underline{b}$ directions.[6]

As part of an investigation to accurately determine the far infrared optical constants of GeS and its isomorphs, we have re-examined the polarized power reflection spectra of SnS.[8]

In view of the failure of the classical oscillator fit to GeS, we have attempted to fit the reflectivity data of SnS with the aid of a four parameter dispersive model based on the factorized form of the complex dielectric function.[9,10]

$$\varepsilon(\omega)=\varepsilon'(\omega)+i\varepsilon''(\omega)=\varepsilon_\infty \prod_{j=1}^{N} \frac{\Omega^2_{Loj} - \omega^2 - i\gamma_{Loj}\omega}{\Omega^2_{Toj} - \omega^2 - i\gamma_{Toj}\omega} \qquad (1)$$

Here Ω_{Toj}, Ω_{Loj}, γ_{Toj}, γ_{Loj} are the frequencies and dampings of the TO and LO modes of the jth oscillator. Eq. 1 has been shown to have several advantages,[8,9] including the fact that the model equation allows the damping constants γ_{jTO} and γ_{jLO} to have separate identities so that

fits may be made to reflection features having wide bands, as found in SnS. A non-linear least-squares minimization algorithm to fit the experimental data was used.[11] Table 1 lists the resulting fit parameters. The value of the static dielectric constant is given by:

$$\varepsilon_o = \varepsilon_\infty \prod_{j=1}^{N} \frac{\omega^2 Loj}{\omega^2 Toj} \qquad (2)$$

and are shown in Table 1, including the corresponding mode frequencies and dielectric constants obtained from a KK analysis.[4] Table I indicates that the mode frequencies and dielectric parameters are in overall good agreement with those obtained from the KK analysis. However, for the $\underline{E}||\underline{c}$ polarization there is a discrepancy outside the range of experimental error. The LO fit frequency situated at 215.9 cm^{-1} lies well outside the estimated frequency obtained from the KK results. Fig. 1 shows the oscillator fit (solid line) to the observed data for $\underline{E}||\underline{c}$ obtained with the relevant parameters of Table 1 inserted in eq. 1. Discrepancies outside the range of experimental error are particularly noticeable in certain regions surrounding the two prominent reststrahl bands. Hence, model eq. 1 cannot adequately describe the power reflection for this particular orientation and so allow the dielectric function to be obtained.

It was decided to obtain directly the experimental 300K complex reflection (amplitude and phase) coefficient for the same orientation using a dispersive Fourier Michelson interferometer,[12] to enable the complex dielectric function to be experimentally obtained without the need for any theoretical models or devices. Sample preparation and polishing techniques have been given elsewhere[4] except that the b face used (surface area ~0.16 cm^2) was polished flat to less than 0.3μm to avoid distortions of the phase coefficient ∅ occurring. The amplitude coefficient (the square root of the power reflection coefficient) revealed essentially the same features as in Fig. 1 and is not given here. The measured phase reflection coefficient is shown over the 80-400 cm^{-1} region in Fig. 2. The phase rises slowly, then descends very quickly at ~280 cm^{-1} where the amplitude coefficient falls to a small value (~0.1). The resulting complex (real ε' and imaginary ε'' part) dielectric function using standard formulae are shown in Fig. 3. The TO and LO frequencies were derived from peaks in the associated energy loss functions and are given in Table 1. The results support the KK calculated mode frequencies.[4] The imaginary part ε'' spectrum reveals an asymmetric line shape particularly on the high frequency side of TO_3. Model eq. 1 implies a constant damping factor while an asymmetric line shape suggests a more sophisticated model is necessary which includes a frequency dependent damping function.

Finally, with typical carrier concentrations of $\rho \sim 10^{18}$/cc. expected for SnS compounds, it has been speculated that coupled plasmon-phonons modes are present.[13] Hughes et al[13] have suggested that SnS exhibits a plasma edge at about 280 cm^{-1}, since the reflectivity data do not conform to

pure phonon behaviour. (Our attempt to account for the reflection spectrum by imposing a secondary oscillator positioned at ~280 cm^{-1} in eq. 1 resulted in much poorer agreement with the experimental data). However, eq. 1 allows for a system of coupled plasmon-phonon modes by setting one of the Ω_{TO} frequencies to zero. This procedure has been recently used to explain the reflectivity data of GaAs,[14,15] CdTe[15] and TiO_{2-x}.[16] Modified eq. 1 included the plasma frequency Ω_p, the plasmon damping γ_p and the damping γ_0 at zero frequency. The parameters of the coupled LO modes are given in Table 1, and resulted in an overdamped plasmon present at 164 cm^{-1}. Identical TO modes were found to those obtained from eq. 1. Agreement between the fit and experimental data was excellent up to ~220 cm^{-1}, but the phonon-plasmon model could not account for the high frequency side of the spectrum, and shows the disadvantage of model fitting for obtaining the optical properties.

References

1. OKAZAKI, A., J. Phys. Soc. Japan 13, 1151 (1958).
2. NIKOLIC, P. M. et al., Proceed. XII Int. Conf. on Phys. of Semiconductors, Stuttgart, 1974, Ed. PILKUHN, M. H., p. 331 (unpublished).
3. HAAS, C. & CORBEY, M. M. G., J. Phys. Chem. Solids 20, 197 (1961).
4. CHANDRASEKHAR, H. R., HUMPHREYS, R. G., ZWICK, U. & CARDONA, M., Phys. Rev. B15, 2177 (1977).
5. FREY, A., Thesis, University of Stuttgart (1977), unpublished.
6. WILEY, J. D., BUCKEL, W. J. & SCHMIDT, R. L., Phys. Rev. B13, 2489 (1976).
7. CHANDRASEKHAR, H. R. & ZWICK, U., Solid State Commun. 18, 1509 (1976).
8. The original experimental data from ref. 4 was used for this investigation.
9. BERREMAN, D. W. & UNTERWALD, F. C., Phys. Rev. 174, 791 (1968).
10. GERVAIS, F. & PIRIOU, B., J. Phys. C7, 2374 (1974).
11. BROWN, K.L. & DENNIS, J. E., Numerische Mathematik 18, 289 (1972).
12. MEAD, D. G. & GENZEL, L., Infrared Phys. 18, 555 (1978).
13. HUGHES, O. H. et al., Phonon Scattering in Solids, p. 312, Plenum Press (1976).
14. KUKHARSKII, A. A., Solid State Commun. 13, 1761 (1973).
15. PERKOWITZ, S. & THORLAND, R. H., Solid State Commun. 16, 1093 (1975).
16. BAUMARD, J. F. & GERVAIS F., Phys. Rev. B15, 2316 (1977).

*Work performed in part at Max Planck Institute für Festkörperforschung, Stuttgart, West Germany.

+A. P. Sloan Fellow

Acknowledgement

We are grateful to Prof. L. Genzel for use of the facilities at M.P.I.

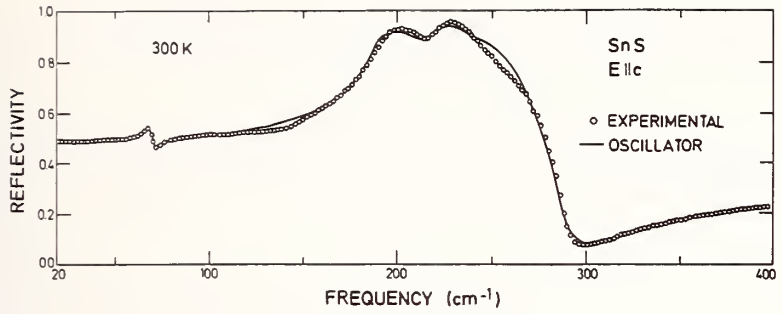

Fig. 1

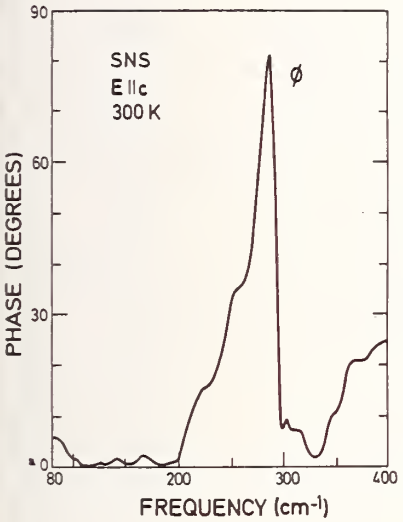

Fig. 2

Table 1

	j	Ω_{TO}	Ω_{LO}	γ_{TO}	γ_{LO}	ε_o	ε_∞
	1.	99.0 (99)	105.9 (107)	1.	8.2		
E‖a	2.	177.8 (178)	213.3 (215)	9.6	6.1	29.0 (32±4)	11.2 (14±2)
	3.	220.2 (222)	276.154 (277)	7.8	29.2		
E‖b	1.	145.1 (145)	265.3 (265)	7.8	30.5	44.5 (48±5)	13.3 (16±2)
	1.	67.5 (69)	68.0 (71)	3.2	4.4		
	2.	189.4 (188) *189.0	215.9 (193) *193.0	6.2	19.0	29.6 (32±4)	12.7 (16±2)
E‖c	3.	216.8 (220) *219.0	288.2 (289) *288	15.7	23.3		

	COUPLED LO MODES	
2.	219.3	8.3
3.	286.1	8.1

PURE PLASMON PARAMETERS

$\Omega_p = 164$ $\gamma_p = 828$ $\gamma_o = 832$

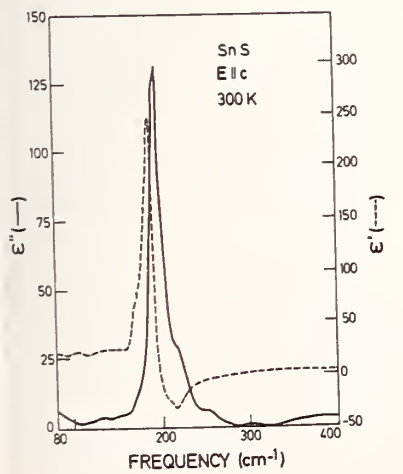

Fig. 3

INFRARED ABSORPTION IN HIGHLY TRANSPARENT CUBIC ZIRCONIA

Bernard Bendow, Herbert G. Lipson and Robert C. Marshall
Solid State Sciences Division, Rome Air Development Center
Hanscom AFB, MA 01731 USA

Didier Billard
Centre de Recherche sur la Physique des Hautes Temperatures
CNRS, 45045 Orleans Cedex, FRANCE

Cubic zirconia possesses an unusual combination of properties which make it attractive as an optical material for a variety of applications:it is very hard, has a very high melting temperature, resists chemical attack and is an excellent insulator. It is readily doped with various rare-earth and transition-metal ions to provide a wide range of potential laser-host materials. The purpose of the present work is to investigate the absorption characteristics of yttria-stabilized cubic zirconia in the highly transparent regime from approximately 1500 to 2300 cm^{-1}, at temperatures ranging from 85 to 1000°K. The present measurements constitute the first detailed analysis of absorption in the highly transparent (three to four phonon) regime of zirconia.

The crystals utilized for this study were produced at RADC employing a relatively new process called "skull melting", in which the melt is contained within a solid "skull" of identical composition[1]. This procedure minimizes difficulties with reaction and contamination encountered in conventional crucible-type growth. Heating is accomplished by coupling RF energy to zirconium metal placed into the charge. Crystals are finally obtained by preferential freezing of the melt when the crucible is slowly lowered through the coil. The yttria-stabilized crystals obtained in this way possess hardness ~ 1370 Knoop, density ~ 5.9 gm/cm^3, thermal conductivity ~ .018 W/cm/°C and visible refractive index ~ 2.15-2.18. The yttria concentration varied from around twelve to twenty-five weight percent. The detailed frequency (ω) and temperature (T) measurements described below were performed on samples containing fifteen weight-percent yttria, with thickness ranging from approximately .2 to 1.3 cm.

The absorption coefficient (α) was deduced from transmission spectra obtained utilizing a Digilab FTS-14 Fourier spectrophotometer operated in the double-beam mode using a dry nitrogen gas atmosphere. For the low temperature measurements, the sample was clamped against an indium ring in contact with the coolant reservoir of a dewar positioned close to the focal point of the spectrophotometer sample compartment. Elevated temperature measurements were made in a small furnace placed in the same position. Temperatures were measured with a Cu-constantan

thermocouple in contact with the polished face of the sample. Absorption values were determined in the usual fashion[2] from measured values of transmittance and reflectivity.

Typical results for the absorption coefficient as a function of ω and T are indicated in Figs. 1 and 2. The spectra in Fig. 1 display a near exponential decrease with increasing frequency, behavior characteristic of intrinsic multiphonon absorption[3]. Only weak structure (shoulders in the 1900-2100 cm^{-1} region) is evident, consistent with the multiphonon spectra of other ionic materials[3]. Raman and Reststrahlen spectra[4] indicate fundamental optical vibrations spanning the 350-700 cm^{-1} regime, which suggests that the shoulders arise from three to four phonon combination processes involving these strong vibrations. To gain more insight regarding the average number of phonons involved, and to corroborate that the absorption is due to intrinsic multiphonon processes, it is useful to analyze the T-dependence of α over a range of frequencies (see Fig. 2). In regimes where the absorption is nearly exponential, α may be represented by the approximate formula[5]

$$\alpha(x,y) = \alpha_o e^{-Ax}[N(y)+1]^x/[N(xy)+1]$$

$$x = \omega/\omega_o, \quad y = \hbar\omega_o/k_B T$$

where N is the Bose-Einstein function, and ω_o is an appropriate average optical frequency. The solid lines in Fig. 2 indicate a fit to the measured data obtained with ω_o = 480 cm^{-1}, $\omega_o A = 7.4 \times 10^{-3}$, $\alpha_o = 2.2 \times 10^5$. The agreement between theory and experiment is quite good, with expected departures due to deviations from exponential frequency dependence. The value utilized for ω_o is consistent with IR data for the fundamental regime, which reveal a broad peak in the range 400-550 cm^{-1}. We conclude, then, that the present data span a range of approximately 3 to 4½ phonons (on the average), with the shoulder occurring in the 4-4 1/3 phonon regime. We have also performed preliminary measurements at higher temperatures 600-1000°K, which indicate similar trends to those displayed in Fig. 2. Detailed analysis of measurements in this temperature range are currently in progress.

In order to assess the effect of yttria concentrations on the absorption in the highly transparent regime, we have measured the room temperature spectrum for a series of samples with different yttria concentrations varying from twelve to twenty-five weight-percent. The data display relatively small shifts (typically 10-30 cm^{-1}) of the absorption edge in the 1600 to 2000 cm^{-1} range. It therefore appears that the dominant contribution to the absorption in this regime stems from zirconia, with only a minor contribution from the yttria.

The authors thank P.D. Gianino for assistance with the numerical computations.

1. See, for example, D. Michel et al, Jour. Crystal Growth 43, 546 (1978) and references therein.
2. See, for example, H. Lipson et al, Phys. Rev. B 13, 2614 (1976).
3. B. Bendow, in "Solid State Physics", H. Ehrenreich et al, eds (Academic, NY, 1978), Vol. 33.
4. C. Perry et al, in Proc. of Sixth Intrnl Conf. on Raman Spectroscopy, Vol 2.
5. B. Bendow, Appl. Phys. Lett. 23, 133 (1973).

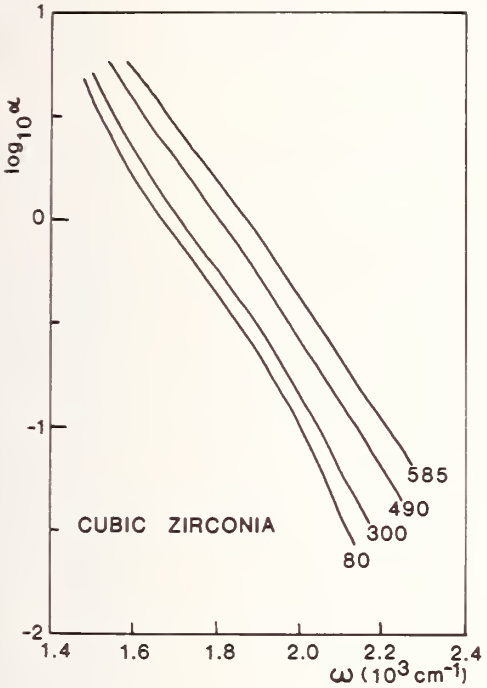

Fig. 1. Log_{10} of the absorption coefficient α measured in cm^{-1}, vs frequency ω for cubic zirconia at various temperatures (^{o}K) indicated in the figure.

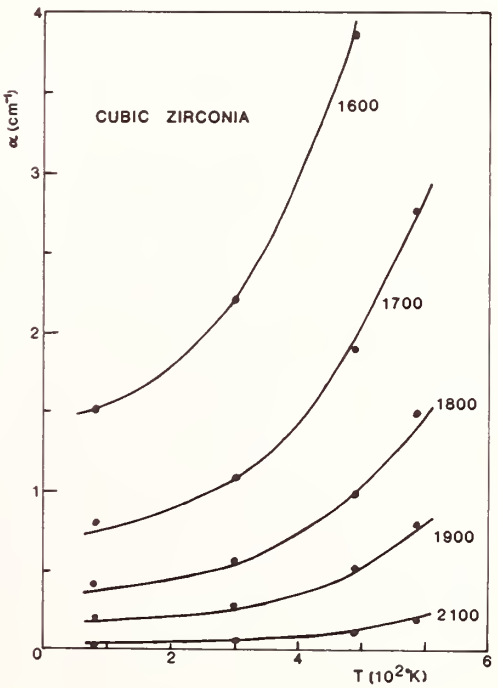

Fig. 2. Absorption coefficient α vs temperature T for cubic zirconia. The discrete points are measured values and the solid curves theoretical predictions.

THE TEMPERATURE DEPENDENCE OF THE OPTICAL ABSORPTION OF METALS*

Michael Bass, David Gallant and Susan D. Allen
Center for Laser Studies
University of Southern California
University Park, Los Angeles, California 90007

The temperature dependence of the optical absorption of metals must be determined in order to throughly understand the optical properties of metals and the interaction between intense laser light and metallic surfaces (1,2). In this paper results are presented for three metals (Mo, Al and 1018 steel), at two wavelengths (10.6 and 1.06 μm), and over the temperature range from room temperature to 600°C. These experimental parameters were selected because: 1, laser metal working most often employs either 10.6 and 1.06 μm lasers for these and similar materials, and 2, these combinations of metals and wavelengths might aid in testing the applicability of the Drude-Lorentz model for the optical properties of metals (1). The model predicts nearly equal room temperature absorptions at 10.6 and 1.06 μm while the experimental results show that at 1.06 μm the absorption is $\gtrsim$10X larger than it is at 10.6 μm. A linear fit can be used to approximate the Drude-Lorentz prediction for the increase of absorption with temperature based on measurements of the dc conductivity. This behavior is experimentally observed for Fe and Mo at both wavelengths and Al at 10.6 μm. However at 1.06 μm the absorption of Al decreases with increasing temperature.

Laser calorimetry was used to measure the absorption as a function of temperature(3). The samples were polished conventionally with the final finish obtained using Linde A polishing compound. Polished samples were placed in a thermally isolated mount in an evacuable quartz chamber with an NaCl window. This window permitted both 10.6 and 1.06 μm laser energy to irradiate the sample. The chamber was evacuated to pressures of $\lesssim 2 \times 10^{-6}$ T using an oil free pumping system consisting of LN_2 sorption pump and an ion pump. With this system, the sample could be heated to 600°C in a radiant heating oven with no significant surface contamination or decomposition.

Thermocouples (0.8 mm diameter chromel-alumel) were attached to the sample to measure its absolute temperature when irradiated relative to a reference sample. The heating and cooling curves obtained with the differential thermocouple pair were analyzed by the "three slope" method(3) to obtain the fractional power absorbed at each temperature. Figure 1 shows the results of such an experiment for Mo at 10.6 μm.

The experimental and theoretical results are summarized in Table I.

The Drude-Lorentz calculations were performed using the formlism of Ref. 1 and the dc conductivity versus temperature data found in Refs. 4 and 5. On the basis of the Drude-Lorentz model the room temperature absorption at 1.06 μm of these metals should be approximately equal and the absorption should increase linearly with increasing temperature.

The experimental results show that the absorption at 1.06 μm is, in general, $\gtrsim$10X that at 10.6 μm. In part, these differences may be attributed to the role of interband transitions in these metals near 1 μm. In any case, it is evident that the Drude-Lorentz formalism is not applicable to these materials at 1.06 μm. For Fe and Mo, the predicted linear increase in absorption with temperature is observed at both wavelengths. For Al, however, the 1.06 μm absorption decreases as the temperature is increased. This type of deviation in the sign of $d\alpha/dT$ from the Drude-Lorentz result was observed by Decker in measurements of the temperature dependence of the reflectivity of vacuum deposited Ag films at 1 and 4 μm(6). At 10 μm, the Ag films behaved as the calculations predicted. However, both Decker(6) and Wieting(7) found Al films have positive $d\alpha/dT$ for wavelengths from 1-20 μm. Further studies will be conducted using laser calorimetry and more ideally finished samples in order to resolve the disagreement between the properties of bulk surfaces and films of Al. In addition measurements of α and $d\alpha/dT$ for Ag will be carried out.

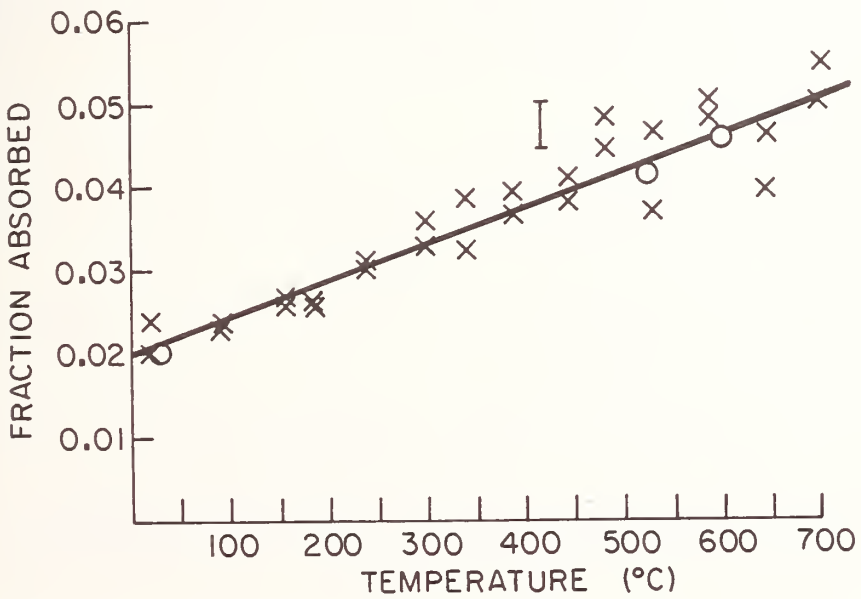

Fig. 1. The 10.6 μm absorption of Mo versus temperature. The X's are data points obtained during heating and the 0's are points obtained as the sample cooled down to room temperature. The straight line is a least squares fit of the data.

TABLE I

Metal	Drude-Lorentz Model		Experimental Results		
	α_{RT} (%)	$d\alpha/dT$ (%)	α_{RT} (%)	$d\alpha/dT$ (%)	(^{o}C)
1018 Steel at:					
10.6 μm	3.4	9.2×10^{-3}	2.3	5.5×10^{-3}	
1.06 μm	4.6	3.8×10^{-2}	22.6	1.1×10^{-3}	
Molybdenum at:					
10.6 μm	1.3	3.6×10^{-3}	2.0	4.5×10^{-3}	
1.06 μm	1.4	5.5×10^{-3}	19.7	1.4×10^{-2}	
Aluminum at:					
10.6 μm	1.0	3.1×10^{-3}	1.4	1.9×10^{-3}	
1.06 μm	1.0	5.2×10^{-3}	20.0	-9.2×10^{-3}	

Temperature Dependent Absorption of 1018 Steel, Mo and Al

The Drude-Lorentz Model gives results that have been approximated by at least squares fit straight line. For each metal, the experimental data has been fit with a straight line, as shown in Fig. 1 for Mo.

REFERENCES

1. T.J. Wieting and J.T. Schriempf, "Free Electron Theory and Laser Interactions with Metals", Report of NRL Progress, June 1972, Naval Research Laboratory, Washington, D.C.

2. M. Sparks and E. Loh, Jr., J. of Optical Soc. Am. 69, 847 (1979) M. Sparks and E. Loh, Jr., J. of Optical Soc. Am. 69, 859 (1979).

3. M. Hass, J.W. Davidson, P.H. Klein and L.L. Boyer, J. Appl. Phys. 45, 3959 (1974).

4. "Handbook of Thermo-Physical Properties of Solid Materials" Vol. I, A. Goldsmith, T. Waterman and H. Hirschorn, eds. (McMillan Co., New York, NY, 1961).

5. P.R. Pallister, J. of the Iron and Steel Institute (1957).

6. D.L. Decker and J.M. Bennett, SPIE Proceedings 140, 32 (1978), and D.L. Decker "High Energy Laser Mirrors and Windows", Semi-Annual Report No. 4, Sept. 1973 - Mar. 1974, D-ARPA Order No. 2175 pp. 66-83.

7. T.J. Wieting, Bull. Am. Phys. Soc. 19, #1, 92 (1974) T.J. Wieting, Bull. Am. Phys. Soc. 19, #3, 339 (1974).

*Research supported by Office of Naval Research through Selected Research Opportunities Program, Contract No. N000 14-79-C-0896.

THE STATISTICAL DESCRIPTION OF OPTICAL INHOMOGENIETIES

E. L. Church
US ARRADCOM
Dover NJ 07801

Index homogeniety is an important attribute of optical materials, which is usually tested by interferometry; that is, by measuring the wavefront distortion, $\delta\varphi$, induced into a plane wave traversing a slab of material. Results are described in terms of an average index fluctuation per unit thickness,

$$\overline{\delta n} = \delta\varphi / kT \qquad (1)$$

mapped over the interferometer field [1]. Here T is the slab thickness and $k = 2\pi/\lambda$.

A representative value is $\overline{\delta n} = 10^{-6}$, which, for T = 2.5 cm, corresponds to a wavefront distortion of $\lambda/25$ at HeNe wavelengths. Distortions of this magnitude decrement the Strehl intensity factor by $\sim 6\%$. Effects of this magnitude are important for high-performance optics, especially in multi-element systems.

In principle, it is possible to reconstruct the distribution of the inhomogenieties in a volume of material by multiscan interferometry, similar to CAT scanning [2]. Both the single- and multi-scan methods lead to a deterministic output which provides the basis for judgement of the quality of the sample under test.

This paper explores the description of the optical inhomogenieties in statistical terms, which may provide a more general basis for quality control and specification. Interest is also prompted by the increasing availability of "digital" interferometers capable of performing on-line analysis, and recent advances in the analogous area of surface-finish specification [3].

The optical properties of an element involving random fluctuations generally depend on the second-order statistics of those fluctuations. Here the natural second-order statistic is the index covariance function, which describes the spatial distribution of the index fluctuations within the sample. To define this quantity, write the index of refraction at any point $\vec{\pi}$ within the three-dimensional sample volume as the sum of an average $\overline{n}$ and a local fluctuation δn:

$$n(\vec{\pi}) = \overline{n} + \delta n(\vec{\pi}) \cdot \qquad (2)$$

For the present discussion we take the medium to be statistically isotropic, homogeneous, and stationary. The index covariance function is then the scalar quantity:

$$C_n(t) = \langle \delta n(\vec{\pi}+\vec{t}) \cdot \delta n(\vec{\pi}) \rangle \qquad (3)$$

where $\langle \cdot \rangle$ denotes the ensemble average and t is the lag parameter.

The gross features of C_n are characterized by "height" and "width" parameters, σ_n and t_n; the rms magnitude of the index fluctuations and their correlation length, respectively. Specifically, $\sigma_n^2 = C_n(0)$ and t_n is the first root of $C_n(t_n) = C_n(0)/e$.

The phase of the transmitted wavefront, φ, can also be written as the sum of two terms; the first corresponding to the average medium and the second to the fluctuations arising from the index fluctuations. The relevant statistic is the phase covariance function:

$$C_\varphi(t) = \langle \delta\varphi(\vec{s}+\vec{t}) \cdot \delta\varphi(\vec{s}) \rangle \quad , \tag{4}$$

where $\vec{s}$ is the position vector in the two-dimensional interferometer field and t is again a lag parameter. This covariance function may be calculated directly from the measured wavefront distortion, although in practice it is only possible to measure C_φ over a limited range of t.

The phase covariance is related to the index covariance via the wave equation applied to a particular model. In the usual geometrical-optics limit, the result for a slab geometry is easily seen to be:

$$C_\varphi(t) = 2k^2 T \int_t^{\sqrt{t^2+T^2}} x\,dx \left[\frac{1}{\sqrt{x^2-t^2}} - \frac{1}{T} \right] C_m(x) \cdot \tag{5}$$

The problem is now this: Given a measurement of $C_\varphi(t)$, which obviously depends on the slab thickness T, how do we deduce C_n? The point of determining C_n is that it is an intrinsic property of the medium, and once obtained, can be plugged back into Eq. (5) or its equivalent for another geometry to determine the optical properties of an element made of the same, or statistically equivalent, material.

Equation (5) is an integral equation for the unknown function C_n, which can be solved in closed form. Here, however, we indicate the physics involved by examining two natural limiting cases: the thin- and thick-sample limits.

In the thin limit, $T \ll t_n$, where the slab thickness is much less than the index correlation length, Eq. (5) reduces to

$$C_\varphi(t) = (kT)^2 C_m(t) \cdot \tag{6}$$

That is, the index and phase covariances are proportional. At the zero-lag point, $t = 0$, this leads to a simple relationship between the rms phase and index fluctuations:

$$\sigma_\varphi = kT\sigma_m \quad , \tag{7}$$

which is a precise version of Eq. (1).

In other words, in the thin-sample limit, the rms phase fluctuations scale as the first power of the sample thickness.

In the opposite, or thick-sample limit, $T \gg t_n$, where the slab thickness is greater than the index correlation length, Eq. (5) reduces to

$$C_\varphi(t) = 2k^2T \int_t^\infty \frac{x\,dx}{\sqrt{x^2-t^2}}\, C_m(x) \quad . \tag{8}$$

This states that the phase covariance is the Abel transform or half integral of the index covariance. The inverse is the half-derivative relationship:

$$C_m(t) = -\frac{1}{\pi k^2 T} \int_t^\infty \frac{dx}{\sqrt{x^2-t^2}} \frac{d}{dx} C_\varphi(x) \quad . \tag{9}$$

In general, there is little resemblance between the analytic expressions for C_n and C_φ in this limit.

For example, the exponential index covariance:

$$C_m(t) = \sigma_m^2 \, \mathrm{EXP}(-t/t_m) \quad , \tag{10}$$

corresponds to the thick-sample phase covariance

$$C_\varphi(t) = 2k^2T\sigma_m^2 t_m \left[u K_1(u)\right] \quad , \tag{11}$$

where $u = t/t_n$ and K_1 is a modified Bessel function [4].

When Eq. (5) and its inverse are evaluated at zero lag, they relate the rms fluctuations in one domain to the covariance function in the other. In the thin-sample limit the measured phase variance is proportional to $C_n(0)$. In the thick-sample limit it is proportional to the area of C_n:

$$\sigma_\varphi^2 = C_\varphi(0) = 2k^2T \int_0^\infty dx\, C_m(x) \quad . \tag{12}$$

Note though, that the area of any simple form of C_n is proportional to the product $\sigma_n^2 t_n$, so that

$$\sigma_\varphi = \# \, k\sigma_m \sqrt{t_m T} \quad . \tag{13}$$

Here # is a number of the order of unity, the precise value of which depends on the form of C_n. Examples are easily generated.

In other words, in the thick-sample limit the rms phase fluctuations are expected to scale as the square root of the sample thickness.

What happens when the sample is neither thin nor thick? That is, when the thickness parameter $Z = T/t_n$ falls between the limits of 0 and ∞ considered above. This region can be explored using the general solution of Eq. (5), a Gaussian form for C_n (for which Eq. (5) can be evaluated in closed form), or by perturbation expansions.

Here we examine the Z dependence of Eq. (5) at the particular point $t = 0$, where it becomes an expression for the measured phase variance:

$$\sigma_\varphi^2 = C_\varphi(0) = 2k^2 T \int_0^T dx\,(1 - x/T)\, C_m(x) \cdot \qquad (14)$$

The transition of this expression between the thin- and thick-sample limits has been explored using different forms for C_n: a Gaussian, an exponential, and a Lorentzian. The ratio of the phase variance for arbitrary thickness to that for infinite thickness is found to increase rapidly as Z^1 for $Z = 0$ to 1, but to approach unity only slowly, as Z^{-1}. Values of $Z = 6 - 20$ are required to reach a ratio of 0.9.

Another important relationship is that between t_φ and t_n. In the thin-sample limit $t_\varphi / t_n = 1$ for any form of C_n, as shown by Eq. (6). In the thick-sample limit, however, the relationship depends on the form of C_n, as shown by Eqs. (8) and (9). For the three cases considered above, direct evaluation gives $t_\varphi / t_n = 1.0$, 1.7 and 1.9, respectively.

Taken together, these results suggest that $T < t_\varphi/2$ and $T > 20 t_\varphi$ are required to ensure the practical applicability of the thin- and thick-sample results, Eqs. (6)-(7) and Eqs. (8)-(13), respectively.

SUMMARY

This paper discusses the relationship between interferometric measurements of an inhomogeneous optical medium and the statistics of its index fluctuations. It is hoped that these results will focus interest on experimental studies of this method of materials characterization.

Subjects not covered in this Summary are the validity of the underlying physical and statistical assumptions, the practicality of obtaining sufficient and sufficiently accurate data for analysis, and bandwidth-limit effects such as those which appear in the related analysis of random surface-height fluctuations [3].

ACKNOWLEDGEMENTS

I thank Dr. H. E. Bennett at the Naval Weapons Center for drawing attention to the importance of index inhomogenieties on system performance, Dr. J. A. Cochran at Washington State University for his inversion of Eq. (5), and Dr. J. M. Zavada at ARRADCOM for helpful discussions.

REFERENCES

1. F. W. Rosberry, App. Opt. 5 961 (1966); F. E. Roberts and P. Langenbeck, ibid. 8 2311 (1969).
2. R. D. Matulka and D. J. Collins, J. Appl. Phys. 42 1109 (1971); D. W. Sweeney and C. M. Vest, App. Opt. 12 2649 (1973).
3. E. L. Church, H. A. Jenkinson and J. M. Zavada, Opt. Engineering 18 125 (1979); E. L. Church, J. Opt. Soc. Am. 69 1404A (1979).
4. Tables of Integral Transforms, Vol. 2 (McGraw Hill Book Company, 1954). A. Erdelyi Ed.

PHOTOCONDUCTIVITY AT 77K IN UNDOPED TELLURIUM

N.G. Shyamprasad, C.H. Champness and I. Shih
Electrical Engineering Dept., McGill University,
3480 University Street, Montreal, Canada H3A 2A7.

1. Introduction Apart from the potential of tellurium as an infrared detector material [1] between 3 and 4 μm wavelength, there is a need for better characterization of photoconductivity in this substance. This is especially so in crystals with a minimum of imperfections, since tellurium is known to be very sensitive to lattice damage. Arising from the high quality crystals grown in our laboratory [2] by the Czochralski method, the present work was carried out. It consisted of a study of the wavelength and thickness dependence of the photoconductivity in monocrystalline undoped tellurium samples at 77K. Some preliminary results on polycrystalline thin film samples are also reported.

2. Samples The bulk samples were cut using a solvent saw [3] from single crystal ingots, pulled in the c-direction from melts of high purity undoped tellurium. The dimensions of the samples are given in Table I and the orientations are illustrated in Fig. 1. Transport measurements showed such samples to be intrinsic at room temperature but extrinsically p-type at 77K. Three thin film polycrystalline samples were also prepared by evaporating tellurium on Pyrex slides on which gold end and side electrodes had been previously sputtered.

3. Method of Photoconductivity Measurements The samples were mounted in a dewar with an IRTRAN 2 window. Monochromatic polarized light at wavelengths between 1 and 4.5 microns and chopped at 13 hertz from a Perkin Elmer model 13 spectrophotometer was focused on to the sample, maintained at 77K. The voltage change across the sample was measured using a lock-in amplifier. The intensity level at each wavelength was determined from the vacuum thermopile detector within the monochromator.

4. Experimental Results Plots of photoconductive sensitivity against wavelength (λ) are shown in Figs. 2 and 3 for a set of samples cut with the longest dimension (i.e. the direction of bias current) parallel to the c-axis, see inset. The ordinate is $\Delta\sigma h\nu/(\sigma_o J)$, representing the relative conductivity change per incident photon. Here, $\Delta\sigma$ is the photo-induced change of conductivity, σ_o is the dark conductivity, J is the incident energy flux at a frequency ν and h is Planck's constant.

The difference between having the E-vector of the incident polarized radiation parallel or perpendicular to the c-axis is contrasted in Fig. 4 for two samples with the same thickness. It is evident that on the short wavelength side of the maxima the photoconductivity falls off faster with decreasing λ for $E \perp c$ than $E // c$. This was observed previously by Grosse and Winzer [4]. Similar results were obtained on samples

TABLE I

Bulk Samples used in Photoconductivity Measurements

Sample no.	Dimensions (mm)			Orientation	
	Length	Width	Thick.	Bias curr. to c-axis	Plane of illum.
CZ-77-1/A	9	1.8		parallel	$(10\bar{1}0)$
CZ-77-1/B	8	2.0	0.25	perpend.	$(10\bar{1}0)$
CZ-77-1/C	8	1.9		perpend.	(0001)
CZ-76-10/A	8	2.1		parallel	$(10\bar{1}0)$
CZ-76-10/B	7	2.5	0.80	perpend.	$(10\bar{1}0)$
CZ-76-10/C	8	2.0		perpend.	(0001)
CZ-76-20/A2	9	1.8		parallel	$(10\bar{1}0)$
CZ-76-20/B2	8.5	1.9	1.20	perpend.	$(10\bar{1}0)$
CZ-76-20/C2	9	1.7		perpend.	(0001)
CZ-76-20/A1	9	2.0		parallel	$(10\bar{1}0)$
CZ-76-20/B1	10	1.8	2.20	perpend.	$(10\bar{1}0)$
CZ-76-20/C1	10	1.7		perpend.	(0001)

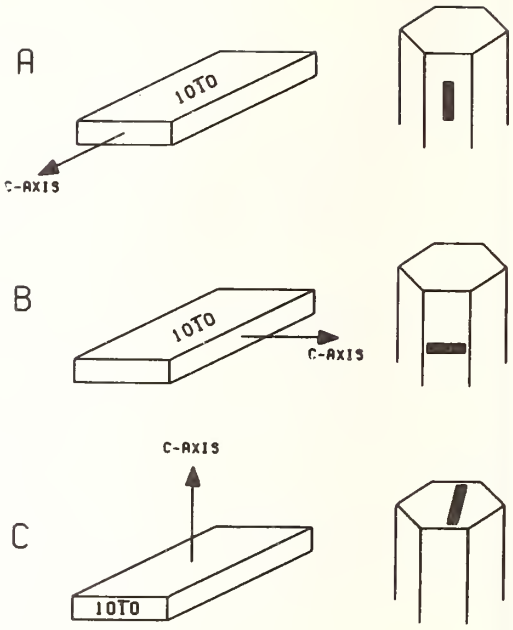

Fig.1 Orientation of samples chemically cut from Te crystals.

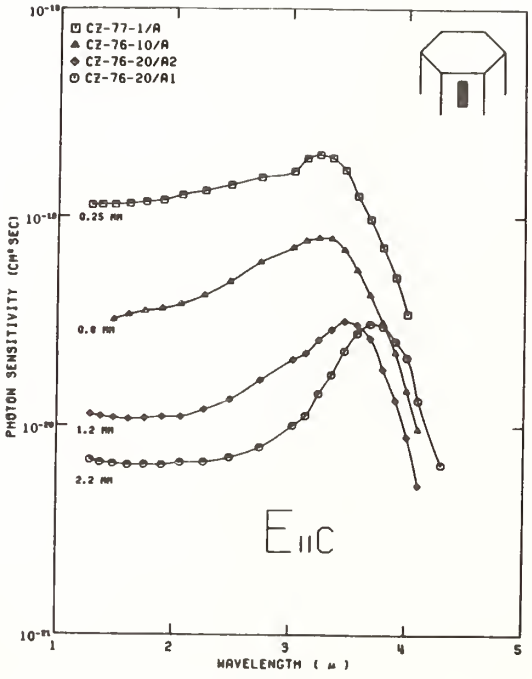

Fig.2 Photoconductive photon sensitivity, $\Delta\sigma/(\sigma_o J_{ph})$, for E-vector parallel to c-axis of 4 bulk Te samples cut with orientation shown in the inset.

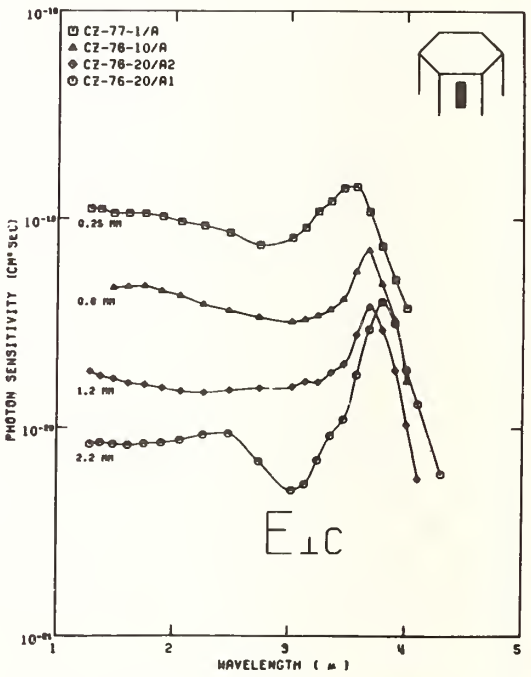

Fig.3 Photoconductive photon sensitivity, $\Delta\sigma/(\sigma_o J_{ph})$, for E-vector perpendicular to c-axis of 4 bulk Te samples cut with orientation shown in the inset.

cut in the other orientations shown in Fig. 1 but, within the reproducibility of the data, no dependence of photoconductivity on current orientation was observed.

The effect of sample thickness (d) is brought out more clearly in Fig.5, which shows photoconductive sensitivity $\Delta\sigma/(\sigma_o J)$ at λ = 2μm plotted against d. For the bulk samples ($E_\perp c$), the photoconductivity increases with decreasing thickness, at least down to 0.25 mm. On the other hand, results for the thin film polycrystalline samples indicate a slight decrease with decreasing thickness.

5. Theory The relative change of conductivity under a photon flux $J_{ph} = J/h\nu$ can be shown, with certain assumptions, to be given by:

$$\frac{\Delta\sigma}{\sigma_o} = \frac{\mu_n + \mu_p}{\mu_p p_o d} \frac{J_{ph}\tau}{1-K^2L^2} \left[1 - \exp(-Kd) + KL \frac{(KL-\alpha)\exp(-Kd) - (KL+\alpha)}{1 + \coth(d/2L)}\right], \quad (1)$$

where $\alpha = sL/D$, s is the surface recombination velocity, L the diffusion length, D the diffusivity, τ the lifetime, K the absorption coefficient, μ_n the electron mobility, μ_p the hole mobility and p_o the extrinsic equilibrium hole concentration.

(i) Thick Sample If $d \gg 1/K$ & L, eq. (1) gives: $\frac{\Delta\sigma}{\sigma_o} = \frac{\mu_n + \mu_p}{\mu_p p_o} \frac{J_{ph}}{d}$, (2)

so that the photoconductivity varies inversely as sample thickness.

(ii) Thin Sample If $d \ll 1/K$ & L, eq. (1) gives: $\frac{\Delta\sigma}{\sigma_o} = \frac{\mu_n + \mu_p}{\mu_p p_o} KJ_{ph}\tau$, (3)

if $s = \alpha = 0$, so that photoconductivity is thickness independent. However, if $s > 0$, consideration of equation (1) shows that $\Delta\sigma/\sigma_o$ increases weakly with increase of d.

6. Discussion and Conclusions The variation of photoconductivity with sample thickness, shown in Fig. 5, is qualitatively in accordance with the theory presented above. The decrease with increasing d for the bulk samples evidently corresponds to the "thick" regime, while the slight increase for the evaporated film samples corresponds to the "thin" regime. The maximum response appears to lie at a thickness between 10 and 100 μm. Analysis of the spectral variations, such as those shown in Fig. 4, indicates s-values between 1000 and 5000 cm/sec. These calculations were done using eq. (1) and taking τ to be 100μ sec. A smaller value of s for the $(10\bar{1}0)$ surfaces compared with that for (0001) surfaces, as reported by Grosse and Winzer [4], was not observed in the present work. Absorption coefficients were calculated from the results using eq. (1) with an assumed L-value of 3.6×10^{-2} cm. These results, as shown in Fig. 6, extend to lower wavelength than those of Blakemore and Nomura [5]. The larger K-values for $E_\perp c$ than E//c are consistent with direct photoelectron transitions across the gap for the former orientation. It is apparent from the present work that photoconductivity does offer a convenient method of determining absorption coefficient in a

λ-region where the large values make transmission measurements difficult.
[1] D.F. Edwards and M. Mercado, Infrared Phys., 1, 17, 1961.
[2] I. Shih and C.H. Champness, J. Cryst. Growth, 44, 492, 1978.
[3] M.El-Azab, C.McLaughlin, C.H.Champness, J.Cryst.Growth, 28,1,1975.
[4] P. Grosse and K. Winzer, Phys. Stat. Solidi, 13, 269, 1966.
[5] J.S. Blakemore and K.C. Nomura, Phys. Rev. 127, 1024, 1962.

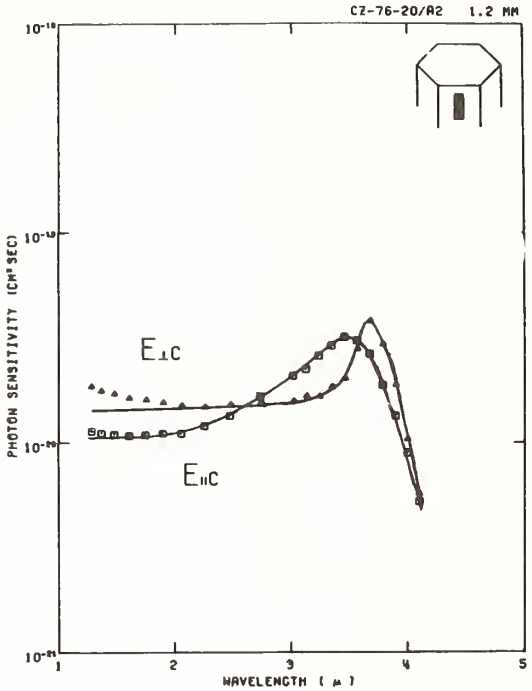

Fig.4 Photoconductive photon sensitivity, $\Delta\sigma/(\sigma_o J_{ph})$, for two samples of same thickness 1.2 mm, with the orientations E//c and E⊥c.

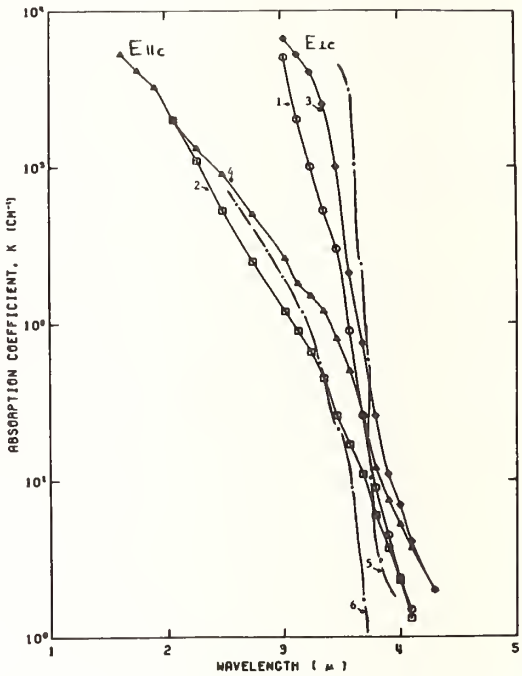

Fig.6 Absorption coefficient calc. from photoconductive data. Curves 1,2: sample CZ-76-20/A2; curves 3,4: sample CZ-76-20/B2; curves 5,6: data of reference [5].

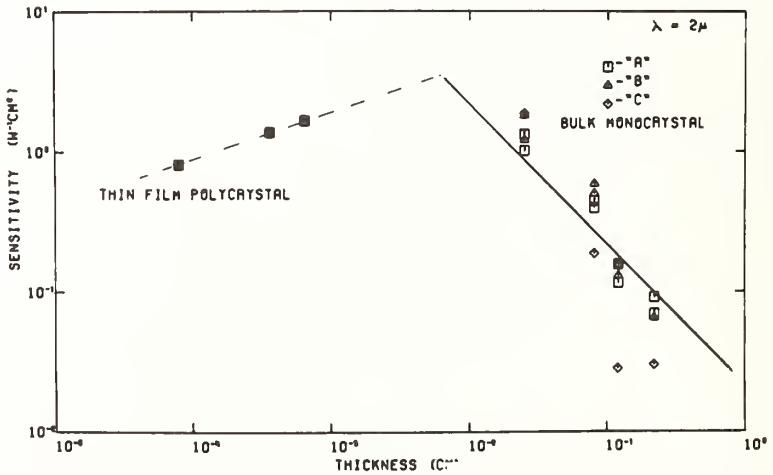

Fig.5 Photoconductive sensitivity, $\Delta\sigma/(\sigma_o J)$ at λ=2μm plotted against sample thickness, d. The solid line for the bulk samples (E⊥c) corresponds to a 1/d variation.

EXTRINSIC STATES IN CINNABAR (α-HgS) GROWN BY CHEMICAL VAPOR TRANSPORT

C. T. Simpson, W. Imaino, and W. M. Becker
Department of Physics, Purdue University
West Lafayette, Indiana 47907

INTRODUCTION

Cinnabar, the trigonal form of mercury sulfide, is a wide band-gap semiconductor whose crystal structure belongs to the space group $P3_121$ (D_3^4) [1]. Some of the interesting properties exhibited by cinnabar are a pronounced band-edge dichroism [2], a large birefringence [3], remarkable optical activity [4], and one of the strongest acousto-optic effects observed [5]. Because of the potential applications of cinnabar, it is important to establish the nature of extrinsic states due to native defects or chemical impurities introduced during the growth process. A further stimulus for this study is the recent observation of new Raman modes in cinnabar grown by chemical vapor transport (CVT) [6]; these modes exhibit striking resonant enhancement for exciting photon energies near the electronic transitions discussed in this paper. We have used photoluminescence (PL), optical absorption and excitation spectroscopy to study CVT-grown cinnabar. An understanding of the observed spectra presents new opportunities for the characterization of this material.

EXPERIMENTAL

Both dendritic and tabular habit (TH) crystals occur in a single growth run. As we reported previously [7], narrow spectral features were observed only in the TH crystals; we confine our discussion to these samples. The volume of TH samples ranged up to ~ 5 mm^3 with a typical sample having dimensions 0.3 × 1 × 2 mm. The largest crystal face was bounded by the basal plane, c{0001}. Other prominent forms present were r{$10\bar{1}1$}, -r{$01\bar{1}1$}, and m{$10\bar{1}0$}. Impurity analysis revealed that iodine, the transport agent, was the major impurity ($\approx 10^{19}$ cm^{-3}) [7]. The photoluminescence and excitation spectra were measured on a Raman scattering spectrometer system employing various cw laser excitation sources, a double monochromator, a cooled photomultiplier detector and photon counting electronics.

Figure 1 shows a typical PL spectrum for a TH sample when $\hbar\omega_L$, the exciting laser energy, is in the range, $E(X_1) \leq \hbar\omega_L < E_g$. Three peaks, labeled X_1, X_2 and B_2, are observed; at 22 K the peak energies are $E(X_1) = 1.872$ eV, $E(X_2) = 1.854$ eV and $E(B_2) = 1.78$ eV, with half-widths of 3.7, 6.6 and 113 meV, respectively. In the temperature range, $20 \leq T \leq 80$ K, the half-widths of X_1 and X_2 increase linearly with

temperature at rates of 0.25 meV/K and 0.46 meV/K, respectively. At low temperatures, $T \leq 10$ K, the half-widths appear to be temperature independent and are typically a few meV at superfluid helium temperatures. The peak intensity of the B_2 band decreases by over two orders of magnitude from 20 to 60 K. The X_1 and X_2 peak intensities vary only by a factor of 3 for this same temperature range.

Figure 2 exhibits the excitation spectrum of the B_2 luminescence. For $\hbar\omega_L < E(X_1)$ the excitation is weak. A dramatic peak in the excitation occurs for $\hbar\omega_L \simeq E(X_1)$. The excitation decreases but persists for $\hbar\omega_L > E(X_1)$. Because the B_2 excitation remains strong for $\hbar\omega_L$ well above $E(X_1)$, we conclude that a continuum of states is involved in the excitation process. The excitation spectrum of the X_2 luminescence is very similar to that of the B_2 luminescence. We conclude from this similarity that the same excitation process is involved in the excitation of both X_2 and B_2.

DISCUSSION

The results exhibited in Figs. 1 and 2, together with the observation of a sharp, asymmetric absorption at $E(X_1)$, suggest that the X_1 transition involves a discrete state and a continuum. Resistance and Seebeck coefficient measurements indicate that the TH CVT-grown cinnabar samples are n-type with ϵ_F, the Fermi energy, lying $\sim$ 0.5 eV below the conduction band edge. To account for the X_1 PL and absorption, we postulate a donor state at $\sim$ 1.873 eV, which we label 2 in Fig. 3. Excitation spectra lead us to propose that the X_1, X_2 and B_2 PL features result from the excitation of a valence band electron into level 2. The recombination of photoexcited electrons in level 2 with free holes yields the X_1 luminescence. No absorption or PL excitation can be detected for photon energies near $E(X_2)$. For this reason, we conclude that in the TH CVT-grown samples studied, ϵ_F lies above a state at $\sim$ 1.855 eV, which we label 3 in Fig. 3. The recombination of electrons already occupying level 3 with free holes generated by the photoexcitation of electrons into level 2 yields the X_2 luminescence. The mechanism we propose for the broad B_2 band is a donor-acceptor pair transition broadened by strong coupling to lattice vibrations. As indicated in Fig. 3, the zero phonon transitions are between level 2 and level 5, or level 3 and level 5, or both. We cannot distinguish between these two processes because of the lack of structure in the B_2 emission. Levels 1 and 4 shown in Fig. 3 are used to explain PL features not shown in Fig. 1; these features are discussed elsewhere [7,8].

The dramatic decrease in the peak intensity of the B_2 band with increasint temperature can be discussed in terms of a configuration-coordinate model. Further details of this model will be presented elsewhere [8]. The thermal broadening of the X_1 and X_2 PL can be interpreted in terms of a lifetime effect. Due to the electron-phonon interaction the excited state lifetime is reduced, yielding a broadened lineshape [9,10].

In order to account for the peak in the optical absorption and the excitation spectra at $\hbar\omega \sim E(X_1)$, we performed a simple model calculation of band-to-impurity absorption in cinnabar [11]. The details of this calculation will also be presented elsewhere [8], however the result which is of importance here is that the peak is a consequence of the matrix element between the initial and final electronic state wavefunctions.

ACKNOWLEDGMENTS

This work was supported by the NSF-MRL Program No. DMR 77-23798 and the National Science Foundation Grant No. DMR 77-27248.

REFERENCES

[1] K. L. Aurivillius, Acta Chem. Scand. 4, 1413 (1950). $P3_121$ (D_3^4) is the space group for the right-handed form; the enantiomorphic left-handed form belongs to $P3_221$ (D_3^6).

[2] R. Zallen, in II-VI Semiconducting Compounds, edited by D. G. Thomas (Benjamin, New York, 1967), p. 877.

[3] W. L. Bond, G. D. Boyd, and H. L. Carter, Jr., J. Appl. Phys. 38, 4090 (1967).

[4] B. Ayrault, F. Lefin, H. Langlois, Y. Toudic, and J. F. Palmier, Opt. Commun. 5, 239 (1972).

[5] J. Sapriel, Appl. Phys. Lett. 19, 533 (1971).

[6] W. Imaino, C. T. Simpson, W. M. Becker, and A. K. Ramdas, Phys. Rev. B. (to be published).

[7] C. T. Simpson, W. I. Imaino, W. M. Becker, and S. P. Faile, Solid State Commun. 28, 39 (1978).

[8] C. T. Simpson, W. Imaino, and W. M. Becker (to be published).

[9] K. Colbow, Can. J. Phys. 41, 1801 (1963).

[10] R. Barrie and K. Nishikawa, Can. J. Phys. 41, 1823 (1963).

[11] We follow the approach of D. M. Eagles, J. Phys. Chem. Solids 16, 76 (1960) and W. P. Dumke, Phys. Rev. 132, 1998 (1963).

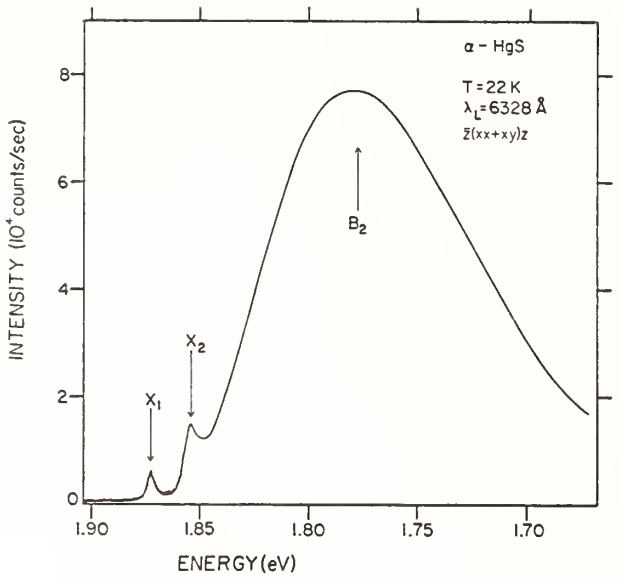

Figure 1

Photoluminescence spectrum of CVT-grown cinnabar excited by 1.959 eV (6328 Å) radiation.

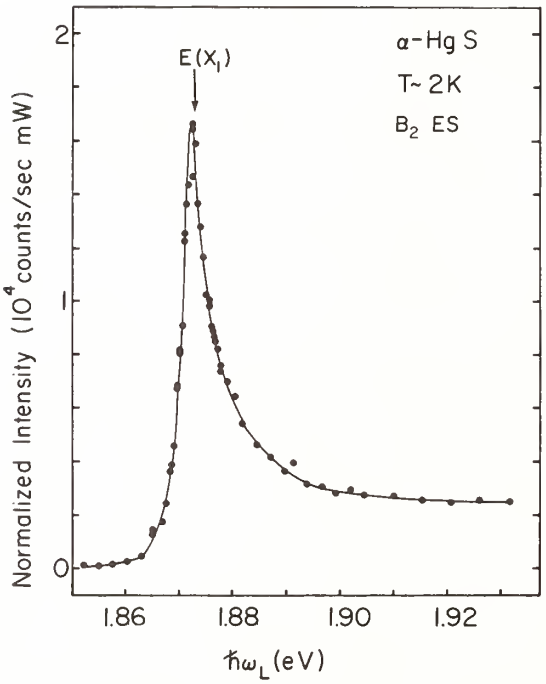

Figure 2

Excitation spectrum (ES) of the B_2 photoluminescence peak in the vicinity of $E(X_1)$, the X_1 emission energy.

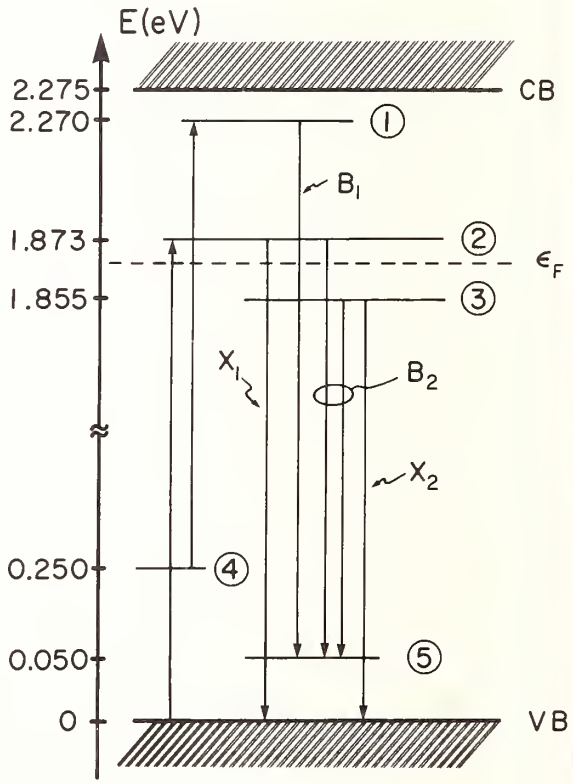

Figure 3

An energy level scheme for tabular habit CVT-grown cinnabar. States labeled 1-5 lie within the forbidden gap. The band continua are represented by cross-hatching.

DIFFERENTIAL REFLECTOMETRY - AN OPTICAL TECHNIQUE FOR INVESTIGATING BAND STRUCTURE CHANGES ASSOCIATED WITH ALLOYING, DEALLOYING, CORROSION AND ORDERING

R. J. Nastasi-Andrews†, J. B. Andrews†, C. W. Shanley*,
J. Finnegan‡ and R. E. Hummel
Department of Materials Science and Engineering
University of Florida, Gainesville, FL 32611 U.S.A.

The differential reflectometer measures the normalized difference in the spectral reflectivity between two specimens mounted side by side. The instrument is capable of determining within a hundredth of an electron volt the energy for interband transitions of electrons.

Light coming from a monochromator is alternately scanned by a vibrating mirror across the two samples (Figure 1). The signal from

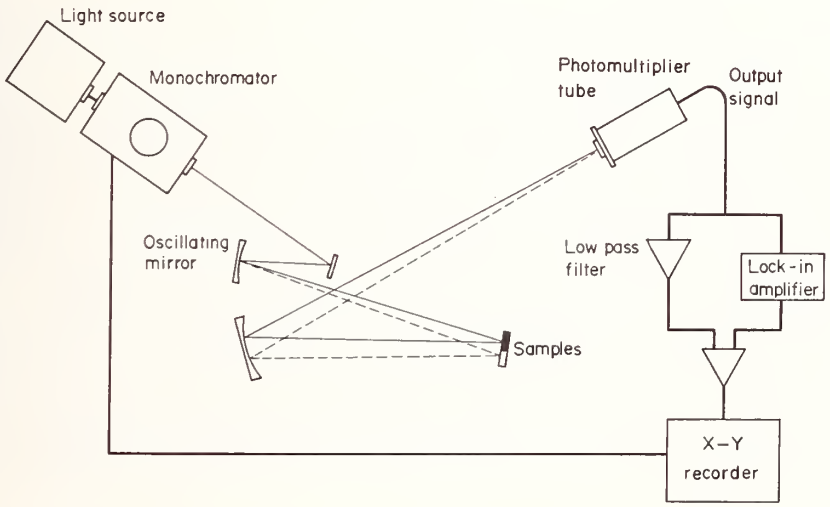

Figure 1. Schematic diagram of the differential reflectometer.

a photomultiplyer tube which picks up the reflected light from the specimens is electronically processed to obtain the normalized difference in reflectivity ($\Delta R/\bar{R}$). An x-y recorder plots $\Delta R/\bar{R}$ automatically as a function of wavelength. A scan between 200 and 800 nm requires between one and three minutes.

For studying changes in the band structure due to alloying, the two specimens which are scanned by the light beam have a small difference in composition (compositional modulation). Applying a line shape analysis to the resulting differential reflectogram, three different

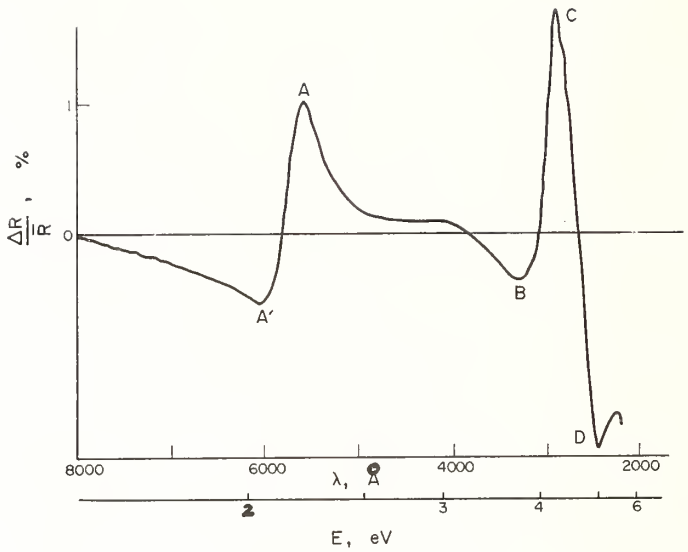

Figure 2. Differential reflectogram of a Cu/Cu - 0.1% Al sample pair.

transitions can be identified (Figure 2): a) A threshold energy for interband transitions around 2.2 eV (peak A) which involves the upper d-bands and the Fermi energy. This transition energy does not change for solute concentrations up to approximately 1 at. %, confirming the theory by Friedel concerning screening of solute charges at low solute concentrations. Experimental evidence is given which suggests that both the d-bands and the Fermi energy are raised by alloying. b) Lower d-band to Fermi energy transitions around 5 eV (peak D) behave in many respects similar to the upper d-band to Fermi energy transitions, except that the lower d-bands appear to be raised much less due to alloying. c) A conduction-band to conduction-band transition around 4 eV (peaks B and C) was observed to decrease in energy with alloying.

In corrosion experiments, one-half of a specimen is protected by an insulating lacquer, while the other half is allowed to form a thin film corrosion product. The use of a transparent lacquer permits monitoring the film in situ. Owing to the differential nature of the technique, the effect of the metal substrate is essentially subtracted out, so that the resulting differential reflectogram is related to the absorption spectrum of the corrosion product. Unique spectra for cuprous oxide, Cu_2O (Figure 3) and cupric oxide, CuO (Figure 4), were obtained and their identities verified either by using conventional optical techniques or by using calculated electronic band structures. The intensity of the structure in the differential reflectogram is related to the thickness of the corrosion film.

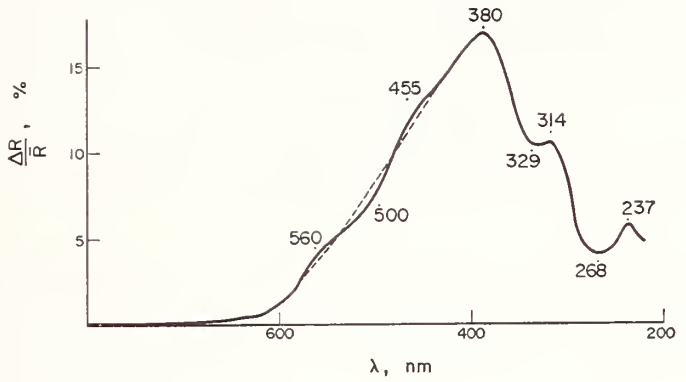

Figure 3. Differential reflectogram for Cu_2O on copper substrate.

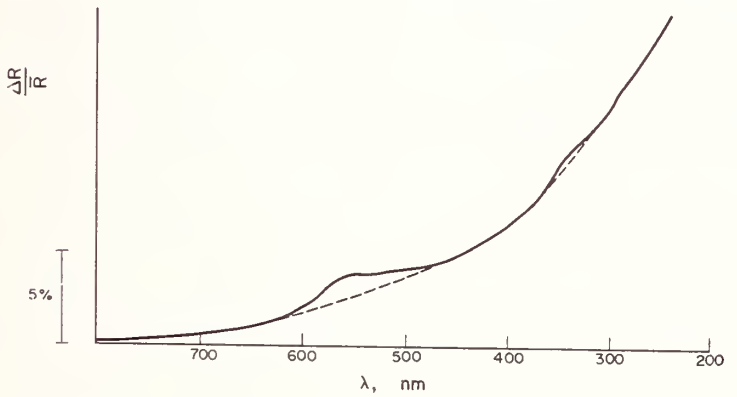

Figure 4. Differential reflectogram of CuO on copper substrate.

Differential reflectometry studies were performed on short-range ordering in a Cu-17 at.% Al alloy. The differential reflectogram of a short-range ordered, versus a disordered specimen, shows a pronounced peak at 2.64 eV which is attributed to new structure in the ordered state. The new structure can be explained using the folding band concept, which yields additional interband transitions. Short-range ordering decreases the energy of peak "C" in the differential reflectograms by 0.04 eV. This shift is equivalent to an increase in solute concentration amounting to one-half of a percent.

Dealloying studies of copper - 5 at. % Zn alloys (red brass) showed that, contrary to literature reports, these alloys dezincify similarly as yellow brass.

†Present address: University of Alabama in Birmingham
*Present address: Motorola, Inc., Plantation, Florida
‡Present address: Bell Labs, Murry Hill, NJ

Bibliography

R. E. Hummel, D. B. Dove and J. A. Holbrook, Phys. Rev. Letters, 25 (1970), 290.

J. A. Holbrook and R. E. Hummel, Rev. of Scientific Instruments, 44, (1973), 463.

R. E. Hummel and J. B. Andrews, Phys. Rev., B8, (1973), 2449.

R. J. Nastasi-Andrews and R. E. Hummel, Phys. Rev. B, 16, (1977), 4314

C. W. Shanley, R. E. Hummel and E. D. Verink, Jr., Corrosion Science, in press.

J. Finnegan and R. E. Hummel, Corrosion Science, submitted for publication.

J. B. Andrews, R. J. Nastasi-Andrews and R. E. Hummel, Phys. Rev., submitted for publication.

FREE CARRIER ABSORPTION IN SEMICONDUCTORS IN QUANTIZING MAGNETIC FIELDS

Harold N. Spector*
Department of Physics
Illinois Institute of Technology
Chicago, Illinois 60616

Free carrier absorption in semiconductors is of interest both because it is the dominant mechanism for the absorption of electromagnetic radiation of frequencies lower than those which give rise to interband transitions (i.e., $\hbar\Omega < E_g$) and because the dependence of the free carrier absorption coefficient on photon frequency and temperature depends critically on the dominant scattering mechanism for the free carriers in a particular semiconductor. We have extended the theory of free carrier absorption in nondegenerate semiconductors to take into account the presence of quantizing magnetic fields for the case where acoustic phonon scattering is the dominant mechanism for the scattering of the free carrier.[1] Previous work only considered the case where the electromagnetic radiation was polarized parallel to the d.c. magnetic field and neglected the possibility of stimulated emission of photons in the semiconductor. The latter assumption is correct if the energy of the photon is much greater than the thermal energy of the free carriers, i.e. $\hbar\Omega >> k_B T$, but is not true in the reverse case. Here the theory is extended to take into account the stimulated emission of photons and to treat the situation where the radiation can either be polarized parallel (longitudinal case) or perpendicular (transverse case) to the d.c. magnetic field. For the transverse case, photons can be absorbed in intraband transitions between adjacent Landau levels even in the absence of collisions of the free carriers with phonons or impurities in the semiconductors when the cyclotron resonance condition is satisfied, i.e., $\Omega = \omega_c$. For the longitudinal case, and also for the transverse case when we are on the low field side of the cyclotron resonance frequency, absorption of the radiation can only occur via phonon or impurity assisted transitions between the various Laundau levels.

In a quantum theory, the free carrier absorption coefficient is calculated by relating it to the transition probability for an electron to make an intraband transition from a given initial state by absorbing or emitting a photon while simultaneously emitting or absorbing the phonon which is involved in the scattering process. This transition probability $W_i^{a,e}$ is given by the Born, second order golden rule approximation,

$$W_i^{a,e} = \frac{2\pi}{\hbar} \Sigma |< f|M|i >|^2 \delta(E_f - E_i \pm \hbar\Omega) \qquad (1)$$

where $\langle f|M|i\rangle$ is the transition matrix element for the electron-photon-phonon interaction and we have neglected the energy of the acoustic phonons in the argument of the energy conserving delta function. This latter approximation is valid at all except the very lowest temperatures since the electrons only interact with the very long wave length acoustic phonons in nondegenerate semiconductors. Here E_i and E_f are the initial and final energies of the carrier and $\hbar\Omega$ is the energy of the photon which is emitted (+sign) or absorbed (-sign). In terms of the transition probabilities for the absorption or emission of the photon, the free carrier absorption coefficient is given by

$$K = \frac{\varepsilon^{\frac{1}{2}}}{c} \sum_i (W_i^a - W_i^e) f_i \qquad (2)$$

where ε is the dielectric constant of the material, f_i is the free carrier distribution and the sum goes over all the initial states of the free carriers. The above expressions have to be evaluated using the energy eigenvalues and eigenfunctions of the free carriers. For electrons in a parabolic energy band, these eigenvalues and eigenfunctions are

$$E_{k,n} = (n+\tfrac{1}{2})\hbar\omega_c + \frac{(\hbar k_z)^2}{2m^*} \qquad (3)$$

$$|k,n\rangle = (L_x L_y)^{-\frac{1}{2}} \exp[i(k_y y + k_z z)]\, \phi_n(x-\lambda^2 k_y), \qquad (4)$$

respectively. Here ϕ_n are the harmonic oscillator wave functions, k_y and k_z are the components of the free carriers wave vector in the y and z directions, m^* is the free carriers effective mass, and $\lambda = (\hbar c/eB)^{\frac{1}{2}}$.

Using the Landau gauge for the vector potential, we can use the eigenvalues and the eigenfunctions for the free carrier in quantizing magnetic fields to evaluate the matrix element for the electron-photon-phonon interaction. Once this matrix element is obtained, it can be used in equations (1) and (2) to evaluate the free carrier absorption coefficient K. It is particularly simple to express the magnetic field dependence of the free carrier absorption by expressing our results in terms of the dimensionless ratio of the free carrier absorption coefficient in the presence of the magnetic field to that in the absence of the magnetic field. The reason for presenting our results in terms of this dimensionless ratio is that all fundamental constants and material parameters, except those that come into the cyclotron resonance frequency ω_c, cancel and therefore, this dimensionless ratio yields a universal relation for the magnetic field dependence of the free carrier absorption which only depends on the photon frequency Ω, the absolute temperature T, and the cyclotron frequency $\omega_c = eB/m^*c$. For the longitudinal case, this dimensionless ratio is

$$\frac{K_{11}(B)}{K(o)} = \frac{3\omega_c}{2\Omega} \exp\left(\frac{\hbar\omega_c}{4K_BT}\right) \frac{\cosh\left(\frac{\hbar\omega_c}{4K_BT}\right)}{\sinh\left(\frac{\hbar\Omega}{2K_BT}\right) K_2\left(\frac{\hbar\Omega}{2K_BT}\right)} \times$$

$$\sum_{n=-\infty}^{+\infty} \left\{ \left[1 - \frac{n\omega_c}{\Omega}\right] \exp\left(\frac{\hbar\Omega}{2K_BT}\right) K_1\left(\frac{\hbar\Omega}{2K_BT}\left[1 - \frac{n\omega_c}{\Omega}\right]\right) - \left[1 + \frac{n\omega_c}{\Omega}\right] \exp - \left(\frac{\hbar\Omega}{2K_BT}\right) K_1\left(\frac{\hbar\Omega}{2K_BT}\left[1 + \frac{n\omega_c}{\Omega}\right]\right) \right\} \quad (5)$$

while for the transverse case, this dimensionless ratio is

$$\frac{K_{\perp}(B)}{K(o)} = \frac{3}{16}\left[\left(\frac{\omega_c}{\omega_c+\Omega}\right)^2 + \left(\frac{\omega_c}{\omega_c-\Omega}\right)^2\right] \frac{\coth\left(\frac{\hbar\omega_c}{4K_BT}\right)}{\sinh\left(\frac{\hbar\Omega}{2K_BT}\right) K_2\left(\frac{\hbar\Omega}{2K_BT}\right)} \times \quad (6)$$

$$\sum_{n=-\infty}^{+\infty} \left\{ \exp\left(\frac{\hbar\Omega}{2K_BT}\right) K_o\left(\frac{\hbar\Omega}{2K_BT}\left[1-\frac{n\omega_c}{\Omega}\right]\right) - \exp\left(\frac{\hbar\Omega}{2K_BT}\right) K_o\left(\frac{\hbar\Omega}{2K_BT}\left[1+\frac{n\omega_c}{\Omega}\right]\right) \right\}$$

In equations (5) and (6), $K_n(x)$ is the modified Bessel function of order n and argument x. The results for the longitudinal polarization reduce to those previously obtained when the photon energy is much greater than the thermal energy of the free carriers. In this case, the contribution of stimulated photon emission to the free carrier absorption coefficient can be neglected as all initial states from which stimulated emission of photons could occur have negligible population. The absorption coefficient for this case is an oscillatory function of the magnetic field which increases in magnitude as the magnetic field increases.[1] The results for the transverse case are similar in that the absorption coefficient is an oscillatory function of the magnetic field on the low field side of the cyclotron resonance frequency. However, instead of reaching a peak value at certain values of the ratio of the cyclotron frequency to the photon frequency as in the longitudinal case, the absorption coefficient diverges logarithmically at these values of the ratio. The reason for this logarithmic divergence in the transverse case is the same as for the logarithmic divergence of the transverse magnetoresistance in nondegenerate semiconductors[2], namely that the collision time for the electron-phonon interaction diverges for carriers traveling with low velocities along the magnetic field for this configuration and the Born approximation can no longer be used to calculate the absorption coefficient. In fact, one would

expect that the correct approach would be to follow a procedure similar to that used by Arora and Peterson[3] to extend the theory of the magnetoresistance of nondegenerate semi-conductors beyond the simple Born approximation. Such an approach has proved to be successful in calculating the cyclotron resonance linewidth in nondegenerate semiconductors.[4]

*Research supported by a grant from the NSF Material Research Laboratory Program, Grant No. DMR 76-24466.

REFERENCES

1. E. R. Generazio and H. N. Spector, Phys. Rev. B (in press).
2. E. N. Adams and T. D. Holstein, J. Phys. Chem. Solids 10, 254 (1959).
3. V. K. Arora and R. L. Peterson, Phys. Rev. B 12, 2285 (1975).
4. V. K. Arora and H. N. Spector, Phys. Stat. Solidi (b) 94, 701 (1979).

MULTIPHOTON ABSORPTION IN DIRECT GAP SOLIDS

S.S. Mitra
Department of Electrical Engineering
University of Rhode Island
Kingston, R.I. 02881

Introduction

Because of the availability of high power laser sources, non-linear absorption processes in gases and solids have been the subject of extensive investigations in recent years. This interest has been stimulated in part by the role of non-linear absorption in laser-induced damage of optical components, as well as by its many fundamental applications such as determination of non-linear susceptibility, band perturbation under strong illumination (dynamic Franz-Keldysh effect), parity and selection rule assignments, band structure analysis in semiconductors, etc. In this review, we shall limit our discussion to multiphoton absorption processes in non-metallic solids.

Phenomenological Description

The multiphoton absorption can be described in a phenomenological manner by the generalized Beer-Lambert's law:

$$\frac{dI}{dx} = -\sum_n \alpha_n I^n \tag{1}$$

where α_n is the n-photon absorption coefficient $\left[(\text{length})^{2n-3}/(\text{power})^{n-1}\right]$, I the light flux ($Wm^{-2}$) and x the propagation direction. If for a given field strength and frequency the nth order process dominates, the attenuation rate of the light flux is

$$\frac{dI}{dt} = -\frac{c}{\sqrt{\varepsilon_\infty}} \alpha_n I^n \tag{2}$$

where c is the speed of light in vacuum and ε_∞ the high frequency dielectric constant of the material. The relation between I and the peak electric field amplitude E_o (Vm^{-1}), as well as the photon number density N_{ph} (m^{-3}) is given by

$$I = E_o^2 (\varepsilon_\infty)^{1/2} / 2Z_o = \frac{c}{\sqrt{\varepsilon_\infty}} \hbar\omega N_{ph} \tag{3}$$

where Z_o is the vacuum impedance. Accordingly, the rate of photon absorption per unit volume is expressed as

$$\frac{dN_{ph}}{dt} = \frac{\alpha_n}{\hbar\omega} I^n = - n \frac{dN_e}{dt} \tag{4}$$

where N_e is the density of conduction electrons created by the n-photon absorption process. In terms of the transition rate $W(= \frac{dN_e}{dt})$, α_n is given by

$$\alpha_n = \frac{2n\hbar\omega \, (2Z_o)^n \, W \, (E_o^{2n})}{\varepsilon_\infty^{n/2} \, E_o^{2n}} \tag{5}$$

Theory

The general theory of multiphoton absorption in atoms was outlined by M. Goppert-Mayer.[1] There are essentially two approaches to calculate α_n for solids, viz., the second[2,3] and higher-order time dependent perturbation theories, and the "dressed-state" model of Keldysh.[4]

By assuming that the transitions take place between Stark-shifted energy bands, and that the wave functions are described by Houston functions, Keldysh obtained the following expression for W

$$W = \left(\frac{2}{9\pi}\right) \left(\frac{m^*_{vc} \, \omega}{\hbar}\right)^{3/2} \left(\frac{e^2 E_o^2}{16 \, m^*_{vc} \, \omega^2 \, E_g}\right)^{\langle x+1 \rangle}$$

$$\times \, \Phi \left[(2\langle x+1 \rangle - 2x)^{1/2}\right]$$

$$\times \exp\left[2\langle x+1 \rangle \left(1 - \frac{e^2 E_o^2}{4m^*_{vc} \, \omega^2 \, E_g}\right)\right] \tag{6}$$

where $x \quad \frac{\bar{E}_g}{\hbar\omega}$ and the effective band gap

$$\bar{E}_g = E_g + \frac{e^2 E_o^2}{4m^*_{vc} \, \omega^2} \tag{7}$$

subject to the condition

$$\frac{e^2 E_o^2}{4m^*_{vc} \omega^2 E_g} << 1 \qquad (8)$$

The photon multiplicity is given by

$$n = \langle x+1 \rangle \qquad (9)$$

where $\langle\ \rangle$ denotes the integer part of the argument, m^*_{vc} the reduced mass of the valence (v) and the conduction band (c) electrons. The Dawson integral $\Phi(z)$ is defined by

$$\Phi(z) = \exp(-z^2) \int_o^z e^{y^2}\, dy \qquad (10)$$

The transition rate for a two-photon process from the second order perturbation theory[2,3] is given by

$$W = \frac{2\pi}{\hbar} \int d^3 \vec{k} \sum_n \left| \frac{H_{vn} H_{nc}}{E_{vn}(\vec{k}) - \hbar\omega} \right|^2 \delta\{ E_{vc}(\vec{k}) - 2\hbar\omega \} \qquad (11)$$

where H_{ij}'s are the interaction matrix elements. The $\vec{k}$ integral extends over the entire first Brillouin zone, the index n extends over all possible intermediate states, and the delta function expresses the energy conservation required. Braunstein and Ockman[2] assumed only one intermediate state situated above the conduction band, and all three bands were parabolic and isotropic. Depending on the symmetries of the bands, three types of two-photon transitions were possible: allowed-allowed, allowed-forbidden and forbidden-forbidden. Basov et al.[3] assumed that the intermediate states were in the valence and the conduction bands themselves. They also used isotropic and parabolic energy bands.

Recent Work

Mitra, Vaidyanathan and co-workers have recently critically examined[5] the three models. They have used both the parabolic and a non-parabolic[6] energy bands, given, respectively by

$$E_{vc}(\vec{k}) = E_g + \frac{\hbar^2 k^2}{2m^*_{vc}} \qquad (12)$$

$$\text{and } E_{vc}(\vec{k}) = E_g \left(1 + \frac{\hbar^2 k^2}{m^*_{vc} E_g}\right)^{\frac{1}{2}} \qquad (13)$$

Keldysh's model uses only the non-parabolic band structure (13). We have shown that the Keldysh formula is closely related to Braunstein's for allowed-allowed transitions, while Basov's proposed formula more closely corresponds to Braunstein's for allowed-forbidden transitions. A number of improvements and corrections to both Braunstein and Basov formulas will be indicated. The two-photon absorption coefficients for several direct-gap seminconductors and alkali halides are calculated from these formulas and compared with the available experimental data. The formulas of Keldysh and Braunstein for describing allowed-allowed transitions, where one considers excitonic intermediate states and nonparabolic energy bands, are found to give results in fair agreement with published experimental results. Basov's and Braunstein's absorption coefficients for allowed-forbidden transitions are smaller than available experimental data by orders of magnitude.

Vaidyanathan, Guenther, and Mitra[7] have recently proposed a new model that combines the elements of second order perturbation theory and electronic energy band structure calculations. This procedure is found to represent a significant improvement over currently available theoretical models reviewed above. Results for CdTe, GaAs, InP and ZnSe are in good agreement with available experimental data.

Keldysh model is capable of predicting the n-photon absorption coefficient for any value of n. For example, Fig. 1 shows such a calculation for PbTe for up to 4-photon transitions. In the passing, it may be remarked that we have previously shown[8] that the one-photon absorption edge in direct-gap crystals predicted by the Keldysh formula agrees with the results of conventional perturbation theory to within a factor of order unity. This is in contrast to the frequently stated opinion that the Keldysh formula is incorrect or invalid when the photon multiplicity is small.

Kovarskii and Perlin[9] have treated the three-photon absorption in direct gap solids by an improved but similar model to that of Keldysh. Bassani and Hassan[10] have presented a perturbation calculation for the third order coefficient. Judell, Mitra, and Vaidyanathan[11] have used the third-order time dependent perturbation theory to determine the three-photon absorption coefficient for several direct-gap semiconductors using both parabolic and non-parabolic band structures. Intermediate levels needed in these calculations are the higher energy bands obtained from band structure calculations. The dispersion of α_3 closely follows that of Keldysh's result in shape but not in magnitude as shown in Fig. 2. Our result for CdS agrees closely with the experimental value[12].

Acknowledgment

The author is very grateful to Dr. A. Vaidyanathan for many helpful discussions.

References

1. M. Gioppert-Mayer, Ann. Phys. (Leipzig) 9, 273 (1931).

2. R. Braunstein, Phys. Rev. 125, 475 (1962); R. Braunstein and N. Ockman, Phys. Rev. 134, A499 (1964).

3. N.G. Basov, A.Z. Grasyuk, I.G. Zubarev, V.A. Katulin and O.N. Krokhin, Sov. Phys. JETP 23, 366 (1966).

4. L.V. Keldysh, Sov. Phys. JETP 20, 1307 (1965).

5. S.S. Mitra, L.M. Narducci, R.A. Shatas, Y.F. Tsay and A. Vaidyanathan, Appl. Opt. 14, 3038 (1975); A. Vaidyanathan, T. Walker, A.H. Guenther, S.S. Mitra, and L.M. Narducci, Phys. Rev. B (in press).

6. E.O. Kane, J. Phys. Chem. Solids 1, 249 (1957).

7. A. Vaidyanathan, A.H. Guenther and S.S. Mitra, to be published.

8. L.M. Narducci, S.S. Mitra, R.A. Shatas, P.A. Pfeiffer and A. Vaidyanathan, Phys. Rev. B14, 250 (1976); A. Vaidyanathan, T. W. Walker, A.H. Guenther, S.S. Mitra and L.M. Narducci, Phys. Rev. B20, 3526 (1979).

9. V.A. Kovarskii and E. Yu Perlin, Phys. Status Solidi 45, 47 (1971).

10. F. Bassani and A.R. Hassan, Nuovo Cimento B7 313 (1972).

11. N. Jodell, S.S. Mitra and A. Vaidyanathan, to be published.

12. A. Penzkofer and W. Falkenstein, Opt. Commun. 16, 247 (1976); I.M. Catalano and A. Cingolani, J. Appl. Plys. 50, 5638 (1979).

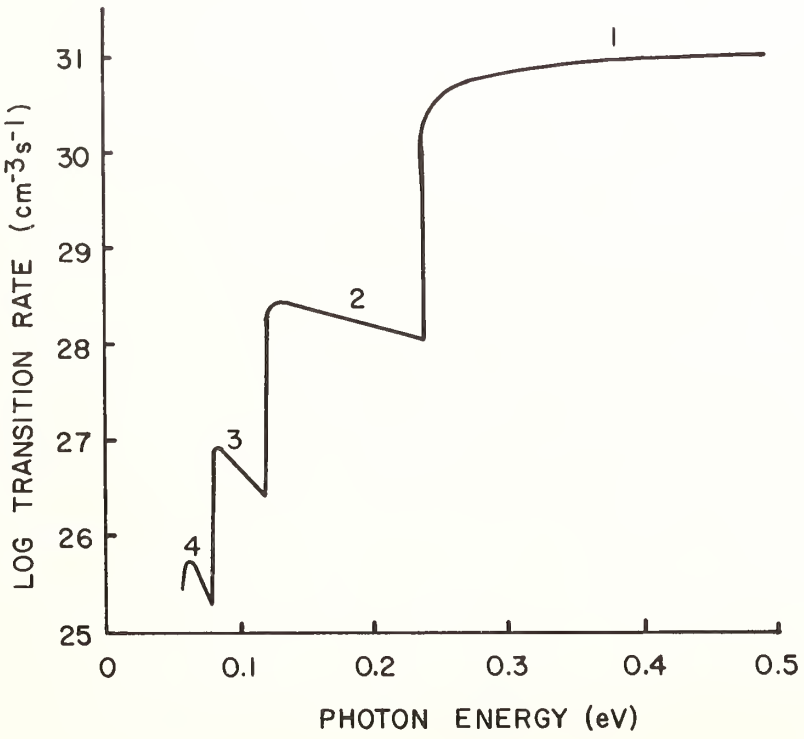

Fig. 1: Multiphoton transition rate for PbTe ($E_o = 10^4$ V cm^{-1}).

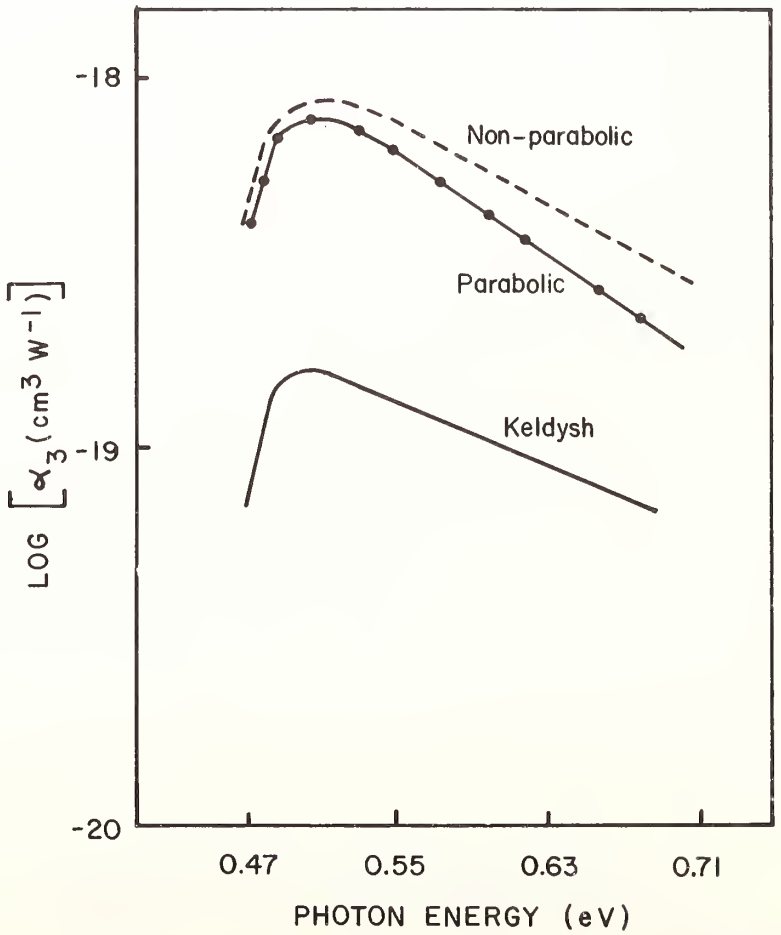

Fig. 2: Dispersion of α_3 of GaAs.

MEASUREMENTS OF TWO PHOTON ABSORPTION*

Alan F. Stewart and Michael Bass
Center for Laser Studies
University of Southern California
Los Angeles, CA 90007

Since the first observation of a two photon absorption (TPA) process by Kaiser and Garrett in 1961(1), there have been many conflicting experimental results and theoretical predictions (2,3). An absolute measurement of the TPA coefficient, β, for any given material has proven to be experimentally difficult and reported values differ by an order of magnitude or more. New measurements of TPA are reported here for several zincblende and wurtzite materials employing the technique of nonlinear laser calorimetry (4). Internal reflections in our samples were eliminated by appropriate antireflection coatings and an accurate determination of the TPA coefficient was possible. The results are in agreement with previous state-of-the-art measurements using the transmission technique (5).

The propagation of light in a medium which exhibits both linear and TPA is described by

$$\frac{dI(x,y,z,t)}{dz} = -(\alpha + \beta I(x,y,z,t)) I(x,y,z,t) \qquad (1)$$

where $I(x,y,z,t)$ is the light intensity in MW/cm^2, z is the direction of propagation, α is the linear absorption coefficient in cm^{-1} and β is the TPA coefficient in cm/MW. Internal reflection at the exit surface creates a counterpropagating field which may interfere with the incident radiation inside the crystal. In a semiconductor with a large refractive index the reflectivity may reach 30% per surface. Thus constructive interference between incident and reflected beams can increase the intensity inside the crystal by a factor of 2.4. An unmeasurable enhancement of this magnitude would distort the results of any experiment designed to measure an intensity squared dependent process such as TPA. How much enhancement occurs in the crystal will depend on the reflectivity, surface figure and the angle between incident and reflected beams.

In order to account for internal reflections we consider only that occurring at the exit surface of the sample. The following equations for the incident and reflected intensities were obtained from the contributing terms of the nonlinear polarization assuming perfect spatial overlap and constructive interference:

* This work was supported by National Science Foundation
Grant No. ENG-7820470

$$\frac{dI}{dz} = -\alpha I - \beta I (I + 2I_R) \quad (2)$$

$$\frac{dI_R}{dz} = \alpha I_R + \beta I_R (I_R + 2I) \quad (3)$$

where I is the incident intensity and I_R is the reflected intensity. In reference (4) the coefficient of the cross terms was set equal to unity because it was felt that the lack of parallelism and the imperfect surface quality of the sample faces resulted in imperfect constructive interference of the two beams. Intuitively, one would expect the coupling between the two beams to be greatest near the exit surface. The coupling should decrease to zero as the two beams physically separate and lose their phase coherence nearer the entrance surface. The surface parellelism required in order to observe interference effects in transmission from a low reflectivity etalon is typically less than one arc minute for 1 μm light (5). However, field enhancement in a 1mm thick slab of material would occur over most of the thickness with a required parallelism of slightly less than one degree. Thus, field enhancement must be present in a typical TPA experiment but the magnitude of the effect has not been determined until now.

The experimental procedure used in this study follows that outlined in reference (4). A passively Q-switched Nd:YAG laser which operates in the TEM_{00} mode at low repetition rate (4Hz) was the source for this work. The beam intensity reaching the sample was adjusted using a two polarizer attenuator. The total absorption of the sample was measured as a function of the incident intensity using standard procedures for laser calorimetry (6). The Gaussian intensity distribution reaching the sample was measured by scanning the beam with a narrow slit in front of a pyroelectric detector. The temporal profile was measured with a fast photodiode (risetime of 0.1 nsec) and was completely smooth and nearly Gaussian when observed on a R7912 Transient Digitizer. Any temporal structure in the laser pulse represented intensity fluctuations which precluded accurate measurement of β and hence that condition was carefully avoided.

The crystals used in this study were selected from three lattice families: sphalerite or zincblende structure, wurtzite structure and simple cubic. The orientation of these crystals was chosen to preclude second harmonic generation which if followed by linear absorption would also appear as an intensity squared dependent process. For zincblende materials the incident light propagated along the (110) direction and was polarized in the (001) direction. For wurtzite materials the incident light propagated along the optic axis. The linear absorption was measured using conventional calorimetric techniques and a CW Nd:YAG laser. All crystals were high resistivity ($>10^8$ Ω-cm) except for the Cd $S_{0.25}$ $Se_{0.75}$ which was accidentally uncompensated and showed a resistivity of $<10^3$ Ω-cm.

The role of internal reflections was determined by applying multilayer antireflection coatings to one surface each of samples of CdTe, CdSe and GaAs. In this way, the total absorption as a function of intensity could be measured with no internal reflection or exactly one internal reflection simply by turning the sample around. The TPA coefficient, β, was obtained from data taken with the antireflection coating on the exit surface using Eq. (1). Once the value of β was known the data obtained with the antireflection coating on the entrance surface was analyzed using Eqs. (2) and (3) with the coefficient of the cross terms as the fitting parameter. As a final check, uncoated but otherwise identical samples of these materials were measured and again the best fit coefficient for the cross terms in Eqs. (2) and (3) was determined. In order to use Eqs. (1), (2) and (3) to analyze the experimental results numerical integrations were carried out over the temporal and spatial profiles of the incident pulses.

The results of these experiments appear in Table I. In all cases a cross term coefficient in Eqs. (2) and (3) of unity resulted in the best fit to the data. Also we have observed no spot size dependence in our measurements indicating that diffusion of free carriers is not important on a nanosecond time scale for beams with 1/e radii greater than 100 μm.

Table I

Measured Absorption and TPA Coefficients

	GaAs	CdTe	CdSe
$\alpha(cm^{-1})$	1.50 $\pm$0.15	0.049 $\pm$0.005	0.026 $\pm$0.003
β(cm/MW)	0.030 $\pm$0.009	0.041 $\pm$0.012	0.043 $\pm$0.013

	$CdS_{0.25}Se_{0.75}$	$CdS_{0.5}Se_{0.5}$	KRS-V
$\alpha(cm^{-1})$	0.028 $\pm$0.003	0.254 $\pm$0.03	0.0047 $\pm$0.0005
β(cm/MW)	0.075 $\pm$0.023	0.031 $\pm$0.009	0.0016 $\pm$0.0005

A good example of the sensitivity of this technique is demonstrated in our measurement of KRS-V. Since nonlinear calorimetry compares the magnitudes of linear and TPA processes the minimum detectable TPA coefficient is limited by the maximum intensity that does not damage the sample and linear absorption coefficient. In KRS-V, which has a linear absorption of only 4.7×10^{-3} cm^{-1}, a 400% increase in the total absorption was detected with only 20 MW/cm^2 of incident intensity. This same intensity would result in only a one percent change in transmission. Nonlinear laser calorimetry shows its greatest promise in measuring TPA in highly transparent materials.

The experimental errors indicated in Table I were primarily caused by uncertainty in the absolute determination of the incident intensity of each pulse. The uncertainty comes from calibrations of both the

pyroelectric detector and the average power meter used. Additional contributions arise from laser intensity fluctuations and uncertainties in the measurements of the laser spot size and temporal profile. As with any calorimetry experiment there is some additional uncertainties resulting from analysis of the heating and cooling curves.

In conclusion, we have measured the TPA coefficient in six materials and have obtained results in good agreement with those obtained in a very different type of experiment. This suggests that the experimental results are asymptotically approaching the true value of β. It is clearly impractical to apply antireflection coating to all materials to be tested for nonlinear absorption. In this research it has been demonstrated that a cross term coefficient of unity in Eqs. (2) and (3) allows proper analysis of data obtained from uncoated samples. It should be noted that if the true coupling coefficient had some other value between 0 and 2, assuming a value of unity leads to an estimated uncertainty in β which is at most 20%.

REFERENCES

1) W. Kaiser and O.G.B. Garrett, Phys. Rev. Lett. 7, 229 (1961)
2) C.C. Lee and H.Y. Fan, Phys. Rev. B 9, 3502 (1974)
3) J.H. Bechtel and W.L. Smith, Phys. Rev. B 13, 3515 (1976)
4) Michael Bass, Eric W. Van Stryland, and A.F. Stewart, Appl. Phys. Lett. 34, 142 (1979)
5) Raoul Weil and Dalia Neshmit, Appl. Opt. 16, 2847 (1977)
6) A. Hordvik, Appl. Opt. 16, 2827 (1977).

THREE-PHOTON ABSORPTION IN Nd:YAG

Robert W. Boyd and Mark A. Kramer
Institute of Optics
University of Rochester
Rochester, New York 14627

The narrow spectral linewidths characteristic of transitions of rare-earth ions (Fig. 1) make rare-earth-doped crystals interesting systems in which to study resonant and near-resonant optical nonlinearities. While population inversion and consequent laser action is a common example of a nonlinear effect involving the rare earths, other types of optical nonlinearity also exist. The generation of sum and difference frequencies of applied laser fields through a second-order $\chi^{(2)}$ nonlinearity is such an example. For a laser frequency close to a resonance frequency of the rare-earth ion, these nonlinearities are by theoretical arguments expected to become very large.

Another type of optical nonlinearity involving the rare earths, and the subject of this article, is three-photon absorption in Nd:YAG. In the schematic setup of Fig. 2, a 6 nsec pulse of 30 kW peak power at 5933 Å is focussed to an 18 μm spot size in a 5-mm-long sample of 1 wt percent Nd:YAG. Blue fluorescence light is found to be emitted from the focal volume, and it is of sufficient intensity to be easily observed by eye. A spectrum of the fluorescence is shown in Fig. 3. No fluorescence is observed at wavelengths shorter than that of the intense doublet at 4000 Å. In addition, a number of longer wavelength lines appear throughout the visible. The fluorescence spectrum for wavelengths greater than the excitation wavelength closely mimics the normal, low intensity, one-photon-induced fuorescence spectra, such as those shown in Fig. 4, which were also taken with the apparatus of Fig. 2 but with the laser defocussed.

The intensity of the 4000 Å fluorescence is found to vary as the third power of the laser intensity over a range of 30 in laser intensity. The process giving rise to this fluorescence is thus interpreted as three-photon absorption followed by a partly radiative and partly nonradiative de-excitation, and is illustrated in Fig. 5. Following

excitation to level 2 by three-photon absorption, the atom decays nonradiatively to level 3, radiatively to level 4, and nonradiatively back to level 1. In principle, levels 2 and 3 or levels 1 and 4 could be coincident, but the observed fluorescence spectrum suggests that the dominant decay route is as illustrated in Fig. 5.

Nd:YAG is known to be essentially opaque for wavelengths shorter than 2400 Å.[1] Three-photon absorption thus permits the probing of levels such as level 2 which are more than 42,000 cm^{-1} above the ground state and are thus inaccessible by conventional spectroscopic techniques.

The intensity of the 4000 Å fluorescence is plotted as a function of laser wavelength in Fig. 6a; below it the product of the laser power (shown in 6b) and the crystal transmission is plotted in 6c. It should be noted that each peak in 6a matches a dip in 6c, thus indicating that an enhancement of the three-photon-absorption process occurs whenever the laser is tuned to a one-photon resonance. Similarly, theory predicts an enhanced three-photon absorption rate if the energy of two photons is equal to the energy of a two-photon-allowed transition. Since three-photon absorption necessitates the existence of level 2 of Fig. 5 at an energy equal to that of three incident photons, it can be concluded from the data of Fig. 6 that a broad energy level or several overlapping levels exist some 51,000 cm^{-1} above the ground state of Nd:YAG.

In conclusion, a method is presented for studying the energy-level structure of Nd:YAG and similar rare-earth-doped crystals in an energy region where one-photon techniques are not possible. This three-photon-absorption process is presently being studied over a much broader range of laser wavelengths, and the results of this investigation will be reported in the future.

This work was partially supported by NSF grants SER77-06914 and ENG79-08038.

Reference

1 W. F. Krupke, IEEE J. Quantum Electron., QE-7, 153, 1971

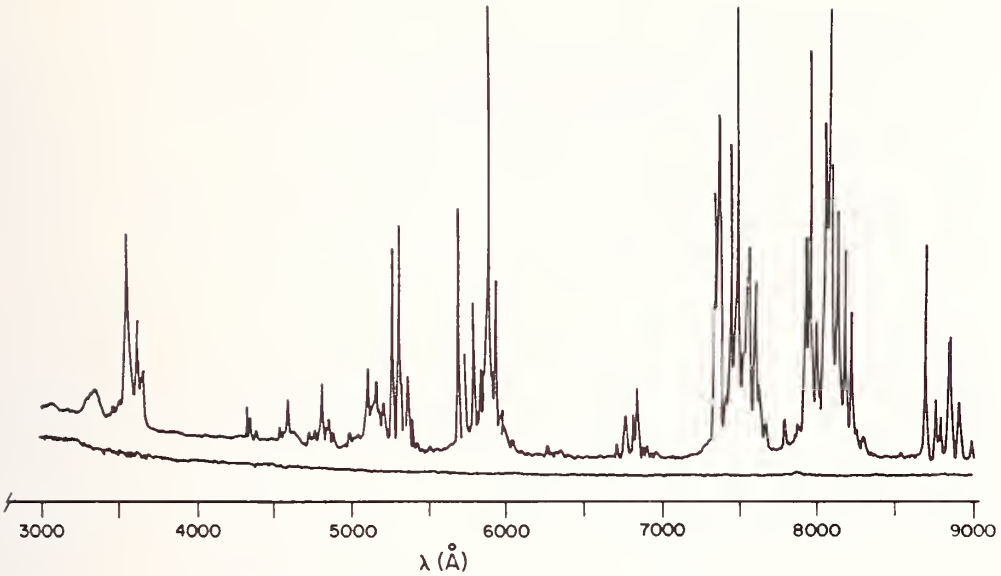

Figure 1. Absorption spectrum of Nd:YAG at 300 K.

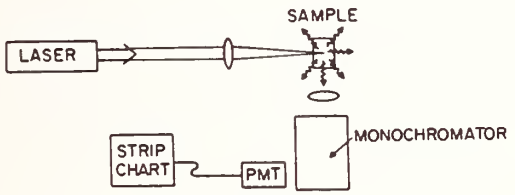

Fig. 2. Experimental setup.

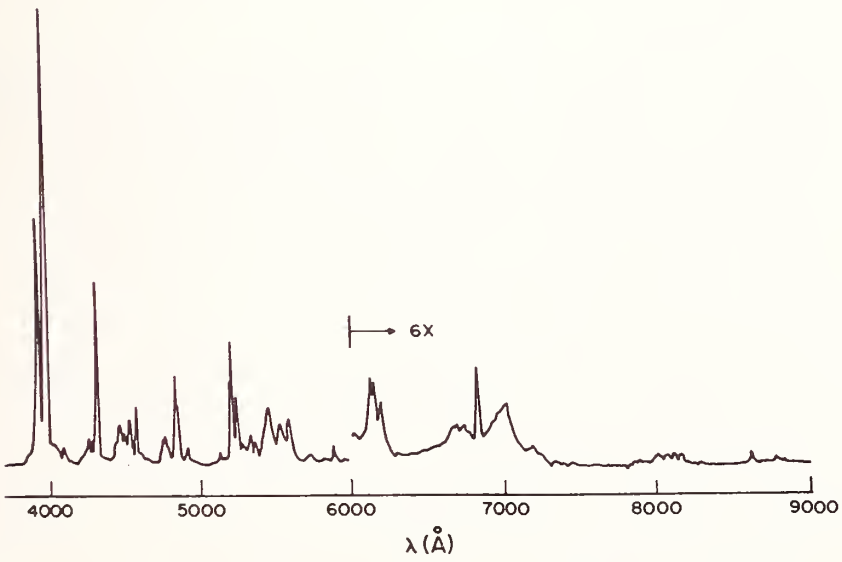

Fig. 3. Emission spectrum for three-photon excitation at 5933 Å.

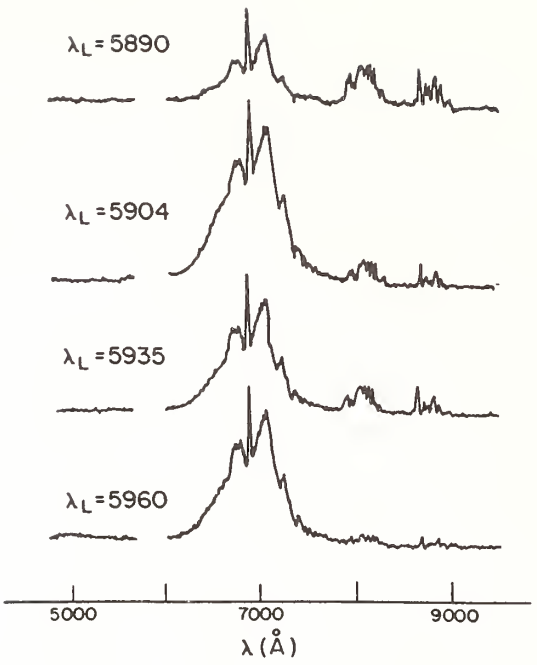

Fig. 4. Emission spectra for one-photon excitation at several wavelengths.

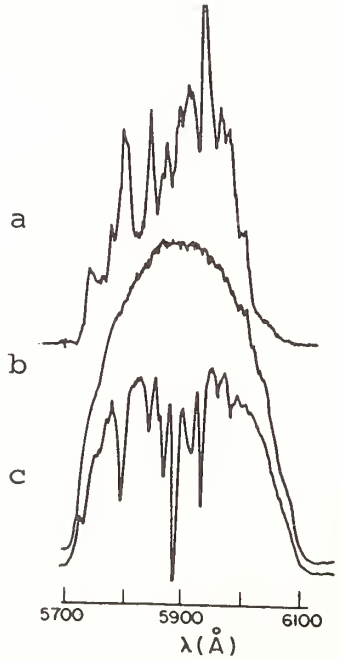

Fig. 6. a) Intensity of 4000Å fluorescence. b) Laser power vs. wavelength. c) Power transmitted by 5mm sample.

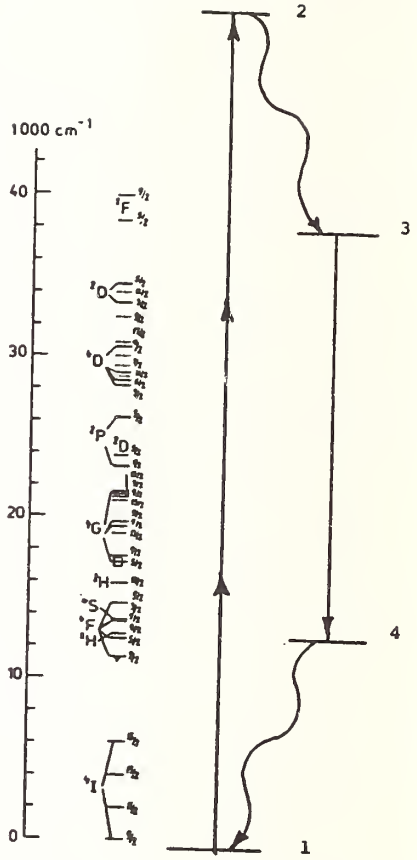

Fig. 5. Three-photon absorption process and Nd^{3+} energies.

REFRACTIVE INDEX AND THERMO-OPTIC COEFFICIENTS OF CD*A

L. G. DeShazer and K. E. Wilson
Hughes Research Laboratories
3011 Malibu Canyon Road
Malibu, CA 90625

The refractive indices of CD*A were measured at 29 wavelengths by the method of minimum deviation. The crystal was cut into a prism with the optic axis parallel to the prism apex edge enabling both the ordinary and extraordinary refractive indices to be measured without altering the position of the prism in its mount. The index measurements were made in a dry environment to prevent deterioration of the CD*A polished surfaces by moisture. The level of deuteration of the measured crystal was about 90%.

A two-resonance Sellmeier formula was fit by the method of least squares to the measured index values. The formula used was

$$n^2 = 1 + A\lambda^2/(\lambda^2-B) + C\lambda^2/(\lambda^2-D).$$

The determined Sellmeier constants are listed in Table 1 for both the ordinary and extraordinary indices. For example, the indices at 1.0642μm are Ne = 1.5366 and n_o = 1.5531.

Table 1. Sellmeier Constants for CD*A

	A	B(μm^2)	C	D(μm^2)
Ordinary	1.402934	0.0132	0.14654	24.0117
Extraordinary	1.34951	0.012227	0.062868	25.0

The thermo-optic coefficients $\alpha_n(\equiv n^{-1}dn/dT)$ of CD*A were measured as a function of wavelength from 325 to 632.8 nm using a double interferometric technique involving both Twyman-Green and Fizeau configurations. The thermal coefficient of linear expansion of CD*A perpendicular to the optical axis was also measured by this technique and was determined to be $8.7\pm0.2\times10^{-6}$/°C. At 632.8nm, dn/dT = 25.78×10^{-6}/°C for ordinary polarization and -20.19×10^{-6}/°C for extraordinary polarization. Using this data, Type I phasematch solutions were calculated for CD*A as a function of temperature. Figure 1 shows the phasematch plots for three frequency mixing in CD*A at room temperature which can be used to design sum frequency generators(SFG), difference frequency generators, and optical parametric oscillators. For example, in SFG the wavelength on the abscissa represents the sum frequency and the wavelengths on the ordinate axis represents the input frequencies.

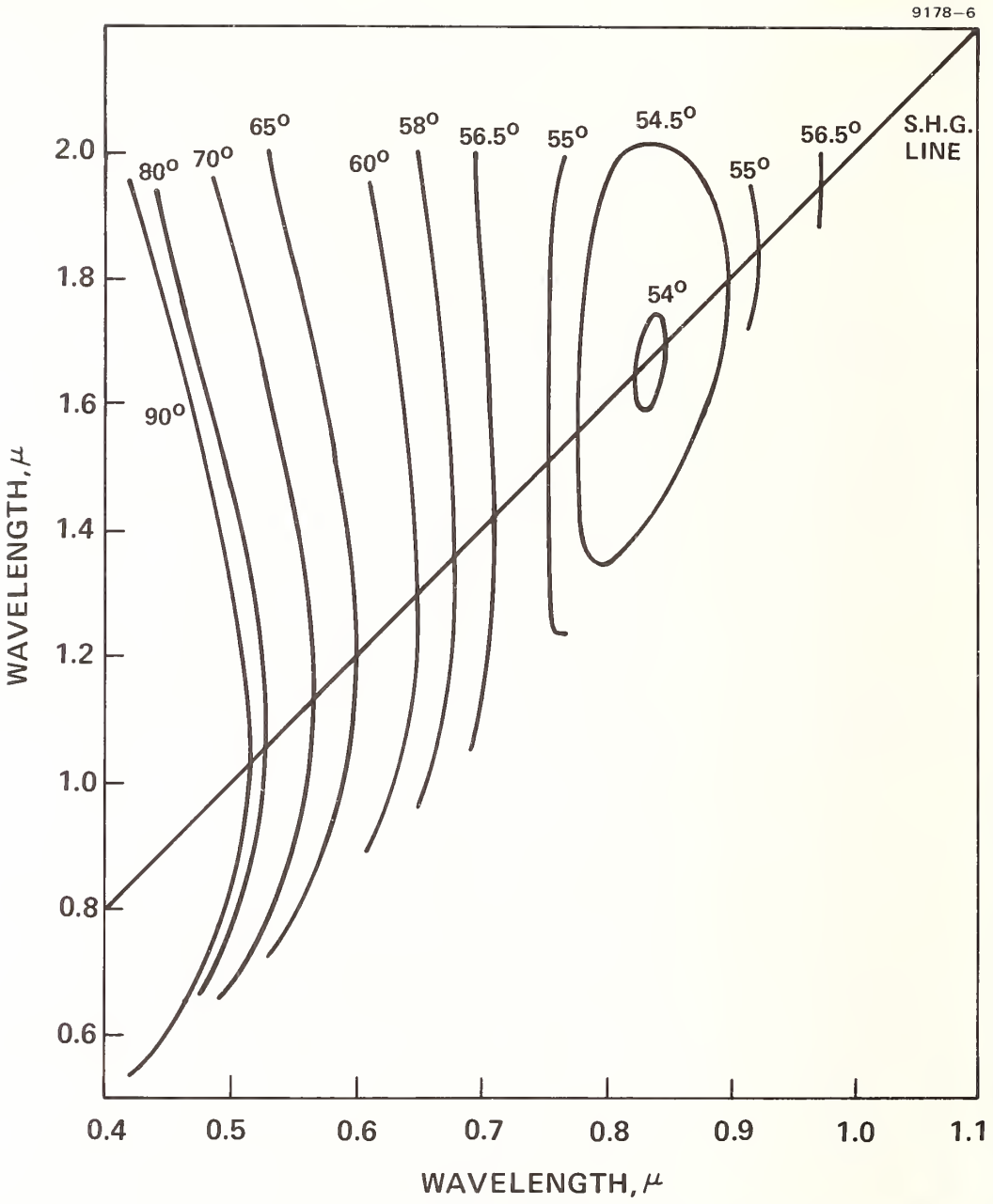

Figure 1. Type I phasematch plot for CD*A at room temperature.

ON THE USE OF A CALORIMETER TO INVESTIGATE LOSS MECHANISMS IN OPTICAL FIBERS

F. T. Stone
Bell Laboratories
Norcross, Georgia 30071

Loss mechanisms in optical fibers are classed as intrinsic, i.e., caused by the inherent limits of the materials and structure, and extrinsic, i.e., added on during processing. To attain low loss in fibers, the fundamental limits must be understood; then any additional contributions to fiber loss must be identified and reduced to negligible levels. In our lab we have used a calorimeter to aid in meeting these objectives. Calorimetry has the capability to: (1) directly measure absorption and total loss, (2) measure the loss of short (~1m) samples to determine uniformity over the fiber length, (3) measure extremely low fiber losses (~0.01 dB/km), (4) measure mode-dependent loss for multimode fibers (to determine the variation of loss over the core region) or measure the loss accurately in small-core-diameter fibers by exciting only a single mode even when these fibers support more than one mode (thus avoiding mode-cut off complications), and (5) measure the loss of the same segment of the fiber coated (or even completely packaged) and bare to quantify coating (or packaging) loss. We present here examples illustrating a variety of uses of calorimetry in fiber loss measurements.

MODE DEPENDENT LOSS

Since short lengths of fiber can be measured, the mode distribution set up at the input face of the fiber is essentially the distribution in the fiber length being measured. (Extremely lossy cladding, leaky, and marginal bound modes are eliminated immediately after launch with a mode stripper.)

Different mode groups are excited in the graded-index multimode fibers studied by scanning a focused laser beam across the fiber core. Lowest order modes are excited with the beam focused at the center of the core, highest order modes with beam focused on the core-cladding boundary. Figure 1 presents the mode-dependent loss of two fibers: for fiber 399, which exhibits a large amount of higher-order mode attenuation, other measurements indicate core-cladding boundary problems; fiber 434, on the other hand, is a

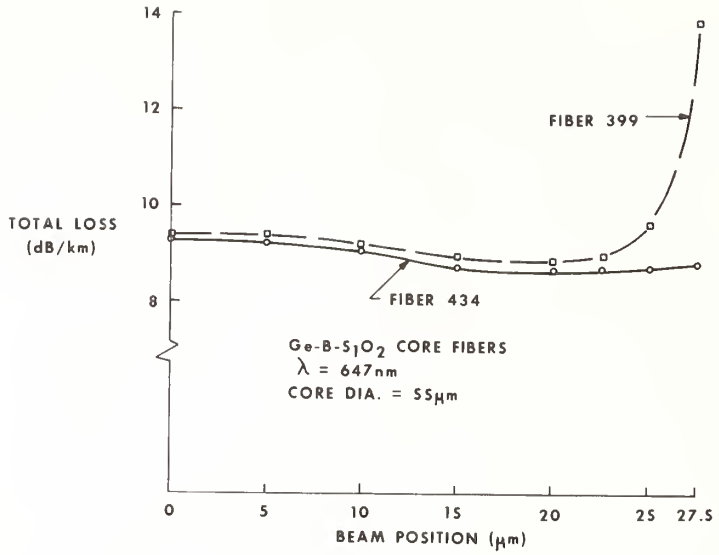

Fig. 1. Mode-dependent loss characteristics of two fibers

reasonably good fiber of the same type inserted for comparison. These plots illustrate how mode-dependent loss data aids in localizing the region of excess fiber loss.

UNIFORMITY OF THE LOSS OF VARIOUS SEGMENTS OF A LONG FIBER

The title of this section presents one aspect of a fundamental problem in fiber manufacture - how uniform are the fiber parameters with position down the fiber. This question is also pertinent in evaluating a technique such as calorimetry that provides information on limited regions of the fiber. We have examined the loss-uniformity of many fibers using an optical time-domain reflectometer, a scattering cube, and a calorimeter. Figure 2 is a presentation of absorption

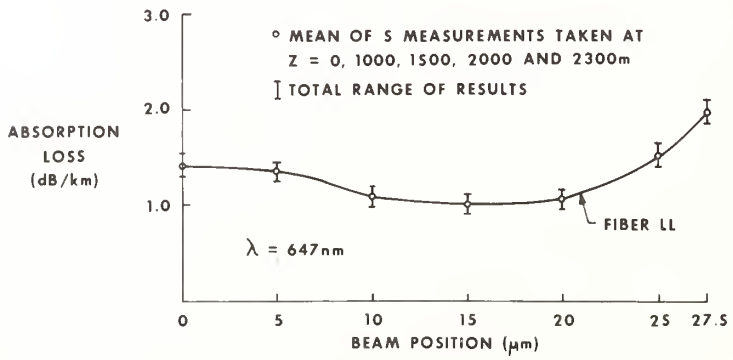

Fig. 2. Absorption loss measured on segments taken from different regions of a 2300m long fiber.

data of fiber segments taken from various places along a 2.3-km fiber. As can be seen, the absorption appears uniform throughout the fiber; hence, measurements on any one segment are typical of the whole fiber.

Using calorimetry, the loss versus length of a fiber can also be measured for situations where loss differences are caused by changes in the mode distributions in the fiber, not by changes in the fiber itself. By doing this, one can, for example, study the effectiveness of different excitation conditions in launching an approximation to the steady-state mode distribution.

EFFECT OF COATING

Figure 3 demonstrates the way a coating can increase the

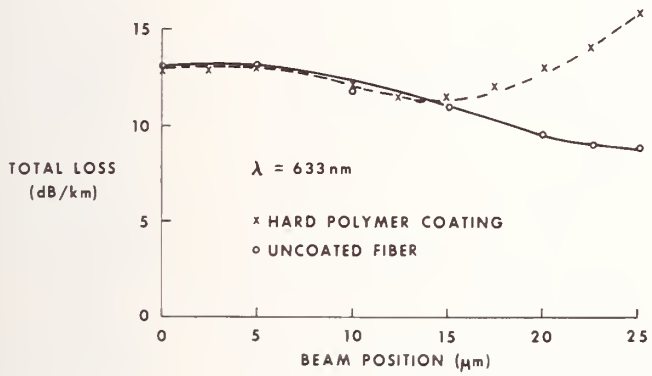

Fig. 3. Coated vs. uncoated fiber loss illustrating the measurement of packaging loss

higher-order mode loss, probably by causing microbending. Such results can be used to compare different packaging materials, for instance, in an environmental study, and to settle questions such as whether or not a given coating is responsible for excess loss measured in a fiber by other techniques.

SPECTRAL LOSS

Figure 4 is the absorption loss of an experimental single-mode fiber that was examined to determine the cause of the excess loss. The results show absorption far greater than that of a good fiber (see 647-nm data point in Figure 4). By using various lines of a Krypton laser, the absorption can be obtained at a number of wavelengths in the visible and near IR, giving a good outline of the spectral characteristics of the absorber. In this case the outline matches that of nickel in sodium borosilicate glass as reported by Beales et al.[1] This has not been directly verified, however. Another aspect of the usefulness of calorimetry is illus-

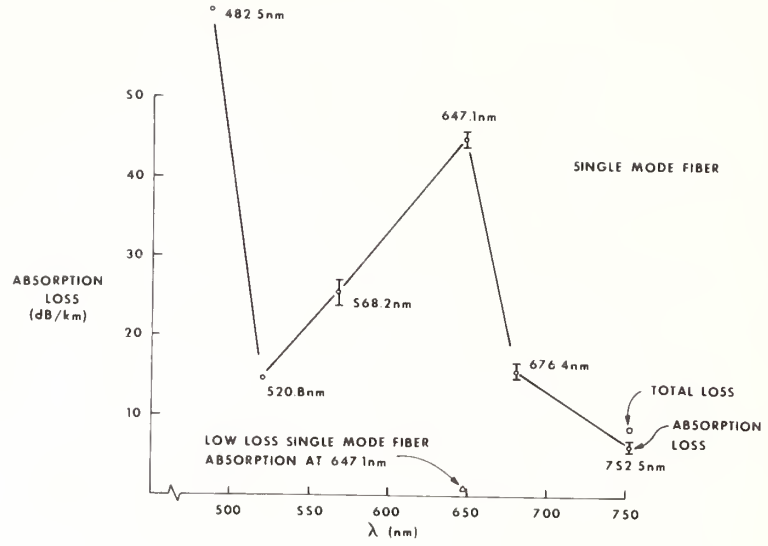

Fig. 4. Spectral absorption loss of a single mode fiber with large extrinsic absorption

trated by this example, namely the capability to measure separately the fiber absorption and the total fiber loss.

FUNDAMENTAL LOSS MEASUREMENTS

Since only short lengths of fibers are needed for calorimetry, the lack of mode mixing enables the power distribution to be determined rather exactly, for example, by measuring the near-field radiation pattern. Thus, power distributions can be excited that probe only the regions of the fiber that one wishes to study. If one wished to examine the loss of the glass itself, one could avoid launching energy in the vicinity of the core-cladding boundary, thereby avoiding complications caused by the unknown nature of this boundary. Furthermore, the loss history of the glass could be examined as a function of various environmental conditions - heat, humidity, radiation, etc. - and this glass effect could be separated out from any effects due to packaging changes.

Because calorimetry can detect very low losses, these various measurements mentioned can be made with great sensitivity and repeatability (~0.01 dB/km for ~1 watt through the fiber). By optimizing the calorimeter structure and the measurement electronics, appreciably lower losses could be measured. For these reasons calorimetry is a useful measurement technique to examine the intrinsic and extrinsic loss characteristics of optical fibers.

K. J. Beales, C. R. Day, W. J. Duncan, J. E. Midwinter, and G. R. Newns, Proc. IEE 123, 591 (1976).

COMPUTERIZED REFRACTIVE INDEX MEASUREMENT FOR FIBER OPTIC GLASSES

D. L. Wood and J. W. Fleming
Bell Laboratories
Murray Hill, New Jersey 07974

In screening glass compositions for possible waveguide applications it is necessary to evaluate the refractive index and its first and second derivatives with respect to wavelength. We have constructed an apparatus to perform this task with a minimum of operator time required but with accuracy in the fifth decimal place of the index routinely achieved.

The apparatus is built around a 20-bit digital angle sensor which measures the deviation of monochromatic radiation through a prism of the composition to be investigated. A minicomputer controls the experiment, records the data and calculates the index values from the measured angles. We chose an optical system involving an off-axis parabolic collimating mirror and a reflecting rear face on the prism so that measurements at other than room temperature can also be conveniently made, and a broad wavelength range can be covered.

Index values for germanium silicate glasses of various compositions have been measured, and these results together with temperature coefficients near room temperature will be reported.

STRESS OPTIC COEFFICIENT OF OPTICAL FIBERS

N. Lagakos
The Catholic University of America
(Present Address: Naval Research Laboratory
Code 8133, Washington, D.C. 20375)

Introduction: The introduction of a mechanical clad under compression as a possible solution to the static fatigue problem of optical fibers[1] has necessitated the develovpment of a polariscope for measuring the stress optic coefficient and the stress profile of optical fibers. Such a polariscope has been developed. This polariscope could be used for evaluating the acoustic response of the optical fiber acoustic sensors[2].

Experimental set-up: The stress optic coefficient of fibers, f, was determined by the experimental set-up shown schematically in Fig. 1, which is based on the Friedel's method of compensation[3]. The light from an Argon ion laser after becoming partly incoherent by passing through a scrambler (a rotating semitransparent plastic disc) was incident perpendicularly on the fiber. The observed part of the fiber was immersed in a refractive index matching liquid and it was placed between a polarizer and an analyzer with their vibration axes perpendicular to each other and at 45° with the fiber axis. A quarter-wave plate was placed before the analyzer to ensure linear light polarization. A 20x microscope objective and a projection lens focused the fiber cross section on the plane of a 0.7mm diameter pinhole in front of a photomultiplier. By slight translation of the projection lens the transmitted light from different parts of the fiber could be detected. The fiber was held horizontally with one end fixed and the other clamped by a mount which could freely slide horizontally in a slot. A weight suspended at the end of a string, which was attached to the moveable mount around a pulley, was applied along the fiber axis introducing some stress σ_z. This stress would rotate the light polarization (retardation) by an angle θ, which is given by the rotation angle of the analyzer axis for minimum transmitted light. It can be shown that $\sigma_z = Nf/L$, where $N(= \theta/180)$ is the relative retardation and L is the light path length in the fiber. It can be shown that f can be obtained from the slope, S, of the plot of weight, W, vs resultant light retardation θ as follows:

$$f = \frac{180LS}{\pi R^2} \quad ; \quad W = \left(\frac{\pi R^2 f}{L180}\right)\theta = S\theta . \qquad (1)$$

The retardation profile of the clad was obtained by translating the projection lens in small steps. This would translate the fiber image

on the pinhole plane allowing different parts to be detected. The retardation was then obtained directly from the rotation angle of the analyzer for minimum transmitted light power. From the retardation profile and the stress optic coefficient the stress profile was obtained and the average clad compression was calculated.

Experimental Results: The stress optic coefficient, f, was first determined for a suprasil fiber without clad. (In this case the light path was a diameter). The results of this experiment are shown in fig. 2, where the applied weight is plotted against the resultant retardation. From the best linear fit of these data the slope S was determined, and from eq (1), f was found to be 3.19 ± 4% brewsters, in agreement with the literature[4]. In addition, f was also determined for a phasil fiber[5] (a 96% silica type glass made by sintering a purified leached porous glass), without clad. The value was found to be 3.16±4%, which is almost identical to that for suprasil. Finally, f was determined in the clad of four different fibers with phasil clad and silica core doped with Cs_2O for the first three fibers and Cs_2O-K_2O-Bi_2O_3 for the fourth (table I, column I). For these four fibers as well as for four more fibers with core dopant Cs_2O-K_2O-Bi_2O_3 the stress profile was determined from the clad retardation and the stress optic coefficient and the average clad stress was calculated (table I, column III). (For the last four fibers f was taken to be equal to the one found for the fourth fiber). These results were compared with the stress determined on the fiber preforms (table I, column II) using an optical polarizing microscope equipped with a tilting compensator. (The values for f found for the fibers were used). It seems that the stress found in the preforms is slightly but consistently higher than the fiber clad compression. Finally, the compression strengthening of these fibers was obtained directly from tensile tests[6] using an Instron testing machine (table I, column IV) and it was found to be in good agreement with the results of the above described technique.

References

1. D.A. Krohn and A.R. Cooper, J. Amer. Ceram. Soc. 52 (12) 661-64 (1969).
2. FOSS Workshop at NRL, Washington, D.C., December 12-14, 1979.
3. A.J. Durelli and W.F. Riley, Introduction to Photomechanics, Prentice Hall, Englewood Cliffs, N.J. (1965).
4. M.J. Saunders, Rev. Sci. Instrum. 47, 496 (1976).
5. P.B. Macedo, et. al., U.S.A. patent 3, 938,974, Feb. 17 (1976).
6. O.H. El-Bayoumi, R.K. Mohr, N. Lagakos, and P.B. Macedo, "Residual Stress Measurements of Optical Fibers with Surface Compression," to be submitted for publication to the J. of the Am. Ceram. Soc.

TABLE I

Strees Optic Coefficient brewsters	Preform Stress kpsi	Fiber Average Stress kpsi	Fiber Strength results kpsi
3.16 ± 7%		19 ± 15%	24 ± 7%
2.80 ± 5%	14 ± 5%	10 ± 12%	11 ± 4%
2.69 ± 7%	12	10 ± 12%	10 ± 5%
2.78 ± 7%	26	21 ± 12%	22 ± 5%
	33	33 ± 10%	32 ± 6%
	34	31 ± 8%	36 ± 5%
	31	26 ± 9%	24 ± 5%
	25	20 ± 13%	22 ± 4%

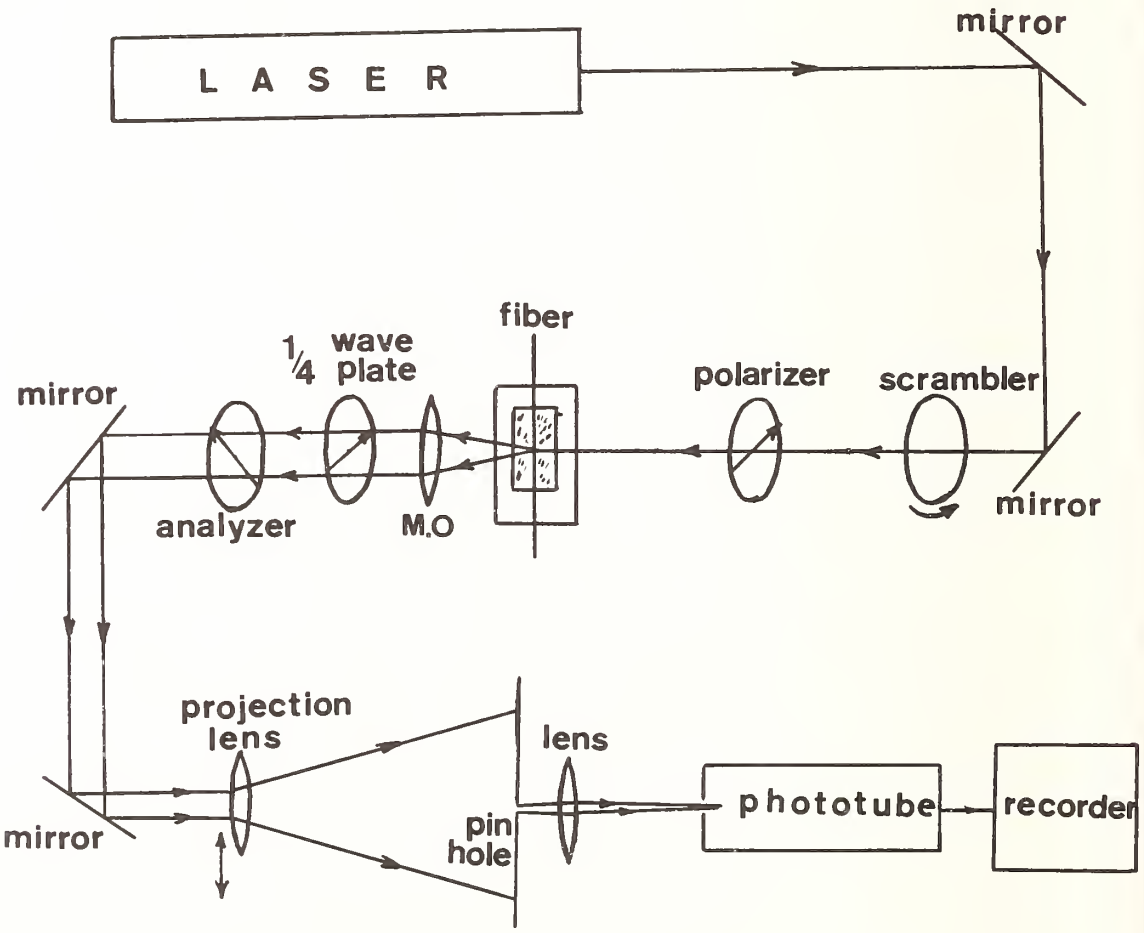

Fig. 1 Experimental set-up for measuring stress optic coefficient and stress profile in fibers.

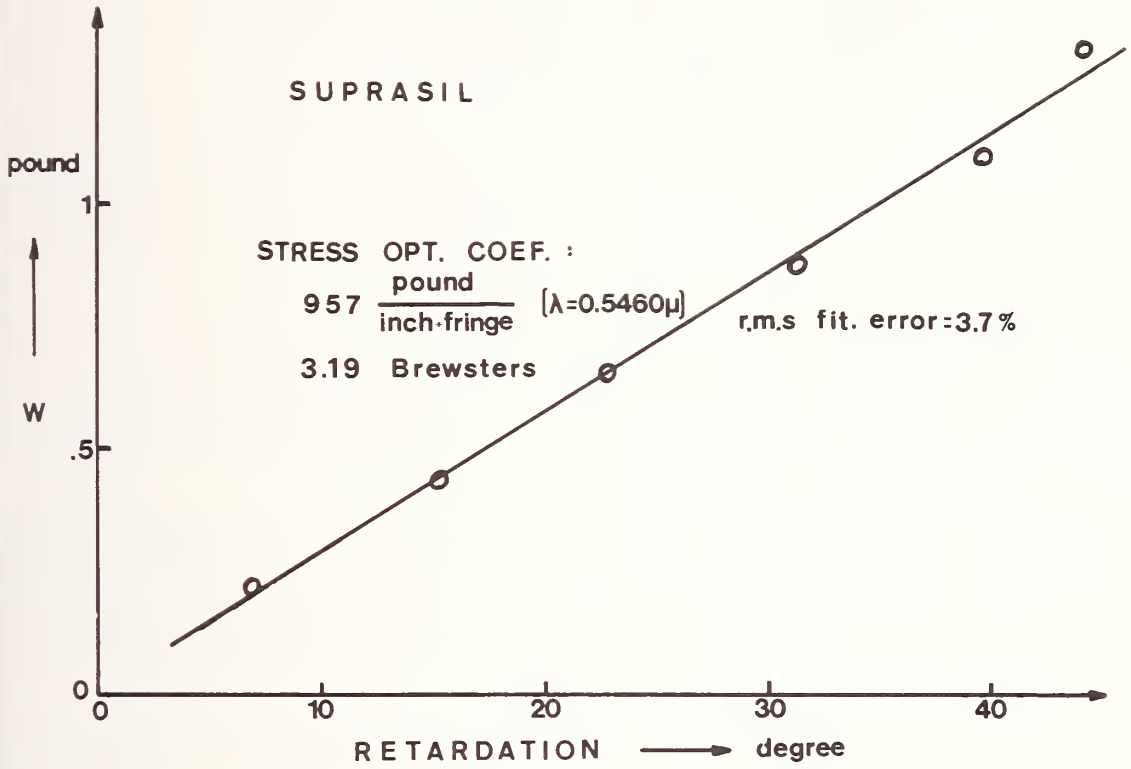

Fig. 2 Applied weight vs. resulted retardation for a suprasil fiber (circles). The straight line is the best linear fit to these data.

CHROMATIC MEASUREMENTS OF GRADIENT INDEX MATERIALS BY MULTIPLE WAVELENGTH INTERFEROMETRY

Danette P. Ryan
Gradient Index Laboratory
The Institute of Optics
University of Rochester
Rochester, New York 14627

Gradient index materials have been studied at the University of Rochester. The samples studied are several centimeters in aperture and are applicable to high performance lens systems. The design of components using these materials requires accurate measurement of the index of refraction profile and the dispersion.

Models[1] predict the existence of achromatized gradient index materials. These materials would make possible the manufacture of color corrected fibers and single element lenses (Wood lenses). Accurate dispersion measurements are required to verify the existence of these materials.

Multiple wavelength a.c. interferometry has been used to obtain the index of refraction profile and the chromatic properties with a single measurement. Two simultaneous wavelengths are used for any single measurement.

The theory has been developed for a Mach-Zehnder interferometer. The standard two beam interference equation can be written out for each of the two wavelengths incident upon the interferometer. The final irradiance is given by

$$I(x,y,\lambda_1,\lambda_2) = I_{11} + I_{21} + I_{12} + I_{22} + 2\sqrt{I_{11}I_{21}}\cos\delta_1 + 2\sqrt{I_{12}I_{22}}\cos\delta_2 \qquad (1)$$

where I_{11}, I_{21} and δ_1 are dependent upon x, y and λ_1 and I_{12}, I_{22} and δ_2 are dependent upon x, y and λ_2.

Using a standard trigonometric identity, one obtains

$$I(x,y,\lambda_1,\lambda_2) = I_{11} + I_{21} + I_{12} + I_{22} + 2(\sqrt{I_{12}I_{22}} - \sqrt{I_{11}I_{21}})\cos\delta_2 + 4\sqrt{I_{11}I_{21}}\cos 1/2\,(\delta_1 - \delta_2)\cos 1/2\,(\delta_1 + \delta_2) \qquad (2)$$

The term of interest is the term containing the product of the two cosines. The cosine whose argument contains the sum of the phases at the two wavelengths is at a relatively high frequency. The cosine

whose argument contains the difference of the phases at the two wavelengths is at a relatively low frequency and is the envelope function. It contains the dispersion of the gradient as a function of the spatial coordinates.

In order to automate the data acquisition process, one mirror of the interferometer is modulated. The phase is then a function of both space and time. For two wavelength a.c. interferometry, the phase is written as a function of spatial coordinates and time for each of the two wavelengths

$$\delta(x,y,\lambda_1,t) = \delta_1 + \delta(\lambda_1,t)$$

$$\delta(x,y,\lambda_2,t) = \delta_2 + \delta(\lambda_2,t) \qquad (3)$$

Assuming $\delta(\lambda_1,t) = \delta(\lambda_2,t) = \delta(t)$, $I_{11} = I_{12}$ and $I_{21} = I_{22}$, equation 1 becomes

$$I(x,y,\lambda_1,\lambda_2,t) = 2I_{11} + 2I_{21} + 2\sqrt{I_{11}I_{21}}\left\{\cos\delta(t)\left[\cos\delta_1 + \cos\delta_2\right] - \sin\delta(t)\left[\sin\delta_1 + \sin\delta_2\right]\right\} \qquad (4)$$

Using standard trigonometric identities this becomes

$$I(x,y,\lambda_1,\lambda_2,t) = 2I_{11} + 2I_{21} + 4\sqrt{I_{11}I_{21}}\cos 1/2(\delta_1 - \delta_2)\cos\left[1/2(\delta_1 + \delta_2) + \delta(t)\right] \qquad (5)$$

Only one term of this equation has time dependence. The amplitude of this a.c. signal is given by

$$4\sqrt{I_{11}I_{21}}\cos 1/2(\delta_1 - \delta_2) \qquad (6)$$

The amplitude of the a.c. signal contains the information of importance for the dispersion measurements. It corresponds to the envelope function of equation 2 which gives the dispersion of the gradient as a function of the spatial coordinates.

Figure 1 is a schematic of the a.c. Mach-Zehnder interferometer used for the measurements. Two colinear laser lines enter the interferometer. The sample is conjugate to detectors 1 and 2. The light is filtered at detectors 2 and 3. The signal at detector 2 is a measure of the index profile at one wavelength. Detector 3 is used as a phase reference at that same wavelength. The signals from detectors 2 and 3 are processed in hard-wired electronics and analyzed by a minicomputer to yield the index of refraction profile. Detector 1 detects the sum of the irradiance patterns due to the separate wavelengths. The signal is processed electronically to yield the amplitude of the a.c. signal given by equation 6. This signal is then

analyzed by the minicomputer to yield the dispersion of the gradient as a function of position.

Figures 2 and 3 show the experimental results for a gradient index sample. Figure 2 is the index of refraction profile obtained from detectors 2 and 3. Figure 3 compares an experimental plot of the amplitude of the a.c. signal to a theoretical plot of that same quantity. The experimental plot is modulated due to an intensity mismatch between the two laser lines. This modulation is predicted by equation 2. The envelope of the experimental curve is found to be in good agreement with the theoretical curve. These results are consistent with the results obtained by Moore and Ryan using a conventional a.c. interferometer.[2]

The multiple wavelength a.c. interferometer has an advantage over the conventional a.c. interferometer. It yields the index profiles for two wavelengths in a single measurement. In addition, a direct measure of the dispersion can be obtained.

References:

1. Stephen D. Fantone, Design, Engineering and Manufacturing Aspects of Gradient Index Optical Components, Ph.D. Thesis, University of Rochester, 1979.
2. Duncan T. Moore and Danette P. Ryan, Measurement of the Optical Properties of Gradient Index Materials, J. Opt. Soc. Am. 68, No. 9, pp 1157-1166.

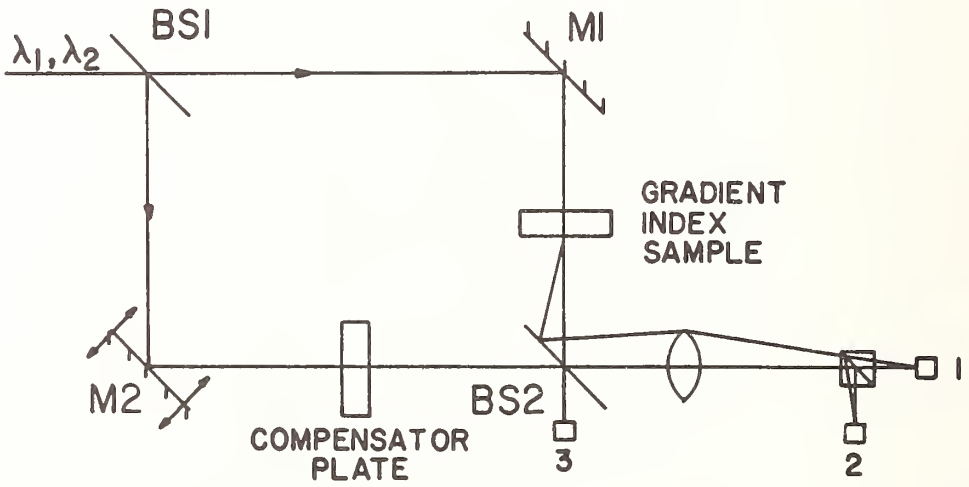

Figure 1

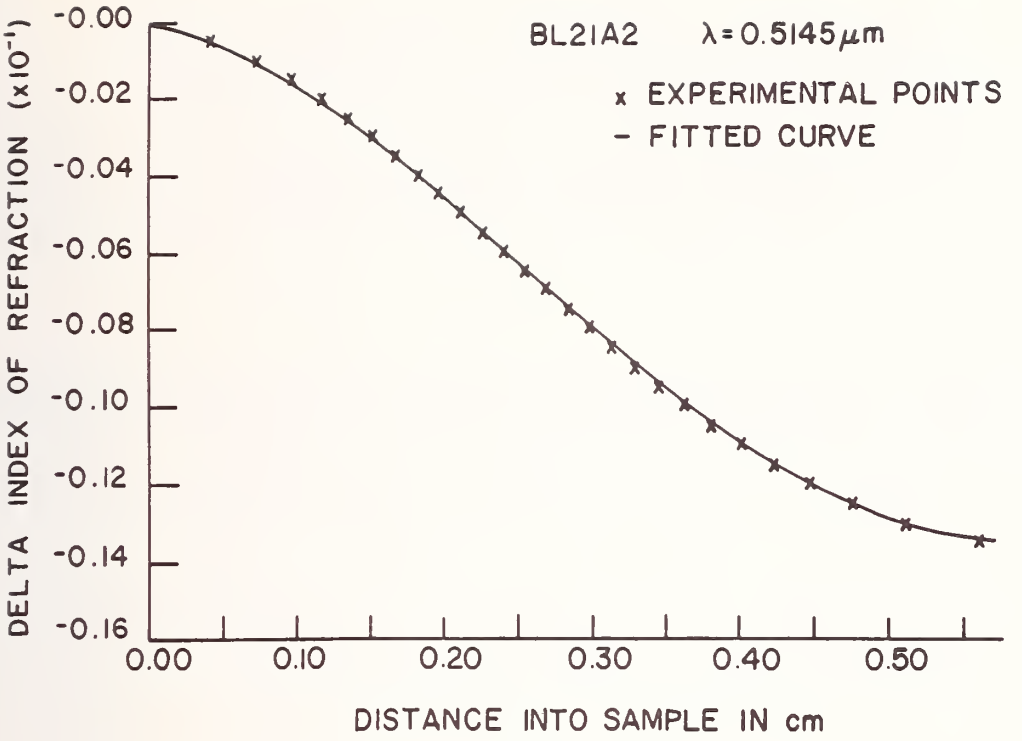

Figure 2

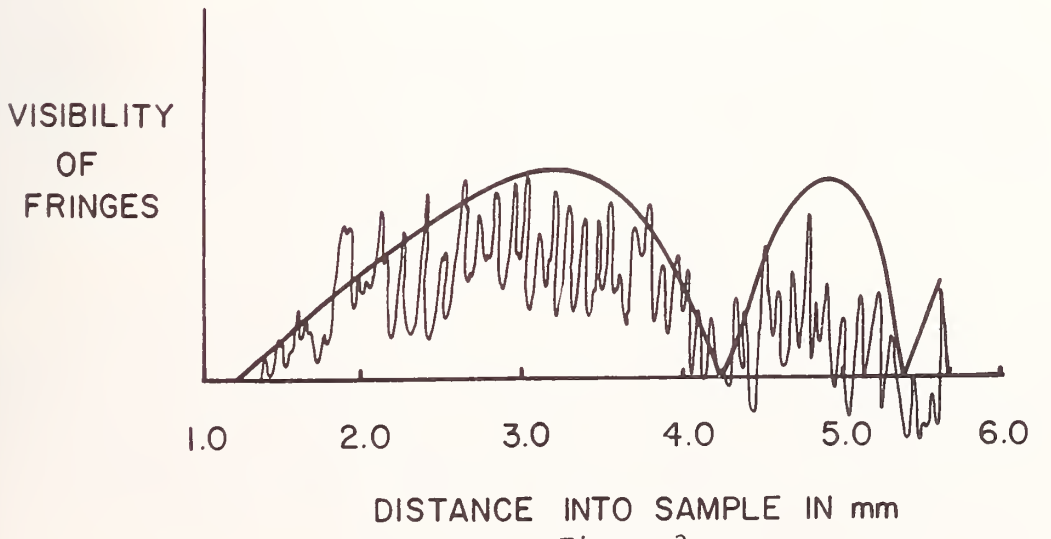

Figure 3

OPTICAL COUPLING COEFFICIENTS FOR PULSED CO_2 LASER RADIATION ON BARE AND PAINTED ALUMINUM SURFACES

S. C. Seitel, J. O. Porteus, and W. N. Faith
Michelson Laboratory, Physics Division
Naval Weapons Center, China Lake, California 93555

Introduction

The response of a material sample to laser radiation is specified by the coupling coefficient, defined as the fractional energy absorbed in a given time interval. The coupling of 10.6 μm radiation to planar aluminum samples has been studied extensively; reference 1 contains a recent bibliography. In all cases, the coupling coefficient was determined by observing the temperature rise or rise rate of an appropriately instrumented sample. In this paper, a fundamentally different method of measurement, based on thermal expansion of the laser-heated sample, is reported. Coupling coefficients for bare and painted aluminum are presented for pulsed laser fluences up to 145 J/cm^2.

Theory

The total energy absorbed is given by the volume integral of the temperature rise ΔT in the material; it does not depend upon the details of the temperature distribution. In a sample of length L and constant cross-sectional area A, the absorbed energy E(t) depends only on the irradiation time t:

$$E(t) = \rho CA \int_{o}^{L(t)} \Delta T(z,t)dz \quad . \tag{1}$$

Here z represents position along the length of the sample. Equation (1) presumes that the sample area A, specific heat C, and mass density ρ are constant, and that thermal losses to radiation and convection are negligible. After irradiation, the sample length satisfies Eq. (2):

$$L(t) = L_o + \frac{F(t)\ L(t)}{YA} + r \int_{o}^{L(t)} \Delta T(z,t)dz \quad , \tag{2}$$

where L_o is the unstretched length. The remaining terms represent sample elongation due to tensile load F(t) and to thermal expansion. Young's modulus Y and the thermal expansion coefficient r are presumed constant. Before irradiation (t = 0), elongation is determined only by the applied tensile load F(0), since $\Delta T = 0$. The net length change $\Delta L(t)$ is taken up by the load cell, which has elastic compliance $\gamma_L = -\Delta L(t)/\Delta F(t)$. Thus, the instantaneous tensile relaxation $\Delta F(t) = F(t)-F(0)$ must satisfy

$$-\gamma_L \Delta F(t) = \frac{\Delta F(t)\ L(0)}{YA}\left[1 - \gamma_L \frac{F(0)}{L(0)}\right] + r \int_0^{L(t)} \Delta T(z,t)dz \quad . \qquad (3)$$

The second term in brackets is negligibly small if the experimental parameters F, L, and γ_L are chosen carefully. Equations (3) and (1) together yield the desired expression for total optical energy absorbed as a function of the observed peak tensile relaxation:

$$E(t) = -\frac{1}{r}\rho CA(\gamma_L + \gamma_S)\Delta F(t) \quad . \qquad (4)$$

Here $\gamma_S = L(0)/YA$ is the elastic compliance of the sample. The coupling coefficient is the slope of the curve obtained when E(t) is plotted against the total energy incident on the sample. In the experiments reported here, values for C, ρ, and r were taken from tables of physical data, while A, γ_L, and γ_S were measured directly.

Experiment

Samples 1.0 mm wide by 50 mm long were cut from the .030 mm thick 2024-T3 aluminum [2], using a pair of slitting saws on a common mandrel in a milling machine. Earlier attempts to shear samples to size induced distortion and caused paint delamination. Sample thickness was reduced to 0.15 mm (including paint, if any) in a single pass with the edge of a milling cutter. This increased the energy per unit (sample) volume deposited in a single pulse and, hence, system sensitivity by a factor of two. The samples were cleaned carefully with acetone to remove machining residues.

The sample was clamped between the jaws of a tensioning device, shown schematically in Fig. 1; a static tensile load, approximately 50% of the elastic limit, was applied by increasing the jaw separation. The elastic limit was established for each sample from a measurement of elongation vs. applied load; it is the maximum load which caused no permanent deformation. For virgin samples, the elastic limit was approximately 4.4 N (8 pounds). Pulsed 10.6 μm laser radiation of 100 nsec duration was focused on the sample center with a ZnSe lens. The spatial profile at the target, inferred from pinhole scans, was very nearly Gaussian, but elongated (with a Ge prism) to overfill the narrow sample dimension. The $1/e^2$ full widths in the elongated direction, and normal to it, were 1.399 and 0.393 mm, respectively. Approximately half of the total energy was intercepted by the sample.

The total optical energy delivered to the sample was determined by deflecting a known fraction of the incident radiation onto a calibrated reference detector with a beamsplitter. That portion of the incident laser pulse which was absorbed was converted into heat, causing the sample to expand thermally. The expansion was taken up internally by a fast load cell which, together with bridge circuit and chart recorder, sensed and displayed the resultant tensile relaxation. System response

to a typical thermal pulse was limited by the recorder to 20 msec. Sensitivity was 8.8×10^{-4} N (2×10^{-4} pounds). Recovery to ambient temperature and tension was governed by the rate at which absorbed laser energy was removed. The dominant mechanism was heat conduction to the massive sample supports, with a characteristic time of approximately 1 sec. This is long compared to the time required to diffuse heat across the sample (1 msec); thus the linear integrations in Eqs. (1) and (2) are justified.

Results

Figure 2 shows the energy absorbed by an unpainted sample as a function of intercepted incident energy. The slope, which is the coupling coefficient, increases dramatically at the flash threshold ($\sim$ 17 mJ), from 0.03 to 0.25, in agreement with published values obtained by direct temperature measurements [1,3,4]. Coupling above threshold is dominated by the laser-produced plasma, which absorbs more strongly than the reflective bare metal. Unpainted samples show little evidence of damage above threshold in spite of the large amount of energy absorbed. Plasma expansion evidently enlarges the area over which energy is transferred to the aluminum, so that the effective fluence is reduced. At very high incident fluences, the slope decreases; this is consistent with more rapid plasma expansion or detachment, with reduced transfer to the sample [1,5]. No permanent laser-induced deformation was observed, even in samples stretched to the elastic limit. The maximum fluence (145 J/cm^2), which was sufficient to produce an intense flash and crater the sample surface, is well above that required to produce the slip phenomena reported previously [6]. It is concluded that laser-induced slip has no significant adverse effect on mechanical strength under load. Shock effects from individual pulses produce no measurable reduction in strength under these conditions.

Also shown are similar results for a painted sample. The peak absorption coefficient occurs at very low incident energies and was measured as 1.15. This remarkable result is, in fact, consistent with an overall energy measurement accuracy of 20%. No significant change in slope occurs at the flash threshold, since absorption already is near total. The roll-off above threshold is attributed to plasma shielding as above, except that the painted surface produces a rapidly expanding plasma at lower energies. This is consistent with the observation that the painted samples are damaged severely above threshold.

References

[1] J. A. McKay et al., J. Appl. Phys. 50, 3231 (1979).
[2] Sample materials were supplied by G. F. Thomas of Vought Corporation.
[3] S. Marcus, J. E. Lowder, and D. L. Mooney, J. Appl. Phys. 47, 2966 (1976).

[4] W. E. Maher and R. B. Hall, J. Appl. Phys. 49, 2254 (1978).
[5] J. O. Porteus et al., NBS Spec. Publ. 509, 204 (1977).
[6] J. O. Porteus, M. J. Soileau, and C. W. Fountain, NBS Spec. Publ. 462, 165 (1976).

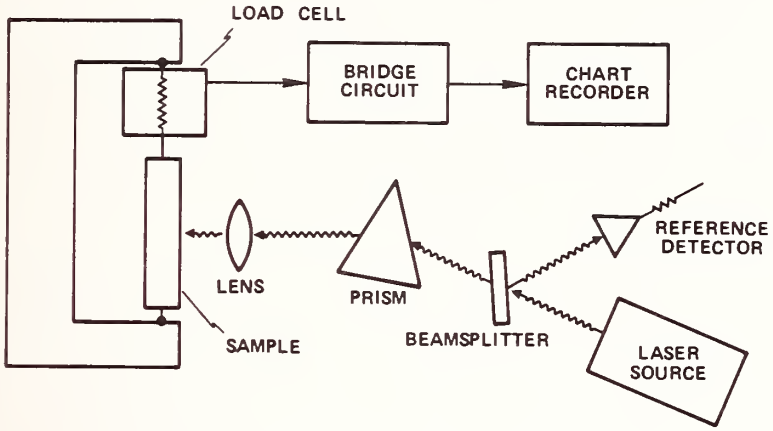

Figure 1. Experimental apparatus.

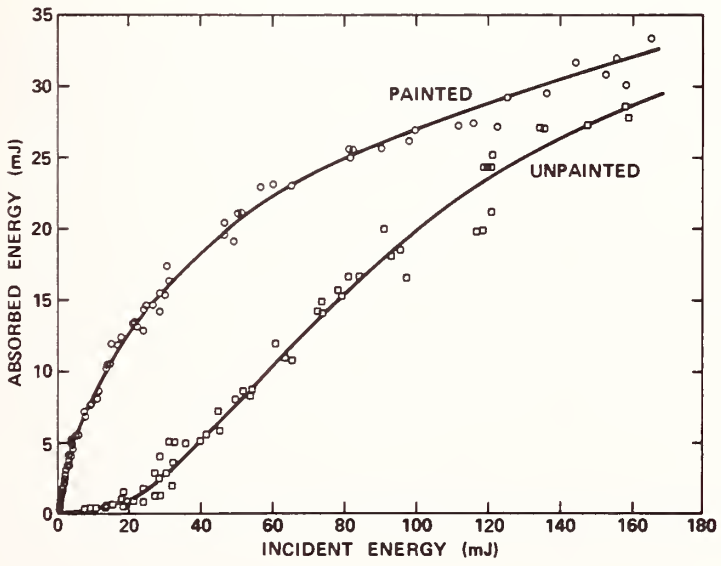

Figure 2. Absorbed versus incident energy.

THERMOMODULATION SPECTRA OF HIGH-ENERGY INTERBAND TRANSITIONS IN Cu, Pd, Ag, Pt, AND Au

C. G. Olson and D. W. Lynch
Ames Laboratory-USDOE and Department of Physics
Iowa State University, Ames, Iowa 50011
and
R. Rosei
Ames Laboratory-USDOE and Department of Physics
and
Istituto di Fisica del'Universita, Rome, Italy*

Many f.c.c. metals exhibit a rise in the reflectance at about 18eV, leading to a broad peak. Thermomodulation spectra in this region reveal a richly-structured spectra. We have made thermotransmission measurements [1] on unsupported thin films of Cu, Pd, Ag, and Au, and thermoreflectance measurements on Pt in the 15-30eV spectral region. The temperature-modulated transmittance spectrum can be shown to be simply $-d\Delta\mu$, the sample thickness multiplied by the negative of the temperature-induced change in the absorption coefficient. No data treatment is necessary. For Pt the thermoreflectance spectra were Kramers-Kronig analyzed to get $\Delta\mu$. The data obtained for these metals is given in Fig. 1. The spectra do not change appreciably when the ambient temperature is changed.

There are no core electron excitations in this spectral region. The structures in $\Delta\mu$ arise from excitations of the 3d, 4d, or 5d electrons. Band structures for many of these metals have been calculated by Christensen, [2,3,4] all with the same method and potential, so comparisons between metals are meaningful. Figure 2 shows his band structure for Au. The region of structure beginning around 18eV corresponds to excitations from the top of the 5d band complex to the relatively flat bands centered around Γ, about 11eV above the Fermi energy. These flat bands are based on 5f wave functions at Γ with mixing of p components away from Γ. The shifts in the structures from one metal to another correlates with the shift in the d-bands as can be seen in Fig. 1. The phase space associated with Γ is very small and critical points at Γ should not contribute strongly to either the absorption spectrum or the modulated absorption spectrum. However one can see, even in Fig. 2, many places where possible initial bands and final bands are parallel, especially along Σ and Λ, and these may produce critical points very close to those at Γ, critical points at nearly the same energies and with more associated phase space.

*Present address.

We fit Christensen's bands for Au to a parametrization scheme and sought interband critical points along Σ and Λ, finding over 40 such points, all rather close to the zone center. Of these, we eliminated a few by selection rules, then looked for those which involved the same band pairs as the interband critical points at Γ, assuming that they all would be modulated by the same mechanism, since nearly the same states were being considered. The critical point transitions may be modulated by a thermal-expansion-induced shift of the energy, a thermally-induced broadening, or both. Each type of critical point has a characteristic line shape for each mechanism.[5] We synthesized the expected spectrum for each of the Γ interband critical points and for the nearby Σ and Λ critical points involving the same bands. Figure 3 is an example. It is clear that the Γ critical points contribute little, but the Σ and Λ points dominate. The line shapes are such that either a red shift or a broadening with increasing temperature or both is consistent with the data for all of the major structures seen.

The spectra for the metals other than Au, e.g., Ag, show less fine structure in the corresponding region. This appears to be the result of more overlapping of the structures. A mapping of all the Γ critical points expected from the band calculations onto the measured spectra, the letters u-z in Fig. 1, shows this to be the case. Critical point transitions at L, shown as letters a-r contribute some structure and a background, while critical point transitions at X contribute as well, but not just in the region of prominent structure. Note that the calculated critical points have not been shifted before plotting.

Pt has a different spectral feature at about 15eV, a positive peak followed by a negative peak. This is the characteristic shape of a transition from the Fermi level to a relatively flat band [6] and it agrees in energy with the energy of the flat band at Γ above E_F. A similar transition is not present in Pd, although it might be expected, because the density of d states at E_F is lower.

The sharpness of the structures in the thermoreflection spectrum for Au, about 0.1eV, implies that these excited states, over 15eV above E_F have relatively long lifetimes, long compared with those for electrons in free electron-like bands just below them in energy.[7,8,9] This long lifetime probably is the result of selection rules for electron-electron scattering.

This work was supported by the U.S. Department of Energy, contract No. W-7405-Eng-82, Division of Materials Sciences budget code Ak-01-02-02-2. It was carried out at the Synchrotron Radiation Center of the Physical Sciences Laboratory of the University of Wisconsin. The storage ring was operated under NSF contract DMR-77-21888. We wish to thank N. E. Christensen for tables of energy eigenvalues for Au at several lattice spacings, and for partial joint densities of states for Au and Ag. We

also acknowledge assistance from B. N. Harmon and D. J. Peterman in the use of the interpolation program and a program to produce plots of interband energies vs. wave vector.

References

1. R. Rosei, M. Meuti, C. Coluzza, and C. Quaresima, Opt. Letters 1, 217 (1977).

2. N. E. Christensen, Phys. Rev. B 13, 2698 (1976).

3. N. E. Christensen, Phys. Stat. Solidi (b) 54, 551 (1972).

4. N. E. Christensen, Phys. Rev. B 14, 3446 (1976).

5. E. Matatagui, A. G. Thompson, and M. Cardona, Phys. Rev. 176, 950 (1968).

6. R. Rosei and D. W. Lynch, Phys. Rev. B 5, 3883 (1972).

7. J. A. Knapp, F. J. Himpsel and D. E. Eastman, Phys. Rev. B 19, 4952 (1979).

8. P. Thiry, D. Chaudesris, J. Lecante, C. Guillet, R. Pinchaux, and Y. Petroff, Phys. Rev. Lett. 43, 82 (1979).

9. P.S. Wehner, R. S. Williams, S. D. Kevan, D. Denley, and D. A. Shirley, Phys. Rev. B 19, 6164 (1979).

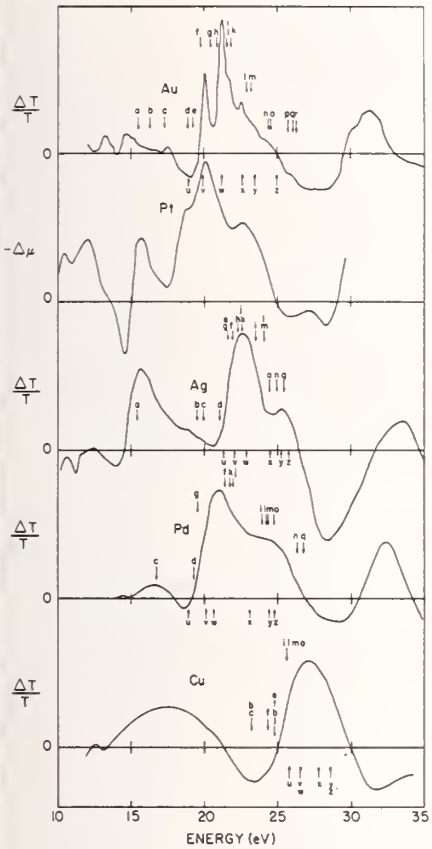

Figure 1. Thermotransmission spectra ($\Delta T/T = -d\Delta\mu$) for Au, Ag, Pd and Cu, and $-\Delta\mu$ for Pt. The ambient temperatures are 52K for Au and about 200K for the other metals. $\Delta T/T$ is in arbitrary units and the magnitudes of two spectra cannot be compared.

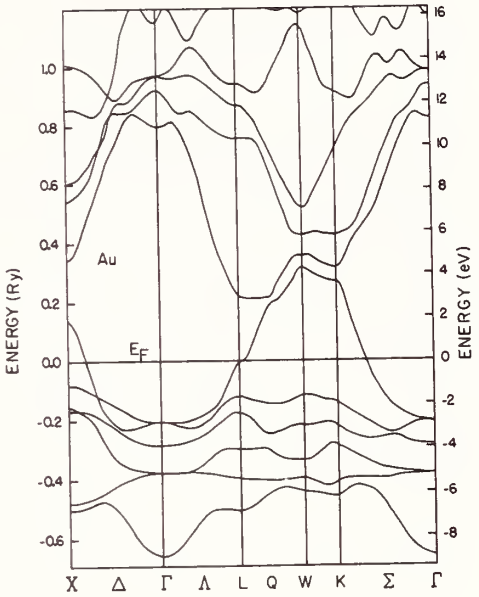

Figure 2. Energy bands of Au obtained by a Fourier series fit to the eigenvalues of Ref. 2.

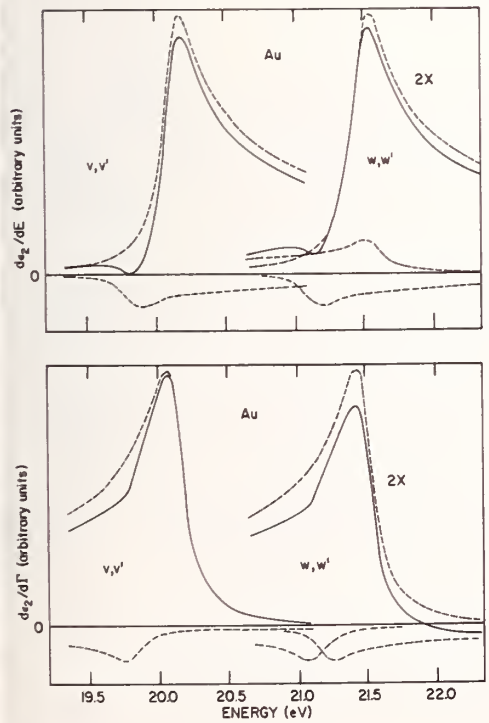

Figure 3. Line shapes for $-\Delta\epsilon_2(n-\Delta\mu)$ spectra for an $M_0(V)$ and $M_3(w)$ critical point at Γ and the associated critical points along Σ and Λ (v' and w') upper: Modulation by a red shift of the critical point energy. Lower: Modulation by thermal broadening.

ELLIPSOMETRIC OBSERVATIONS ON THERMALLY GROWN OXIDE FILMS ON TITANIUM

Alia H. Musa and W. E. J. Neal
Physics Department
University of Aston in Birmingham
Birmingham, B4 7ET, U.K.

Apart from the use of oxide films of titanium as transparent anti-reflection coatings (Fan and Bachner[1], Yoshida[2]), recently there has been increased interest in their possible application in the photo-reduction of water to produce hydrogen. The work reported here on optical properties of oxide films on titanium forms part of an on going investigation into properties of materials for solar applications. The equipment used for the optical studies was the two angle ellipsometer described by Neal[3] but in this investigation only one angle of incidence (63.8°) was employed. The wavelength range was in the visible region from 397.1 nm to 576.6 nm. Details of the ellipsometric technique have been adequately described elsewhere; see for example Neal[4].

The basic equation of ellipsometry is:

$$R_p/R_s = \tan \psi \exp(i\Delta). \qquad (1)$$

In general, film growth on a surface changes the values of both ψ and Δ. The magnitudes of the changes depend on film thickness, the optical constants of the substrate and film material and the radiation wavelength. For the growth of thin films on a pure clean substrate (up to 10 nm thick) the changes $\delta\psi$ and $\delta\Delta$ can be assumed to be proportional to thickness for a given substrate and film. For thick films this approximation is not valid and exact equations proposed by Drude must be used. The exact equations have been used for all calculations in this work. Winterbottom[5] drew attention to the fact that a polar diagram plot of tan ψ against Δ, for film growth on a surface, produced a closed loop for nonabsorbing films but the curve for an absorbing layer was not closed. In this work plots of tan ψ against Δ for different thermally grown oxide layers on titanium have been compared with computer generated values using assumed optical constants n and k for the oxide and measured constants for the titanium substrates which were mechanically polished in air.

The titanium substrates were examined optically prior to the grow of oxide films and were characterised by the instrument angle settings ψ and Δ as previously mentioned. The values were measured

for light radiation of five wavelengths in the range 397.1 nm to 576.6 nm. Because of the wavelength spread the Beattie-Conn method was employed as opposed to the use of the compensator method. The values obtained are given in Table 1 together with the corresponding optical constants n and k for the clean substrate. Figure 1 shows plots of computed values of ψ and Δ as a function of n for values of k ranging from 3.22 to 3.28. Experimentally determined values of ψ and Δ at a given wavelength for the surface of a clean titanium substrate are shown as horizontal lines. The points of intersection giving the same value of n and k are the values taken to characterise the substrate prior to oxide growth.

Table 1. Optical constants of titanium substrate.

λ (nm)	ψ degrees	Δ degrees	n_2	k_2
576.6	32.48	139.29	2.52	3.36
546.1	32.62	137.76	2.36	3.28
499.7	33.65	134.29	2.01	3.26
454.1	32.60	131.08	1.94	2.96
397.1	32.46	127.34	1.76	2.78

Figure 2 shows an example of a plot of tan ψ against Δ at a wavelength of 546.1 nm for the growth of an oxide film on bulk titanium in air at 750 K as measured at stages during the growth. Computed values of ψ and Δ are also shown for films of different thickness on a substrate with optical constants determined experimentally as indicated above. In the example shown the computed values were generated by using optical constants n = 2.40, k = 0.24 for the titanium oxide on a titanium substrate having n = 2.36, k = 3.28 (from fig. 1). The values of n and k were determined as indicated above and the optical constants obtained at the various wavelengths are given in Table 2, together with substrate reflectances.

The reflectance of the (TiO_2 - Ti) system was calculated from the expression as given by Heavens[6] for an absorbing surface covered by an absorbing layer. Figures 3A and 3B show reflectance against wavelength for differing thickness of oxide on titanium and reflectance against oxide thickness for the two extreme wavelengths.

The optical constants obtained by other workers for titanium films and bulk titanium can be compared with the present values given in

Table 2. The optical constant of titanium free film, titanium oxide and the calculated reflectances.

λ (nm)	Optical Constant of metal free film (Ti)		Optical Constant of Film (TiO_2)		% R
	n_2	k_2	n_1	k_1	Substrate
576.6	2.52	3.36	2.45	0.23	57.4
546.1	2.36	3.28	2.40	0.25	57.1
499.7	2.01	3.26	2.39	0.25	59.2
454.1	1.94	2.96	2.38	0.24	55.9
397.1	1.76	2.78	2.38	0.23	54.1

Table 1. In the region of 580 nm the present values lie between those of Smith[7] for films deposited in UHV and those of Winterbottom[8] for mechanically polished material. At a wavelength of 540-550 nm published values of n lie between 1.78 for mechanically polished surfaces in air to 3.09 for bulk material polished in UHV.[5,8 11] The highest value of n for films deposited in UHV is 3.03. It can be assumed in general that the cleaner the surface the higher will be both the n and k values. Published values for k over the same wavelength region vary from 3.73 for films prepared in UHV to 2.46 for mechanically polished bulk. The optical constants of n = 2.36 and k = 3.28 at a wavelength of 546.1 nm are lower than the best values reported for UHV prepared films and much higher than bulk samples polished in air indicating a good quality substrate for oxide growth.

Hass and Bradford[12] in 1957 assuming that k = 0 for the oxide obtained a value of n = 2.7 at a wavelength of 546 nm on evaporated titanium film. Menard[13] gives values of n = 2.4 and k = 0.17 in the wavelength range 588.9 nm to 589.5 nm for TiO_2 thermally grown in oxygen at 755 °K. The corresponding values for air grown TiO_2 are n = 2.40 and k = 0.25, obtained in the present work shows only a small variation in n from 2.45 to 2.38 over the wavelength range 576.6 nm to 397.1 nm and a variation in k from 0.23 to 0.25. The present work clearly shows slight absorption of TiO_2 in the visible region and is in close agreement with the work of Menard[13] at 589 nm.

Plots of oxide thickness (t) against log time (T) for a given temperature showed linear relationships relating to the expression

$$t = A + B \log T \qquad (2)$$

suggested by Vermilyea (14) for oxide growth on tantalum where A and B are constants at a given temperature.

REFERENCES

1. J. C. C. Fan and F. J. Bachner, Applied Optics 15, 1012 (1976).
2. S. Yoshida, Thin Solid Films, 56, 321 (1979).
3. W. E. J. Neal, Surface Technology 6, 81 (1977).
4. W. E. J. Neal, Applications of Surface Science 2, 445 (1979).
5. A. B. Winterbottom, Optical Studies of Metal Surfaces, Bruns Bokhandel, Trondheim, (1955).
6. O. Heavens, Optical Properties of Thin Solid Films (Dover, New York), (1955).
7. T. Smith, Surface Science 38, 292 (1973).
8. A. B. Winterbottom, Trans. Farad. Soc., 42, 487 (1946).
9. A. B. Winterbottom, J. Opt. Soc. Am. 38, 38 (1948).
10. A. B. Winterbottom, J. Iron & Steel Ind. (London) 165, 9 (1950).
11. A. B. Winterbottom, Ellipsometry in the Measurement of Thin Films.
12. G. Hass and A. P. Bradford, J. Opt. Soc. Am. 47, 125 (1957).
13. C. R. Menard, J. Opt. Soc. Am., 52, 427 (1962).
14. D. A. Vermilyea, Acta Metall. 6, 166 (1958).

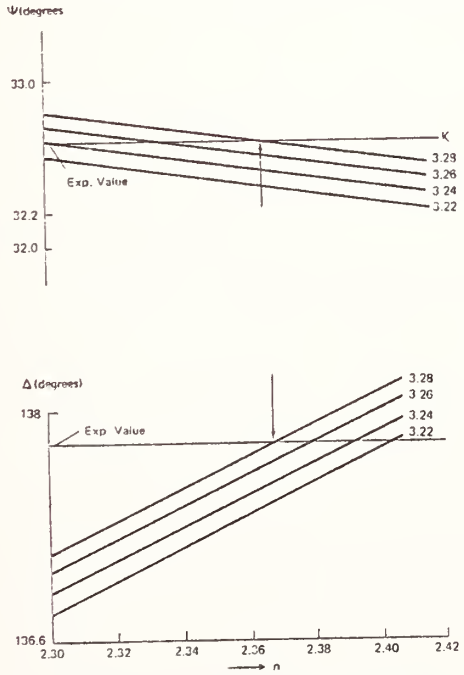

FIG. 1 ANGLES ψ AND Δ VERSUS n FOR DIFFERING VALUES OF k.

FIG. 2 TAN ψ VS. Δ FOR (TiO_2-Ti) SYSTEM
x - Experimental, • - computed, ϕ_o = 63.6°,
λ = 546.1 nm

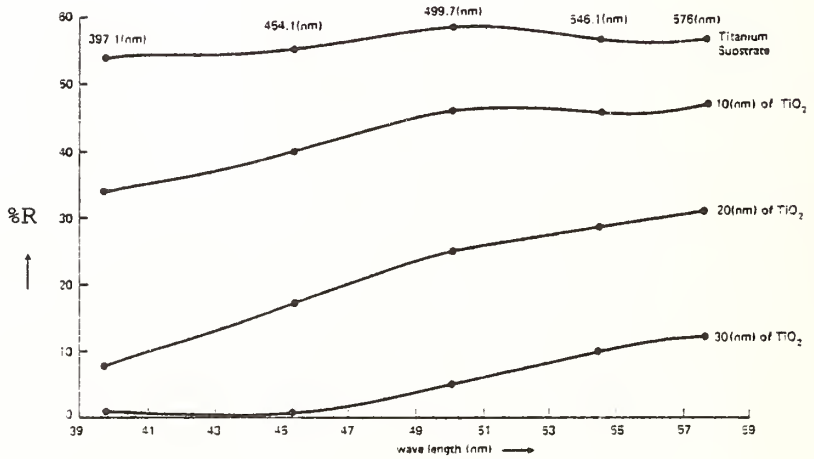

FIG. 3A REFLECTANCE AGAINST WAVELENGTHS FOR DIFFERING THICKNESSES OF TITANIUM OXIDE ON TITANIUM

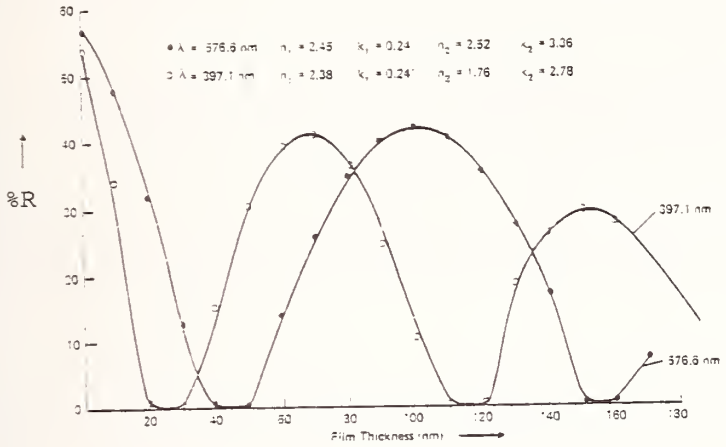

FIG. 3B REFLECTANCE CURVES FOR (TiO_2-Ti) SYSTEM

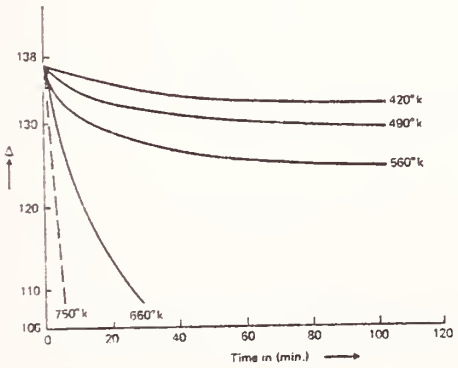

FIG. 4 Δ AGAINST TIME DURING OXIDATION OF BULK TITANIUM IN AIR AT VARIOUS TEMPERATURES FOR λ = 546.1 (nm)

OPTICAL PROPERTIES OF A-15 THIN FILMS AND SINGLE CRYSTALS

R. C. McKee, D. W. Lynch, C. G. Olson, and J. W. Osmun
Ames Laboratory-USDOE and Department of Physics
Iowa State University, Ames, Iowa 50011
and
J. H. Weaver
Synchrotron Radiation Center, University of Wisconsin
3725 Schneider Drive, Stoughton, Wisconsin 53589

Much interest has been paid to A-15 compounds in recent years but not a great deal of work has been done on their optical properties. There have been some reflection studies in the optical range [1] on V_3Si, V_3Ge, V_3Pt and Ti_3Sb and in the infra-red on V-Ga alloys [2] and Nb-Sn alloys.[3] Ellipsometry measurements [4] have been made on several A-15 compounds in the near i.r. in an attempt to extract effective Drude parameters.[5,6] There is a question if these parameters are meaningful since calculations [7] on ten A-15 compounds having Nb and V as the A element show possible interband transitions in the optical range. This problem seems to be solved for V_3Si [8] by doing far i.r. transmission studies which are below any interband transitions.

Our work has two parts. Most of the work has been on optical absorptance studies. These have been made on sputtered thin films of Nb_3Ge, Nb_3Al, Nb_3Ir, and V_3Ga; polycrystalline bulk samples of V_3Ga, V_3Ge, V_3Si, and single crystal Cr_3Si. The measurements were made in the energy range of 0.2 eV to 4.0 eV using a calorimetric technique operating at 4.2K. Reflectance measurements on Nb_3Ge, Nb_3Ir and Nb_3Al in the range 4.0 eV to 30.0 eV were done using synchrotron radiation at the University of Wisconsin. The second part of our work is to modulate thermally the sputtered films and measure the change in reflectance in the range 0.4 eV to 3.5 eV. The optical absorptance data is Kramers-Kronig analyzed and compared to existing band structures.[7,8]

The films were sputtered onto heated (850°C) sapphire substrates (5.0 mm x 12.5 mm x 0.05 mm) using the getter sputtering technique.[10] Transition temperatures and superconducting onset widths for Nb_3Ge, Nb_3Al and V_3Ga were respectively; (18.4K, 1.1K), (16.7K, 0.9K), and (14.6K, 0.1K). These samples have a surface roughness the same size as that of the substrates which are hundreds to several thousands of Angstroms. This appears in S.E.M. pictures and in non-specular reflection from synchrotron radiation data above 6.0 eV. This roughness will cause trouble in the visible also.

The calorimetric data was K-K analyzed using a Drude extrapolation for energies less than 0.2 eV with parameters chosen to match the slope and magnitude of the data. The vanadium compounds and the single crystal

Cr_3Si use vanadium absorption data [11,12] for the energy range 4.0 to 300.0 eV and an E^{-x}(x between 3.5 and 4.0) function used as a high energy extrapolation.

The optical absorptance data are shown in Fig. 1. The single crystal Cr_3Si has the sharpest structure with a peak in the absorptance at 0.85 eV. Spectra from sputtered films of V_3Ga show a small peak at 0.85 eV and structure at 0.3 eV, while data from a polycrystalline bulk sample yielded a shoulder at 0.85 eV but not the low energy structure, otherwise being the same. Bulk samples of V_3Si and V_3Ge produced spectra which are in agreement with some of the literature [1,4] with the main structure being a shoulder at 0.75 eV. This is shifted from the peak in the Cr_3Si and V_3Ga spectra.

The absorptance data obtained from the sputtered films of the niobium compounds show structure which is smeared when compared to the vanadium and chromium compounds. Spectra from Nb_3Ge shows broad structures at 1.0 eV and about 1.6 eV. Data from Nb_3Ir appears as a shoulder at 0.45 eV and a peak at 1.3 eV, while Nb_3Al spectra yields small shoulders at 0.45 eV, o.75 eV and 2.0 eV.

Figure 2 graphs the conductivity obtained from the K-K analysis. The conductivity shows a peak for V_3Ge and V_3Si at 1.0 eV which shifts for V_3Ga to 1.1 eV and to 1.45 eV for Cr_3Si. Nb_3Ge has structure at 1.3 eV. A peak at 0.55 eV and one at 0.95 eV constitute most of the structure for Nb_3Al.

Figure 3 shows a band structure calculation [7] for V_3Ga showing the complication of bands caused by the transition metal. The broad 1.1 eV structure in the conductivity of V_3Ga has possible origins at M and along parallel bands in the S, T and Λ directions.

Spectra obtained from thermomodulation studies of these films show signals one part in 10^4 to 10^5, smaller than that of Cr which are one part in 10^3. This is expected since these films have low resistance ratios between one and three.

This work was supported by the U.S. Department of Energy contract No. W-7405-eng-82, Division of Materials Sciences budget code AK-01-02-02-2. Most of the work was carried out at Ames Laboratory-USDOE and the Department of Physics at Iowa State University. The remainder of the work was done at the Synchrotron Radiation Center of the Physical Sciences Laboratory of the University of Wisconsin. The storage ring was operated under NSF contract DMR-77-21888.

References

1. J. A. Benda, T. H. Geballe and J. H. Wernick, Phys. Letters, 46A, 389 (1974).

2. A. I. Golovashkin, I. S. Levchenko, T. A. Leskova, V. M. Sokolov, and N. S. Vorob'yeva, Fiz. metal. metalloved 36, 1187 (1973).

3. A. I. Golovashkin, E. D. Donner, I. S. Levchenko, and G. P. Motulevich, Soviet Physics JEPT 32, 1064 (1971).

4. B. Y. Yao Ph.D. thesis (Princeton, 1978) (unpublished).

5. I. Tüttö, L. M. Kahn, and J. Ruvalds, Phys. Rev. B 20, 952 (1979).

6. M. H. Cohen, Phil. Mag. 3, 762 (1958).

7. B. M. Klein, L. L. Boyer and D. A. Papaconstantopoulos, Phys. Rev. B 18, 6411 (1978).

8. S. W. McKnight, S. Perkowitz, D. B. Tanner, and L. R. Testardi, Phys. Rev. B 19, 5689 (1979).

9. W. E. Pickett, K. M. Ho and M. L. Cohen, Phys. Rev. B 19, 1734 (1979).

10. H. C. Theuer and J. J. Hauser, Transactions of the Metallurgical Soc. of A.I.M.E. 233, 588 (1965).

11. B. Sonntag and R. Haensel, Solid State Comm. 7, 597 (1967).

12. D. W. Lynch, J. H. Weaver and C. G. Olson, Phys. Rev. B 10, 501 (1974).

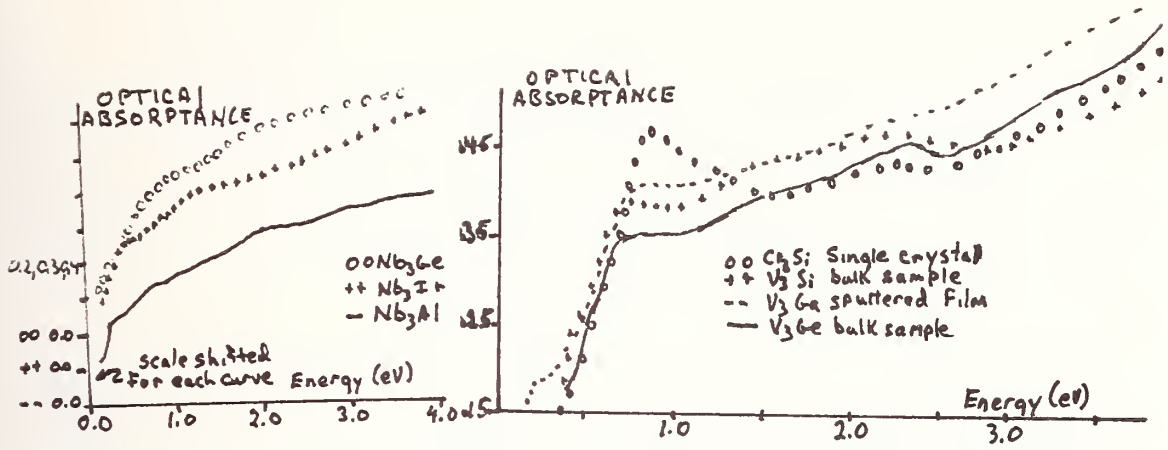

Figure 1. Optical absorptance of Nb_3Ge, Nb_3Al, Nb_3Ir, V_3Ga sputtered films; single crystal Cr_3Si; and V_3Ge and V_3Si bulk samples.

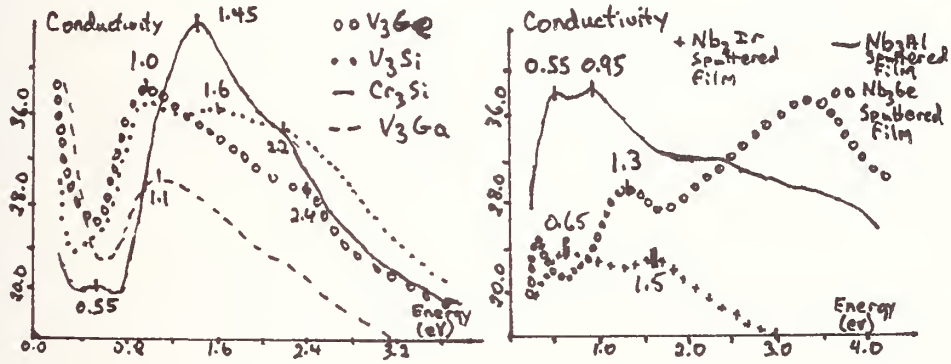

Figure 2. Conductivity of A-15 compounds obtained from K-K analysis. Note the main feature, the peak shift at 1.0 eV in going from V_3Ge and V_3Si to 1.1 eV in V_3Ga and to 1.45 eV in single crystal Cr_3Si.

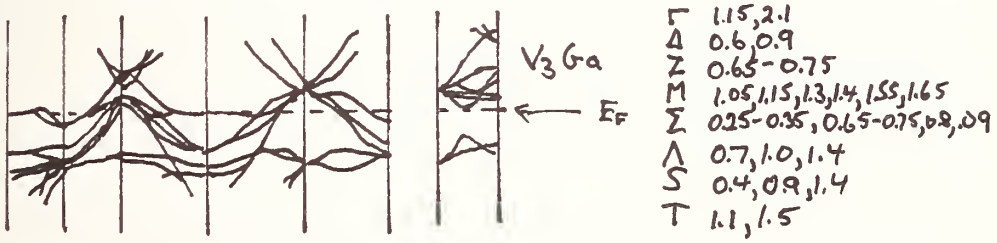

Figure 3. Band structure calculation [7] of V_3Ga and listing of energies (eV) of allowed direct interband transitions at symmetry points.

IR ABSORPTION BANDS IN MULTILAYER THIN FILMS OF SOME II/VI, V/VI MATERIALS

J.S. Seeley, R.Hunneman, A.Whatley
Department of Cybernetics
University of Reading
Reading, England

In an empirical investigation of materials for use in FIR interference and/or absorption filters we have given attention to the thin layer forms of familiar bulk materials. These comprise ZnS, ZnSe, CdSe and CdTe (II/VI) and As_2S_3, As_2Se_3 (V/VI). A prerequisite of the materials is that they be available in pure and stoichiometric evaporable form[1][2], and that their dissociation (if any) during evaporation be recoverable during deposition in the manner described by Ritter and Hoffman[3]. The deposition surface comprises polished, non-oriented polycrystalline substrates the temperature of which is precisely controlled by a thermal contact technique; at about 100°C for single layers, at about 180°C with bled-in O_2 for "hard" multilayers on silicon substrates, at 20°C for "soft" multilayers on KRS-5 or 6 substrates.

Many of the materials have been investigated in the configuration of the optical multilayer, for the dual purpose of demonstrating interference possibilities and minimising the specific thickness of each contributory layer of the material: the significance of this latter being that thick, single, layers become excessively rough and are known to yield inadequate delineation of the reststrahlung band[4].

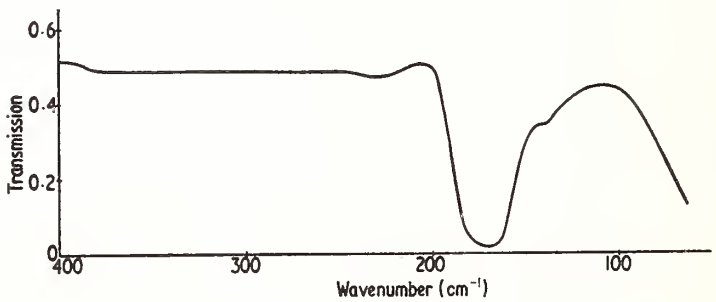

Fig. 1 CdSe/PbTe multilayer on Si substrate containing about 3 μ equivalent of CdSe

The possibility that a sharp and fully absorbed reststrahlung band could be obtained from one constituent in a multilayer initially came to our attention in CdSe/PbTe-based interference filters transmitting

to 40 μ. The CdSe band at 185 cm^{-1} is shown in Fig.1, where the onset of PbTe absorption beyond 100 cm^{-1} can also be clearly seen: the CdSe band appearing classical in shape. The cut off in ZnS (Fig. 2), and in ZnSe (Fig. 3) and CdTe also appear classical; their occurrence being found at longer wavelengths than was formerly supposed and being sufficiently abrupt to provide definitive filtering action when a suitable continuum of absorption is provided for the longer wavelengths.

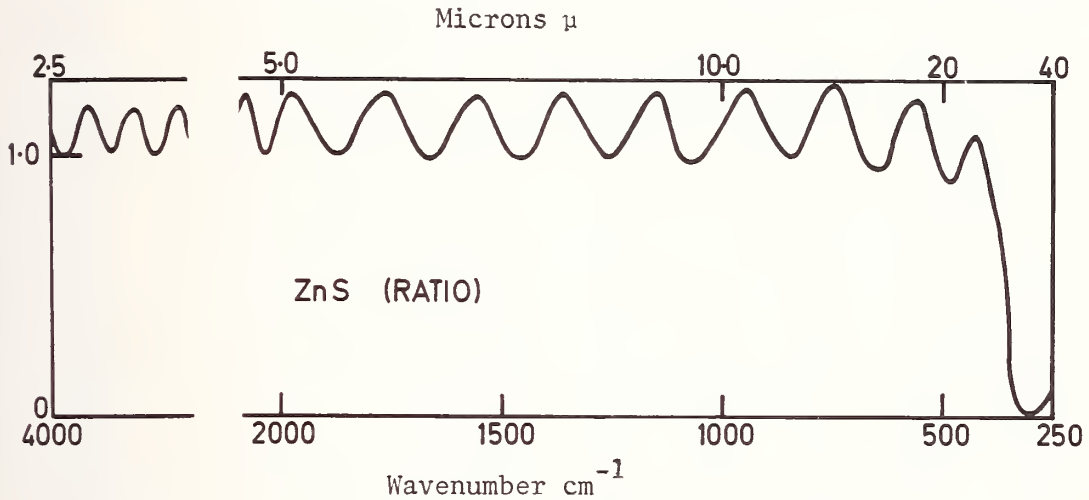

Fig. 2 Double-beam ratio spectrum of thick layer of ZnS on Si substrate

The cut on in ZnS (Fig. 4) occurs at 40 μ and was suspected in a study from an earlier period[5]. We are at present using it to strengthen filter action at 40 μ where it is complementary to thin quartz also cutting on there.

In comparison with these classical profiles thin-layer As_2Se_3 (Fig. 5(a) and (b)) shows a pronounced rectangularity having transmission less than 0.01% in its band but still retaining good transparency adjacent to the band indefinitely in both directions. As_2Se_3 reverts to a classical profile and in neither this or the sulphide glass does the thin layer absorption relate to the known bulk spectrum.

These studies continue and we are presently engaged in examining the thin layer reststrahlung at 4 deg K for use in cooled filters where various continuum of absorption are required in the region 20-100 μ.

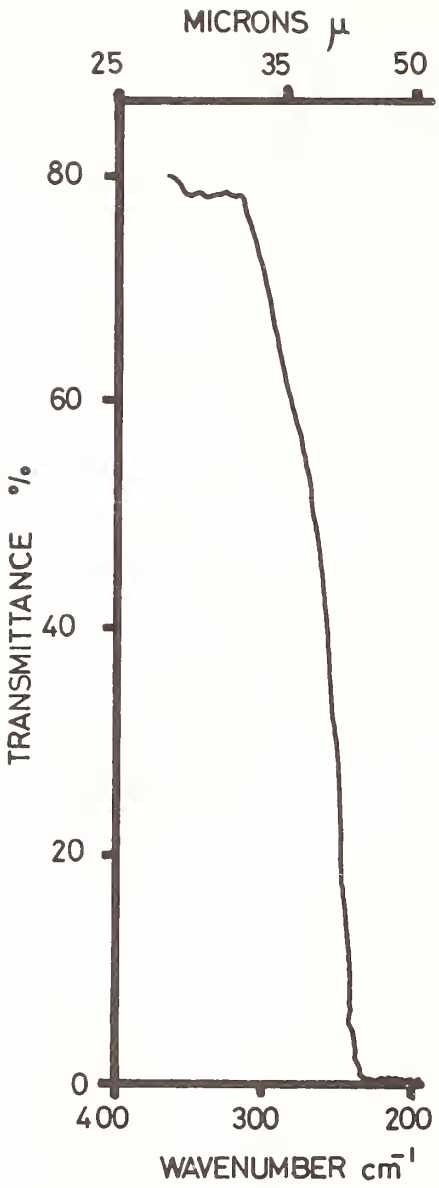

Fig. 3 Cut off of ZnSe in ZnSe/KRS-6 multilayer on thin KRS-6 substrate: about 8 μ total thickness ZnSe

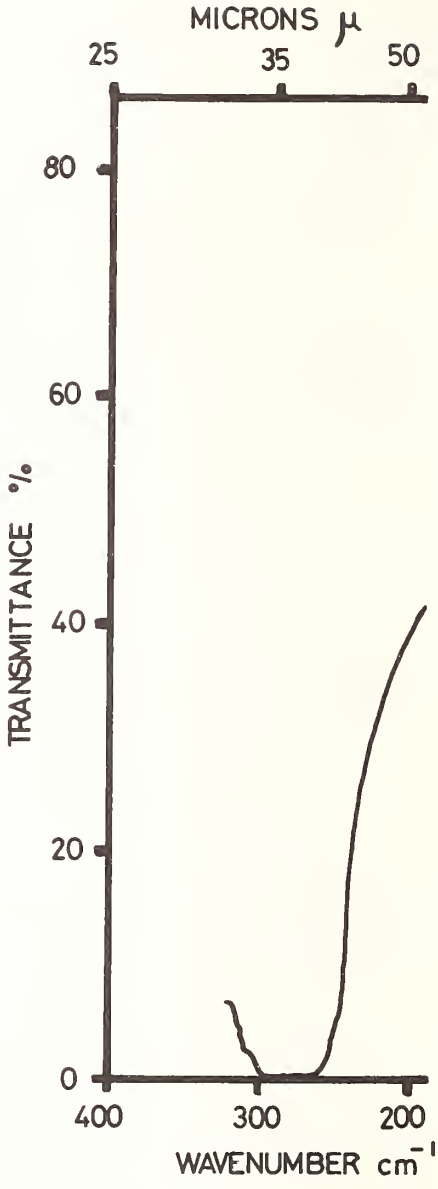

Fig. 4 Cut on of PbTe/ZnS multilayer on Si substrate containing in excess of 8 μ ZnS

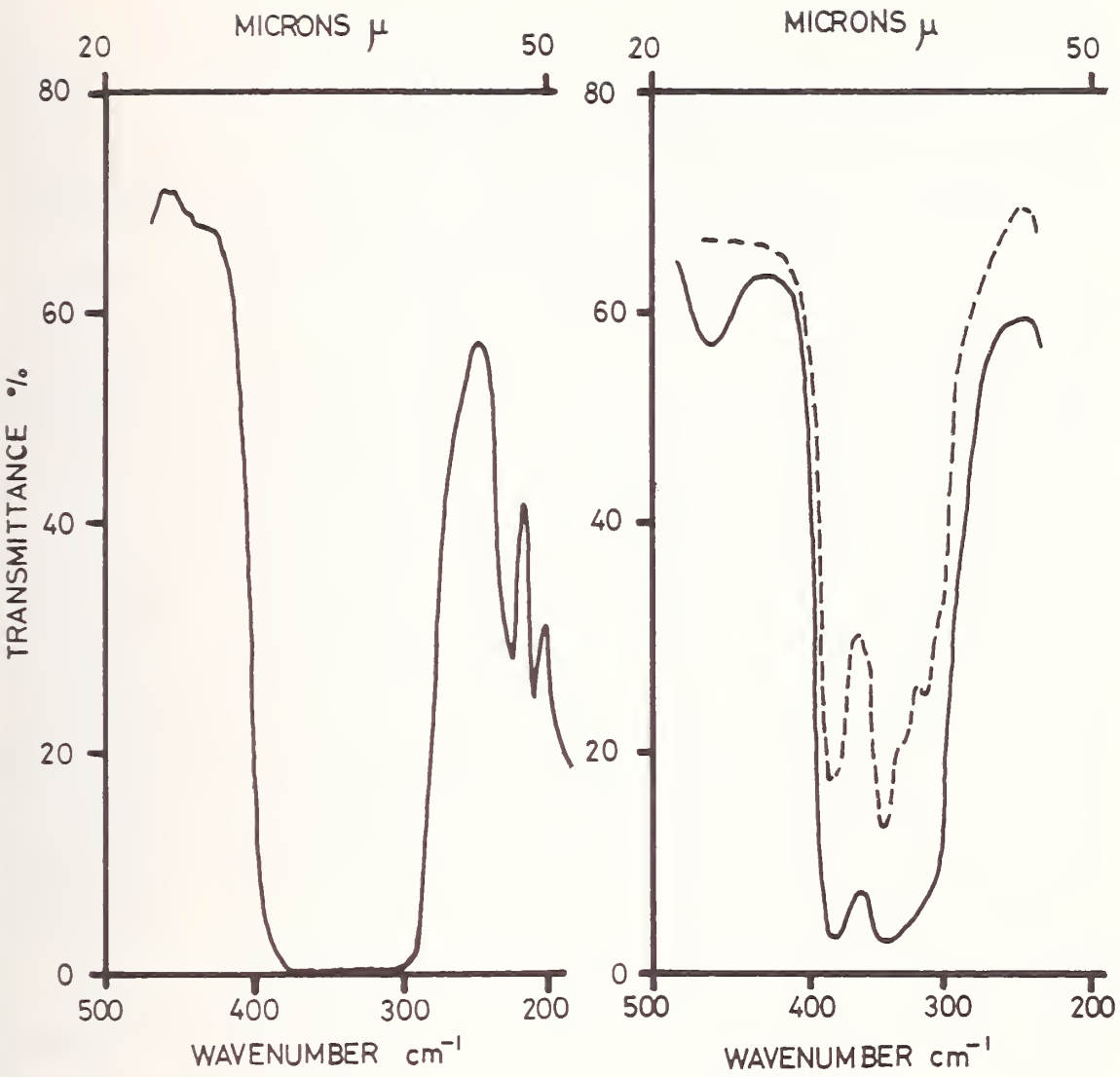

Fig. 5(a) As_2S_3 ~15 μ thick in As_2S_3/KRS-6 multilayer on KRS-6 substrate

(b) Intermediate thicknesses of As_2S_3

References

1. ZnS, ZnSe, CdTe procured from Eastman Kodak.
2. CdSe, As_2S_3, As_2Se_3 procured from BDH Chemicals Ltd.
3. Ritter E, Hoffman R. J. Vac Sci Technol 34 (1967) 803.
4. Evans C.S., Hunneman R., Seeley J.S. J. Phys D: Appl Phys 9 (1976) 309.
5. Smith S.D., Seeley J.S. Final Rep, May 1968, USAF Contract AF61 (052)-833.

MULTIWAVELENGTH LASER RATE CALORIMETRY ON VARIOUS INFRARED WINDOW MATERIALS

G. S. Coble, D. V. Dempsey, J. A. Detrio, N. C. Fernelius, J. A. Fox, P. R. Greason, G. T. Johnston, D. B. O'Quinn
University of Dayton Research Institute
Dayton, Ohio 45469

Over a period of several years we have measured the optical absorption coefficient, β, using the slope method of laser rate calorimetry[1] on a variety of materials for the Air Force Materials Laboratory. The lasers used to obtain these results include a modified Nd:YAG laser at 1.319 μm, an HF laser at 2.7 μm, a DF laser at 3.8 μm, a CO laser at 5.3 μm and a CO_2 laser at 9.27 μm and 10.6 μm. The purpose of this work was to provide β values at various wavelengths on a sample in which the sample received similar mountings in a calorimetry box, received similar data analysis, and which did not undergo the rigors of shipping to another location for measurement.

The NaCl samples were single crystals grown by Harshaw Chemical Company. Some samples were grown by the Stockbarger technique while others were Kyropoulos grown. Raytheon fabricated the six-inch CaF_2 ingot by remelting CaF_2 pieces. From this 38 mm diameter discs were cut. The RAP-grown (Reactive Atmosphere Processed) Rb-doped KCl samples were made by Hughes. Note the large absorption value in this material at 2.7 μm. The LiF samples were grown by Harshaw. One sample was forged by Honeywell. The Al_2O_3, sapphire, samples were made by Crystal Systems, Inc. Fused silica, SiO_2, samples were obtained from a variety of vendors. The Suprasil samples were obtained from Heraus-Amersil

and BK-7 from Zygo Corporation. The SrF_2 samples were prepared by Optovac. Gadolinium gallium garnet, $Gd_3Ga_5O_{12}$ (GGG) is a material developed as a substrate for magnetic bubble memories. We obtained samples from Lambda/Airtron and Allied Chemical. Since GGG is not normally regarded as an infrared material we include a Perkin-Elmer 180 transmission curve in Figure 1. The ZnSe samples were from CVD (chemical vapor deposition) plates grown by Raytheon for the Air Force Materials Laboratory Manufacturing Technology program MT-11. The silicon sample was cut from an ultrahigh-purity boule grown by Texas Instruments. The β slope results are listed in Table 1 in the order of increasing value at 1.3 μm.

Acknowledgment

We wish to acknowledge the support of the Air Force Materials Laboratory, Wright-Patterson Air Force Base, Ohio for this work.

References

1. M. Hass, J. W. Davisson, P. H. Klein and L. L. Boyer, J. Appl. Phys. 45, 3959 (1974).

TABLE 1 SUMMARY OF MULTI LASER WAVELENGTH MATERIALS STUDY

Material	$\beta_{slope} \div 10^{-3}cm^{-1}$					
	@1.3μm	@2.7μm	@3.8μm	@5.3μm	@9.27μm	@10.6μm
NaCℓ Harshaw single xtal	0.33	0.80	0.27	0.15	0.90	1.4
CaF_2 Raytheon	0.39	1.12	0.39	0.68	-	-
RAP Rb:KCℓ Hughes	0.53	4.18	0.20	0.22	0.74	0.53
LiF Harshaw	0.53	1.10	1.96	-	-	-
$Aℓ_2O_3$, Sapphire Crystal Systems, Inc.	0.75	0.75	20.2	-	-	-
SiO_2, Fused Silica						
Suprasil W-1	0.83	-	-	-	-	-
GE124 (125?)	1.08					
Suprasil II	2.83					
Corning 7940	3.18					
BK-7	3.19					
SrF_2 Optovac	1.56	1.98	1.95	0.560	-	-
GGG, $Gd_3Ga_5O_{12}$						
Lambda/Airtron	5.26	1.10	3.53	-	-	-
Allied Chemical	11.6	6.35	6.83	-	-	-
CVD ZnSe Raytheon	7.38	2.45	1.58	0.541	2.32	2.26
Silicon Texas Inst.	11.1	14.4	11.1	13.9	-	-

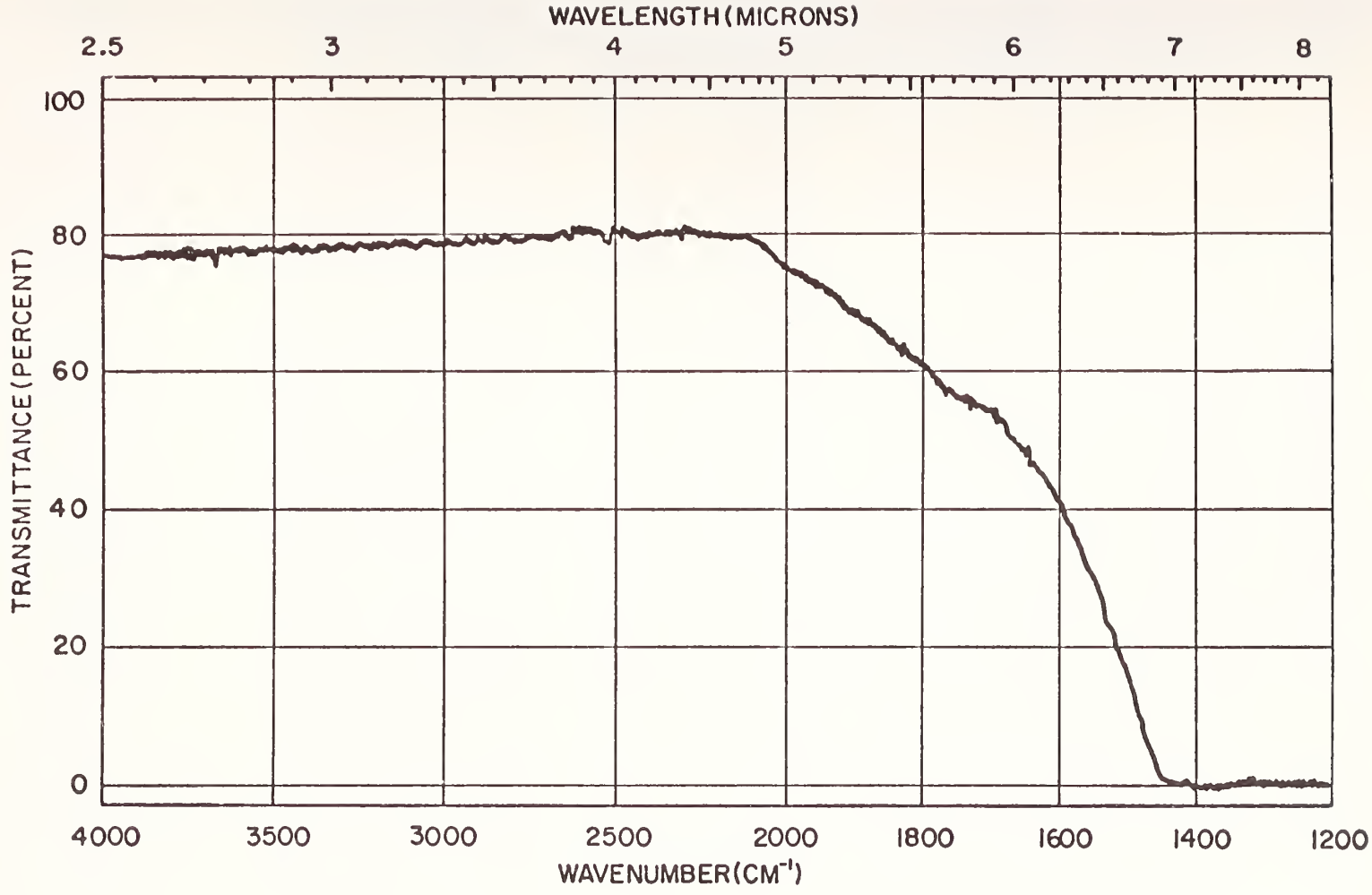

Figure 1 Transmittance Versus Wavelength in the IR for AFML #2667 - Allied Chemical GGG.

OPTICAL CONSTANTS OF BORON CARBIDE IN THE INFRARED

James L. Lauer and Hedy Adari
Rensselaer Polytechnic Institute
Troy, New York 12181

I. INTRODUCTION

Boron carbide has been suggested as a material suitable for obscuration against thermal imaging. It has an absorption band peaking at about 9.5 μm, which is fairly wide and therefore potentially able to block a substantial portion of the 8 - 14 μm atmospheric window. Since the CO_2 laser emits at 9.6 and/or at 10.6 μm, a material absorbing strongly at these wavelengths is more effective than an aerosol spray with only general absorption and scattering.

The optical constants n and k determine the behavior as an obscurant. They depend on many variables in addition to chemical composition, however, and are difficult to determine. Particle size and shape are among them. Perhaps the most direct way of measurement is unsymmetrical Michelson interferometry (UMI) in which the phases of reflection spectra are directly and independently recorded. This procedure has been very successful with liquids and appears to be applicable to fine powders or compacted powders, provided both theory and procedures are properly modified.

While UMI would still be our preferred method, the availability of compacted material of flatness and surface finish better than 1.0 μm made specular reflection a promising initial step for background information. This procedure has many well-known drawbacks, especially since boron carbide is hexagonal or rhombohedral and the bulk density was less than the crystal density, but it nevertheless gives some information on the location, relative strength, and width of the infrared bands and helps pinpoint problems to be overcome by UMI later. This paper describes the reflection method used and preliminary results.

II. MATERIAL

Compacted Norbide (boron carbide plates) was obtained from the Norton Company. Pieces of 10 x 10 x 5 mm size were cut with a diamond saw and diamond-polished. A representative piece was coated with a thin layer of gold and examined under the scanning electron microscope (SEM). A particle size of average diameter of 2.0 μm was noted. Surface examination by X-rays in the SEM apparatus revealed the presence of iron, presumably as iron oxide on the surface. An estimate of the surface

area potentially covered is 1 - 5%, which is considerably above the 0.9% by weight of Fe for the bulk material. Therefore it could be a factor influencing the optical constants.

III. APPARATUS

The instrument used for the reflectance measurements was a Model 221 Perkin Elmer double-beam grating spectrophotometer with a Harrick[1] reflectance adapter (VRA and VARA) containing a mirror system automatically equating angles of incidence and reflection. Different attenuating screens could be put into the reference beam to balance the instrument for a gold reference surface. A wire grid polarizer of fine mesh size (0.4 μm) could be inserted in front of the sample slit.

IV. PROCEDURE

Measurements were made at several angles of incidence for both unpolarized[5], and p-polarized radiation in the 700 - 1200 cm^{-1} wavenumbers range. The standard gold surface and the boron carbide surface were examined under identical conditions. Careful attention was given to having the surfaces clean.

V. DATA PROCESSING

The processing procedure adapted was that of Simon[2], although the form of the Fresnel equations used by Rusch, Koehler, and Lagowski[3] proved to be more readily programmable. For every 10^{o} degrees of incidence, plots, of which Figure 1 is an example, were drawn to supplement those of Simon for 20 and 70^{o} only. Furthermore the computer program and plotting routine can generate plots at any angle. It was found to be best to compare R_p, R_s, and R at one angle only and find the best combination of n and k to satisfy at least two R's simultaneously. This is the method of Heilmann.[4] The advantage is that no change need be made in the area irradiated; it proved to be difficult to maintain a constant area, especially at large angles of incidence. The experimental arrangement was optimized at 60^{o} incidence, although other angles were also used.

VI. RESULTS

Figure 2 shows n and k for the 700 - 1200 cm^{-1} region. There are two absorption bands, a minor one at 810 cm^{-1} and major one at about 1050 cm^{-1}. Figure 3 shows typical reflectance spectra from which Figure 2 was derived.

VII. DISCUSSION

The limitations of the reflectance method are quite clear as the comparison given by Huffman[5] has shown. An "absorption" spectrum of a KBr disc containing suspended particles of a very limited size range appears to be more direct. This author is, however, well aware of many difficulties of the pressed KBr technique in quantitative infrared spectroscopy and some of them would seem to be applicable here as well. As our SEM/X-ray measurements have shown, contaminants prefer to accumulate on interfaces. The interface area of suspended particles is extremely large. Infrared-invisible contaminants may affect the scattering characteristics of other materials.

We tried to correct for the differences between bulk and particle densities by assuming a proportion of "black" holes on the reflecting surfaces. However, it turned out to be impossible to get consistent results. Judging from the SEM photos, it would seem that the holes were "filled in" in the polishing operation.

ACKNOWLEDGEMENT

This work was supported in part by Naval Air Systems Command under Contract No. N00164-79-M-2522.

REFERENCES

1. Harrick, N. J., "Internal Reflection Spectroscopy". Second Edition 1979. Harrick Scientific Corporation, Ossining, N.Y. 10562.

2. Simon, I., J. Opt. Soc. Am., 41, 336 (1951).

3. Rusch, P. F., Koehler, W. H., and Lagowski, J. J., Spectrochim. Acta, 25A, 1537 (1969).

4. Heilmann, G., Z. Naturforsch. 18, 1103 (1962).

5. Huffman, D. R., Adv. in Physics, 26, 129 (1977).

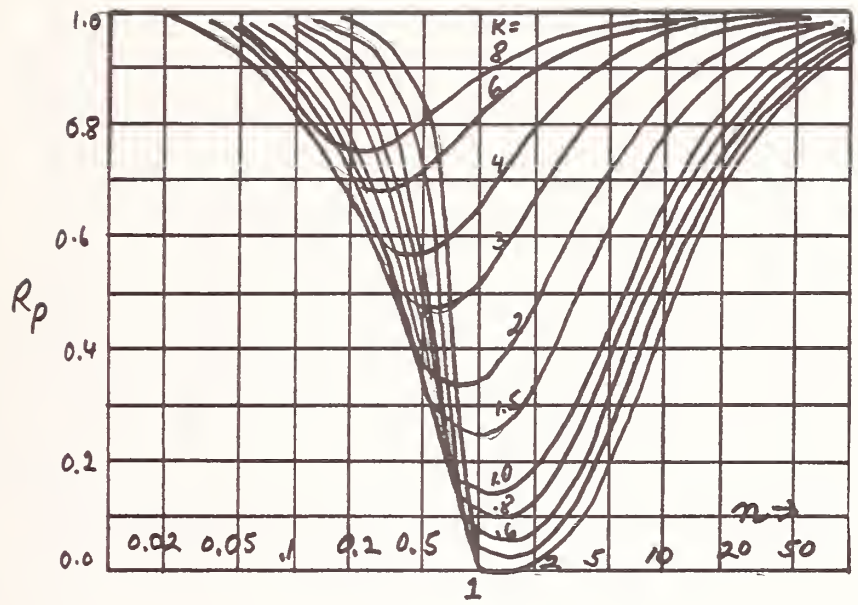

Figure 1: Complex refractive index versus absorption at one angle of incidence.

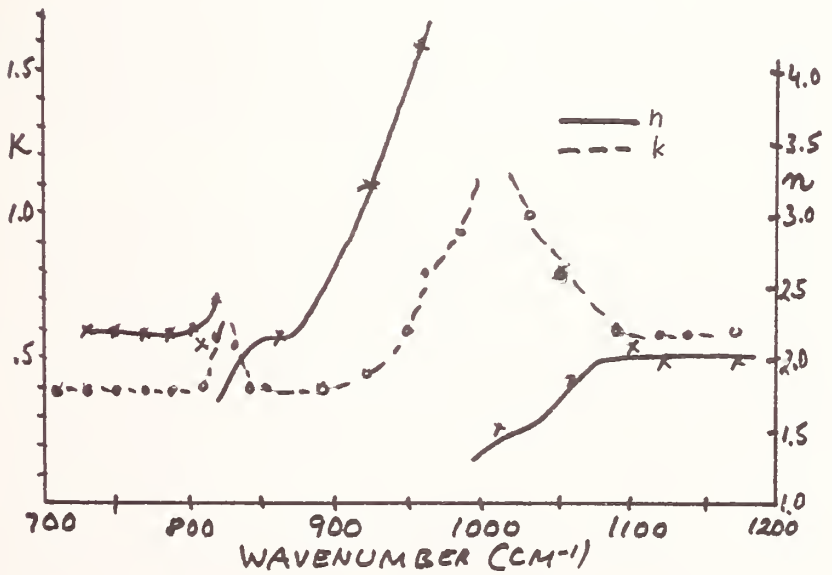

Figure 2: Complex refractive index spectrum.

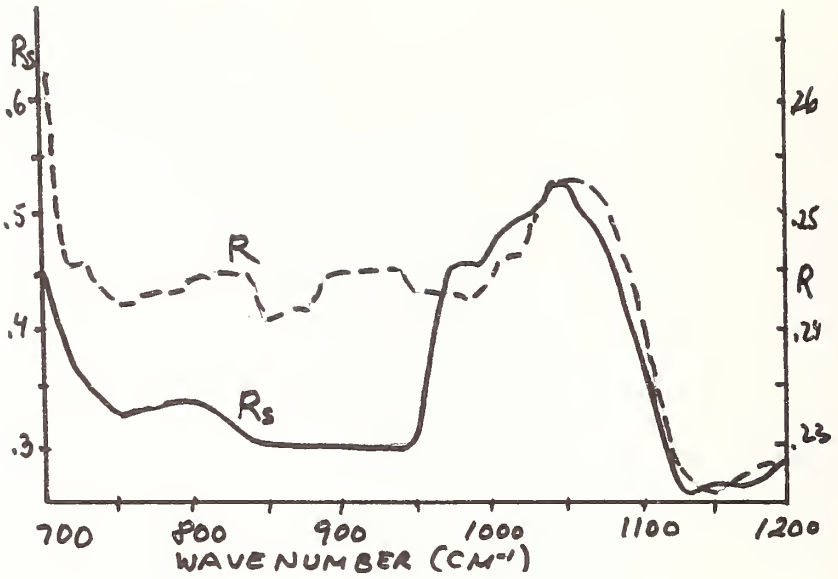

Figure 3: Reflectance spectra

CRITICAL POINT ANALYSIS OF MULTIPHONON INFRARED ABSORPTION IN ZINC SELENIDE

Claude A. Klein and Robert N. Donadio
Research Division, Raytheon Company
Waltham, Massachusetts 02154

Multiphonon lattice-absorption processes in cubic ZnSe have been the subject of a number of investigations, beginning in 1961. Infrared reflectance and transmittance measurements by Aven et al. [1] first led Mitra [2] to attempt an interpretation in terms of characteristic phonon energies and, subsequently, to carry out a partial critical point analysis [3]. Inelastic neutron-scattering [4] and second-order Raman scattering [5] data having since become available, it should now be feasible to interpret multiphonon infrared absorption in ZnSe on a much sounder basis. Furthermore, the development of chemically vapor-deposited (CVD) ZnSe has stimulated a great deal of interest in obtaining absorption spectra covering a range of multiphonon regimes [6,7,8], primarily for the purpose of characterizing the nature of light-absorption processes of relevance in a CO_2-laser environment. In this context, Bendow et al. [9] succeeded in demonstrating that, even in the three- and four-phonon regions, ZnSe exhibits structure, which appears to be consistent with the results of calculations that emphasize the effect of phonon density of states. For this reason, it will be the purpose of the present paper to take advantage of the availability of CVD-ZnSe specimens of widely differing thickness in order to examine the room-temperature infrared spectrum over the entire wavelength range of interest and, in particular, to identify significant features of the absorption and assign them to phonon summations at critical points of the Brillouin zone.

Figure 1 shows the far-infrared transmission profile of a thin specimen of CVD ZnSe (t = 0.0225 cm), which illustrates the type of structure that this material can exhibit in the two-phonon absorption regime [$LO(\Gamma) \lesssim \nu \lesssim 2\ LO(\Gamma)$]. Twelve features have been identified and assigned to critical-point phonon combinations as indicated in column 2 of Table I. In this connection, we note that, of the three sets of room-temperature zone-edge mode frequencies presently available [4,5,10], only those of Irwin and LaCombe were found to be compatible with both infrared lattice absorption and Raman spectral characteristics. Further comments are in order:

(a) At frequencies above the one-phonon cutoff [$LO(\Gamma) = 250\ cm^{-1}$], electric-dipole allowed two-phonon summations occurring at stations X and L all have been assigned to specific features of the spectrum, with the exception of the TO(L) + LA(L) combination.

(b) On assuming that three-phonon processes can be ruled out, it appears necessary to assign two of the features to events occurring at station W; feature 5 then must be attributed to an acoustic phonon

overtone, which violates the usual dipole selection rule but confirms that, for ZnSe as for ZnS [11], electric quadripole moments indeed play a significant role in the multiphonon absorption mechanism.
(c) Most of our assignments also apply to Irwin and LaCombe's second-order Raman features and properly describe their polarization characteristics [12].

Since the highest-frequency zone-boundary phonons [LO(X,L)] are at approximately 224 cm^{-1}, it follows that the absorption edge shown in Fig. 2, and which refers to an 0.264-cm thick specimen of CVD ZnSe, must be attributed to three-phonon processes operating up to a cutoff at 3 × LO ≈ 670 cm^{-1}. There are many such processes that are infrared active thus giving rise to considerable complexity if one attempts to elucidate the details of the spectrum in this frequency range; also, structural features are seen to be much less prominent than earlier. For this reason, it should be more meaningful to describe the gross features of the absorption in terms of combinations of four characteristic phonons, or in other words, on the basis of assigning a single phonon energy to each of the main branches of the dispersion. In this regard, it is interesting that the density-of-states distribution generated by means of neutron diffraction [13] has four major peaks, which are indicative of weighted average populations at the Brillouin-zone boundary and, hence, might provide a set of suitable characteristic phonons: LO = 222, TO = 204, LA = 131, and TA = 65 cm^{-1}. In this approximation, and following Bendow [9], we may assume that for high-multiplicity ($n \geq 3$) phonon events selection rules are of little consequence. In this manner, we arrive at assignments as specified in Table I, which points to some impressive correlations in terms of shoulder positions (see Fig. 2) and reemphasizes the importance of optical phonon overtones in shaping the absorption profile of zinc-blende type semiconductors [11].

Work in progress involving 1-in. thick specimens has allowed us to identify four-phonon summations in the infrared transmission, at frequencies up to 750 cm^{-1}. In this connection, we note that both Fourier transmission spectroscopy [14] and thermal emittance work [15] performed at Hanscom AFB disclose that structure persists in the absorption spectrum of CVD ZnSe, over the entire four-phonon region. Figure 3 illustrates the situation as recorded by Lipson [14] together with relevant assignments as obtained from our previous set of characteristic phonon energies. Evidently, this procedure confirms the contention that structure in the absorption spectrum of CVD ZnSe, at wavelengths above 11 μm, can be attributed to the phonon dynamics and reflects the main features of the phonon density-of-states distribution.

REFERENCES

1. *M. Aven, D. Marple, and B. Segall, J. Appl. Phys. 32, 2261 (1961).*
2. *S. S. Mitra, Phys. Rev. 132, 986 (1963).*
3. *S. S. Mitra, J. Phys. Soc. Japan 21, supplement, 61 (1966).*
4. *B. Hennion, F. Moussa, G. Pepy, and K. Kunc, Phys. Letters 36A, 376 (1971).*

5. J. Irwin and J. LaCombe, Can. J. Phys. 50, 2576 (1972).
6. T. F. Deutsch, J. Phys. Chem. Solids 34, 2091 (1973).
7. J. M. Rowe and J. A. Harrington, in Optical Properties of Highly Tranparent Solids (Plenum Press, New York, 1975), p. 109.
8. P. Miles, in Proc. Fifth Conf. Infrared Laser Window Materials (AFML, Wright-Patterson AFB, 1976), p. 8.
9. B. Bendow, H. Lipson, and S. Yukon, Phys. Rev. B16, 2684 (1977).
10. B. A. Weinstein, High Pressure Sc. and Tech. 1, 141 (1979).
11. C. A. Klein and R. N. Donadio, J. Appl. Phys., to be published.
12. W. G. Nilsen, Phys. Rev. 182, 838 (1969).
13. R. Beserman, M. Zigone, W. Drexel, and C. Marti, Solid State Comm. 18, 419 (1976).
14. H. G. Lipson, Appl. Opt. 16, 2902 (1977).
15. L. Skolnik, A. Kahan, R. Brown, H. Lipson, A. Golubovic, and J. Engel, in Proc. Fifth Conf. Infrared Laser Window Materials (AFML, Wright-Patterson AFB, 1976), p. 806.

Table I. Two- and Three-Phonon Summation Bands in Cubic ZnSe

Feature[a]	Assignment	Position (cm^{-1})[b]	Comment[c]
1	LA(X)+TA(X)	262	Also TO(L)+TA(L);R
2	TO(X)+TA(X)	276	R
3	LO(L)+TA(L)	282	
4	LO(X)+TA(X)	293	R
5	$2A_1(W)$	300	Dipole forbidden
6	$O_1(W)+A_2(W)$	329	Also $O_2(W)+A_2(W)$
7	2LA(L)	362	R
8	2LA(X)	380	Dipole forbidden; R
9	TO(X)+LA(X)	401	Also LO(L)+LA(L);R
10	2TO(X)	412	2TO(L);LO(X)+LA(X);R
11	LO(X)+TO(X)	430	Also LO(L)+TO(L);R
12	2LO(L)	448	R
13	TO+2LA	466	R
14	2TO+TA	473	
15	LO+2LA	484	
16	LO+TO+TA	491	
17	2LO+TA	509	
18	2TO+LA	539	
19	LO+TO+LA	557	
20	2LO+LA	575	
21	3TO	612	
22	LO+2TO	630	
23	2LO+TO	648	
24	3LO	666	

(a) See Fig. 1 and Fig. 2.

(b) Based on critical-point mode frequencies as listed in Ref. 5 and characteristic zone-edge phonons derived from a density-of-states distribution reported in Ref. 13.

(c) R means Raman active as observed in Ref. 5.

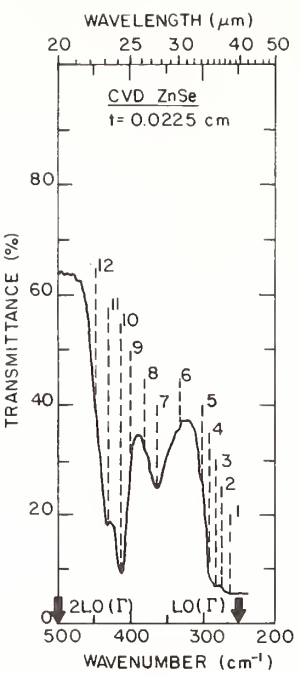

Fig. 1. Optical transmittance of chemically vapor-deposited ZnSe in the two-phonon absorption regime.

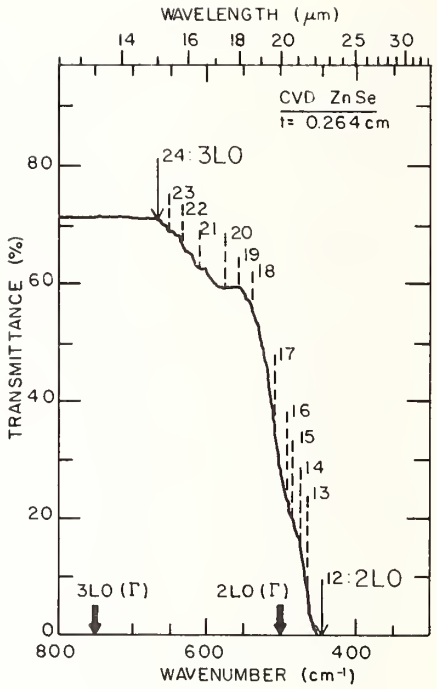

Fig. 2. Optical transmittance of chemically vapor-deposited ZnSe in the three-phonon absorption regime.

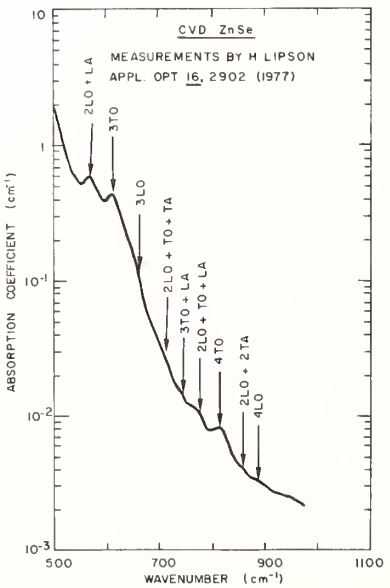

Fig. 3. Room-temperature absorption spectrum of chemically vapor-deposited ZnSe in the three- and four-phonon absorption regimes. Assignments are based on a set of characteristic phonons specified in text.

MULTIPHONON ABSORPTION IN INFRARED GLASSES BASED ON ZIRCONIUM AND HAFNIUM FLUORIDES

Herbert G. Lipson, Bernard Bendow and Martin G. Drexhage
Solid State Sciences Division, Rome Air Development Center
Hanscom AFB, MA 01731

There has been considerable interest in recent years in highly transparent mid-IR glasses for applications such as IR-domes, laser windows and guided-wave optics (1). The preparation of one such class of glasses based on zirconium (2-5) and hafnium (6) fluorides has been reported recently. These glasses possess high densities ($\sim$4.5-6 gm/cm^3), fairly low refractive indices ($\sim$1.53) and low glass transition temperatures ($\sim$600-620°K), and are highly resistant to attack by water or acids. Most importantly, they offer the potential for high transparency (absorption coefficient $\alpha \lesssim 0.1 cm^{-1}$) throughout the visible, out to IR wavelengths in the vicinity of 6μm and beyond. In the present work we conduct experimental investigations of the vibrational edge absorption of these glasses and compare the results with theoretical predictions. In particular, we perform detailed frequency (ω) and temperature (T) dependence studies of α for one zirconium fluoride based glass, and interpret the results in terms of intrinsic multiphonon absorption. The analysis also yields parameters which can be utilized to predict α in ranges which are not usually accessible to experiment.

The glasses utilized for the present study were synthesized using reagent grade ZrO_2, HfO_2, BaO, ThO_2, La_2O_3 and $NH_4F \cdot HF$ as starting materials. The preparation techniques were similar to those reported previously (2-6). The required amounts of the oxides were thoroughly mixed with twice the stoichiometric amount of $NH_4F \cdot HF$ needed to fluorinate them and placed in a vitreous carbon crucible loosely covered with platinum foil. Batches of $\sim$25g were fired under argon atmosphere, first at $\sim$400°C for 1.5h to achieve fluorination and then briefly at $\sim$800°C to melt the glass and to assure the removal of any excess $NH_4F \cdot HF$. Melts were cast into room temperature brass molds and then annealed at $\sim$300°C, yielding clear vitreous discs $\sim$2.5cm in diameter by 2-4mm thick.

The glass compositions, selected from the center of the glass formation regions reported in references 2-5, are as follows (mol %): Glass ZBT, 57.5 ZrF_4, 33.75 BaF_2, 8.75 ThF_4; Glass HBT, 57.5 HfF_4, 33.75 BaF_2, 8.75 ThF_4; Glass HZBT, 28.75 HfF_4, 28.75 ZrF_4, 33.75 BaF_2, 8.75 ThF_4, Glass HBL, 57.5 HfF_4, 33.75 BaF_2, 8.75 LaF_3.

The absorption coefficient was deduced from transmission measurements conducted utilizing a Digilab FTS-14 Fourier spectrophotometer. A small furnace was added for measurements above room temperature. Readers interested in details of the measurement technique are directed to Ref. 7.

Room temperature absorption spectra for glasses with the four compositions indicated above are displayed in Fig. 1. The results are in good agreement with spectra obtained previously for $\alpha > 0.1 cm^{-1}$ utilizing a Perkin-Elmer 221 spectrophotometer (6). The values obtained here for α below $\sim 0.1 cm^{-1}$ are sensitive to corrections for background noise, and to the values used for the reflectivity for each ω and T. A measure of confidence in the data for this range is provided by the very good agreement between theory and experiment obtained in a detailed analysis of ZBT glass data, as described below.

ZBT and HBL display an overall exponential-like decrease in α (see Fig. 1) characteristic of intrinsic multiphonon absorption over the frequency range under consideration (8); HZBT departs somewhat from such behavior, while HBT departs markedly. The absence of structure in the ZBT spectrum, combined with the similarity in bonding between Zr and Hf, strongly suggests that the observed structure in the other spectra are due to extrinsic processes. This is likely the result of utilizing 0.97 purity HfO_2, as compared to 0.999 purity ZrO_2; Hf-based samples with improved purity are currently in preparation. We note that a smooth, structureless spectrum is indeed a familiar characteristic of intrinsic multiphonon absorption in most ionic materials (8). The shift in the exponential-like portion of the curves may, as shown previously (6), be attributed to differences in reduced mass between Hf and Zr in the present glasses.

Since its spectrum appeared closest to intrinsic, ZBT was chosen for more detailed investigations over a range of elevated temperatures. Experimentally determined values of α are displayed in Fig. 2, along with a theoretical fit based on Ref. 9. The latter theory fits the absorption in the exponential-like regime with just three parameters via the approximate formula

$$\alpha\ (\omega,T) = \alpha_0 \left(N(\omega_0) + 1\right)^{\omega/\omega_0} \left(N(\omega) + 1\right)^{-1} \exp(-A\omega)$$

where N is the Bose-Einstein function and ω_0 an appropriate average phonon frequency. The overall good agreement between theory and experiment suggests that the observed absorption is due to intrinsic multiphonon processes. Departures between theory and experiment may be due to deviations in the data from the purely exponential dependence assumed in the theory. The value utilized for ω_0 is consistent with Raman (various peaks between 350-600cm^{-1}) and reststrahl reflectance (peaking near 500 cm^{-1}) (10). Thus the shoulder in the data spanning the 1300-1700 cm^{-1} may well be due to three-phonon conbination bands involving these vibrations. One also notes a weakening

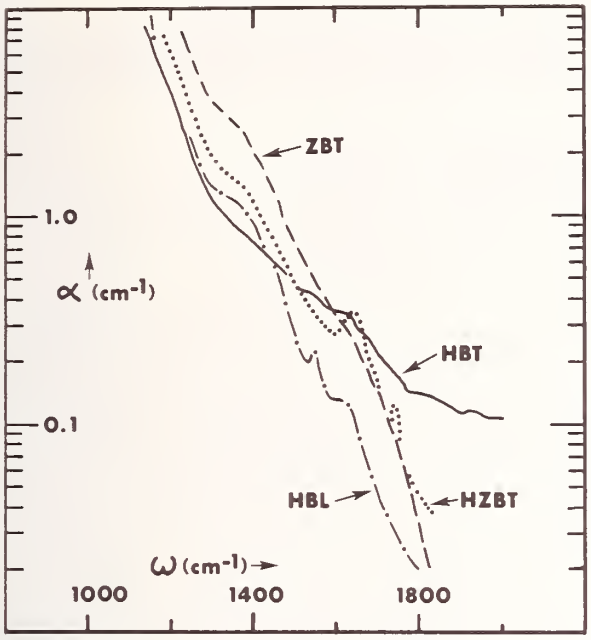

FIGURE 1

Measured absorption coefficient vs. frequency for four fluroide glasses.

FIGURE 2

Absorption coefficient versus temperature at selected frequencies for ZBT glass; circles are experimental points and the curves a theoretical fit (see text) with ω_0 = 500 cm^{-1}, A = 0.00908, α_0 = 452091 cm^{-1}.

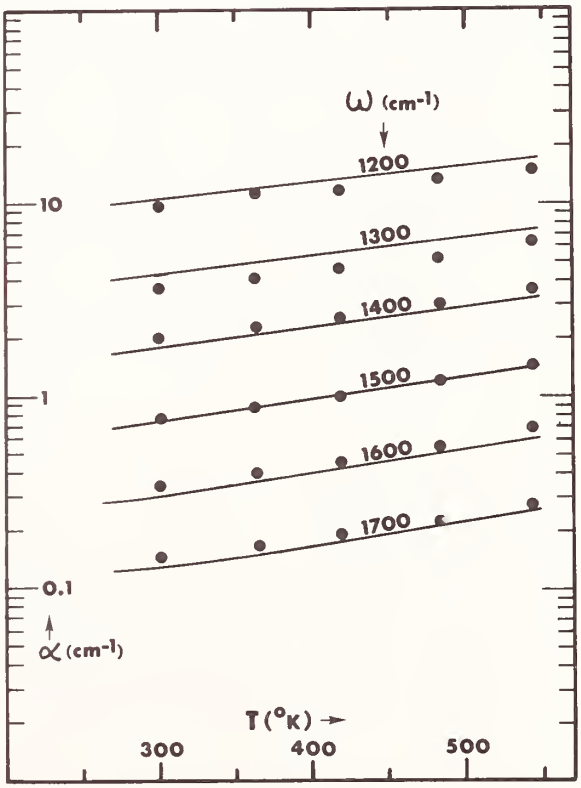

of the spectral structure at elevated temperatures, as expected from the increase in phonon linewidth as a function of temperature.

The authors thank M. Clark for assistance with the computations, and C.T. Moynihan and M. Saleh of Catholic Univ. for useful discussions.

References

1. See, e.g., "Optical Properties of Highly Transparent Solids," S.S. Mitra and B. Bendow, eds. (Plenum, N.Y., 1975).

2. M. Matecki, M. Poulain, M. Poulain and J. Lucas, Mat. Res. Bull. 13, 1039 (1978).

3. A. Lecoq and M. Poulain, J. Non-Cryst. Solids 34, 101 (1979).

4. M. Poulain and J. Lucas, Verres Refract. 32, 505 (1978).

5. M. Poulain, M. Chanthansinh and J. Lucas, Mat. Res. Bull. 12, 151 (1977).

6. M.G. Drexhage, C.T. Moynihan and M. Saleh, Mat. Res. Bull., in press.

7. See, e.g., B. Bendow et al, Phys. Rev. B, 20 1747 (1979).

8. B. Bendow, in "Solid State Physics", H. Ehrenreich et. al., eds. (Academic, N.Y., 1978) Vol. 33.

9. B. Bendow, Appl. Phys. Lett. 23, 133 (1973).

10. Unpublished data, courtesy of S.S. Mitra, Univ. of R.I.

OPTICAL CHARACTERIZATION OF BULK GRADED INDEX MATERIALS

Duncan T. Moore
Gradient Index Laboratory
The Institute of Optics
University of Rochester
Rochester, New York 14627

The implementation of the large gradient index materials into optical systems relies on the development in four areas. These are the design and analysis algorithms for including gradient index optics in lens systems, the fabrication and modeling of glass materials with these index variations, the measurement of the optical properties, and the fabrication of the materials into finished lens elements. This paper is restricted to the discussion of the measurements of gradient index materials; in particular, the materials whose geometries are larger than 1 mm. In the systems which are being developed and produced at this time, the gradients may be as large as 10 mm. In the next few years the size will increase to multiple centimeter geometries.

In the telecommunications business, the important parameter is the bandwidth that can be transmitted through a fiber. In the optical systems design, it is more important to know the quality of an image. Thus the types of testing equipment that one uses for telecommunications applications are not applicable to that for bulk materials. Typically, the most important parameters for bulk gradient index materials are: 1) the index of refraction profile of the material, 2) the derivative of the index of refraction profile (the slope), 3) the variation of the index of refraction with wavelength, 4) the index of the variation of index of refraction profile with temperature, 5) the variation of thermal expansion coefficient with temperature, 6) the transmittance of the material, and 7) the three-dimensional variation of the gradient.

The geometries of the gradients are not as simple as they are in telecommunications. There are currently four types of gradients that are being investigated: 1) axial gradient in which the index of refraction varies in the direction of the optical axis, 2) the cylindrical or radial gradient which varies perpendicular to the optical axis, 3) the spherical gradient which has symmetry about a point, and 4) the conical gradient which has surfaces of a constant index which are ellipses, parabolae, etc. Each of these geometries creates unusual problems for the measurements, particularly in systems which have spherical or conical symmetries.

The effect of each of these gradients on the aberrations of a lens system are now well understood. The axial, spherical and conical

gradients have the same effect on aberrations as an aspheric surface does. This implies that any aspheric surface can be replaced with one of these types of gradients and have equal performance by proper choice of the gradient profile and its depth. The radial gradient, on the other hand, is much more important from a design standpoint, although it is much more difficult to manufacture in large geometries. The principle advantage of radial gradients is in their ability to correct field aberrations (particularly the field curvature) and chromatic aberrations. Unlike homogeneous elements, where the focal length of the lens depends upon the index of refraction, a slab of radial gradient material (called a Wood lens) has a focal length which depends only on the gradient. Therefore, if a gradient profile can be manufactured which is independent of wavelength, then this single element lens can be achromatized. Based on models predicted by Fantone[1] glasses have been manufactured which exhibit no chromatic variation of the gradient. Of course, there is a variation in the base index, but the profile itself is unchanged as a function of wavelength. This results in a chromatically corrected single element lens.

A number of techniques have been proposed for measuring the index of refraction profile in bulk materials. These techniques include prism methods, moire techniques, Schlieren, interferometry, auto-collimation and holography. In some of these techniques, the index profile is not measured, but rather the derivative of the index of refraction profile, and thus they are not usable for characterization of the gradient index profiles because the profile is needed. Furthermore, we are restricted to techniques which provide accuracies of the index profile of the order 10^{-5} in change in index. The most likely prospect is that of interferometry. However, interferometry has the necessary drawback that the readout is a series of contours, each of which represents a change in index determined by the thickness and the optical path difference in material. In typical examples, the number of fringes will reach several hundred, and thus the measurement of a photographic plate becomes very tedious. Furthermore, in standard interferometry, there are ambiguities of hills and valleys, that is, you cannot tell from a simple interferogram whether the phase, i.e. the optical path and the index, is increasing or decreasing. To eliminate these problems a technique was developed called AC interferometry (also called phase-locked interferometry, homodyne interferometry, and heterodyne interferometry) which will allow for the automatic measurement of phase into a computer or onto a x-y recorder. This technique was not originally designed for measurement of index profiles, but was considered a general technique for reading of phase maps of complicated objects.

For the last eight years the group at the University of Rochester has used this AC interferometry technique for regular measurement of index of refraction samples. The technique involves the modulation in time of one path of a Mach-Zehnder interferometer. By introducing this

time variation in phase in one arm relative to the other, the output of a detector varies in time depending upon the initial location of the detector in the field. The actual phase of the optical wave can be determined.

The current problems of measurement of bulk gradient index materials include the variation of the gradient with wavelength. While it can be argued that the measurement of the phase at one wavelength can then be subtracted from the data at a second, this becomes a tedious operation and is subject to a series of registration and magnification errors. Therefore, a two wavelength interferometry technique has been developed and is described in a subsequent paper.

The most important type of gradient at todays writing is the axial gradient. This gradient can replace an asphere in a lens system and is readily manufactured by a number of different techniques. It is our feeling that these gradients will be implemented in gradient index systems in the next three years. We therefore need to be able to measure the index of refraction in the lens blanks. In such a lens blank the index profile is in the direction of light propagation. Therefore, a standard interferometer will not make such a measurement. To be able to measure non-destructively the index profile in each blank it is necessary to develop a new type of instrumentation. This instrument is based on AC interferometry techniques. As a sample is rotated in a beam, the phase varies in a well-known way as a function of rotation. If the general shape of the gradient is known, then the index of refraction profile can uniquely be determined. Such an instrument has been developed and tested.

The next series of problems to be solved are those of the index of refraction measurements in the infrared and the measurement of thermal properties of gradient index materials. In the infrared, the problems become one of using the same phase modulation techniques where the modulation has to be much larger than in the visible. Linearity of the system becomes more important. The measurement of thermal properties is a very difficult one. It is necessary to measure not only the change in index of refraction profile as a function of temperature, but also to measure a thermal expansion coefficient as a function of position. The latter is important in actual manufacturing of gradient index materials at elevated temperature. A system using a Fabry-Perot interferometer with multiple internal interferometers will be discussed for such a measurement.

The implementation of gradient index components into conventional optical systems relies heavily on the measurement technique. While it is now possible to design with such materials and many materials have now been made, the measurement technique ultimately will determine the cost and use of bulk gradient index materials.

1. S. D. Fantone, Design, Engineering and Manufacturing Aspects of Gradient Index Components, Ph.D. Thesis, University of Rochester, 1979.

MEASUREMENT OF AXIAL, GAUSSIAN INDEX DISTRIBUTION

Glen W. Johnson
The Institute of Optics
University of Rochester
Rochester, New York 14627

Two examples are presented that illustrate the measurement capabilities of a modified Mach-Zehnder interferometer (see Fig. 1), its support electronics and computer programs. Presently, two types of measurements are possible. First, two-dimensional scans of the sample may be made. In this case, two galvanometer driven mirrors are positioned such that successive points of the object plane (at the sample) are imaged onto the detector. Second, with the galvanometers fixed at preset positions, the sample may be rotated to selected angles, either manually or under program control.

Figure 2 illustrates the orientation of the sample in the sample arm of the interferometer. When two-dimensional maps are made, the rotation angle ω is (very nearly) zero and the surface of the sample is imaged onto the detector plane. When measurements of optical path length versus angle are made, a point (along the axis of rotation, for this study) is selected using the galvanometers.

Data derived from measurements of the latter type are analyzed (with a specially written ray trace program (1)) by simulating the optical system in the neighborhood of the sample as follows. From a point on the exit plane, a ray traveling towards the sample originates. Upon passing through the sample, the ray terminates on the offset plane. At this plane, the ray's optical path length is compared with the experimentally derived optical path length. The position of this offset plane is adjusted automatically during the analysis.

The index profile of a class of gradient index materials is described accurately by a Gaussian distribution (2) as in the equation

$$n(z) = n(0) + \Delta n \exp(-\sigma(z-d)^2)$$

where $n(0)$ is the base index, Δn is the maximum index change, σ is the shape factor of the distribution and d is a displacement representing the location (along the z axis) of the peak of the Gaussian. These four Gaussian coefficients are also construction parameters whose values may be adjusted automatically by the ray tracing program during the analysis of experimental data.

As in the various forms of tomography, in order to compute information about the index as a function of position within a sample region, a series of measurements are made of a beam that probes the sample at different angles. To show how this can be done with a system for which a model of the refractive index distribution is assumed, measurements made using the wavefront tracking capabilities of the modified Mach-Zehnder interferometer are analyzed.

For rays traced through a homogeneous glass plate (1 cm. thick) over a range of incident angles a plot of the optical path length versus angle of incidence shows a characteristic parabolic shape. When a typical axial Gaussian index distribution is introduced into the glass plate, the shape of the curve (optical path length versus angle) is slightly different. If measurements of such a system are to be made over incident angles of plus and minus 60 degrees, optical path length variations of the order of two millimeters (approximately 4000 fringes) must be tracked. In addition, to resolve the small differences between the homogeneous and inhomogeneous cases, measurements of optical path length differences that are of the order 0.1 micrometer must be made.

When a gradient sample or a homogeneous plate of glass is mounted on the stepping motor driven rotary stage and measured under program control, a plot of the optical path length versus incident angle is generated. Once the experimental data and the optical system have been described to the ray tracing program, the construction parameters that are free to vary must be described. For the measurements of the homogeneous plate, the thickness and the index are known fairly accurately. These values are held fixed, initially, while the two quantities (position of the offset plane and the offset angle) are allowed to vary. After good estimates for these quantities are generated by the program, all four construction parameters (offset angle, position of offset plane, glass plate thickness and index) are allowed to vary.

For the homogeneous sample, the optimization proceeds quite rapidly towards a solution. The thickness of the homogeneous sample, as measured by a micrometer, is 1.001 $\pm$.001 cm. and the thickness, computed from measurements made with the interferometer, is 1.0012 cm. The index of refraction, computed from measurements using a Pulfrich refractometer, is 1.5206 $\pm$.0002 and the index computed from the interferometrically measured data is 1.5205.

For the analysis of the measurements of the gradient sample, a subset of data points was selected initially. After the initial fit to the data was performed, the residuals were plotted. From that plot, gross errors in properly assigning the fringe count were obvious. To reduce the time required to compute better estimates for the construction parameters, a representative set of 10 data points was selected for fitting. The residuals associated with these initial points are plotted in Figure 3. After optimizing using this subset of data, the residuals were plotted again. Finally, optimization was performed on the entire dataset. Most of the optical path differences (between computed and measured values) lie within about one fifth of a wavelength. Given the conditions of the experiment, the magnitude of these residuals is attributed primarily to errors made in the phase measurements. Using a micrometer and a standard, an estimate of the thickness was 1.0028 $\pm$.0005 cm. After final optimization, the computed thickness (1.0026 cm.) is found to lie within this range. With the exception of d, good estimates for the values of these Gaussian parameters are known. The table below reviews the measured Gaussian coefficients.

Measured Gaussian coefficients (Sample: BL44)

Coefficient	Moore/Ryan	present work
n(0)	1.505	1.5044
Δn	.0294	.02876
σ	8.140 cm^{-2}	8.149 cm^{-2}
d (*)	-.0303 cm	.00005 cm (-.015 cm approx. removed in preparation)
wavelength of measurement	.5145 µm	.5309 µm

(*) Due to unresolvable differences in experimental procedures, the values for this coefficient can not be compared.

Procedures for reconstructing index profile information from measurements of optical path length have been given. These procedures have been applied in the reconstruction of an axial, Gaussian index profile.

References

1. G. W. Johnson, Measurement of Strongly Refracting Three-Dimensional Index Distributions, Ph.D. Thesis, University of Rochester, 1979

2. D. T. Moore and D. P. Ryan, "Measurement of the Optical Properties of Gradient Index Materials," J. Opt. Soc. Am., pp. 1157-1166 68 (1978)

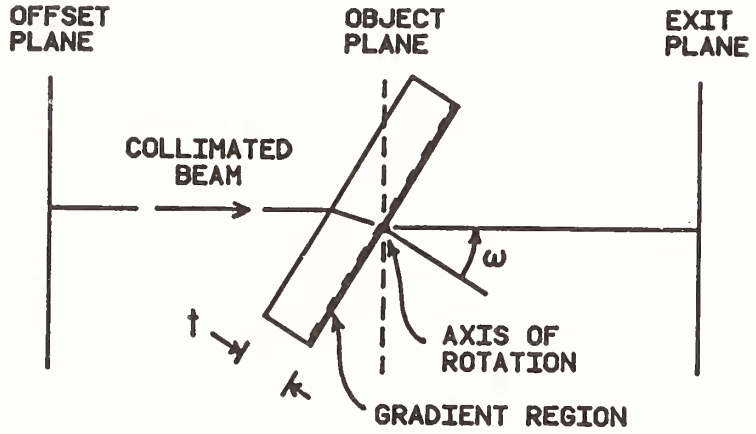

Figure 2

SAMPLE ORIENTATION IN THE SAMPLE ARM OF THE INTERFEROMETER

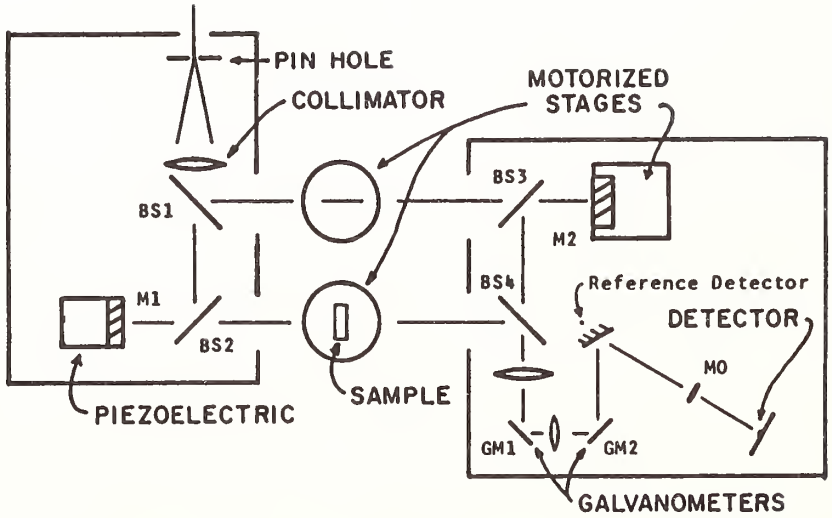

MODIFIED MACH-ZEHNDER INTERFEROMETER

Figure 1

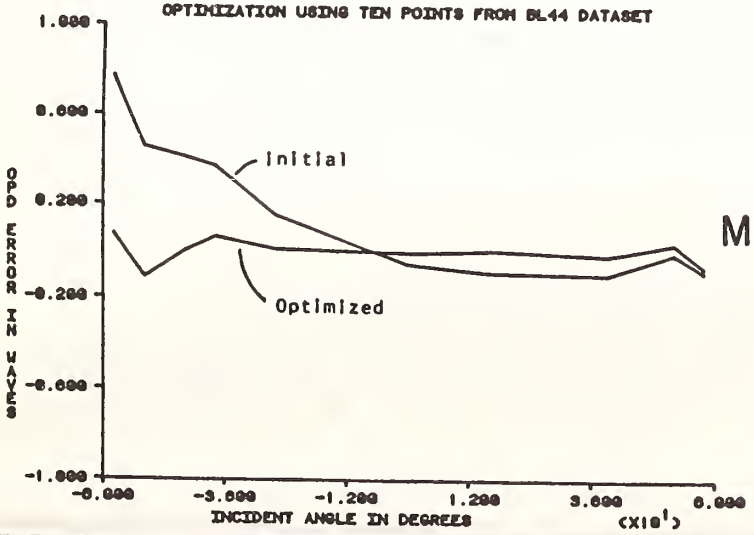

Figure 3

GRADED-INDEX AR SURFACES FOR IMPROVED LASER-DAMAGE RESISTANCE

W. H. Lowdermilk and D. Milam
Lawrence Livermore Laboratory
University of California
Livermore, CA 94550

Thin-film AR (antireflection) coatings have traditionally been the most easily damaged elements in laser amplifier chains. Their damage thresholds limit the output fluence of high power lasers for pulsewidths in the 1-10-ns range. The 1-ns threshold for commercial thin-film AR coatings of 4-6 J/cm^2 has resisted numerous experimental attempts to improve it. These attempts included variations of substrate materials and surface finish, coating design, materials, and deposition processes. In exploring alternate techniques for AR surfaces we found that graded-refractive-index AR surfaces, which can be developed on certain types of glass by acid etching, have median damage thresholds two and one-half times greater than the electron beam evaporated, thin-film SiO_2/TiO_2 AR coatings now used extensively in large Nd:glass laser systems.

M. J. Minot[1] introduced the formation of a graded-index surface based on separation of certain glass compositions into silica-rich and silica-poor phases. Acid etching the more soluble, silica-poor phase forms a microporous high-silica-content surface layer. The pores have typical dimensions of 100 Å, so scattering of visible and longer-wavelength light is negligible. Reflectivity of the surface can be 0.1-0.2% (comparable to thin-film coatings) over a very broad bandwidth (<1/2% for 0.35-2.5-μm light) and range of incidence angles. Such optical behavior is characteristic of a graded refractive index as opposed to a homogeneous low-index layer.

Damage threshold measurements were made with 1.06-μm, 1-ns, linearily polarized pulses, focused to a 2-mm spot diameter on the sample. Before and after irradiation, each site was examined and photographed using a Nomarski microscope at 100x magnification. Sites were irradiated, once each, at increasing fluence levels until physical change occurred. At threshold, 1-10 spots, ~10 μm in diameter, of apparently melted material were formed with random distribution over the irradiated surface.

The laser-damage thresholds of more than 60 graded-index samples have been measured. The median threshold of 12 J/cm^2 is 2.5-times greater than the median threshold of state-of-the-art SiO_2/TiO_2 thin-film AR coatings. Some samples were further irradiated at fluences of 20-50 J/cm^2. Even then, the extent of damage was not severe; in fact, it was difficult for the unaided eye to detect. Such behavior is distinctly different from thin-film coatings, where irradiation at fluences only 10-20% above threshold causes catastrophic damage.

We believe the high damage thresholds of graded-index AR surfaces are due to the absence of the highly contaminated substrate/film interface region where AR coatings normally damage, and/or the removal of surface impurities by the acid etch.

In conclusion, research samples of graded-index AR surfaces have exhibited a median, 1-ns damage threshold of 12 J/cm^2, compared to a median threshold of 5 J/cm^2 for commercial thin-film AR coatings, and some samples withstood fluence of 20-50 J/cm^2 without catastrophic damage. The transmission and scatter throughout the visible and near-IR spectral regions were found to be acceptable for laser-transmitting optical components.

REFERENCES

1. M. J. Minot, J. Opt. Soc. Am. 66, 515 (1976).

REFLECTANCE PROPERTIES OF PRESSED TETRAFLUOROETHYLENE POWDER

Jack J. Hsia and Victor R. Weidner
National Bureau of Standards
Washington, D. C. 20234

Good white diffusers are useful in diffuse reflectance spectrophotometry both as diffuse reflectance standards and as coatings for increasing the reflectance efficiency of integrating spheres used in measuring diffuse reflectance. Historically, the most commonly used materials have been magnesium oxide and barium sulfate powders or paints. Much has been written on the optical properties of these materials, and the advantages and disadvantages of their use in spectrophotometric applications have been experienced by nearly anyone faced with the problems of reflectance spectrophotometry.

This paper will describe some of the properties of tetrafluoroethylene[1] powder that make it attractive as a substitute or replacement for the commonly used magnesium oxide or barium sulfate coatings.

Basically, tetrafluoroethylene powder exhibits the highest diffuse reflectivity of any known material in the wavelength range 200 nm to 2500 nm, its reflectance being above 96% in this wavelength range and greater than 99% over the wavelength range 400 nm to 1800 nm. It is manufactured in such high purity that samples prepared from different lots over a 5 year period are found to have the same reflectance to within ±0.2%. Its reflectance properties are not affected by changes in humidity. Exposure to intense ultraviolet radiation causes little or no change in its reflectivity in the visible and infrared and only slight degradation of the ultraviolet reflectance[2]. The mechanical properties of pressed tetrafluoroethylene powder are excellent from the standpoint of using it as an integrating sphere coating.

The absolute 6°-hemispherical spectral reflectance of tetrafluoroethylene powder for sample densities of approximately 0.8 g cm^{-3} has been determined by means of the NBS Reference Spectrophotometer[3] for diffuse reflectance and the reflectance accessories used in conjunction with this instrumentation. These reflectance accessories include integrating spheres for measuring 6°-hemispherical reflectance, directional-hemispherical reflectance, and a specular reflectometer which can be used to measure bidirectional reflectance in the plane of the incident beam.

The term "6°-hemispherical" refers to a geometry in which the incident sample beam is 6° from the normal to the sample plane and the hemispherical reflectance of that beam is measured. This is a commonly used geometry in many commercial spectrophotometers equipped with integrating spheres for measuring diffuse reflectance. The geometry allows the

specular component of the reflected sample beam to be included in the hemispherical reflectance measurement, a condition which would not be possible with the sample beam normal to the sample plane.

Measurements of the absolute reflectance of tetrafluoroethylene powder were made by means of the reference spectrophotometer, using the auxiliary sphere or Van den Akker method[4]. Briefly, the technique utilizes a measuring integrating sphere equipped with a suitable detector and a second sphere (auxiliary sphere) which is attached as a sample to the sample port of the measuring sphere. The auxiliary sphere is lined with a coating of the material to be measured (in this case, tetrafluoroethylene powder). The auxiliary sphere, and several flat samples of the same material used to line the auxiliary sphere, are measured. These flat samples are prepared in the same manner and with the same thickness and surface finish as the auxiliary sphere coating. Calculations from these measurements will yield the absolute reflectance of the sphere coating for the bihemispherical geometry represented by this double sphere geometry. The 6°-hemispherical reflectance will be slightly lower than the bihemispherical value. In order to make this adjustment to the 6°-hemispherical geometry, the directional-hemispherical distribution of the tetrafluoroethylene powder reflectance must be determined by means of a special integrating sphere which will be described.

Measurements of the hemispherical reflectance of tetrafluoroethylene powder as a function of angle of incidence (directional-hemispherical) are made with an integrating sphere in which the sample is suspended in the center of the sphere[3]. A stepping-motor-driven turntable located on top of the sphere can control the angle of incidence of the sample beam by rotating the suspension rod on which the sample is mounted. The detector is located at the bottom of the sphere where it is baffled so as to prevent direct viewing of the sample or sphere port. Directional-hemispherical reflectance measurements are made at angles of incidence in 5° increments between 5° and 75°. All measurements are then normalized to the value at 6° incidence, thus showing the relative diffuse reflectance of the sample at the selected angles of incidence.

In addition to the 6°-hemispherical reflectance and the directional-hemispherical reflectance, measurements were also made of the directional-directional or bidirectional reflectance of tetrafluoroethylene powder for the plane of the incident sample beam. The tetrafluoroethylene powder samples were prepared with both smooth and rough finishes for this measurement. Angles of incidence of -10°, -30°, -50°, and -70° were selected and the reflected signal was measured at viewing angles of -80° to +80° in increments of 10°. The limiting aperture of the detector system for these measurements subtended an angle of 3.6° at the sample. The measurements were made at 300 nm, 600 nm, and 1500 nm.

Among the other optical properties of tetrafluoroethylene powder that have been investigated at NBS are its reflectance as a function of

thickness, and its fluorescence properties. It was found that the maximum reflectance of tetrafluoroethylene powder was obtained for densities of approximately 0.8 g cm^{-3} and thicknesses of 6 mm or more, for the wavelength range of these investigations. The reflectance of tetrafluoroethylene powder as a function of density is reported in reference 2.

Although there is no direct evidence that tetrafluoroethylene powder itself fluoresces, there is an indication that there is some weak fluorescence associated with contaminants, possibly introduced into the powder from the plastic bag in which the material is shipped. It is known that tetrafluoroethylene powder can be contaminated by tobacco smoke and that this introduces a weak fluorescence effect. The observed excitation wavelengths are in the wavelength range 270 nm to 290 nm with very weak emission in the wavelength range 300 nm to 330 nm. For most spectrophotometric application where the sample is illuminated with essentially monochromatic sources the fluorescence does not introduce a problem. No fluorescence has yet been observed for the visible or infrared spectral range.

A detailed description of the diffuse reflectance properties of tetrafluoroethylene powder and the techniques used in their determination is being prepared for publication. An Information Sheet describing techniques for using tetrafluoroethylene powder and tabulated results of the absolute reflectance measurements of the powder is available from the authors. The absolute 6°-hemispherical reflectance is given at 10-nm intervals over the spectral range 200 nm to 2500 nm. Data is also given for the measurements of directional-hemispherical reflectance and bidirectional reflectance.

REFERENCES:

1. Tetrafluoroethylene resin is manufactured by Allied Chemical Co., under the trade name Halon. This product is mentioned by trade name for purposes of identification, but in no way implies recommendation or endorsement by the National Bureau of Standards.

2. Grum, F. and Saltzman, M.; P-75-77 New White Standard of Reflectance, Compte Rendu 18^{e} Session, Londres 1975, CIE Publication No. 36, 91 (1976).

3. Venable, William H. Jr., Hsia, Jack J., and Weidner, Victor R., Development of an NBS reference spectrophotometer for diffuse reflectance and transmittance, Nat. Bur. Stand. (U.S.), Tech. Note 594-11, 47 pages (October 1976).

4. Venable, William H. Jr., Hsia, Jack J., and Weidner, Victor R., Establishing a scale of directional-hemispherical reflectance factor I: The Van den Akker Method, J. Res. Nat. Bur. Stand. 82, 29, (July-August 1977).

MEASUREMENTS OF LARGE OPTICAL ABSORPTION COEFFICIENTS BY DIFFUSE REFLECTANCE

R. K. Waring
Central Research and Development Department
E. I. du Pont de Nemours & Co.
Experimental Station
Wilmington, Delaware 19898

INTRODUCTION

The dilution method of diffuse reflectance[1] is, in principle, suited to the measurement of large absorption coefficients ($\alpha_p > 10^4$ cm^{-1}). A small concentration, on the order of 0.01, of the unknown is mixed with a white diluent powder of very low absorption coefficient, but of known scattering function, S. Then, the Kubelka-Munk theory yields,

$$\frac{(1-R_\infty)^2}{2R_\infty} = \frac{K}{S}, \qquad (1)$$

where R_∞ is the diffuse reflectance of a thick layer of powder, and K is the Kubelka-Munk absorption coefficient of the mixture. Then, making the assumption that the small amount of absorber has negligible effect on S, but dominates the absorption,

$$\alpha_p = \frac{1}{2}\frac{K}{v_p}. \qquad (2)$$

Here v_p is the fraction of the powder volume (including air space) occupied by the unknown. The factor 1/2 implies that the optical path length between two points in the diffusing medium is twice the linear distance between them. This has been justified on theoretical grounds[2] for the relatively high reflectance ($R_\infty > 0.26$) of the diluted samples used in this work. The technique has been applied to measure the absorption coefficient of airborne particulates[3]. The diluent used in this work was Eastman #6091 $BaSO_4$ White Reflectance Standard[4]. The scattering power, for this material has been published[5].

EXPERIMENTAL DETAILS

It is implicit in the Kubelka-Munk theory that the absorber is molecularly dispersed. For particles of diameter d, the condition $d < \alpha^{-1}$ should be approximated for K to be linear in α. For $d >> \alpha$, K will become insensitive to changes in α. In this work, stable water suspensions of powders were centrifuged to remove particles with a Stokes radius, $r_s > 10^{-5}$ cm. The fines were then heteroagglomerated with the $BaSO_4$ under conditions that prevented homoagglomeration of absorbing

particles with each other. The mixture was then dried and pressed into low density pellets at 2.4×10^6 Pascals (350 pounds/in.^{2}). Reflectance of loose $BaSO_4$ powder is not reduced at this pressure[6]. To improve strength, a few drops of a 1% water solution of polyvinyl alcohol were diffused into the pellet and dried. This also did not measurably affect reflectance or scattering power. Diffuse reflectance was measured on a Cary 14 fitted with a #1411 diffuse reflectance attachment. Eastman $BaSO_4$ White reflectance Standard was used as a reference.

To correct for finite absorption in the diluent, intrinsic or possibly introduced during sample preparation, the following formula was used:

$$\alpha_p = \frac{S}{2v_p}\{F[R_\infty(\frac{mix}{abs})] - (\frac{v_d - v_p}{v_d})F[R_\infty(\frac{dil}{abs})]\} \qquad (3)$$

where R_∞(mix/abs) is the absolute reflectance of the pigment/diluent mixture, R_∞(dil/abs) is the absolute reflectance of the diluent alone, and v_d is the fraction of the volume occupied by the diluent in the sample of diluent alone. Equation (3) reduces to equation (2), if absorption by the diluent is negligible. Further, if we imagine the colored pigment to be replaced by white diluent, (3) reduces to the intrinsic absorption coefficient of the diluent.

In a measurement R_∞(dil/st) is determined according to the relation

$$R_\infty(dil/abs) = R_\infty(dil/st) \cdot R_\infty(st/abs) \qquad (4)$$

where R_∞(dil/st) is the reflectance of the diluent alone measured relative to the standard, and R_∞(st/abs) is the published absolute reflectance of the standard.[7] R_∞(mix/abs) is then measured according to the relation:

$$R_\infty(mix/abs) = R_\infty(mix/dil) \cdot R_\infty(dil/abs) \qquad (5)$$

where R_∞(mix/dil) is the reflectance of the pigmented mixture measured relative to the diluent.

For minimum dependence of α_p on errors in measured reflectance, the colored pigment loading in the mixture should be sufficient to insure that $0.2 < R_\infty < 0.6$ in the spectral region of interest[8].

RESULTS

As an example of spectra obtained with this technique, Fig. 1 shows the absorption coefficients of $PbCrO_4$ and $BaCrO_4$. The shoulder in the visible, which accounts for the exceptionally strong, pure yellow color of $PbCrO_4$ is not seen in $BaCrO_4$. The additional transition has been attributed[9] to $Pb^{2+}(6s)$-$Cr^{6+}(3d)$ charge transfer. Szabo[10] has suggested a similar interpretation of a qualitative diffuse reflectance spectrum. A detailed band theory calculation[11] indicates that the transition

occurs between a filled hybrid $O^{2-}(2p)+Pb^{2+}(6s)$ state and an empty $Cr^{6+}(3d)$ state.

Zumsteg[12] has measured the absorption coefficient of $PbCrO_4$ by ellipsometry. While the spectrum is qualitatively similar, the absolute values are substantially higher. It is of interest to consider possible sources of error in the diffuse reflectance measurement. Unexpected difficulties were encountered in measurement of v_p, where

$$v_p = c_p P \rho_d / \rho_p \qquad (6)$$

Here c_p is the mass concentration of colored pigment in the mixture, P is the volume packing fraction, and ρ_d and ρ are the intrinsic densities of the diluent and pigment, respectively. While, in principle, c_p could be determined from the mass of a dried aliquot of the stable suspension of fines, the measurement is complicated because the relative concentration of dissolved contaminants such as surfactants is enhanced in the classification step. Therefore, in this work, X-ray fluorescence was used with known mixtures of unclassified pigment and diluent as standards. Using this technique, we should obtain a value of c_p correct to within ±10%.

Other sources of error reside in assumptions implicit in the Kubelka-Munk theory. While $\alpha > 10^5$ cm^{-1} for a strongly colored solid, particle diameters less than 10^{-5} cm are not readily obtainable by grinding. Colorant concentrated in a particle will be less effective in absorbing light than an equal amount molecularly dispersed[13]. No adequate particle size correction for light diffusing systems is known to this author. In any event, the difference between ellipsometric and diffuse reflectance values persists for $\alpha < d^{-1}$.

An experimental plot of the remission function (1) *vs.* $c_p (c_p < 0.02)$ for constant particle size distribution displays slight downward concavity. This indicates a failure in the assumptions of the Kubelka-Munk theory or of the dilution method. If the curves for different parts of the spectrum, and thus different absorption are normalized to superpose them at one concentration, they are nearly identical, indicating that the non-linearity is a function of concentration, not of α in the ranges tested. Accordingly, the non-linearity does not appear to be a particle size effect. Further, it cannot account for an error larger than 2% in our results.

None of the identified sources of error seems adequate to account for the differences (∿X2) between diffuse reflectance and ellipsometric determinations. A remaining possibility is that the cause can be found in the abrupt change in refractive index at the surface of the strongly absorbing solid particles.

The collaboration of J. A. Perry in developing the data analysis is gratefully acknowledged.

1. G. Kortüm, Reflectance Spectroscopy (Springer-Verlag New York, Inc. 1969) p. 175 ff.
2. K. Klier, J. Opt. Soc. Am. 62, 882 (1972).
3. J. D. Lindberg, Appl. Opt. 14, 2813 (1975).
4. Eastman White Reflectance Standard #6091, Eastman Kodak Co., Rochester, NY.
5. E. M. Patterson, C. E. Shelden, and B. H. Stickton, Appl. Opt. 16, 729 (1977).
6. E. A. Schatz, J. Opt. Soc. Am. 56, 389 (1966).
7. F. Grum and T. E. Wightman, Appl. Opt. 16, 2775 (1977).
8. G. Kortüm, op. cit., p. 250.
9. A. W. Sleight, private communication.
10. Z. G. Szabo et al., Spectrachimica Acta 64A, 607 (1978).
11. R. V. Kasowski, submitted to Bull. Amer. Phys. Soc., for March 1980 meeting of APS.
12. F. C. Zumsteg, next paper, this conference.
13. G. Kortüm, op. cit., p. 59ff.

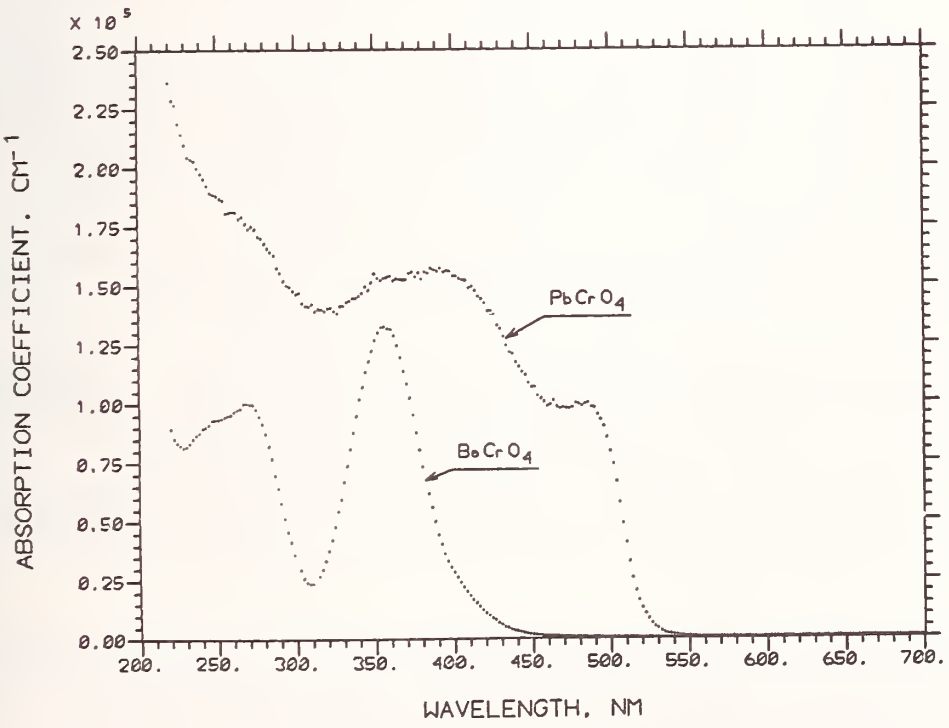

Fig. 1. Intrinsic absorption coefficients of $PbCrO_4$ and $BaCrO_4$ obtained by diffuse reflectance.

ELLIPSOMETRIC MEASUREMENTS OF THE OPTICAL PROPERTIES OF COMPACTED POWDERS

F. C. Zumsteg
Central Research and Development Department
Experimental Station
E. I. du Pont de Nemours & Company
Wilmington, Delaware 19898

Transmission and normal incidence reflection spectroscopy are the most common methods for determining optical constants. Both have serious drawbacks when used for many highly absorbing ($\alpha > 10^4$ cm^{-1}) materials. Both techniques require moderate size single crystals that may not be readily available. Transmission measurements require samples so thin that only micaceous materials can seriously be considered for measurement. In addition, these measurements do not provide refractive index information. Normal incidence reflection measurements require spectral data over an extremely broad range so that an accurate Kramers-Kronig transformation can be made.

Spectroscopic ellipsometry provides a partial solution to these problems. When single crystals are available, the optical constants of even anisotropic crystals can be determined at any given wavelength without the need for additional spectral information[1]. In addition, we have found that ellipsometry can be used to obtain semiquantitative values of the optical constants of powders which have been compressed into specularly reflecting pellets.

Pellets with densities near 100% were produced by compressing a powdered sample between the faces of a small Bridgeman anvil at pressures ranging from 100-600 atmospheres. The powder was contained by a 30 mil-thick washer of Teflon® fluorocarbon resin. The tungsten carbide faces of the anvil were highly polished, so that in most cases the resulting pellets needed no additional treatment before measurements were made.

Ellipsometric measurements were made using a Rudolph Model 200E ellipsometer setup in a standard polarizer-compensator-sample-analyzer configuration. The light source was a Perkin-Elmer 112 monochrometer illuminated with a quartz-halogen lamp. A Babinet-Soliel compensator was used so that 1/4 λ retardation could be used at all wavelengths.

Figs. 1 and 2 show the absorption coefficient, α, and the refractive index of $BiVO_4$ as a function of wavelength. Absorption data is shown for ellipsometric measurements on a single crystal and a compressed powder, as well as R. K. Waring's data obtained by diffuse reflectance.[2] One can see that there is excellent agreement between the ellipsometric data while the diffuse reflectance values of α are appreciably smaller. Although the ratio is not always the same, the ellipsometric value is always larger than that determined by diffuse reflectance. This difference may result from particle size effects in the diffuse reflectance method where, for large values of α, light does not interact with the entire volume of the crystallites.

To a certain extent, the agreement between single crystal and compressed powder is fortuitous. Inasmuch as $BiVO_4$ is anisotropic, one would not necessarily expect agreement between data obtained from a single crystal and a powder of randomly oriented crystallites. Fig. 2, in fact, shows a substantial difference between the single crystal refractive index data and that of the compressed powder.

Ellipsometry is particularly useful for measuring the optical properties of thin surface layers. As a result, surface layers, whether they be of a second phase, adsorbed liquid layers, or irregularities, can cause appreciable errors. Most of the materials we have examined have been stable oxides, so our primary concern has been with adsorbed water and surface roughening. In both cases, errors caused by either appear to be less than $\alpha = 3 \times 10^4$ cm^{-1}.

One should note that ellipsometry is limited to measurement of relatively large absorption coefficients, $\alpha > 10^4$ cm^{-1}. For values of α less than this, sensitivity is greatly reduced and surface effects play an increasingly important role. An example of this can be seen in Fig. 1 where there appears to be a residual absorption of 3×10^4 cm^{-1} for $\lambda > 550$ nm in the ellipsometric data. From other measurements, however, we know that $BiVO_4$ has an absorption coefficient of $<.1$ cm^{-1} in this wavelength region. Similar discrepancies have been seen in our measurements on other materials.

Although there are some limitations to the technique described here, it provides a method by which optical properties can be obtained when only very small crystallites or powders are available. One can determine the shape and location of absorption peaks with a moderate degree of precision and determine the refractive index and the magnitude of the absorption to a lesser degree.

1. M. Elshazly-Zaghloul, A. M. A. Azzam, and N. M. Bushara, Surface Science 56, 281 (1976).

2. R. K. Waring, preceeding paper, this conference.

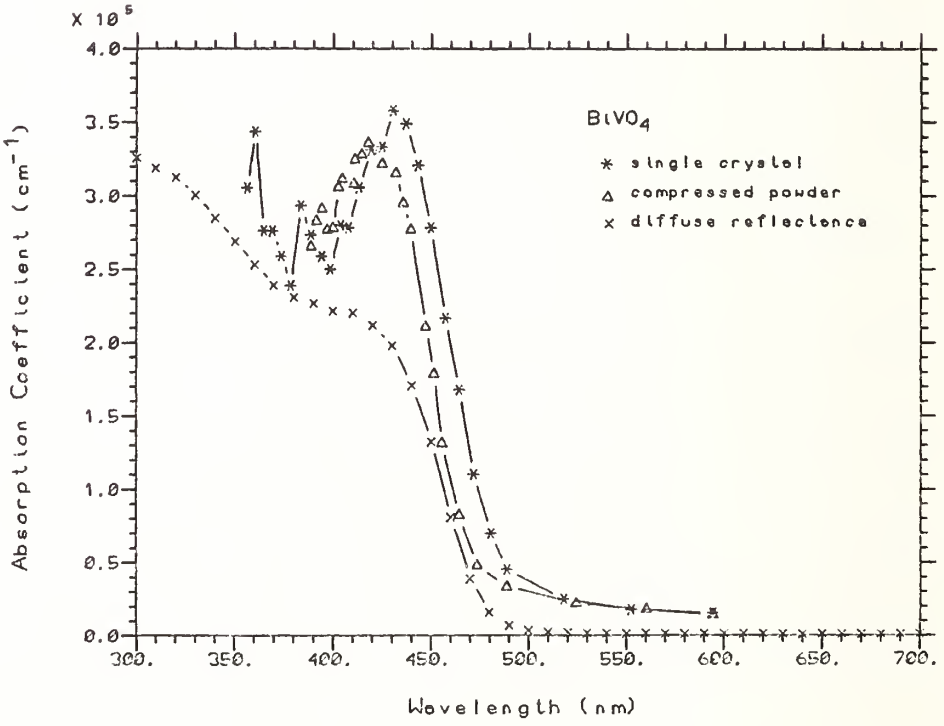

Fig. 1. Absorption coefficient vs. wavelength of $BiVO_4$.

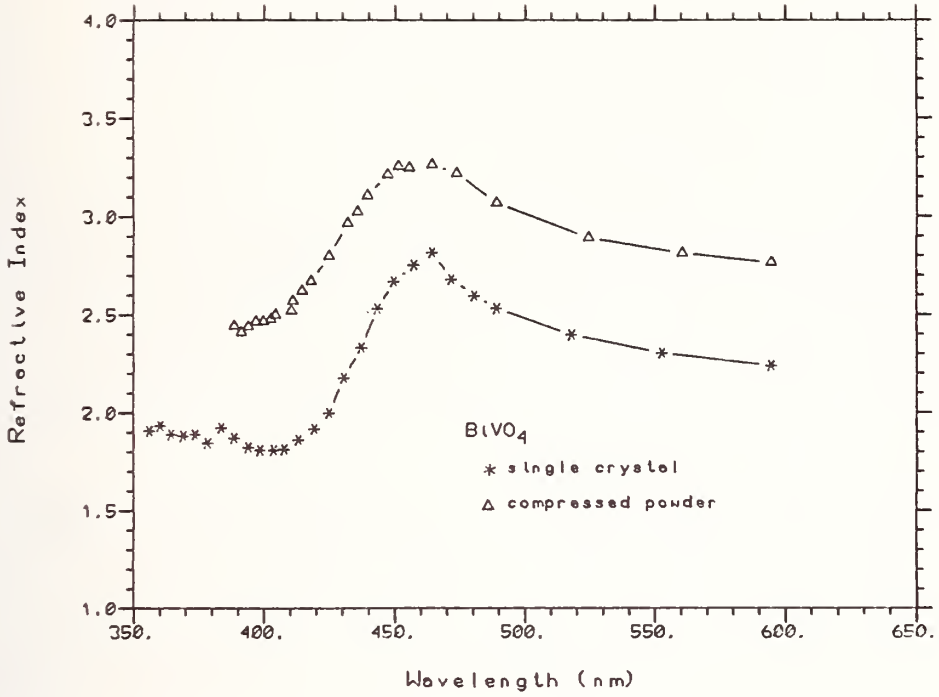

Fig. 2. Refractive index vs. wavelength of $BiVO_4$.

MATERIAL PROPERTIES BY SPECTROSCOPIC ELLIPSOMETRY

D. E. Aspnes
Bell Laboratories
Murray Hill, N. J. 07974

An ellipsometer is an optical device that measures the change in polarization state which occurs when light is reflected at non-normal incidence from a surface.[1] The polarization state is a complex quantity having both amplitude and phase, and is independent of the average light intensity. As a result, ellipsometry offers several significant advantages with respect to reflectance or transmittance techniques for determining the basic optical properties of materials.

First, two parameters are determined in a single measurement instead of one. These two parameters can be used to calculate both real and imaginary parts of the dielectric function of a uniform sample at a single wavelength; extended wavelength measurements and Kramers-Kronig analyses are not needed. Laminar or otherwise nonuniform samples which are too complicated to investigate in single-wavelength measurements can be analyzed more definitively for structure and composition because two spectra are available for interpretation instead of one. Alternatively, the values of parameters in models describing such samples can be determined more precisely. This is particularly important if material properties are to be deduced from their measured visible-near uv optical response.

Second, accurate ellipsometric measurements can be made on surfaces that are too rough for reflectance spectroscopy.[2] Ideally, samples should be prepared with undamaged, atomically clean, and specular surfaces. It is relatively easy to obtain clean, undamaged surfaces by cleaving, ion bombardment and annealing, or chemical processing techniques. But quite often these surfaces are macroscopically rough, causing light scattering which leaves them unsuitable for reflectance spectroscopy although quite adequate for ellipsometric spectroscopy.

Third, the fast measurement and analysis capabilities of automatic ellipsometers allow cleaning procedures to be monitored and surface conditions to be assessed essentially in real time. This is almost trivial to do with spectroscopic instruments that can be tuned to the wavelength corresponding to the peak in the ε_2 spectrum of a sample. At this wavelength, surface sensitivity is maximized because light penetration is least, and surface overlayers (including microscopic roughness) almost invariably act to reduce the apparent value of ε_2 by reducing the impedance mismatch between substrate and ambient.[3,2] This leads to a "highest is best" rule that can be applied with virtually no modeling assumptions or a prior knowledge of sample

properties, but which nevertheless insures that the subsequent data are taken with the sample in its cleanest possible state. Using these techniques the dielectric functions of materials as diverse as Nb[4] and GaAs[5] were recently revised by as much as 20% and 30%, respectively, in the visible-near uv spectral range relative to values previously determined by reflectance measurements and Kramers-Kronig analysis.

Because instrumentation[6] and the determination of the intrinsic dielectric properties of materials in their pure bulk form are now basically solved problems, attention is turning to the determination of properties of heterogeneous samples from their visible-near uv optical response. Spectroscopic ellipsometric techniques can go much further than simply measuring thicknesses and refractive indices of films, as a recent analysis of the interface between Si and its thermally grown oxide has shown.[7] For example, we recall that the dielectric function is defined as a polarization per unit volume. Thus it is clear that ellipsometry can also be used to estimate the density of bulk materials.[8] Noting that a microscopically rough surface layer can be considered as density-deficient bulk material, it is not surprising that ellipsometric measurements can yield information about microscopic roughness that is virtually impossible to attain any other way.[9] Likewise, the sensitivity of the dielectric response to long-range order makes it an ideal probe for detecting the presence, or determining the fraction, of crystallinity in otherwise amorphous materials.[10]

The determination of the properties of a heterogeneous sample from its optical response is a three-step process.[9] First, accurate dielectric function data must be acquired for the pure bulk forms of its constituents as well as accurate ellipsometric data for the sample itself. Second, the physical microstructure must be mathematically represented in some way, for example by n-phase models[1] for laminar structures or by effective medium theories for heterogeneous materials. Third, the model parameters must be determined from the data. By analogy to circuit analysis, the sample can be viewed as a black box but with the usual frequency-independent parameters of resistance, capacitance, and inductance replaced by thicknesses, compositions, and void fractions.

The modeling of heterogeneous materials requires some comment. It is generally assumed that the characteristic length of inhomogeneities is much less than the wavelength of light, but that this length is sufficiently large so the inhomogeneities themselves possess their own dielectric identity. This avoids the local-field problem even while recognizing that everything is heterogeneous on an atomic scale. The macroscopic (observable) dielectric function is now obtained by solving the microscopic problem exactly for the microscopic electric field $\vec{e}(\vec{r})$ and polarization density $\vec{p}(\vec{r})$, then spatially averaging the microscopic quantities to calculate the observed macroscopic equivalents $\langle\vec{E}\rangle$ and $\langle\vec{P}\rangle$ from which $\langle\varepsilon\rangle\langle\vec{E}\rangle = \langle\vec{E}\rangle + 4\pi\langle\vec{P}\rangle$.[11] It is clear that internal boundaries and the distribution of the resultant screening

charge will play an important part in determining $\langle\varepsilon\rangle$. Either the boundaries are known in detail or suitable approximations to them must be made. The latter approach is usually taken because internal structure is not generally known, or else requires far too many parameters to describe, except in idealized models.[12] We simply use the self-consistent Bruggeman effective medium model, which differs from the more common Lorentz-Lorenz and Maxwell Garnett models only in the choice of dielectric background.[9] The advantage of so doing is that the number of parameters are minimized; the disadvantage is that the parameters that remain are effective averages whose values may differ somewhat from those corresponding to the actual compositions.

The parameters themselves can be determined by linear regression analysis[13] (LRA). LRA yields not only the best-fit values and the residual mean-square deviations on a systematic basis, but it also provides correlations and confidence limits. The latter are important if meaning is attributed to the best-fit values, for it establishes which parameters are being determined by the data and which are not. Because correlations are included, the confidence limits also prevent abuses such as using too many parameters. While adding another parameter always reduces the mean square deviation, it can also cause catastrophic increases in confidence limits if it is not being determined independently by the data.

The above approach has been applied in detail to Au.[14] Representative dielectric function spectra are shown in Fig. 1. Data include those taken on bulk materials (Winsemius, Pells and Shiga) unannealed thin films deposited in moderate pressure (Johnson and Christy, "this work"), and annealed thin films deposited in ultrahigh vacuum (Thèye). The spectra at energies above the interband transition threshold at 2.5eV differ almost entirely because the samples contain different void fractions, as shown in Fig. 2. Here, using the locally prepared film data as a basis, void fractions were calculated in a one-parameter Bruggeman effective medium approximation using linear regression analysis. The model describes the major differences satisfactorily in the interband transition region not only in terms of absolute values but also with regard to spectral variations. Below 2.5eV the ε_2 spectra are dominated by the Drude tail, which provides a measure of the importance of bulk and surface scattering. The former can be related to grain size, and the latter to microscopic roughness.

REFERENCES

1. R. M. A. Azzam and N. M. Bashara, Ellipsometry and Polarized Light (North-Holland, Amsterdam, 1977).
2. M. D. Williams and D. E. Aspnes, Phys. Rev. Letters 41, 1667 (1978).
3. D. E. Aspnes, in Proceedings of the Conference on Non-Traditional Methods to the Study of Solid-Electrolyte Interfaces, ed. by T. Furtak and D. W. Lynch (North-Holland, Amsterdam, 1980)(in press).

4. D. E. Aspnes and E. G. Lluesma (to be published).
5. D. E. Aspnes and A. A. Studna (to be published).
6. P. S. Hauge, in Proceedings of the Fourth International Conference on Ellipsometry, ed. by R. H. Muller, R. M. A. Azzam, and D. E. Aspnes (North-Holland, Amsterdam, 1980)(in press).
7. D. E. Aspnes and J. B. Theeten, Phys. Rev. Letters 43, 1046 (1979).
8. D. E. Aspnes and A. A. Studna, in ref. 6 (in press).
9. D. E. Aspnes, J. B. Theeten, and F. Hottier, Phys. Rev. B20, 3292 (1979).
10. B. G. Bagley, D. E. Aspnes, A. A. Studna, A. C. Adams, and F. B. Alexander, Jr., Bull. Amer. Phys. Soc. 24, 363 (1979).
11. J. Sipe and J. S. Van Kranendonk, in Progress in Optics, vol. 15, ed. by E. Wolf and A. C. Jones (Academic, New York, 1977), p. 245.
12. O. Hunderi, in ref. 6 (in press).
13. E. S. Keeping, Introduction to Statistical Inference (Van Nostrand, Princeton, 1963), Ch. 12.
14. D. E. Aspnes, E. Kinsbron, and D. D. Bacon, Phys. Rev. B21 (in press).

FIGURES

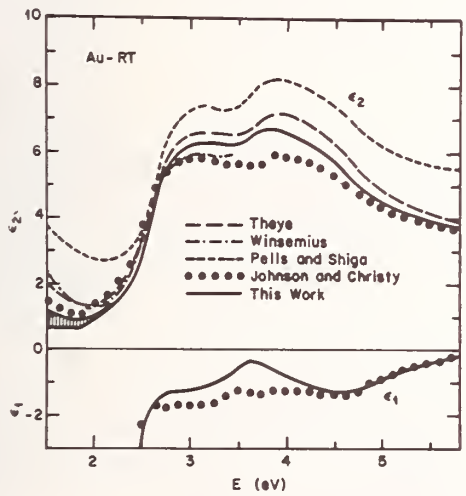

Fig. 1. Representative dielectric function spectra for Au (after ref. 14).

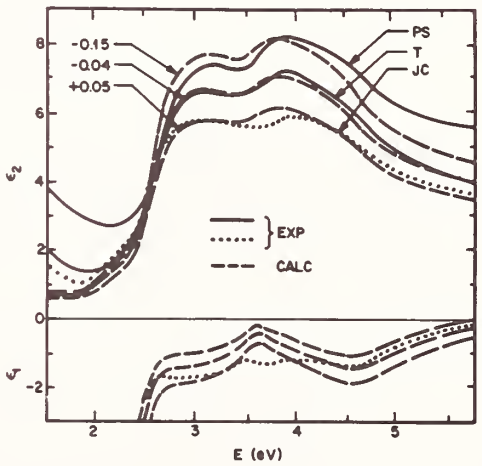

Fig. 2. Comparison between dielectric function spectra and one-parameter (void fraction) model calculations for several spectra of Fig. 1.

DIELECTRIC FUNCTION OF SUPERLATTICE MATERIALS

P.J. Price
IBM T.J. Watson Research Center
Yorktown Heights, New York 10598

In a "superlattice" formed from alternating layers of GaAs and (Ga,Al)As alloy, the conduction band edge of the alloy is higher than that of the GaAs by a few tenths of an eV. Consequently an individual GaAs layer acts as a "potential well" for electron motion in the growth (say, X) direction, with quantized energy levels E_n. These levels are the minima for the electron energy including motion in the YZ plane:

$$E_n + (\hbar^2/2m^*)(k_y^2 + k_z^2) \tag{1}$$

in the parabolic range.[1] A similar situation for holes applies with those levels that can be formed in the shallower valence-band wells. The lowest level in (1) is

$$E_1 = (\hbar^2/2m^*)(\pi/a_1)^2 \tag{2}$$

where to sufficient approximation a_1 may be equated to the layer thickness a.[2] (For example, $a_1 = 0.7 \times 10^{-6}$ cm gives $E_1 = 0.1$ eV.) The interconnection of wavefunctions through the alloy "barriers" between neighboring GaAs layers is believed to result in the individual well states (with the same k_y and k_z) combining into Bloch-like itinerant states; but if the barrier thickness, b, is fairly large then this phenomenon may be disregarded here. At the same time, with wavelengths at optical and infrared frequencies large compared to the layer spacing c = a + b, the response to an electromagnetic field should be given by the dielectric function $\varepsilon(\omega)$ for a uniform electric field.

The contribution to ε that is dealt with here comes from the dipole matrix elements between electron and hole Bloch states, in GaAs, at energies near the band edges, and compares with the corresponding contribution to $\varepsilon(\omega)$ in homogeneous GaAs. The latter may be calculated on the assumption of constant momentum matrix elements [that is, constant dipole matrix element times energy difference, $\langle c \mid x \mid v \rangle E_{cv}(k)$] between all

the pairs of Bloch states with the same wavevector. The result is

$$\varepsilon_{cv}(\omega) = \varepsilon_o \; G(\hbar\omega/E_g) \tag{3}$$

where

$$G(u) = (4/u^2)\big(2 - (1 + u)^{1/2} - (1 - u)^{1/2}\big), \tag{4}$$

so that $G(0) = 1$ and $G(1) = 2.34$. This formula can be fitted to the measured values of Marple,[3] by assuming that the background $\varepsilon - \varepsilon_{cv}$ is a linear function of ω over the range of the data, and taking $\varepsilon_o = 1.0$. (The value of ε_o that one obtains theoretically, using experimental values of mass and energy and momentum matrix element,[4] agrees well with this empirical value.)

A similar analysis for the GaAs "potential wells" of the superlattice case gives

$$\varepsilon_{cv}^{(1)}(\omega) = \varepsilon_o^{(1)} \; H\big(\hbar\omega/E_g^{(1)}\big) \tag{5}$$

where

$$H(u) = \frac{1}{u^2}\ell n\Big(\frac{1}{1-u^2}\Big) \tag{6}$$

The superscript "1" signifies that this contribution is from the two-dimensional continuum associated with the lowest level, E_1 in eq. (1). From the theory one has approximately (neglecting the difference between E_g and $E_g^{(1)}$, as well as spin-orbit splitting in the valence band)

$$c \quad \varepsilon_o^{(1)}/\varepsilon_o \simeq 2\hbar/(m_{cv}E_g)^{1/2} \tag{7}$$

where m_{cv} is the appropriate joint-density-of-states mass. With the latter approximately 0.1 times the free electron mass, the right hand side of (7) equals 1.3×10^{-7} cm. Accordingly, we expect $\varepsilon_o^{(1)} \sim 10^{-1}$ for the usual values of layer spacing $c = a + b$.

The infinity in (6) should be not very pronounced in practice, even when the superlattice band width is not appreciable; for example, at $1 - u = 10^{-3}$, H is only 6.2 . There is a possibility, however, of observation of the peak by the electroreflectance method.[5] In an electric field $\mathcal{E}$, the quantization energy E_1 changes by $-\frac{1}{2}\alpha_1\mathcal{E}^2$, where α_1 is the polariza-

bility, and similarly $E_g^{(1)}$. It can be shown that (disregarding the difference between a_1 and a)

$$\alpha_1 = 7 \times 10^{-3}(e^2 m_e/\hbar^2)\ a^4$$

$$= (0.92 \times 10^5\ \text{cm}^{-1})\ a^4 \qquad (8)$$

the second line of (8) being for GaAs. For a = 10^{-6} cm and $\mathcal{E}$ = 10^5 V/cm, this gives $\frac{1}{2}\ \alpha_1\ \mathcal{E}^2$ = 3.2 milli eV. In this idealized model, such a shift would give a maximum $\delta\epsilon$ of about 0.5. For the next level, α_2 is calculated to be only about 8% of α_1, however. It is not clear, at the time of writing, whether electron and hole in this system can bind into an exciton.

1. For example, R. Dingle, W. Wiegmann and C.H. Henry, *Phys. Rev. Lett.* 33, 827 (1974); R. Tsu, A. Koma and L. Esaki, *J. Appl. Phys.* 46, 842 (1975).

2. The correction, from the finiteness of the barrier height and from the atomic-scale "mismatch" of wavefunctions in the two layer materials, is a few lattice constants at most. (The mismatch effect *is* important, however, in the strength of the interaction between GaAs layers which is associated with the superlattice band.)

3. D.T.F. Marple, *J. Appl. Phys.* 35, 1241 (1964).

4. C. Hermann and C. Weisbuch, *Phys. Rev. B* 15, 823 (1976).

5. M. Cardona, K.L. Shaklee and F.H. Pollak, *Phys. Rev.* 154, 696 (1967).

DETERMINATION OF THIN FILM OPTICAL DISPERSION FROM SPECTROPHOTOMETER DATA

Arnold L. Bloom and Dennis Fischer
Coherent, Incorporated
3210 Porter Drive
Palo Alto, California 94304

This paper describes work being done on a project in which an attempt is made to determine the dispersive characterstics of optical thin films using relatively common laboratory instruments, such as a transmission spectrophotometer. It is well known that the real part of the refractive index can be measured very accurately by ellipsometry and the imaginary part can be measured by calorimetry, but these techniques are time-consuming and the instruments are not always available in the laboratory. The output of a spectrophotometer, on the other hand, provides data rapidly over wide wavelength ranges and should be particularly convenient for the purpose if the output data can be analyzed properly.

In our laboratory the experimental procedure is as follows. The material whose dispersion curve is to be measured is coated on a substrate whose refractive index is well known and which is highly transparent over the wavelength range in question (for example, fused silica in the visible and near UV). The coating is monitored at a highly transparent wavelength for the material and the layer is made relatively thick, for example 5 to 9 (an odd number) quarter waves at the monitoring wavelength. The transmittance of the entire sample is then measured over the entire wavelength range of the spectrophotometer, along with zero and full-scale calibrations of the strip chart recorder. Because the layer is many wavelengths thick, the chart will show rapid oscillations between maximum and minimum transmittance as a function of wavelength, with the average transmittance decreasing rapidly to zero at the short-wavelength end of the chart. It is clearly desirable to make the layer as thick as possible, in order to get rapid oscillations, but not so thick that the short-wave transmittance decreases below 20 or 30 percent of full scale.

In initial experiments the values of refractive index, n, and absorption, k, at various wavelengths were estimated by hand calculations based on the oscillation frequency, maximum and minimum values after correction for the back-surface reflection of the sample. The values obtained from this relatively crude technique turned out to be surprisingly good in predicting the behavior of multilayer stacks using the material. However, it appeared desirable to improve the method by using a computer program to reduce the data. The remainder of this paper describes the computer data reduction and the results

obtained in this way.

To start with, we assume that the optical thickness at the monitoring wavelength is known approximately, and that there is a wavelength region around the monitoring wavelength in which the index is relatively constant and in which there is negligible absorption. We have available several computer algorithms that can adjust the thickness and index of thin films to make a least-squares fit to a given transmittance or reflectance curve. These algorithms are used normally for optimization of multilayer designs, but here they are used essentially as curve-fitting devices. The spectrophotometer output in the monitoring range, corrected for back-surface reflection, is entered into the program and the algorithm solves for accurate values of n and of the physical thickness to fit the data. Experience has shown that good fits to the data can be obtained consistently in this way and we believe the values of thickness and index that are obtained are reliable. It is necessary to include, in the input data, enough values of transmittance so that the sine wave variation of transmittance is clearly delineated over part of a period including a minimum value (hence the odd number of quarter-waves). Transmittances near the curve maximum are essentially those of the bare substrate and convey no information to the program. In addition, the curve-fitting process can be expedited considerably by a proper choice of variables in the algorithm. The algorithm requires both the function (transmittance in this case) and first partial derivatives with respect to the variables. In initial experiments we used, as variables, the index and the physical thickness. It was found that the optimization program did not work well with this choice of variables and the reason is not hard to find: Over a limited range of wavelengths a small change in thickness has nearly the same effect on the transmittance curve as a small change in index. A much better choice of variables is index and phase (or optical) thickness. In this case the variables are nearly orthogonal, one varying only the amplitude and the other varying only the period of the sine wave, and the optimization process proceeds efficiently.

With the thickness determined accurately, the next step is to use the curve-fitting algorithm to determine n and k at other wavelengths. Our present efforts are aimed at making transmittance curve fits by determining single values of n and k for use in restricted wavelength ranges, or pairs of values with linear interpolation in between for longer wavelength ranges. Attempts to fit constants of Lorentzian or complex Sellmeier equations were unsuccessful because of difficulties involved in making optimization algorithms work with complex variables. Interpolation using polynomials of order higher than linear is esthetically pleasing but not suitable for cases where k may vary between small and large values. The reason is that such interpolations may result in k changing sign unexpectedly over some wavelength ranges (i.e., giving gain), which is extremely undesirable in thin film design work. Experience with the curve-fitting has shown that the linear interpolation is quite satisfactory in wavelength regions in which n and

k do not vary too rapidly over the region. Where there is rapid variation of k with wavelength, as near the absorption edge of the material, linear interpolation can be used only over very narrow wavelength ranges.

The problems that arise in using this method are as follows. First, the strip chart data must be nearly noiseless and the data transcription to numeric values must be done carefully (it is not necessary to make baseline and back-surface corrections by hand as this can be done in the program). Secondly, when n and k values at each end of a wavelength range have been computed, it would be nice to have the values of n and k agree with those calculated in an abutting wavelength range, however this will not always be the case. An additional problem that has arisen is that the transmittance is not particularly sensitive to n in regions where k is large, and small deviations in the initial conditions presented to the curve-fitting program may result in widely different final values for n, although the values for k will always be consistent.

EXAMPLE

A layer of TiO_2 was coated on a fused silica substrate. The operator was instructed to lay on 5 quarter waves at a monitoring wavelength of 633 nm. The thickness was computed from data between 590 and 650 nm. The results are as follows:

Physical thickness = 327.5 nm
Refractive index = 2.3793
Quarter wave thickness = 3117 nm

(Note this differs slightly from the assumed quarter wave thickness of 3165 nm.) The fit to the data curve was better than 1% over the entire range and better than 0.5% over most of it.

Table I shows the calculated values of n and k over several wavelength ranges:

TABLE I.

Range, nm.	wavelength	n	k
600 - 800	600	2.3781	0.
	800	2.3371	-0.0069
500-600	500	2.4490	-0.0057
	600	2.3905	-0.00072
400-500	400	2.6430	-0.0040
	500	2.4539	-0.0018
360-400	360	2.8328	-0.0197
	400	2.5648	-0.0060

CONCLUSIONS

The results given above show that the method has promise but there are also problems, particularly the need to get highly accurate spectrophotometer data. The anomalous wandering of the k values in the vicinity of zero is undoubtedly due to the fact that the calculated value will be very sensitive to the value of the transmittance maximum, and in this case could have been affected by very small errors in the baseline correction. The differences in index for the same value of wavelength calculated in different wavelength ranges is an effect of the linear interpolation and could be reduced by using shorter wavelength ranges.

Despite the relatively crude appearance of the results, this output should be quite satisfactory for most thin films design work. Above all it points out the fact that hand calculations, based only on maximum and minimum values of transmittance, are not nearly as reliable as one might be led to expect naively on the basis of equations that can be solved from these data.

OPTICAL PROPERTIES OF DOPED-SILICA WAVEGUIDE GLASSES IN THE 0.8-1.8 μm REGION

Robert Olshansky
Corning Glass Works
Corning, NY 14830

In optical quality glasses prepared by conventional melting techniques, the principal source of attenuation is absorption from transition metal impurities. To attain the very low loss required for telecommunications the transition element contamination must be kept below a few parts per billion.

The vapor phase oxidation technique[1] provides a simple and practical method for achieving these purity levels. High purity raw materials such as $SiCl_4$, $GeCl_4$, BBr_3 and $POCl_3$ are readily available and can be oxidized and deposited under controlled conditions to form glass preforms from which optical fibers can be drawn.

Once the absorbtive losses of transition metals are eliminated, these doped-SiO_2 glasses exhibit a broad transmission window encompassing the range from 0.8-1.8 μm of interest for optical communications. In the region from 0.8 to 1.2 μm, Rayleigh scattering losses from intrinsic density and concentration fluctuations of the glass matrix are the dominant loss sources. These scattering losses decrease as the fourth inverse power of wavelength. In the region between 1.2-1.8 μm losses are dominated by O-H absorption bands, Rayleigh scattering and, in the case of B_2O_3 doped waveguides, the tail of the B-O infrared vibrational absorbtion bands.

1. Rayleigh Scattering

The Rayleigh scattering of optical waveguides and of bulk samples appears to vary somewhat according to the details of sample preparation.[2] It is convenient to characterize the Rayleigh scattering by the form

$$\gamma_{RS} = a/\lambda^4. \qquad (1)$$

The lowest value reported for bulk SiO_2 is 0.63 dB/km-μm^4.[3] As shown in Fig. 1 the scattering values observed in optical waveguides vary with composition.[3-7]

As there appears to be considerable variability among the various techniques used for determining dopant concentration, it is useful to compare data from different laboratories by using Δ, the relative

difference in refractive index between the core and fused SiO_2

$$\Delta = \frac{(n_1 - n_o)}{n_1} \quad . \tag{2}$$

Fig. 1 shows that as the Δ increases (or equivalently the GeO_2 concentration) the scattering level also increases. This presumably is the result of the increase in concentration fluctuations as dopant is added.

Many of the earliest waveguides were made with a low level of B_2O_3 added to reduce the sintering temperature of the glass and to facilitate the deposition process. The scattering data of Yoshida et al[6] clearly shows that substitution of a low level of P_2O_5 for the B_2O_3 reduces the Rayleigh scattering by 40-50%. At 0.85 μm this is a significant difference, amounting to 1 dB/km.

Horiguchi and Osanai have reported[4] the lowest scattering value for any waveguide. Their waveguide doped with 2 m/o P_2O_5 had a Rayleigh scattering coefficient of 0.60 dB/km-μm^4.

Because of the large viscosity difference between glassed doped with higher P_2O_5 levels (>10 m/o) and fused SiO_2, fabrication of graded-index multimode waveguides is very difficult in the P_2O_5-SiO_2 binary system. Little work has been reported in this compositional system.

Blankenship et al[7] have reported a Δ=1.0%, P_2O_5-GeO_2-SiO_2 waveguide in which the P_2O_5 level is high enough to contribute about 50% of the index difference. The scattering coeffient of 1.0 dB/km-μm^4 is the lowest reported for a graded-index multimode waveguide.

2. Infrared Absorption Edge

All oxide glasses have very strong cation-oxygen vibrational bands in 4-25 μm region. Multiphonon excitation of these states[8] produces an absorptive tail of the form

$$\gamma_{IR} = C_{IR} \exp\ (-E/E_o) \tag{3}$$

where E is the photon energy and C_{IR} and E_o are empirically determined constants. Izawa et al[9] have measured this absorption in the 1.8 to 20 μm region using both bulk and fiber samples of SiO_2 and B_2O_3-doped SiO_2. The SiO_2 edge is well represented by the constants

$$E_o = .0235 \text{ eV}$$

$$C_{IR} = 1.19 \times 10^{13} \text{ dB/km} \cdot$$

This edge falls off rapidly with increasing energy. At 1.6 μm the intrinsic absorption of fused-SiO_2 is 0.06 dB/km.

The position of the fundamental vibrational band depends on the reduced mass of the cation-oxygen pair. Because of the low atomic mass of boron, the B-O bands and the resulting band edge are shifted to shorter wavelengths. As shown in Fig. 2 the B-O infrared absorbtion edge is apparent in any fiber doped with more than a fraction of a percent B_2O_3.

The large atomic mass of germanium is expected to shift the edge to longer wavelengths. No direct observation of this in optical waveguides has yet been reported.

The little available data[10] for the P_2O_5-SiO_2 absorption edge indicates no obvious shifts due to the presence of phosphorus.

The Rayleigh scattering and intrinsic absorption data can be combined to predict the total intrinsic losses of doped-SiO_2 waveguides[11]. For SiO_2 slightly doped with GeO_2 the minimum loss is predicted to be 0.2 dB/km at 1.55 μm (see Fig. 3). Miyashita et al[12] have reported a singlemode waveguide which attains this minimum value.

3. O-H Absorption Bands

The other important sources of attenuation which must be considered are the harmonics and sidebands of the fundamental O-H vibrational band at 2.75 μm[13,14] . As shown in Fig. 4, the first and second harmonics occur at 1.39 μm and 0.95 μm respectively. Sidebands due to simultaneous excitation of a Si-O vibrational mode and an O-H band occur at 2.25 μm and 1.25 μm.

The operating wavelength of 1.3 μm is a desirable choice for a telecommunication system because of the low intrinsic scattering losses (0.3-0.5 dB/km) and the proximity of the zero-dispersion wavelength (1.27-1.35 μm depending on the GeO_2 dopant level). As 1.3 μm is in the minimum between the 1.39 μm harmonic and the 1.25 μm sideband the OH absorbtion at 1.3 μm is usually significant. Approximately 0.7 dB/km absorbtion occur at 1.3 μm for each ppm O-H.

In P_2O_5-doped SiO_2 a very broad P-O-H absorbtion band occurs at 3.05 μm[15]. The first harmonic is a broad band centered at 1.65 μm[16]. Absorbtion from this harmonic extends beyond 1.3 μm and even in low OH content glasses the contribution at 1.3 μm can be as large as 1 dB/km if the P_2O_5 level is high[7].

Because of this P-O-H band, the very low intrinsic losses in the 1.5-1.6 μm region are more easily achieved in P_2O_5-free compositions.

4. Refractive Index Dispersion

Refractive index dispersion is of great importance for understanding waveguide bandwidth. The difference in index dispersion between the on-

axis and the cladding composition is a key parameter for determining the index profile shape required for highest information bandwidth[17]. Further discussion of this aspect of dispersion can be found elsewhere[2,22].

Refractive index dispersion is also important because of the pulse broadening it produces in proportion to the source spectral linewidth.

For a source of width $\Delta\lambda$ the pulse spreading $\Delta\tau$ is given as

$$\Delta\tau = \frac{L}{C} \Delta\lambda \left| \lambda \frac{d^2n}{d\lambda^2} \right| \qquad (3)$$

where L is the fiber length and C is the speed of light.

The refractive index of any glass possesses an inflexion point ($d^2n/d\lambda^2 = o$) somewhere between the electronic absorbtion bands and the infrared vibrational bands. At this zero-dispersion wavelength very high bandwidth can be achieved even with LED sources having linewidths as large as 50 nm.

The zero-dispersion wavelength varies with composition.

Bulk sample index measurements show that for fused SiO_2 it occurs at 1.27μm[18]. For GeO_2-doped silica it shifts to longer wavelengths, and for B_2O_3-doped silica to shorter wavelengths. This effect has been confirmed by direct measurements of delay time as a function of wavelength for GeO_2-doped fibers[19,20,21] and B_2O_3-doped fibers[19]. The zero dispersion wavelength does not shift with P_2O_5 doping[20,21].

In an analysis of all available data for GeO_2-SiO_2 glasses Adams et al[22] find that the zero dispersion wavelength increases by about 6 nm per mole % GeO_2 doping.

References

(1) For a review see P. C. Schultz, Applied Optics 18, 3684 (1979)

(2) R. Olshansky, Review of Modern Physics 51, 341 (1979

(3) J. R. Schroeder, R. Mohr, R. B. Macedo and C. J. Montrose, J. Am. Ceram. Soc. 56, 510 (1973)

(4) M. Horiguchi and M. Osanai , Electron. Lett. 12,310 (1976)

(5) W. A. Gambling, D. N. Payne, C. R. Hammond, and S. R. Norman, Proc. Inst.Electr. Eng. 123, 570 (1976)

(6) K. Yoshida, Y. Furui, S. Sentsui and T. Kuroha, Electron. Lett 13, 609 (1977)

(7) M. G. Blankenship, D. B. Keck, P. S. Levin, W. F. Love, R. Olshansky, A. Sarkar, P. C. Schultz, K. D. Sheth and R. W. Siegfried, Post-deadline Paper Topical Meeting on Optical Fiber Communications, March 6-8, 1979, Washington, D.C.

(8) For a review see T. C. McGill in Optical Properties of Highly Transparent Solids ed. by S. Mitra and B. Bendow, Plenum Press (1975)

(9) T. Izawa, N. Shibata, A. Takeda, Appl. Phys. Lett. 31, 33 (1977).

(10) S. Kobayashi, W. Shibata, S. Shibata and T. Izawa, Rev. Elect. Comm. Lab. 26, 453 (1978).

(11) M. Osanai, T. Shioda, T. Moriyama, S. Araki, M. Horiguichi, T. Izawa, M. Takata, Electron Letts 12, 549 (1976)

(12) T. Miyashita, T. Miya and M. Nakahara, Post-deadline paper Topical Conference on Optical Fiber Communication, March 6-8, 1979, Washington, D.C.

(13) D. B. Keck, R. D. Maurer and P. C. Schultz, Phys. Letts 22, 307 (1973)

(14) P. Kaiser, A. R. Tynes, H. W. Astle, A. D. Pearson, W. G. French, R. E. Jaeger and A. M. Cherin, J. Opt. Soc. Am. 63, 1141 (1973)

(15) Y. Mita, S. Matsushita, T. Yanase and H. Nomura, Electron. Tett. 13 , 55 (1977)

(16) T. Edahiro, M. Horiguchi, K. Chida and Y. Ohmori, Electron. Lett. 15, 275 (1979)

(17) R. Olshansky and D. B. Keck, Appl. Opt. 15, 483 (1976)

(18) I. H. Malitson, J. Opt. Soc. Am. 55 , 1205 (1965)

(19) L. G. Cohen and C. Lin, Appl. Opt. 16, 3137 (1977)

(20) D. N. Payne and A. H. Hartog, Electron. Lett. 13, 627 (1977)

(21) C. Lin, L. G. Cohen and V. A. Foertmayer, Electron. Lett. 14, 170 (1978)

(22) M. J. Adams, D. N. Payne, F. M. E. Sladen and A. H. Hartog, Electron Lett. 14, 703 (1978)

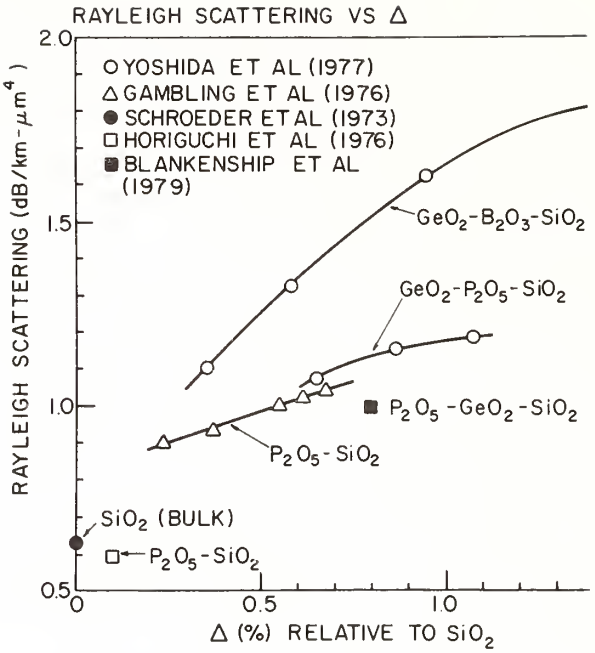

Fig. 1 Rayleigh scattering loss versus relative index difference is shown for different optical waveguide compositions.

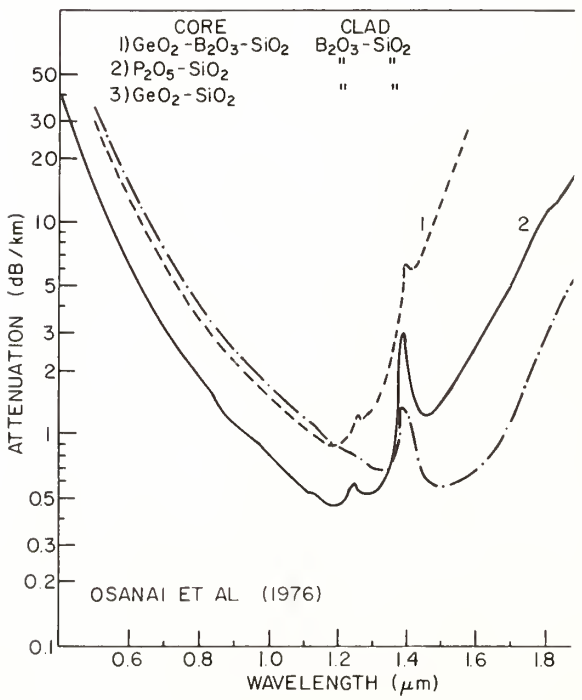

Fig. 2 Spectral attenuation for three low-loss waveguides reported by Osanai, et. al.

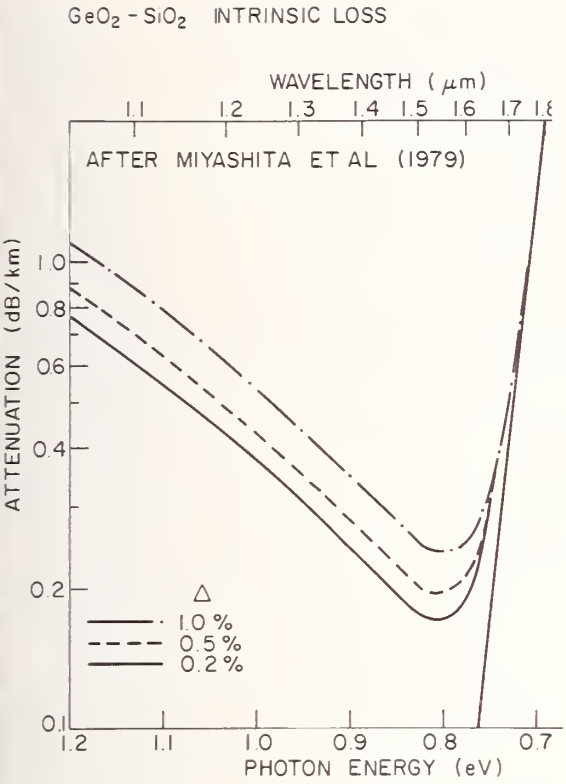

Fig. 3 Intrinsic attenuation predicted by Miyashita, et. al. for three GeO_2 - SiO_2 compositions.

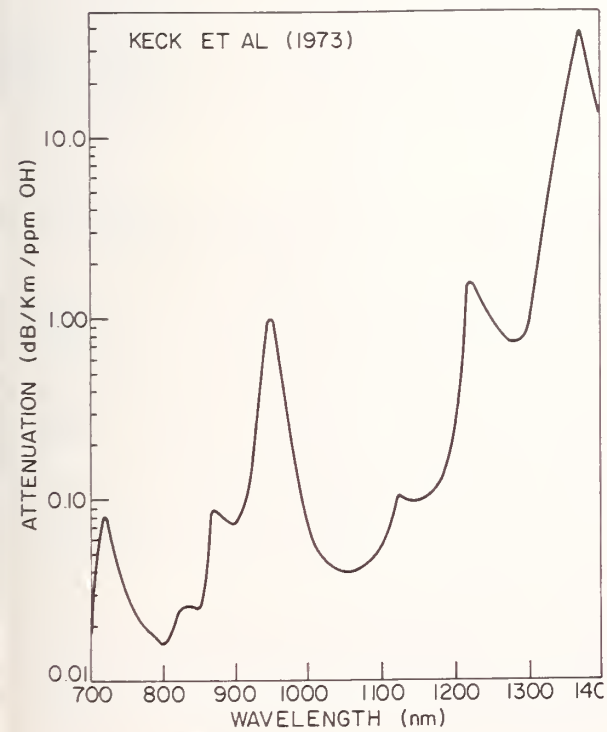

Fig. 4 Harmonics and sidebands of the hydroxyl absorption spectrum reported by Keck, et. al.

THE USE OF A SCATTERING CUBE TO CHARACTERIZE THE SPECTRAL LOSS OF OPTICAL FIBERS

Dan L. Philen and Frank T. Stone
Bell Laboratories
Norcross, Georgia 30071

In many instances, it is useful to separate the scattering loss of an optical fiber into a wavelength dependent component, Rayleigh Scattering = a/λ^4, and a wavelength independent component, b, caused by scattering mechanisms with dimensions large compared with the signal exciting wavelength. These scattering components provide important data characterizing the fiber material system and manufacturing process. When they are obtained by curve fitting total loss data versus frequency, errors are introduced because of band-edge and other forms of absorption. These errors can be eliminated by measuring only the scattering loss with a scattering cube. Using this technique with a laser source and relatively short fiber samples, it is also possible to: (1) excite different mode groups in multimode fibers, thereby determining the scattering intensity from different regions within the fiber core, and (2) obtain accurate data on single mode fibers that can be difficult to get from two-point loss measurements. For example, by careful scrutiny of the near field pattern of short (several meter) lengths of fiber and appropriate adjustment of launch conditions, a single mode can be excited even at wavelengths where the fiber supports several modes. This avoids effects due to mode cut-off, and yields useful data on the basic glass properties. Two-point loss measurements do not isolate the scattering component, and require fibers so long that mode-mixing is difficult to avoid.

The essential component to this measurement is the scattered light detector. Since the scattered light exits in all directions, this detector must surround the fiber completely to collect all the scattered radiation. Two types of detectors have been used to do this: an integrating sphere[1], and a scattering cube[2], which was used in this work. This scattering cube is constructed of 1-cm-square silicon solar cells with a 0.25mm hole drilled through the center of two opposite faces to allow the fiber to pass through the cube. One side of the cube is removable to facilitate the insertion of the fiber and allow the cube to be filled with index-matching fluid. The sensitivity and impedance of all the cells are matched as closely as possible. Final matching is accomplished by trimming potentiometers that equalize the outputs of the individual cells.

The linearity of the scattering cube at 633nm was determined by launching a He-Ne laser beam into a fiber pigtail and inserting the other end of the pigtail into the scattering cell. The input power

was varied over eight orders of magnitude using a set of calibrated neutral density filters and the cell was found to be linear over six orders of magnitude. During the experiments, the detector was always operated well within the linear region.

Since the scattering cube is composed of silicon solar cells, its sensitivity is wavelength dependent. This spectral dependence was obtained by using a He-Ne laser and a Krypton laser as sources and a Scientech calorimeter to measure the absolute optical power. The sensitivity at 633nm was measured to be 100.5 μv per μw. The relative sensitivity is given in the following figure.

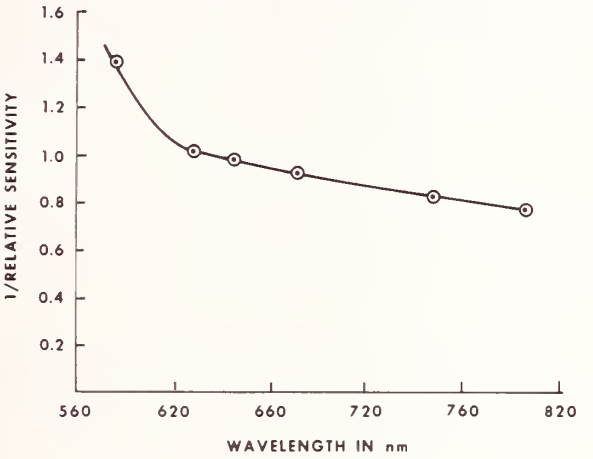

The experimental set-up is illustrated in the following figure.

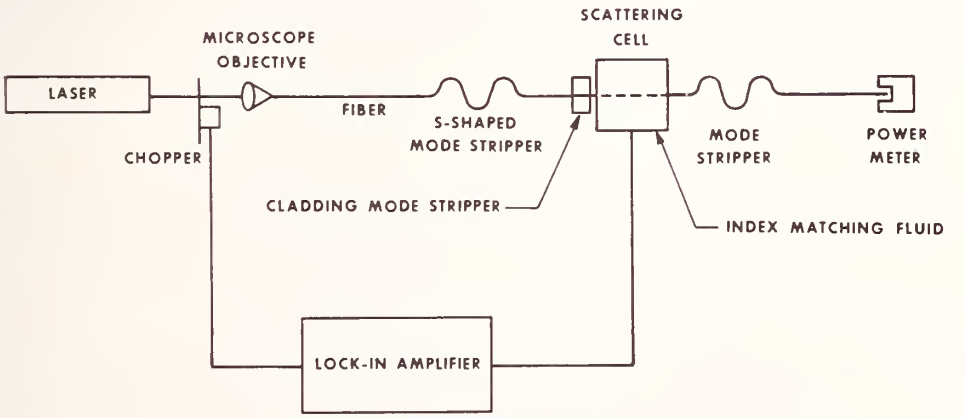

Samples of fiber a few meters in length were selected for test, stripped of their coating, cleaned to remove adhering dust particles, and threaded through the scattering cell. Bends in the fiber immediately before or after the cell were avoided. Scattering from cladding, leaky, or marginal bound modes was suppressed to a high

degree by using an S-shaped mode stripper before the scattering cube. To insure that no cladding modes had built up in the straight section of fiber between the S-shaped mode stripper and the scattering cell, an additional cladding mode stripper consisting of black paper saturated with index oil was placed 1mm in front of the scattering cube. The remaining power guided by the fiber into the scattering cube was now largely confined to the bound modes of the fiber. The scattering cube was filled with index oil to prevent any scattered light from being trapped in the cladding, and the end of the fiber was terminated in index matching fluid to prevent light reflected from the fiber end from being scattered back into the scattering cube.

The input laser light was chopped mechanically and the output of the silicon detectors was measured on a lock-in amplifier. The total light incident on the fiber was measured on a Scientech calorimeter. The scattering loss in dB/km for a particular wavelength is given by:

$$\alpha_S = \left(\frac{VD(\lambda)}{CP}\right) 4.34 \times 10^5 \text{ dB/km}$$

where V = signal from the lock-in in microvolts.
D = normalized spectral response of the scattering cube. (Fig. 1)
C = sensitivity of scattering cell = 100.5 μv/μw/cm at 633nm.
P = total incident power in microwatts.

By using several lines of the Krypton laser, the spectral dependence of the fiber scattering loss could be obtained at well-spaced wavelengths in the region from λ = 0.568 μm to λ = 0.799 μm. Since we model the scattering loss by an $\alpha_S = a/\lambda^4 + b$ relationship, a linear least squares fit to the loss data on a $1/\lambda^4$ scale gives the "a" coefficient as the slope and the "b" coefficient as the intercept. The following figure is a plot of the average scattering loss versus wavelength for a germanium-borosilicate-core, silica-clad multimode fiber that was measured many times to determine the experimental repeatability.

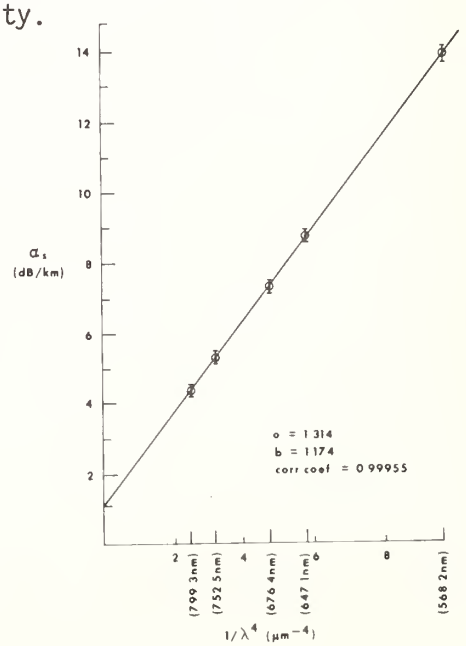

The fiber was excited using a 5x microscope objective to focus the Krypton laser beam to a spot positioned at the center of the core where maximum compositional fluctuations should occur. The repeatability was of the order of ± 1-2%, even when measurments occured several weeks apart and were taken on different 1-cm-long regions of the fiber. The correlation coefficient for the $a/\lambda^4 + b$ curve-fit was 0.9995. The "a" coefficient obtained this way was approximately 0.2 μm^4dB/km lower than the value obtained by curve-fitting to total loss data, as might be expected from the effect of band-edge absorption.

We have examined a number of other multimode and single mode fibers. The next figure gives an interesting example of a single mode fiber (borosilicate core, borosilicate inner cladding, silica outer cladding) that had high total loss.

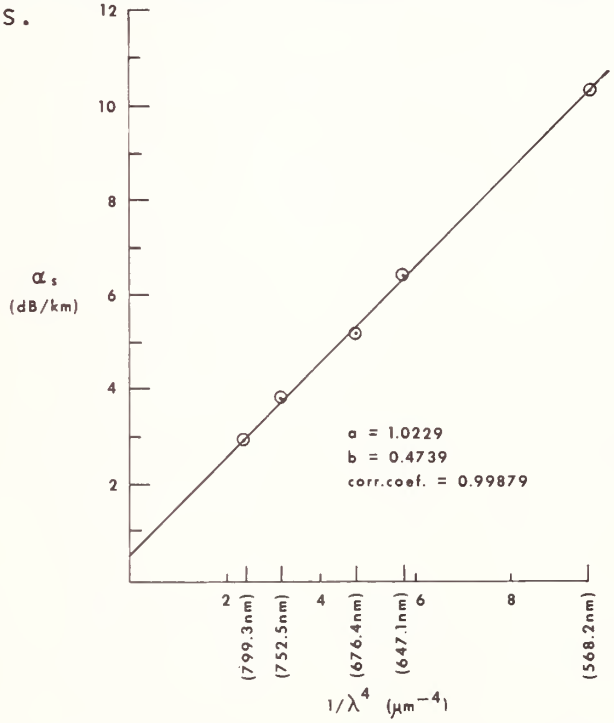

The plot of the scattering loss, however, is what is expected from a good fiber, indicating the source of the added loss is absorption. This was confirmed calorimetrically.

In summary, the direct measurment of the scattering component of the spectral loss of an optical fiber is a useful diagnostic technique. It can be used to eliminate the errors in the a and b coefficients due to absorption, and to determine whether scattering is the cause of excess fiber loss.

REFERENCES

1. D. B. Keck, P. C. Schultz, and F. Zimar, Appl. Phys. Lett. 21, 215 (1972).

2. A. R. Tynes, Appl. Opt. 9, 2706 (1970).

TRANSITION ELEMENT ABSORPTION IN MOLECULARLY-DOPED OPTICAL FIBER GLASSES

Aaron Barkatt, Dahn C. Tran* and Joseph H. Simmons

Vitreous State Laboratory
The Catholic University of America
Washington, DC 20064

The presence of transition elements in fiber optic waveguide glasses, even at trace levels, causes high absorption losses (in some cases, higher than 1dB/km for each ppb of impurity) in the wavelength range of most interest in the development of long-range communication systems (600-1300nm). Controlling the resulting absorption losses is hard because of the difficulties encountered in identifying and determining the levels of the important absorbing impurities. Chemical analysis is complicated because of the trace concentrations involved, while the absorption spectra in the region of interest often consist of broad bands and often reflect the presence of a transition element in several oxidation or coordination states. The relative amounts of different states are determined by the conditions of preparation.

It is therefore desirable to develop methods of characterizing the various species which are likely to contribute to absorption losses in the near-IR region by searching for intense, sharp, characteristic features in other spectral regions such as the visible and the UV. The molecular doping method is particularly suitable for such studies because it can be used to produce large, uniformly doped samples at relatively low temperatures ($\leq$ 850° C), where individual oxidation states can be isolated by means of controlling the atmosphere under which the doped porous preform is sintered.

Glasses prepared by this method, with a base composition of approximately 92mol% SiO_2, 4.5mol% B_2O_3, 3.5mol% Cs_2O, 0.03 mol% Na_2O and 0.03mol% K_2O, were doped with several transition elements at a level of 0.05wt% (only in the case of Ru a concentration of 0.008wt% was used). Samples doped with each of these elements were consolidated in each of three atmospheres: oxygen (oxidizing), helium (intermediate) and 5% hydrogen in nitrogen (reducing). The samples had a diameter of about 0.6cm and were 0.1-5cm long, polished at both ends. The spectra of each of the doped glass prepared under these conditions were analyzed in order to identify the important absorbing species in each case. The findings are summarized in the following Table.

Spectra of Transition Elements in Molecularly Doped High-Silica Glasses

Transition Element	Atmosphere	Spectral Features nm	Principal Chemical Species	Approximate Absorbance, 1060nm, $dBkm^{-1}ppb^{-1}$
Fe	O_2,He	375,412,437, 470	Fe(III)	0.008
	H_2	820,950	Fe(II)	3.0
Cu	O_2,He	785,1050,1080	Cu(II)	0.90
	H_2	------	Cu(I)	< 0.01
Co	O_2	778,1552	Co(III)	0.80
	He,H_2	547,600,648, 1329,2556,1750	$Co(II)_{tet}$	0.21
Ni	O_2,He	512,568,640, 1158,1500	$Ni(II)_{tet}$	1.1
	H_2	430,1125	$Ni(II)_{oct}$	0.05
Cr	O_2	435,600,750, 1000	Cr(VI)	0.13
	He	435,587,723, 1000,1850	Cr(IV)	1.4
	H_2	354,499,700, 1075,1850	Cr(III)	1.2
Mn	O_2	363,520	Mn(III)	0.27
	H_2	325,358,370, 422,435,470, 515,650	Mn(II)	< 0.006
Rh	O_2	312,470	Rh(III)	0.03
	H_2	------	Rh(III)	0.08
Ru	He	480,815	Ru(VI)	0.19
Ag	O_2,He	------	Ag(I)	< 0.005
	H_2	229,300,399	Ag_n^{n-1}	< 0.01
Zr	O_2,He,H_2	------	Zr(IV)	< 0.005

The results show that the molecular doping method is very suitable for the isolation of individual oxidation or coordination states and obtaining characteristic "fingerprints" consisting of a series of well-defined spectroscopic features in the near-IR, visible or near-UV regions. In particular, detailed band structures are evident in the cases of Fe(III), Co(II), Ni(II), Mn(II) and the various forms of Cr. Such "signatures" can serve as convenient, sensitive methods of identifying transition metal species which cause absorption losses in fiber optic glasses. Moreover, identification of the oxidation state makes it possible to try to reduce losses by changing the redox conditions of the environment during the preparation of the glasses. Of the species identified, Fe(II) and Cu(II) are of major concern because of their ubiquity and their high specific absorption in the near-IR. Fe(II) can be eliminated by oxidation, Cu(II) by reduction. Cr is a problem under all conditions. Oxidized Cr absorbs to a smaller extent than Cr doped under He or H_2/N_2 around 1060nm (by one order of magnitude), but bands in this region are still observed, probably due to the difficulty in oxidizing all traces of the lower oxidation states (Cr(III) and Cr(IV)) to Cr(VI).

The results also show that because of the presence of a relatively large concentration of the highly basic oxide Cs_2O and the low temperature of preparation these glasses provide a unique opportunity, especially when produced under an oxygen environment, of isolating and characterizing the spectra of species accessible only at unusually high basicities, such as the high oxidation states Co(III), Cr(VI) and Mn(VII) and the low coordination state $Ni(II)_{tet}$, in a high-silica matrix.

*Present address: Battelle Laboratories, Columbus, Ohio

MEASURED POCKELS COEFFICIENTS AND PREDICTED STATIC PRESSURE SENSITIVITY FOR INTERFEROMETRIC FIBER OPTIC HYDROPHONES

R. Hughes, N. Lagakos, H. Dardy and J. Bucaro
Naval Research Laboratory
Code 5133
Washington, D.C. 20375

Introduction: Optical phase modulations induced in glass fibers have been investigated[1], especially since potential use of fibers for detecting sound was established [2]. In sound detection, efforts were concentrated on describing theoretically and experimentally pressure induced effects in step index, single mode fused silica cored fibers positioned in interferometers [1]. More recently, consideration is being given to fibers with numerical apertures larger than that found in fused silica cored fibers because microbend loses are reduced [1].

Variations in optical phase induced by an externally applied sound field have been examined by several groups [2-5]. The primary causes of phase variation for an applied static pressure have been attributed to certain effects: axial strain alters the physical length of the fiber waveguide and axial and radial strains alter the refractive index of the fiber waveguide. For purposes of calculating pressure (sound) sensitivities of fiber optic hydrophones, experimental values for mechanical elasticity and Pockels coefficients are needed [5].

Predicted static pressure sensitivity of particular fiber optic hydrophones depend directly on the values of Pockels coefficients for the specific fiber used. Measurements were made on two glass specimens to determine values of their respective Pockels coefficients. Using these determined values, predictions of pressure sensitivities for the two types of fibers are presented.

Experimental Technique: Cylindrical fiber preforms including one with a fused silica core and the other with a GeO_2 doped silica core were polished on the ends normal to the symmetry axis of the preforms. The two preforms were approximately equal in diameter (7mm diameter). Both preforms were of the "w" index profile. The smaller numerical aperture (NA=0.1) preform was composed of a fused silica core with less than 0.1% GeO_2 impurity; a clad of 5% B_2O_3 + 95% SiO_2; and a substrate of the same material as the core. The other preform (NA=0.15) included a 3% GeO_2+97% SiO_2 core; 15% B_2O_3+ 85% SiO_2 clad; and a fused silica substrate.

Brillouin scattering techniques [6] were used in determining Pockels coefficient values. The preforms were immersed in parafin oil and

positioned in the focused beam of an Argon ion laser (λ=0.5145um). Light scattered at 90 degrees with respect to the incident light was analyzed with a Fabry-Perot interferometer at room temperature.

Experimental Results: Calculated values of the Pockels coefficients, P_{44} and P_{12} of the studied preforms are given in Table I. The method of calculation involves analysis of the observed Brillouin Spectra. As given in Table I, the P_{44} value of the NA=0.15 preform is approximately 2 % less than P_{44} for the NA=0.1 preform. The P_{12} coefficient for the NA=0.15 preform is smaller than P_{12} for the NA=0.1 preform by approximately 13%. The Pockels coefficients determined for the NA=0.1 preform are in close agreement with reported values [7] of Pockels coefficients for fused silica.

Calculated Fractional Phase Change: An analytical model for predicting the static pressure sensitivity for a two layered fiber has been derived previously [5]. The model assumes the fiber composite to be a right circular cylinder having a length which is much greater than its diameter. Additionally, each material in the composite is assumed to be isotropic, homogeneous and of uniform diameter. Further, the applied hydrostatic pressure is symmetric. For these considerations it was shown that for an interferometric fiber optic hydrophone the fractional phase change, $\Delta\phi/\phi$, for a change in pressure, Δp, could be expressed as:

$$\Delta\phi/\phi = (e_z - n^2/2(e_r(P_{44}+P_{12})+e_z P_{12}))\ \Delta p \qquad (1)$$

where $\phi = nkl$

The quantities in Eq. 1 include the axial strain, e_z, radial strain, e_r, wave number of the light, k, length of the fiber, l, and refractive index, n. The static pressure sensitivity for a given fiber is defined as $\Delta\phi/\Delta p$.

Calculated fractional phase changes for an applied static pressure of 1 dyne/cm^2 for the two specimens studied are given in Table II. Diameters of materials for the various layers in the fibers used in the calculations are: 1) NA=0.1: substrate 80um, clad 30um and core 4.5um; 2) NA=0.15: subtrate 80um, clad 30um and core 2.2um. The fractional phase change of the NA=0.15 fiber is approximately 1.3 times larger than that calculated for the NA=0.1 fiber. This difference is due not only to values of the Pockels coefficients but also to the elastic properties of the glasses in the fibers. The signs of the fractional phase change are negative for both specimens considered. This indicates that the optical path length of the test arm is reduced compared to that of the reference fiber.

Conclusions: Values of the Pockels coefficients P_{11} and P_{12} for single mode preforms were determined. The numerical apertures of the fibers drawn from the preforms were 0.1 and 0.15. Calculated values of the fractional phase change per unit of applied pressure show the fiber

with numerical aperture .15 has the larger sensitivity of the two specimens studied. Judiciously selected materials for the glass layers in single mode fibers could be combined to enhance pressure sensitivity in interferometric fiber optic hydrophones.

References

1. FOSS Workshop (NRL Washington, D.C.) Dec. 12-14, 1979
2. J.A. Bucaro, H.D. Dardy and E.F. Carome, JASA 62, 1302 (1977); J.H. Cole, R.L. Johnson and P.G. Buta, JASA 62, 1136 (1977)
3. P. Shajenko, J.P. Flatley and M.B. Moffett, JASA 64, 1286 (1978)
4. G.B. Hocker, Appl. Opt. 18, 1445 (1979)
5. R. Hughes and J. Jarzynski, Appl. Opt. 19, 98 (1980)
6. H.Z. Cummings, in Proceedings of the Second International Conference in Light Scattering In Solids, ed. M. Balkanski (Flammarion Sciences, Paris, 1971) p.3
7. J. Schroeder, PhD Thesis, Catholic University of America (unpublished)

TABLE I

Numerical Aperture	Core Material	Pockel's Coefficients P_{44}	P_{12}
0.1	Fused Silica (less than 0.1 % GeO_2)	$-0.0718 \pm 6\%$	$0.270 \pm 2\%$
0.15	3 % GeO_2 + 97 % SiO_2	$-.0736 \pm 6\%$	$0.236 \pm 2\%$

TABLE II

Numerical Aperture	Fractional Phase Change, $\Delta\phi/\phi$
0.1	-2.79×10^{-13}
0.15	-3.73×10^{-13}

ABSORPTION AND SCATTERING IN THIN-FILM AND BULK MATERIALS

Marshall S. Sparks
Pacific-Sierra Research Corporation
1456 Cloverfield Blvd.
Santa Monica, California 90404

The past ten years have seen great improvements in the materials used as reflectors and windows for high-power lasers. Polarizers, gratings, switches, modulators, and partially transmitting reflectors have also benefited, although indirectly, from the search for better optical materials. This review discusses optical attenuation, absorptance, and scattering, considering transparent materials, reflectors, thin films (coatings), and fibers, in the infrared, ultraviolet, and visible regions.

Bulk attenuation, represented by the extinction coefficient β_e, is the exponential decay constant in the Beer law $I = I_0 \exp(-\beta_e z)$, where I_0 is the irradiance at $z = 0$ and I the irradiance at z. It is the sum of absorption and scattering ($\beta_e = \beta_a + \beta_s$). Absorption is of prime importance here because it produces heat, which can limit an optical material's application.

In a transparent material there is also optical attenuation at the surface due to surface absorptance and surface scattering. Total absorptance is determined by bulk absorption $\beta_e \equiv \beta$, surface absorptance A_s, and sample thickness ℓ.

The lowest measurable absorptance obtained by using transmission methods is 0.01. Absorption is now measured directly by calorimetry, emissivity, and photoacoustics; attenuation less than 0.01 is measured by modulation spectroscopy and attenuated-total-internal reflection. The absorption coefficient can be measured from 10^5 or 10^6 cm^{-1}--at absorption peaks--to as low as 0.5 dB/km for optical fiber materials or $\sim 10^{-5}$ cm^{-1} for window materials.*

The required absorptance and absorption coefficient varies with the application, but values much less than 10^{-4} would be useful in high-power studies, spectrometry, and fiber optics. Optical material β's have been reduced from 10^{-2} cm^{-1} to near the current measurable limit of $\sim 10^{-5}$ to 10^{-6} cm^{-1}. Measured values far below 10^{-4} are still suspect, however, and maintaining such low values has not been proved feasible. Temple [1], Hass [2], Harrington and coworkers [3], and Deutsch [4] have measured bulk and surface absorptance separately.

*1 dB/km = 2.3 x 10^{-6} cm^{-1}.

Intrinsic attenuation mechanisms include absorption-multiphonon, multiphoton, direct one-phonon (across the bandgap), or by thermal-equilibrium concentration of vacancies; and scattering--Brillouin, or by random molecular structure in glassy or amorphous material. Extrinsic attenuation comprises absorption by molecular ions (on surfaces or within materials), electron absorption by impurity ions, and absorption by microscopic inclusion.

Intrinsic limits establish the maximum obtainable absorption. Knowing that, neither of the following material-improvement plans could possibly decrease absorptance: reducing the 10.6-μm absorption coefficient of potassium chloride below its current minimum ($\sim 10^{-4}$ cm^{-1})--because it is already at the intrinsic limit; or obtaining 1 percent absorptance in a metal at 250 nm--because it is unlikely that a metal with a lower intrinsic absorptance than aluminum (20 percent at 250 nm [5]) will be found.

For frequency ω greater than several times the fundamental reststrahlen frequency ω_f, β decreases nearly exponentially as ω increases. For alkali halides at room temperature, the coefficient varies smoothly with frequency. The exponential frequency dependence of β was first observed by Rupprecht [6], who suggested it resulted from multiphonon absorption. Horrigan and Deutsch [7] studied the effect in detail; Sparks [8] rediscovered its theoretical multiphonon source.

The temperature dependence of β is considerably weaker than the T^{n-1} predicted [9,10]. Sparks and Sham [11] obtained good agreement between theory and experiment by including the temperature dependence of the other parameters in the calculation of the absorptance dependence. Multiphonon absorption is now considered to explain the exponential frequency dependence of the absorption coefficient.

The highly transparent region of optical materials is bounded by vibrational (phonon) absorption at low frequencies and electron absorption at high frequencies. Electron promotion from a valence band to the conduction band, which often produces an exciton, is primarily responsible for the high-frequency absorption edge. In this region (the Urbach), β increases steeply and exponentially with frequency. Extrapolating the two boundary exponents would yield an intersection at a value of β typically below 10^{-50} cm^{-1}. At frequencies where the intrinsic β is less than, say, 10^{-2} to 10^{-6} cm^{-1}, extrinsic mechanisms determine the absorption coefficient.

Extrinsic absorption mechanisms include point imperfections (e.g., impurities such as molecules in anion sites); extended imperfections (e.g., voids, inclusions, dislocations); electrical carrier absorption (e.g., interband transitions of holes or electrons); and surface effects (e.g., contamination).

Extrinsic absorption due to molecular ions [12] is exemplified by NO_2^-, HCO_3, SO_4^{2-}, and CrO_4^{2-}, which substitute for the halide ions in alkali-halide crystals, vibrating relatively freely of the host/ion environment. Matrix-isolation spectroscopy reveals that a typical impurity absorbed in the infrared region has a large cross section at resonance of $\sigma \simeq 10^{-17}$ cm^2. Thus, $\beta = 10^{-4}$ cm^{-1} is obtained from an impurity concentration $N = \beta/\sigma = 10^{13}$ cm^{-3} (a few parts per billion).

Impurity ions or molecules on a sample surface give rise to absorptances of 0.1 percent per surface [13]. Such large effects follow from an order-of-magnitude argument. For a surface layer 0.5 nm thick having $\beta = 10^5$ cm^{-1} at resonance, the absorptance is $\beta\ell \simeq 5 \times 10^{-3}$, or 0.5 percent absorption per surface. Ions that absorb as a result of electron transitions have absorption bands spanning wide frequencies in the visible and ultraviolet regions, with large cross sections $\sigma = \beta/N$ of $\sigma \simeq 10^{-17}$ cm^2. Only a few parts per billion of strongly absorbing ions can thus yield $\beta \simeq 10^{-4}$ cm^{-1} (the infrared absorption lines are generally more strongly peaked than the visible and ultraviolet).

Isolated-region absorption is the best understood type of absorption (surface or bulk) for transparent materials. The phenomenon has been studied experimentally by Boling and Dubé [14], theoretically by Hopper and Uhlmann [15] and also by Sparks and Duthler [16], who found that volume fractions of strongly absorbing inclusions as low as 10^{-8} yield $\beta = 10^{-4}$ cm^{-1}. The frequency and temperature dependence of the absorption depends strongly on the type of inclusion (strong or weak absorber, metal or dielectric, large or small).

A local increase in absorption can cause fracture, vaporization, melting, or other material failure. Damage almost always occurs in small regions in the laser beam, rather than being uniform across the beam. Such damage is known to occur from polishing compounds embedded in the surface of materials. Other possible sources include polishing-compound inclusions, thermally isolated flakes on metallic surfaces, clusters of microscopic inclusions, scratches, Bloembergen field enhancement, surface contamination, or airborne particles that burn near the surface.

Obtaining low optical attenuation in thin films and optical fibers entails difficulties. The extinction coefficient of both is limited to an optical value much greater than for corresponding bulk materials. When material is deposited as a thin film, its absorption coefficient is almost always three to six orders of magnitude greater than that of the same material in bulk [17]. The reason is not clear, but the most likely cause is contamination--which could occur at the interfaces, in the pores or bulk of the film, or on the surface of the coating. It could occur during deposition--e.g., from residual gas; after deposition--e.g., by surface absorption or by absorption into the

pores; or before deposition--e.g., from substrate or material contamination.

Water is the most important of many contaminates in the 2-to-5 μm wavelength region. Donovan [18] has verified that water accounted for most of a 10-order-of-magnitude increase in the absorptance of thin films of sodium fluoride. At 10.6 μm, only two molecular layers of water (a packing density of 99.95 percent) will give an absorptance of 10^{-4}. Even if films are deposited water-free, water is absorbed by the film pores shortly after removal from the deposition chamber.

Sparks [17] has suggested that a working ultrapurification deposition process would greatly improve all types of optical coatings over all wavelength regions. Though it is unlikely that all sources of extra absorptance could be eliminated, ultrapurification deposition processes have had some success.

Protective coatings are required to prevent degradation by water, other contaminants, and hostile environments. Glassy arsenic-trisulfide films thicker than the maximum diameter of scratches on the surface of the material to be protected have been found to protect sodium chloride from water vapor [19] (the edges would have to be protected for long exposures).

Plasma-polymerized polymers have successfully protected alkali halides from water vapor, despite the fact that the thin, unsupported, pin-hole-free films of polymers transmit much more water vapor than would destroy the halides. Flannery and Sparks [20] explain that plasma deposited by the polymer formed a protective coating on the surface of the sodium chloride.

An otherwise adequate coating may nevertheless have excesssive absorptance. That of most polymers exceeds 10^{-4}, even for extremely thin coatings. However, Braunstein [21] measured $\beta = 4$ to 7 cm^{-1} at 10.6 μm for polyethane films that were plasma-deposited by Shen [22], and the lowest measured 10.6 μm absorptance of thin-film arsenic trisulfide is 0.8 cm^{-1}. Thus, 0.5 μm films of those materials would have absorptances of 2×10^{-4} to 4×10^{-4} and 4×10^{-5}, respectively.

Scattering as a function of surface roughness of metallic reflectors has been studied extensively [23]. In crystalline fibers, it is one of the most likely sources of attenuation, the lowest measured value being 100 dB/km. A lower bound in transparent materials is established by Brillouin scattering. In glassy materials, total scattering is typically 20 times the Brillouin value. It is theoretically possible to approach the Brillouin limit in crystals. However, any of four or five extrinsic mechanisms could cause excessive scattering.

Of the nonlinear and parametric absorption processes, we now appear to have a viable theory of electron-avalanche breakdown [24]. Multiphoton absorption is clear in principle, but multiphoton rates still cannot be calculated accurately for most solids because the energy bands are not well understood. By assuming they are spherically symmetrical and that the oscillator strengths have reasonable values, surprisingly good agreement (within a factor of 2) between experimental and theoretical two-photon cross sections can be obtained [25]. Estimates of higher orders are scant and become more unreliable as the order increases.

REFERENCES

1. P. Temple, this volume.
2. M. Hass et al., "Infrared Absorption in Low-Loss KCl Single Crystals Near 10.6 μm," J. Appl. Phys. 45, September 1974.
3. J. A. Harrington, D. L. Bobbs, and M. Braunstein, Ninth Annual Damage Symposium on Optical Materials for High-Power Lasers, Boulder, Colorado, 4 October 1977 (NBS Spec. Publ. 509).
4. T. Deutsch, "Lattice Absorption in Zinc Sulphide," Proc. of Internat. Conf. on the Physics of Semiconductors, held at Exeter, July 1962; published by the Institute of Physics and the Physical Society, 1962.
5. M. Sparks, "High-Power Ultraviolet Materials and Components," invited paper, Tenth Annual Damage Symposium on Optical Materials for High-Power Lasers, Boulder, Colorado, 12-14 September 1978.
6. G. Rupprecht, Phys. Rev. Lett. 12, 508 (1964).
7. F. A. Horrigan and T. F. Deutsch, "Research in Optical Materials and Structures for High-Power Lasers," Raytheon Research Division, Final Technical Report, Contract DAAH01-70-C-1251, 1971.
8. M. Sparks, National Materials Advisory Board Ad Hoc Committee Meeting, March 1, 1971; "Theoretical Studies of High-Power Infrared Window Materials," Xonics, Inc. Quarterly Technical Progress Report No. 1, Contract DAHC15-72-0129, March 1972.
9. J. A. Harrington and M. Hass, Phys. Rev. Lett. 31, 710 (1973).
10. A. J. Barker, J. Phys. C 5, 2276 (1972).
11. M. Sparks and L. J. Sham, "Theory of Multiphoton Absorption in Insulating Crystals," Phys. Rev. B 8, 3037 (1973).
12. C. J. Duthler, "Extrinsic Absorption in 10.6 μm Laser Window Materials Due to Molecular-Ion Impurities," J. Appl. Phys. 45, 2668 (1974).
13. T. F. Deutsch and R. I. Rudko, "Research in Optical Materials and Structures for High-Power Lasers", Raytheon Research Division, Final Technical Report, Contract DAAH01-72-0194, January 1973.
14. N. L. Boling and G. Dubé, Appl. Phys. Lett.
15. R. W. Hopper and D. R. Uhlmann, J. Appl. Phys. 41, 4023 (1970).
16. M. Sparks and C. J. Duthler, "Theory of Infrared Absorption and Material Failure in Crystals Containing Inclusions," J. Appl. Phys. 44, 3038 (1973).

17. M. Sparks, "Materials for High-Power Window and Mirror Coatings and Multilayer-Dielectric Reflectors," Eighth NBS-ASTM-ONR-ERDA-DARPA Symposium on Laser Induced Damage in Optical Materials, Boulder, Colorado, 13-15 July 1976 (NBS Spec. Publ. 462).
18. T. Donovan, this volume.
19. P. A. Young, Thin Solid Films 6, 423 (1970).
20. M. Flannery and M. Sparks, in [17].
21. M. Braunstein, private communication to M. Shen, 1978.
22. M. Shen, Eighth NBS-ASTM-ONR-ERDA-DARPA Symposium on Laser Induced Damage in Optical Materials, Boulder, Colorado, 13-15 July 1976 (NBS Spec. Publ. 462).
23. H. E. Bennett, "Validity of the Drude Theory for Ag, Au, and Al in the Infrared," Optical Properties and Electronic Structure of Metals and Alloys, edited by F. Abeles, Amsterdam, 1966.
24. M. Sparks et al., "Theory of Electron-Avalanche Breakdown in Solids," 1979 Symposium on Optical Materials for High-Power Lasers, Boulder, Colorado, 30-31 October 1979 (NBS Spec. Publ.).
25. M. Sparks, "Nonlinear Absorption in Optical Materials," in Physics of Transmissive Optical Materials, edited by Marvin Hass, to be published by Springer Verlag.

THE MEASUREMENT OF INTERFACE AND BULK ABSORPTION IN THIN FILMS AND BARE SUBSTRATES

P. A. Temple
Michelson Laboratory, Physics Division
Naval Weapons Center, China Lake, California 93555

Introduction

In recent years, with the availability of large cw infrared lasers, there has been much interest in the problem of optical absorption in highly transparent materials. Early effort was aimed at determining and then lowering the bulk absorption in available optical materials. However, as purer materials were developed, it became clear that absorption at the two surfaces, which was introduced by the required polishing and grinding, frequently dominated the bulk absorption of the optic. Additionally, many of the optical components of a low absorption system require thin-film coatings. These coatings serve as environmentally protective coatings, as antireflection or partially reflecting coatings, or, finally, as highly reflecting coatings for either enhanced metal mirrors or dielectric mirrors. In many cases the absorption introduced by the coating is larger than the optic's bulk absorption. The lowering of this surface and thin-film absorption remains a challenge to the optics industry.

This paper is concerned primarily with the measurement of the absorption which takes place at bare surfaces or, for coated optics, the absorption which takes place within the various coating layers and the interfaces between those layers. Ideally, for bare surfaces, one would like to measure the absorption at the surface for all wavelengths of interest, and in a manner which separates the surface contribution from the bulk contribution. For coated optics, we wish to measure the bulk absorption coefficient, α_i, of the i^{th} film of a stack and the interfacial specific absorptance, a_{ij}, between the i^{th} and j^{th} layers, again for all wavelengths of interest. By determining these quantities, we hope to proceed in an orderly fashion to construct an understanding of the causes and cures for the high absorptance of bare surfaces and thin-film coatings.

Absorptance Measurement Techniques

The bulk of coated windows and mirrors designed for use at one of the laser wavelengths in the 1- to 10-μm range which we have looked at over the last two years at the Naval Weapons Center (NWC) have exhibited absorptances, that is (total absorbed power)/(incident power), of from 2×10^{-3} to 2×10^{-4}. An exception to this has been very carefully

polished and cleaned fused silica, which exhibits, at 1.06 μm, an absorptance of $\sim 2 \times 10^{-5}$. This includes contributions from both surfaces and one-quarter inch of bulk material. The measurement of such low absorptance requires substantial effort.

Several techniques have been developed to measure absorptances as low as those listed above. Two excellent review articles, one by Skolnik [1] published four years ago, and a later one by Hordvik [2] published two years ago, discuss the state of the art in absorptance measurement as of that time. Since that time some of these techniques have been refined or supplemented. Harrington et al. [3] reported on a wavelength modulation scheme which, when calibrated with laser calorimetric data, yielded spectral absorptance data in the 10^{-5} range. A particularly simple technique, that of photoacoustic spectroscopy (PAS) [4-6], has also been used in conjunction with laser calorimetry. The strength of the PAS signal is proportional to the absorptance of the sample but is not directly calibrated. This problem can be overcome by measuring identical samples calorimetrically [7] or by electrical calibration [8]. If this calibration is performed, PAS offers the potential of very rapid evaluation of similar samples. In addition, the PAS response is sufficiently great that a high intensity lamp and monochromator may be used as a source, allowing spectral absorptance measurements to be made. PAS also has the potential of separating surface and bulk contributions [7-10], although this feature has not been extensively exploited as yet. Recently, Farrow [11] described a Fourier-transform PAS technique which improves the signal-to-noise ratio of the PAS signal and also allows rapid data collection. A fundamentally different absorption measurement technique has been reported by Seitel et al. [12] wherein the absorptance of a metal surface is determined by noting the elongation of a long, thin sample due to heating by laser irradiation. Unlike the other techniques, this method uses pulsed laser radiation and is a technique for learning absorptive properties of a surface under dynamic conditions.

In spite of the advantages of the various systems discussed above, there are probably more laser calorimeters in operation at this time than all other instruments combined. In laser calorimetry, the absorptance of a sample is determined by measuring the temperature rise of the sample caused by a timed laser radiation of known power [1]. The reasons for the popularity of laser calorimetry are its mechanical simplicity, reasonable sample turn-around time, and adaptability to various sample sizes. Laser calorimetry is potentially capable of yielding absolute absorptance values and can be electrically calibrated. Finally, not to be discounted is the fact that laser calorimetry is essentially a prototype setup where one measures the actual temperature rise of a sample under actual laser irradiation of the exact same wavelength which will be used in the full size system. It is just this temperature rise which worries the system designer and which has prompted so much activity in the area of absorptance measurement.

Surface Versus Bulk Absorption

Two calorimetric techniques have been employed to differentiate surface absorption from bulk absorption in uncoated samples. In the first [13], the absorptance of rods of various lengths are compared, with the shorter rods showing lower absorptance due to the decreased path length. When a plot of the absorptance data versus sample length is made, the slope of the data is the bulk absorption coefficient, and the extrapolated zero-thickness absorptance is the contribution made by the two surfaces. The problem with this straightforward technique lies in the difficulty of obtaining uniform and repeatable surface absorptance from the various samples.

The second technique, which also uses a long, rod-shaped sample [14], uses the fact that heat generated at the rod's ends must travel half the length of the rod to reach a centrally located temperature sensor while heat generated in the center of the rod by bulk absorption will reach the sensor almost immediately. By analyzing this "prompt" signal, one can determine the bulk absorption coefficient of the rod, while the delayed signal indicates the magnitude of the surface absorption present. This latter technique has also been used to measure the absorption of surfaces coated with thin films to determine the change of absorptance caused by the film [15].

The most common way of measuring coating absorptance is to measure the absorptance of the bare substrate, and then measure its absorptance again after coating. By comparing the two measurements, one can determine the absorptance of the thin-film coating. It is recognized, however, that the increased absorption of the filmed substrate is due not only to absorption in the bulk of the film, but also to absorption in the newly introduced film-substrate interface and the film-air interface. It is not possible to distinguish among these three sources of absorption by any of the measurements discussed above. The remainder of this paper will be concerned with the technique we have been using at NWC to determine these three quantities.

Standing Waves and Optical Absorption

The absorptance of a filmed or unfilmed sample of thickness L under normal incidence radiation is given by the general expression

$$A = \int_0^L p(x)\alpha(x)dx \quad , \tag{1}$$

where $\alpha(x)$ is the absorption coefficient at x, and $p(x) = n(x)|E^2(x)|/n_o|E_o^2|$ is the time averaged relative energy density at position x. $|E_o^2|$ is the time average of the square of the incident electric field external to the sample, and n(x) is the index of refraction of the material at position x.

In the absence of reflections caused by index discontinuities, p(x) is constant, and each portion of a sample contributes to the absorptance in direct proportion to the absorption coefficient at that location. In the usual case, however, there are index discontinuities which cause a portion of the incident light beam to be reflected. This reflected beam combines coherently with the incident beam, resulting in a spatially modulated relative energy density, p(x). It is this varying p(x) which weights regions of the sample to contribute proportionately more or less to the total absorption of the sample. By proper construction of a sample, it is possible to accentuate the contribution of one portion of a sample over another portion and thus enhance that portion's contribution to the absorptance.

At NWC we have been using wedge-shaped single-layer films on uniform substrates to produce samples whose absorptance can be measured at several film thicknesses [16,17]. A portion of the coated surface is left bare to allow the uncoated substrate absorptance to be measured. The adiabatic calorimeter [18] used to make these measurements allows absorptance measurements to be made at any point along a selected diameter. Each film thickness selected on the wedge produces a unique relative energy density at the film-substrate interface, within the film, and at the film-air interface.

We characterize the absorptance at the air-film interface by a specific absorptance $a_{af} = \alpha_{af}\Delta_{af}$, where the air-film interface is a sheet of thickness Δ_{af} with absorption coefficient α_{af}. Similarly, the film-substrate interface is characterized by $a_{fs} = \Delta_{fs}\alpha_{fs}$. We assume that the bulk absorption coefficient of the film, α_f, is constant throughout the remaining thickness of the film. Under these conditions, the filmed-substrate absorptance [using Eq. (1)] becomes

$$A = p_{af}a_{af} + \bar{p}_f\alpha_f\ell_f + p_{fs}a_{fs} + (T_1/T_o)A_o \quad , \qquad (2)$$

where $\bar{p}_f$ is the spatially averaged relative power density within the film, T_1 is the first surface transmittance with the film in place, T_o is the unfilmed-substrate first-surface transmittance, and A_o is the unfilmed-substrate absorptance. The physical thickness of the film is ℓ_f. $\bar{p}_f$, as well as p_{af} and p_{fs} (the relative power densities at the air-film and film-substrate interfaces), are calculable from boundary value considerations. The first three terms in Eq. (2) are the contributions to the absorptance made by the film bulk and its two interfaces, and the last term is the substrate contribution.

The four quantities p_{af}, $\bar{p}_f$, p_{fs}, and T_1 are dependent on the film thickness. By choosing appropriate film thicknesses, a set of independent equations can be generated from Eq. (2). Then, in principle, four measurements of absorptance are required to determine the four quantities a_{af}, a_{fs}, α_f, and A_o. The four measurements we generally make on a wedge sample are at the bare substrate (which determines A_o) and at film thicknesses of 1/4λ, 1/2λ, and 3/4λ optical thickness. Further measurements at λ, 5/4λ, ... are redundant and serve to improve the quality of the data.

Figure 1 shows previously published data [17] from a As_2Se_3 film on CaF_2 measured on the bare substrate and at 1/4λ, 1/2λ, 3/4λ, and λ optical thicknesses at 2.72 and 2.87 μm. The slopes of the two solid lines determine α_f. These data, when analyzed using Eq. (2), indicate that most of the observed absorption can be attributed to water at the film-substrate interface, and very little to the film itself or to the air-film interface. We have found, in fact, that quite frequently a substantial portion of the observed absorption takes place at the first film-substrate interface. The existence of hydrogen at this interface has been verified by a completely independent, nuclear resonance technique [19]. If one assumes that the presence of hydrogen indicates the presence of water, there is very good agreement between the calorimetric data and the nuclear data.

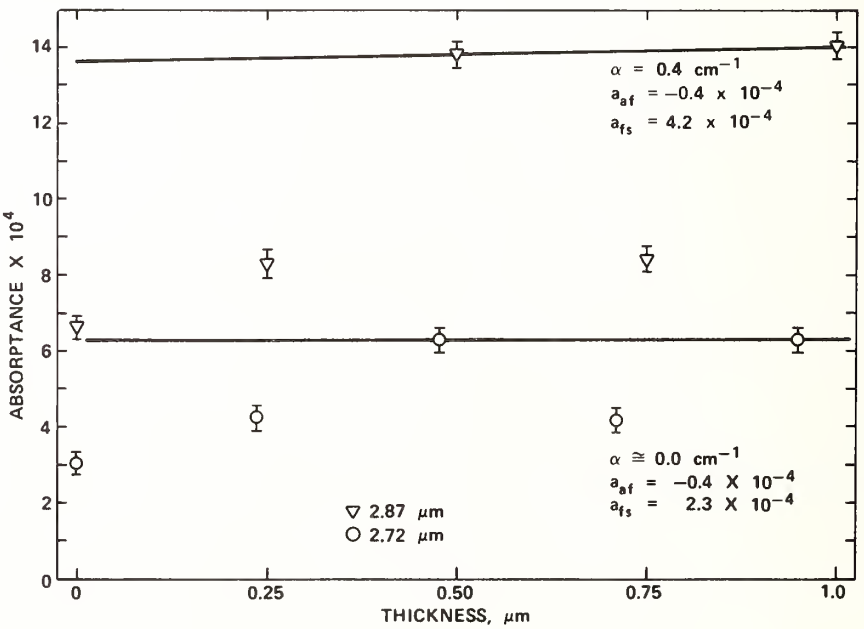

Figure 1. The absorptance of an As_2Se_3 film on CaF_2 measured at 0, 1/4, 1/2, 3/4, and 1λ optical thicknesses at two laser wavelengths. A film of 1/2λ optical thickness is ~ 0.5-μm thick.

As of this time we have looked only at single-layer films at the HF/DF laser wavelengths (2.7 to 2.9 μm and 3.8 to 4.0 μm). We have used single-line wavelengths in the 2.7 to 2.9 μm band to verify the presence of water. Ideally, one would like to extend this technique to the case of two films to measure the absorption present at the film-film interface. In addition, there is evidence that the single-layer film properties are not always representative of that materials behavior in a complicated stack. In particular, hygroscopic materials such as ThF_4 show the presence of substantial amounts of water when measured in single-layer form, while these same films do not contain nearly as much water when sealed by an overlayer of such materials as ZnS. It is hoped that through techniques such as the wedged-film method we can learn enough about the absorptive properties of thin films and their interfaces to make use of the method developed by Bennett and Burge [20,21] for calculating the expected absorptance of both highly reflective and antireflective multilayer stacks from the explicit knowledge of the individual interface and bulk properties of all films in the stack. We would like to point out, as a concluding remark, that while we have used calorimetry to make these measurements, Eqs. (1) and (2) apply in general. Another technique, such as PAS, might be used as an absorptance measurement technique just as well as, and possibly even better than, laser calorimetry.

Conclusion

In this paper we have discussed some of the more recent advances in the measurement of absorption in optical materials. We have put particular emphasis on the problem of measuring the separate contributions of the film interfaces and the film bulk to the overall absorption of a coated sample. The measurement technique developed at NWC, a scheme which uses a wedged-film sample for calorimetric measurement, has shown that, at least in many cases, there is substantial absorption at the first film-substrate interface. We conclude the paper by indicating that this wedged-film technique may be adaptable to two-layer film stacks.

References

[1] L. Skolnik, in *Optical Properties of Highly Transparent Solids*, S. S. Mitra and B. Bendow, Eds. (Plenum, New York, 1975), p. 405.
[2] A. Hordvik, Appl. Opt. 16, 2827 (1977).
[3] J. H. Harrington, B. L. Bobbs, M. Braunstein, R. K. Kim, R. Stearns, and R. Braunstein, Appl. Opt. 17, 1541 (1978).
[4] L. K. Kreuzer, J. Appl. Phys. 42, 2934 (1971).
[5] A. Rosencwaig, Opt. Commun. 7, 305 (1973).
[6] E. L. Kerr, Appl. Opt. 12, 2520 (1973).
[7] A. Hordvik and L. Skolnik, Appl. Opt. 16, 2919 (1977).
[8] J. M. McDavid, K. L. Lee, S. S. Yee, and M. A. Afromowitz, J. Appl. Phys. 49, 6112 (1978).

[9] A. Hordvik, J. Opt. Soc. Am. 66, 1105 (1976).
[10] H. S. Bennett and R. A. Forman, in *Digest of Topical Meeting on Optical Phenomena in Infrared Materials* (Optical Society of America, Washington, DC, 1976).
[11] M. M. Farrow, R. K. Burnham, and E. M. Eyring, Appl. Phys. Lett. 33, 735 (1978).
[12] S. C. Seitel, J. O. Porteus, and W. N. Faith, "Optical Coupling Coefficients for Pulsed CO_2 Laser Radiation on Bare and Painted Aluminum Surfaces," this conference.
[13] T. F. Deutsch, J. Electron. Mater. 4, 663 (1975).
[14] M. Hass, James W. Davisson, Herbert B. Rosenstock, and Julius Babiskin, Appl. Opt. 14, 1128 (1975).
[15] J. A. Harrington, M. Braunstein, and J. E. Rudisill, Appl. Opt. 16, 2893 (1977).
[16] P. A. Temple, D. L. Decker, T. M. Donovan, and J. W. Bethke, NBS Spec. Publ. 541, 37 (1978).
[17] P. A. Temple, Appl. Phys. Lett. 34, 677 (1979).
[18] D. L. Decker and P. A. Temple, NBS Spec. Publ. 509, 281 (1977).
[19] T. M. Donovan, P. A. Temple, Shiu-Chin Wu, and T. A. Tombrello, "The Relative Importance of Interface and Volume Absorption by Water in Evaporated Films," 11th Annual Symposium on Optical Materials for High Power Lasers, Boulder, Colo., 1979 (to be published).
[20] H. E. Bennett and D. K. Burge, NBS Spec. Publ. 541, 266 (1978).
[21] H. E. Bennett and D. K. Burge, "Simple Expressions for Predicting the Effect of Volume and Interface Absorption and of Scattering in High Reflectance or Antireflectance Multilayer Coatings," to be published in J. Opt. Soc. Am. (March 1980).

Added Note: The author is grateful to Dr. A. Feldman for bringing to his attention the recent work of Tam and Patel [22] and its potential usefulness in the measurement of absorption in optical materials. In this technique, called optoacoustic (OA) spectroscopy, a pulsed laser impinges on a sample to which is attached a piezoelectric transducer. The transient acoustic signal is detected by a gated signal processor. When properly gated, this technique has the important advantage over the normal PAS scheme of rejecting the detector's spurious response to scattered light. Such scatter now limits the sensitivity of PAS to absorptances of $\sim 1 \times 10^{-4}$.

[22] C. A. Tam and C.K.N. Patel, Appl. Phys. Lett. 35, 843 (1979).

INFRARED OPTICAL PROPERTIES OF SILICON MONOXIDE FILMS: APPLICATION TO RADIATIVE COOLING

A. Hjortsberg and C.G. Granqvist
Physics Department, Chalmers University of Technology, S-412 96 Gothenburg, Sweden

Radiative cooling during clear weather occurs since the atmosphere can be sufficiently transparent for wavelengths $8 \lesssim \lambda \lesssim 13$ μm that radiative losses in this range are not balanced by reradiation from the sky. A blackbody may reach a temperature which lies 10 to 15°C below that of the ambient because of this effect, while temperature differences as large as 40°C are possible with a *selective* infrared radiator, whose spectral emittance matches the atmospheric transmittance. Previously suggested selectively emitting surfaces have used plastic films bonded to aluminium [1-3]. Below we report on a more efficient approach, whose basis is a determination of the infrared optical properties of silicon monoxide from a novel technique. These data lead us to predict that SiO films on a metallic substrate can give the spectral profile demanded for efficient radiative cooling. This result is verified by measurements.

The optical constant n and k of SiO films were determined from transmittance and reflectance recordings with double beam spectrophotometry in the range 2.5 to 40 μm. Initially, only results from SiO films vacuum evaporated onto infrared transparent KRS-5 (thallium bromide-iodide) plates were used. It was found that only k could be accurately determined, whereas experimental uncertainties affected n to an unacceptable extent. This result is indeed expected, since curves for constant reflectance and transmittance drawn in the n-k plane show branch points in the pertinent intervals for n and k [4]. However, accurate values of n could be obtained by using the additional information from reflectance spectra of SiO films on Al-coated smooth glass plates. Transmittance measurements on films on transparent substrates combined with reflectance measurements on films on highly reflecting substrates in fact make a powerful new technique for determination of infrared optical properties of absorbing films [5].

The solid curves in Figure 1 show our results for $\varepsilon_1 \equiv n^2-k^2$ and $\varepsilon_2 \equiv 2nk$. A strong absorptance peak at $\lambda \sim 10$ μm is noteworthy. For $\lambda < 14$ μm, these data agree rather well with an earlier evaluation [6]. The internal consistency in the results for ε_1 and ε_2 was tested by using the Kramers-Kronig relation to calculate ε_1 from the experimentally determined values of ε_2 (properly extended towards small wavenumbers; cf. the dotted line at the bottom of Figure 1). The circles in the upper part of Figure 1 show good correspondence with the experimentally determined result for ε_1.

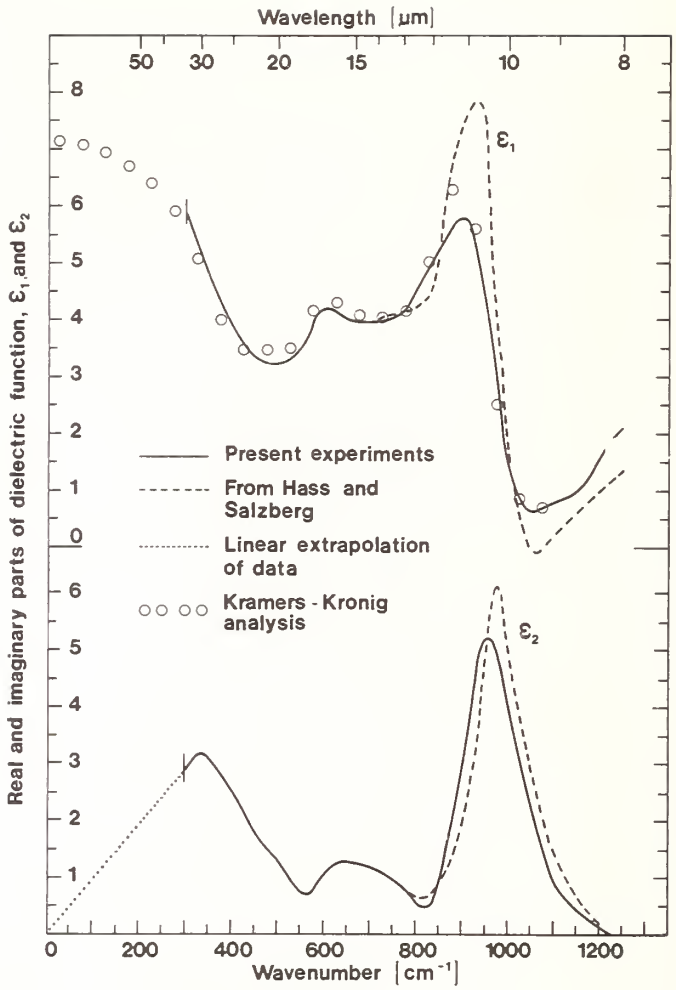

Fig. 1. Real and imaginary parts of the dielectric permeability of SiO. *Solid curves represent this work, while dashed curves represent data from Ref. 6. Circles denote results obtained via Kramers-Kronig analysis.*

The infrared optical properties of SiO will now be used in a discussion of surfaces for radiative cooling. The upper part of Figure 2 depicts zenithal spectral emittance as obtained from an accurate model of a typical midlatitude summer atmosphere by use of published spectral radiance data [7]. Low emittance is noted for the interval $8 \lesssim \lambda \lesssim 13$ μm. Cooling to low temperatures is possible for a surface which radiates predominantly in this "window" range. The ideal spectral reflectance is indicated by the dotted lines in the lower part of Figure 2. Reflectance data which approximate the ideal behaviour could be obtained by computations based on the dielectric permeability of SiO. The dashed curve in the lower part of Figure 2 pertains to a film thickness of 0.9 μm. The

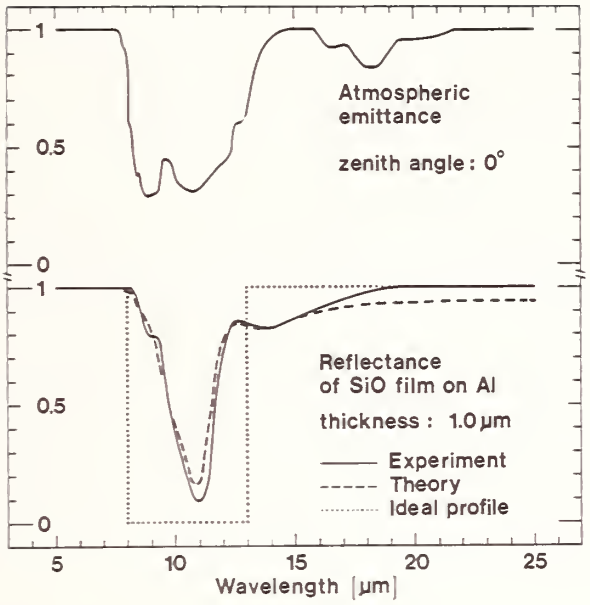

Fig. 2. Upper part shows zenithal atmospheric emittance as derived from Ref. 7. Lower part shows reflectance for SiO *on* Al *as measured and as computed from the dielectric permeability given in Fig. 1.*

strong minimum at $\lambda \sim 10$ µm results from the dominant absorption band in SiO combining with destructive interference. Hence the reflectance data are strongly dependent on film thickness. The solid curve in the lower part of Figure 2 represents a measurement on a SiO film, with an estimated thickness of 1.0 µm, deposited onto Al. Good agreement between theory and experiments in noted. Detailed reports on our work will be given elsewhere [8,9].

REFERENCES

1. F. Trombe, Rev. Gen. Thermique *6*, 1285 (1967).
2. S. Catalanotti, V. Cuomo, G. Piro, D. Ruggi, V. Silvestrini, and G. Troise, Solar Energy *17*, 83 (1975).
3. Ph. Grenier, Rev. Phys. Appl. *14*, 87 (1979).
4. P.-O. Nilsson, Appl. Opt *7*, 435 (1968).
5. A. Hjortsberg, to be published.
6. G. Hass and C.D. Salzberg, J. Opt. Soc. Am. *44*, 181 (1954).
7. P. Berdahl and M. Martin, *Proc. 2nd Nat. Passive Solar Conf.*, Philadelphia, 1978; Vol. 2, p. 684; *Proc. 3rd Nat. Passive Solar Conf.*, San Jose, 1979; to be published.
8. C.G. Granqvist and A. Hjortsberg, Appl. Phys. Lett., in the press.
9. A. Hjortsberg and C.G. Granqvist, to be published.

THE PHOTOELASTIC EFFECT IN OPTICAL MATERIALS*

Albert Feldman and Roy M. Waxler
National Bureau of Standards
Washington, D. C. 20234

The photoelastic constants are components of a fourth rank tensor that relates the change of the dielectric impermeability tensor $\Delta\kappa^{-1}$ and, hence, refractive index n to an applied elastic deformation. Pockels [1] first formulated the relationship of $\Delta\kappa^{-1}$ to the stress tensor σ and the strain tensor η. Using group theory, Bhagavantum [2] corrected some errors that existed in the earlier formulation. In recent years, Nelson and Lax [3] discovered that body rotations make an additional contribution to the photoelastic effect in naturally birefringent materials and this effect has been shown to be significant in the acousto-optic interaction of light with shear waves. In this paper, we will not be concerned with the latter effect.

The earliest theories of the photoelastic effect were based on molecular or atomic polarizabilities. The most comprehensive theory appears to be due to Mueller [4] who considered the following stress dependent factors for cubic and amorphous materials: change of density; change of the local field correction (or the Lorentz-Lorenz field); change in the crystal field (or Coulomb field); and change in the intrinsic polarizability of the atoms. Mueller appears to be the first to recognize the importance of the last factor. His formulation considered only the electronic polarizabilities of the ions, but did not include the effect of stress on lattice polarization, which has been treated only in recent years.

A large body of experimental work has dealt with the effect of hydrostatic stress P on refractive index. These results can be interpreted on the basis of the density dependence of the Lorentz-Lorenz equation

$$\rho\frac{dn}{d\rho} = [(n^2 - 1)(n^2 + 2)/6n](1 - \lambda_o) \qquad (1)$$

where ρ = the density and λ_o = the strain polarizability parameter introduced by Mueller. Values of λ_o have been published for a wide range of materials and they have yielded qualitative information about the amount of heteropolar binding and ionic overlap in crystals [5].

*This work supported in part by the Air Force Office of Scientific Research, Air Force Systems Command, USAF, under Grant Nos. AFOSR-ISSA-79-0001 and -80-00002. The U. S. Government is authorized to reproduce and distribute reprints for governmental purposes not withstanding any copyright notation hereon.

However, they have not been derived on the basis of fundamental calculations. Recent results have shown that $\lambda_0 \approx 0$ for molecular solids [6]. A formulation based on the Drude equation has been shown to be equivalent to the Lorentz-Lorenz formulation described above [7].

Several years ago, some materials were found to exhibit a nonlinear piezo-effect, that is, the change of n was not a linear function of σ. The explanation of the effect was dependent on the material. In ionic materials, it was shown that the nonlinear dependence of n on hydrostatic pressure [8] was due to the nonlinear deformation. When the nonlinear elastic constants were used to calculate the strain, it was found that n was a linear function of strain.

Intrinsic semiconductor materials were shown to exhibit a nonlinear piezo-optic effect at wavelengths near the absorption edge [9,10]; the coefficients for piezo-birefringence, $q_{11} - q_{12}$ and q_{44}, exhibited a large dispersion in this region as well. This nonlinear piezo-optic effect was attributed to the complicated stress-dependence of the valence-band splittings and interband oscillator strength.

Significant nonlinear piezo-optic effects were observed in highly doped n-type Ge [9,11]. Schmidt-Tiedemann [12] was the first to observe piezo-birefringence due to the transfer of free carriers in the highly-anisotropic conduction bands of Ge. Other workers [9,11] used this effect to calculate the shear deformation potential E_2 of Ge. Working at 1.4°K, Feldman [9] found a dramatic nonlinearity in the piezo-birefringence in which the incremental stress-induced birefringence reversed sign. This occurred when the stress was sufficient to transfer all free electrons to a single conduction band minimum.

In the Mueller theory of photoelasticity, dispersion effects had not been treated. In order to account for dispersion, modern formulations treat a material as consisting of oscillators due both to interband band transitions and to the creation of lattice optical phonons. Cardonna and coworkers have calculated the dispersion of the piezo-birefringence of alkali-halide and semiconductor crystals based on band structure models with certain phenomenological parameters fitted to experimental data [13,14]. Wemple and DiDomenico [15] have fitted a wide range of piezo-optic data to a phenomenological oscillator model for electronic transitions.

Van Vechten [16] developed a model for the pressure dependence of the optical dielectric constant of a wide range of materials based on the Penn model for the optical dielectric constant,

$$\varepsilon_\infty = 1 + (g_0 \hbar^2 / E_g^2)(1 - B + \tfrac{1}{3} B^2) \qquad (2)$$

where $B = E_g/4E_F$, E_F = Fermi energy, g_0 = oscillator strength, and E_g = average energy gap consisting of a homopolar part E_h and a heteropolar part C related by

$$E_g^2 = E_h^2 + C^2. \qquad (3)$$

Based on the band structure calculations of others, Van Vechten concluded that E_h was a function only of the interatomic spacing r, and then postulated that there is a power law dependence of E_h on r; thus, $E_h \propto r^{-s}$ with s = 2.48. Biegelson demonstrated a shortcoming of the model by showing that the s parameter calculated from his strain-optic measurements on Si was at variance with the predicted value [17].

Until recently, almost no piezo-optic data in the infrared have been available for ionic materials. A theory for piezo-optic dispersion due to infrared lattice modes has been developed by Humphreys and Maradudin [18] (HM) and extended by Bendow, Gianino, Tsay, and Mitra [19] to a wide range of zinc-blende and alkali-halide crystals. Subsequently, several experiments were conducted that suggested inadequacies in the model [20,21]. However, the experimental data were obtained at few wavelengths and were prone to large experimental errors, and, hence did not provide a stringent test of the model. We have measured the piezo-birefringence coefficients of CaF_2, SrF_2, and BaF_2 over the wavelength range 0.45 to 10.6 μm and have been able to fit the data to the basic phenomenological equation

$$k_i = k_i^{\infty} + \frac{\partial G_1/\partial \eta_i - \partial G_2/\partial \eta_i}{1 - (\nu/\nu_{TO})^2} - \frac{(2G_o/\nu_{TO})(\nu/\nu_{TO})^2 \partial \Delta_i/\partial \eta_i}{[1 - (\nu/\nu_{TO})^2]^2} \qquad (4)$$

where i = index indicating uniaxial strain either along the [100] or [111] crystal axis, k_i = photoelastic constant derived from the piezo-birefringence coefficient q_i, k_i^{∞} = high frequency photoelastic constant, η_i = magnitude of strain, G_o = zero-strain oscillator strength, G_1 = oscillator strength for polarization along strain direction, G_2 = oscillator strength for polarizaton perpendicular to strain direction, ν = optical frequency, ν_{TO} = transverse optic-mode frequency, Δ_i = strain-induced optic-mode frequency splitting. This equation is equivalent to the phenomenological expression of HM. In Figure 1, we show experimental photoelastic constants of BaF_2 plotted as a function of wavelength, and a curve denoting a least squares fit of equation (4) to the experimental data. Analogous results have been obtained for CaF_2 and SrF_2. The fit indicates that the strain-induced oscillator strength anisotropy is negligible suggesting that the Szigeti effective charge remains a scalar. In addition, the shear deformation potentials have been calculated. To our knowledge, this has been the first determination of the splitting of the transverse optic phonon mode due to uniaxial stress (or strain). The complete interpretation of these latest results will depend on the development of a microscopic model for the strain dependence of the dielectric function in fluorite structure materials. Clearly, a large amount of experimental work remains in the measurement of dispersion of the piezo-optic coefficients of ionic materials in the infrared.

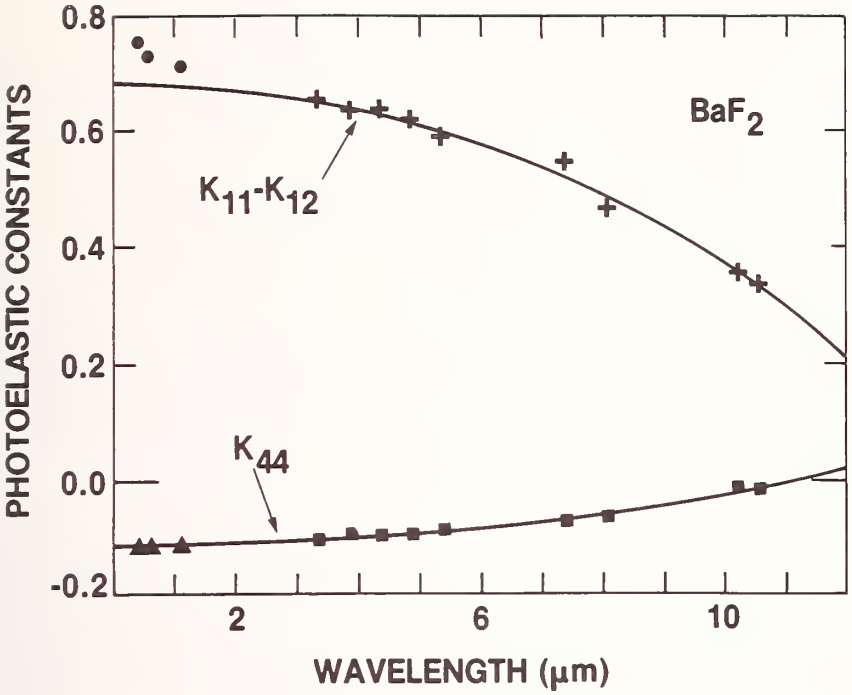

Figure 1. Photoelastic constants of BaF_2 derived from piezo-birefringence data. The curves are least-squares fits to equation (4) of the data points denoted by pluses for $k_{11} - k_{12}$ and squares for k_{44}.

References

1. F. Pockels, Lehrbuch der Kristalloptik, (Leipzig: Teubner) 941, 74 (1906).

2. S. Bhagavantam, Proc. Indian Acad. Sci. A16, 359 (1942); Acta Cryst. 5, 591 (1952).

3. D. F. Nelson and M. Lax, Phys. Rev. Letters 24, 379 (1970).

4. H. Mueller, Phys. Rev. 47, 947 (1935).

5. E. Burnstein and P. L. Smith, Proc. Indian Acad. Science A28, 377 (1948).

6. M. Kastner, Phys. Rev. B 6, 2273 (1972).

7. K. S. Krishnan and S. K. Roy, Phil. Mag. 43, 317 (1952).

8. K. Vedam and E. D. D. Schmidt, J. Mat. Sci. 1, 310 (1966).

9. Albert Feldman, Phys. Rev. 150, 748 (1966).

10. K. Vedam and E. D. D. Schmidt, Phys. Rev. 150, 766 (1966).

11. S. Riskaer, Phys. Rev. 152, 845 (1966).

12. K. J. Schmidt-Tiedemann, Phys. Rev. Lett 7, 372 (1961).

13. A. Gavini and M. Cardonna, Phys. Rev. 177, 1351 (1969).

14. P. Y. Yu, M. Cardonna, and F. H. Pollak, Phys. Rev. B3, 340 (1971).

15. S. H. Wemple and M. DiDomenico, Jr., Phys. Rev. B1, 193 (1970).

16. J. A. Van Vechten, Phys. Rev. 182, 891 (1969).

17. David K. Biegelsen, Phys. Rev. Letters 32, 1196 (1974).

18. L. B. Humphreys and A. A. Maradudin, Phys. Rev. B6, 3868 (1972).

19. B. Bendow, P. D. Gianino, Y. F. Tsay, and S. S. Mitra, Appl. Optics 13, 2382 (1974).

20. J. P. Szczesniak, D. Cuddeback, and J. C. Corelli, J. Appl. Phys. 47, 5356 (1976).

21. A. Feldman, D. Horowitz, and R. M. Waxler, Appl. Optics 16, 2925 (1977).

THE RELATION OF ELASTOOPTIC AND ELECTROSTRICTIVE TENSORS

D. F. Nelson
Bell Laboratories
Murray Hill, New Jersey 07974

BACKGROUND

Electrostriction is the deformation that is produced in a body by the application of an electric field and is proportional to the square of that field. Traditionally the applied electric field is a very low frequency or constant field and is applied by electrodes attached to the body. It is apparent that electrostriction must be characterized by a fourth rank tensor, two indices coupling to the two electric fields and two indices coupling to the relevant measure of deformation, the strain.

The elastooptic effect (also called the photoelastic or piezooptic effect) is the interaction of an elastic deformation with an input light wave to produce an altered output light wave. Since the light waves are determined by their electric fields, the elastooptic effect can also be characterized by a fourth rank tensor with two indices coupling to the two electric fields and two indices coupling to the relevant measure of elastic deformation. From the discovery of the elastooptic effect by Brewster in 1816 through the extensive work of Pockels in the 1890's until 1970 it was believed that the appropriate measure of elastic deformation for the elastooptic effect was the strain. It was thus quite natural to expect that the electrostriction and elastooptic tensors were closely related, the electrostrictive tensor being simply the low frequency limit of the elastooptic tensor. Proofs of this equality, in fact, were given many times[1-4] based simply on reversing the order of partial differentiation of a thermodynamic potential.

In 1970 it was shown[5] that the elastooptic effect had been misrepresented throughout its long history and that the proper measure of elastic deformation relevant to the elastooptic effect is the displacement gradient which is a sum of strain and rotation. Measurements on strongly birefringent crystals such as rutile[6] and calcite[7] showed that the contribution of rotation to the elastooptic effect can be comparable to that of strain. If the proofs[1-4] cited above are correct, then the electrostrictive tensor must also couple to rotation as well as to strain; that is, the application of an electric field to electrodes on a body would cause the body to rotate. That, however, would clearly violate angular momentum conservation. Thus, something must be wrong with the phenomenological proof.[1-4] Since the mathematics of the proof is too simple to be wrong, it must be that the proof inadequately addresses the physics of the processes involved.

In order to avoid any confusion before proceding further let us point out that a converse elastooptic effect in which two light waves are mixed to produce a deformation (such as an acoustic wave) has sometimes been called electrostriction, in particular by Caddes, Quate, and Wilkinson[8] who first observed this effect. We do not use the term electrostriction in this sense here but rather in the traditional sense defined above. Clearly the converse elastooptic effect is properly characterized by the same elastooptic tensor that characterizes the normal elastooptic effect.

Recently a new relationship between the low frequency limit of the elastooptic tensor and the electrostriction tensor was obtained by comparing the results from the application of the same basic theory of long wavelength interactions in dielectric crystals[9,10] to the elastooptic effect[5] and to electrostriction.[11] The difference between the two tensors was attributed to the differing coordinates, spatial and material, that are appropriate in expressing the tensors for the two interactions, the elastooptic effect and electrostriction. Since the length of those two derivations may obscure this interpretation, it is worthwhile to distill from them the essential physics into a compact derivation of the new relationship. It is the purpose of this paper to do that.

The choice of coordinates to which to refer the two tensors is determined by the methods of measurement. In the elastooptic effect the electric fields of the input and output light waves are known relative to the spatial (laboratory) coordinates since the light source and detector are fixed in the laboratory. It is thus natural also to express the deformation with respect to the same coordinates.

In the study of electrostriction as in the study of other phenomena in the low frequency (quasielectrostatic) region electric fields and deformations are known relative to the material coordinates anchored in the crystal. This results because electric fields are typically applied to and detected by electrodes evaporated onto the surfaces of the crystal and deformations are applied and detected by transducers bonded to the crystal surfaces. This means that the electric and deformation fields are known only relative to the crystal surfaces and not relative to the laboratory because the crystal surfaces are moving and deforming relative to the laboratory as a result of the applied influences.

DERIVATION

The deformed position of a matter point is given by the spatial position vector $\vec{x}$ and the designation of a matter point is given by the material position vector $\vec{X}$. The latter can be regarded as the name of the matter point that remains with the matter point during deformation. The relation between these two positions is the deformation transformation $\vec{x} = \vec{x}(\vec{X},t)$. It is convenient to take the material coordinate vector as the undeformed position of the matter point and to represent the deviation of the matter point from this position arising from deformation by the displacement vector $\vec{u}$. Thus

$$\vec{x} = \vec{X} + \vec{u}. \tag{1}$$

Both the spatial and material positions are measured with respect to a rectangular coordinate system. The deformation gradients $\partial x_j/\partial X_j$ and $\partial X_j/\partial x_i$ can be expressed in terms of the displacement gradient, for instance,

$$\partial X_j/\partial x_i = \delta_{ji} - \partial u_j/\partial x_i. \tag{2}$$

The displacement gradient is a sum of strain $u_{(k,i)}$ and rotation $u_{[k,i]}$,

$$\partial u_k/\partial x_i \equiv u_{k,i} = u_{(k,i)} + u_{[k,i]}, \tag{3}$$

where

$$u_{(k,i)} \equiv (\partial u_k/\partial x_i + \partial u_i/\partial x_k)/2 \tag{3a}$$

and

$$u_{[k,i]} \equiv (\partial u_k/\partial x_i - \partial u_i/\partial x_k)/2. \tag{3b}$$

The Jacobian of the deformation transformation is

$$J = \det(\partial x/\partial X) = 1 + u_{i,i} + \cdots \tag{4}$$

Finally we note that a theory is said to be cast in the spatial description (or frame) if $\vec{x}$, t are regarded as the independent variables and in the material description (or frame) if $\vec{X}$, t are regarded as the independent variables.

In the spatial description the polarization $\vec{P}$ relevant to the elastooptic effect is given by[5]

$$P_i = \epsilon_0 \chi_{ij} E_j + 2\epsilon_0 \left(\chi_{ij(kl)} - \frac{1}{2}\chi_{i[k}\delta_{l]j} - \frac{1}{2}\chi_{j[k}\delta_{l]i} \right) E_j u_{k,l}, \tag{5}$$

where χ_{ij} is the linear electric susceptibility, E_j is the spatial frame electric field, ϵ_0 is the permittivity of free space, and the elastooptic susceptibility $\chi_{ij(kl)}$ is related to the Pockels elastooptic tensor p_{mnkl} by

$$2\chi_{ij(kl)} = -\kappa_{im}\kappa_{jn}p_{mnkl}, \tag{6}$$

κ_{ij} being the dielectric tensor. The factor of two before $\chi_{ij(kl)}$ in Eqs. (5) and (6) results because $\chi_{ij(kl)}$ applies to one Fourier frequency component (Stokes or anti-Stokes) and a low frequency limit is taken here in which these two components coalesce. The Pockels term is symmetric upon interchange of k and l and so couples only to the strain part of $u_{k,l}$. The last two terms[5] are antisymmetric upon interchange of k and l and so couple only to the rotation part of $u_{k,l}$.

We now wish to transform Eq. (5) to the material frame. A study[12] of the Maxwell equations in the material frame shows that the material frame polarization $\vec{P}$ and the material frame electric field $\vec{E}$ are related to the corresponding spatial frame quantities by

$$P_m = JP_i \partial X_m/\partial x_i \ , \ E_j = E_n \partial X_n/\partial x_j. \tag{7}$$

If Eqs. (5) and (7) are now combined with the use of Eqs. (2) and (4), we obtain

$$P_m = \epsilon_0 \chi_{mn} E_n + \epsilon_0 \left(2\chi_{mn(kl)} - \chi_{m(k}\delta_{l)n} - \chi_{n(k}\delta_{l)m} + \chi_{mn}\delta_{kl} \right) E_n \partial u_k/\partial x_l. \tag{8}$$

A material frame study of nonlinearities in the quasielectrostatic region[11] yields

$$P_m = \epsilon_0 \chi_{mn} E_n + \epsilon_0 l^s_{mn(kl)} E_n \partial u_k/\partial X_l, \tag{9}$$

where $l^s_{mn(kl)}$ is the electrostrictive susceptibility. Since to first order $\partial u_k/\partial x_l = \partial u_k/\partial X_l$, comparison of the last two equations gives

$$l^s_{mn(kl)} = 2\chi_{mn(kl)} - \chi_{m(k}\delta_{l)n} - \chi_{n(k}\delta_{l)m} + \chi_{mn}\delta_{kl} \tag{10}$$

for the final result.

An alternate form of the last equation can be obtained if the expression[12] for the low frequency material frame electric displacement,

$$D_k = \epsilon_0 J (C^{-1})_{kl} E_l + P_k, \tag{11}$$

where $(C^{-1})_{ij} = (\partial X_i/\partial x_k)(\partial X_j/\partial x_k)$, is expanded to yield

$$D_m = \epsilon_0 \kappa_{mn} E_n + \epsilon_0 l_{mn(kl)} E_n \partial u_k/\partial x_l \, . \tag{12}$$

The expansion gives the electrostriction tensor $l_{mn(kl)}$ in terms of the electrostrictive susceptibility by

$$l_{mn(kl)} = l^s_{mn(kl)} - 2\delta_{m(k}\delta_{l)n} + \delta_{mn}\delta_{kl} \tag{13}$$

and so allows an alternate form for Eq. (10) to be

$$l_{mn(kl)} = 2\chi_{mn(kl)} - \kappa_{m(k}\delta_{l)n} - \kappa_{n(k}\delta_{l)m} + \kappa_{mn}\delta_{kl} \, . \tag{14}$$

We regard both the electrostrictive susceptibility and the electrostriction tensor as equally important. The former, like the linear electric susceptibility, vanishes for a vacuum and so characterizes the medium. The latter, like the dielectric tensor, is nonzero for a vacuum and is the tensor entering the differential equations. It also enters the stress expression as the coefficient of the square of the material frame electric field.

DISCUSSION

Let us note several things about Eq. (10) [similar remarks could be made about Eq. (14)]. First, we see that the essential difference between the electrostrictive susceptibility and the elastooptic susceptibility arises because the former is a material frame tensor and the latter is a spatial frame tensor. As pointed out in the Introduction this difference arises from the differing methods of measurement. Second, the electrostrictive susceptibility couples only to strain, as expected from an angular momentum conservation argument, even though the elastooptic tensor can couple also to rotation. Note that the antisymmetric part of the elastooptic tensor that couples to rotation does not enter Eq. (10). Third, the terms by which the electrostrictive susceptibility and the elastooptic susceptibility differ are terms describing Maxwell stresses arising from the presence of a polarizable medium. These terms are comparable in magnitude to the elastooptic susceptibility in many materials.

REFERENCES

1. H. Osterberg and J. W. Cookson, Phys. Rev. *51,* 1096 (1937).
2. J. F. Nye, *Physical Properties of Crystals* (Clarendon, Oxford, 1957), pp. 255-256.
3. W. P. Mason, *Crystal Physics of Interaction Processes* (Academic, New York, 1966), p. 166.
4. K. Iamsakun, W. Elder, C. D. W. Wilkinson, and R. M. DeLaRue, J. Phys. D *8,* 266 (1975).
5. D. F. Nelson and M. Lax, Phys. Rev. Lett. *24,* 379 (1970); Phys. Rev. B *3,* 2778 (1971).
6. D. F. Nelson and P. D. Lazay, Phys. Rev. Lett. *25,* 1187, 1638 (1970).
7. D. F. Nelson, P. D. Lazay, and M. Lax, Phys. Rev. B *6,* 3109 (1972).
8. D. E. Caddes, C. F. Quate, and C. D. W. Wilkinson, in *Modern Optics* J. Fox, Ed. (Polytechnic Press, Brooklyn, NY, 1967), p. 219.
9. M. Lax and D. F. Nelson, Phys. Rev. B *4,* 3694 (1971); *13,* 1759 (1976).
10. D. F. Nelson, *Electric, Optic, and Acoustic Interactions in Dielectrics* (Wiley, New York, 1979).
11. D. F. Nelson, J. Acoust. Soc. Am. *63,* 1738 (1978).
12. M. Lax and D. F. Nelson, Phys. Rev. B *13,* 1777 (1976).

PHOTOELASTIC PROPERTIES OF MAGNESIUM FLUORIDE

Sunwhee Chung
EMR Photoelectric
P.O. Box 44
Princeton, New Jersey 08540

Herbert R. Carleton*
Department of Materials Science
State University of New York at Stony Brook
Stony Brook, New York 11794

Magnesium fluoride (MgF_2) has the rutile crystal structure with a tetragonal space lattice ($P4/mnm$)[1]. The crystal is uniaxial positive with n_ω=1.378 and n_ε=1.390 for sodium D light[2]. A single crystal of MgF_2 grown by the Materials Research Corporation was used in this study. The crystal was approximately 1 cm^3 with polished faces in the (001), (110), and ($\bar{1}$10) crystal planes as verified by the back-reflection Laue method.

After preparation, the sample was bonded with salol to a fused silica block on which an x-cut 20 MHz quartz transducer was bonded with epoxy cement. A similar fused silica block was prepared with a y-cut 20 MHz quartz transducer for shear wave measurements. Upon the completion of measurements with this configuration, the crystal was cut at an angle 45±0.5° to [110] and [$\bar{1}$10] in order to obtain (100) and (010) faces. Further measurements were conducted with this configuration, which were followed by another cutting at an angle 45±0.5° to [100] and [001]. This orientation was verified by obtaining an angular separation of 11.6±0.5° between [101] and the direction perpendicular to the newly-cut face as determined by the back-reflection Laue method.

The experimental arrangement for ultrasonic laser-diffraction used for all measurements is similar to that previously reported[3]. The intensity of light pulses diffracted from the MgF_2 crystal and the fused silica reference was measured on an oscilloscope after detection with a photomultiplier tube.

It can be shown[4] that the photoelastic constant p_s responsible for optical diffraction by an ultrasonic wave is related to experimentally available parameters by the relation:

$$(p_s)^2 = (I_R)^{1/2}\frac{\rho_s}{\rho_r}\left(\frac{V_s}{V_r}\right)^3\left(\frac{n_r}{n_s}\right)^6(p_r)^2 \qquad (1)$$

where the subscripts r and s stand for reference and sample respectively, I_R is the measured intensity ratio, ρ is the density, V is the

* Research supported in part by NSF Grant GK28383.

sound velocity, and n is the refractive index. The photoelastic constants of the sample were calculated from the known piezooptic constants of fused silica which were measured by Primak and Post[5]. These piezooptic constants at several wavelengths were converted to the photoelastic constants using the elastic moduli reported by Primak and Post, and tabulated in Table I.

Table I. Photoelastic constants of fused silica.

Wavelength(nm)	436.0	546.0	579.0	589.0	644.0
p_{11}	0.121	0.121	0.121	0.121	0.122
p_{12}	0.272	0.270	0.270	0.270	0.270

The ratio of sound velocities was obtained from a knowledge of the Bragg angle θ_B which is one half the angle between incident and diffracted beams. The sound velocities V_S are then calculated from $2V_S Sin\theta_B=\lambda f$ where λ is the laser wavelength in air and f is the frequency of the sound wave.

Six of the seven independent photoelastic constants of MgF_2 have been determined and listed in Table II. The piezooptic constants q_{ij} were derived using elastic constants obtained in this experiment. Since p_{33} could not be measured accurately with a longitudinal wave along [001] because of low diffracted light intensity, p_{33} was determined using quasi-longitudinal and quasi-shear waves along a direction 45° from [100] and [001] in the (010) plane. These results were also used to assign the relative signs of p_{13}, p_{31}, and p_{33}. Diffraction involving p_{44} is "abnormal"[6], i.e. scattering between light beams with different phase velocities requires very large "phonon" frequencies to conserve k-vector. Since this experiment was conducted in the Raman-Nath regime, p_{44} could not be measured.

Table II. Photoelastic and piezooptic constants of MgF_2 at 632.8nm.

Photoelastic Constant	Experimental Result*	Piezooptic Constant	Calculated Value ($10^{-13}cm^2/dyn$)
p_{11}	+0.041±0.002	q_{11}	-0.467
p_{12}	+0.119±0.002	q_{12}	+1.053
p_{13}	+0.078±0.002	q_{13}	+0.197
p_{31}	-0.099±0.003	q_{31}	-0.545
p_{33}	+0.014±0.001	q_{33}	+0.409
p_{44}	--	q_{44}	--
p_{66}	-0.0475±0.0015	q_{66}	-0.498

*Signs are assigned with respect to p_{11} which is assumed positive.

The change of the refractive indices of rutile under hydrostatic pressure dn/dP was reported by Davis and Vedam[7]. For the sake of comparison dn/dP of MgF_2 was calculated using the following relations (2) and compared with those of rutile in Table III where we find that dn_ω/dP is positive while dn_ε/dP is negative.

$$\frac{dn_\varepsilon}{dP} = \frac{n_\varepsilon^3}{2}(2q_{31} + q_{33}), \qquad \frac{dn_\omega}{dP} = \frac{n_\omega^3}{2}(q_{11} + q_{12} + q_{13}) \quad (2)$$

Using known relations for the photoelastic constants, $\rho(dn/d\rho)$ of MgF_2 was calculated using Equations (3) and (4) and is listed in Table III along with the corresponding strain polarizabilities.

$$\rho\frac{dn_\omega}{d\rho} = \frac{n_\omega^3}{2}\{\frac{1}{S}(p_{11}+p_{12})(S_{11}+S_{12}+S_{13}) + \frac{1}{S}p_{13}(2S_{13}+S_{33})\} \quad (3)$$

$$\rho\frac{dn_\varepsilon}{d\rho} = \frac{n_\varepsilon^3}{2}\{\frac{2p_{31}}{S}(S_{11}+S_{12}+S_{13}) + \frac{p_{33}}{S}(2S_{13}+S_{33})\} \quad (4)$$

Here, S_{ij} is the elastic compliance, and $S=2S_{11}+2S_{12}+4S_{13}+S_{33}$.

Table III. Change of refractive indices for MgF_2 and rutile.

Crystal	Refractive Index	λ(nm)	$\frac{dn}{dP}$ (Mbar)$^{-1}$	$\rho\frac{dn}{d\rho}$	Λ_o
MgF_2	n_ω=1.377	632.8	0.102	0.104	0.754
	n_ε=1.389		-0.0915	-0.0927	1.21
TiO_2*	n_ω=2.587	589.3	0.11	0.25	0.92
	n_ε=2.902		-0.49	-0.95	1.21

*Davis and Vedam[7].

It is interesting to note that the ordinary and extra-ordinary refractive indices of MgF_2 and rutile change in opposite directions under hydrostatic pressure.

A total differentiation of the Lorentz-Lorenz equation predicts a density dependence of the refractive index,[7,8,9]

$$\rho\frac{dn}{d\rho} = \frac{(n^2-1)(n^2+2)}{6n}(1 - \Lambda_o), \quad (5)$$

where $\Lambda_o = -(\rho/\alpha)(d\alpha/d\rho)$ is the strain polarizability.

Detailed studies[10] have shown that the polarizability of a cation increases under compression while that of an anion decreases. This is related to a decrease in ionicity of valence-pairs under compression. It can be expected that shifts away from ionicity, and hence to directed bonds, will produce anisotropic changes in refractive index where crystal symmetry permits. The contribution of different ions to changes in refractive index can be considered by introducing an ionic strain polarizability Λ_i,

$$\Lambda_i = -(\rho/\alpha_i)(d\alpha_i/d\rho), \quad (6)$$

so that the molecular strain polarizability is given, for binary systems, by

$$\Lambda_o = \frac{\alpha_+}{\alpha_+ + \alpha_-} \Lambda_+ + \frac{\alpha_-}{\alpha_+ + \alpha_-} \Lambda_- , \qquad (7)$$

where the subscripts + and - represent the cation and anion, respectively. Λ_o is a phenomenological constant which attempts to explain those changes in refractive index which cannot be explained by volume changes alone. It must be interpreted as a tensor in the case of MgF_2. Since the two terms appearing in (7) are of opposite sign, the observed values of Λ_o are consistent with a larger value of Λ_+ for polarization in the basal plane (n_ω) than for polarization along the c axis (n_ε). This is plausible if one takes a close look at the irregular octahedron made by six anions of MgF_2. Along the directions [110] and [$\bar{1}$10], all ions are in close contact with one cation for every two anions. However, along the [001] direction, the anions are not in contact, leaving some space for cations in the direction perpendicular to the c axis.

One can go a step further from this argument and say that dn/dP is negative for more covalent crystals because the former part of Equation (7) is very small or non-existent compared to the latter part which is positive, thus making Λ_o greater than 1. This will in turn make $\rho(dn/d\rho)$ negative. The experimental results for MgO, C(diamond), Si, and Ge support this argument. The values of Λ_o are 1.1 for diamond[7] and 1.2 - 1.4 for MgO[7,11]. Accordingly, $\rho(dn/d\rho)$ and dn/dP for diamond and MgO are negative. Gibbs and Hill[12] reported the change of the static electronic dielectric constant due to pressure for diamond as $(1/\varepsilon_1(0))(\partial\varepsilon_1(0)/\partial P)_T = (-1.07\pm0.09)\times10^{-7}\,cm^2/Kg$. Cardona et al[12] reported $(1/n)(dn/dP) = (-3\pm2)\times10^{-7}\,cm^2/Kg$ for Si and $(1/n)(dn/dP) = (-7\pm2)\times10^{-7}\,cm^2/Kg$ for Ge. Davis and Vedam[7] related the larger values of Λ_o to the more covalent-type bonding and the smaller values to the more ionic-type bonding from the experimental results. This is in agreement with the conclusion derived in this report using the concept of the ionic strain polarizability.

References

1. R.W.G. Wyckoff, Crystal Structure Vol. 1, John Wiley New York (1963).
2. Handbook of Chemistry and Physics, 56th edition, CRC Press.
3. W.T. Maloney and H.R. Carleton, IEEE Trans. on Sonics and Ultrasonics SU-14, 135 (1967).
4. R.W. Dixon and M.G. Cohen, Appl. Phys. Lett. 8, 205 (1966).
5. W. Primak and D. Post, J. Appl. Phys. 30, 779 (1959).
6. R.W. Dixon, IEEE J. Quantum Electronics QE-3, 85 (1967).
7. T.A. Davis and K. Vedam, J. Opt. Soc. Am. 58, 1446 (1968).
8. H.R. Carleton in "Amorphous Materials", John Wiley New York (1972).
9. H. Mueller, Phys. Rev. 47, 947 (1935).
10. S. Chung, "Photoelastic Dispersion of Alkali Halides and Alkaline Earth Fluorides", Ph.D. Thesis (1976) State University of New York.
11. T.S. Narasimhamurty, Acta Cryst. 17, 788 (1964).
12. J.A. Van Vechten, Phys. Rev. 182, 891 (1969).

A MICROSCOPIC APPROACH TO PREDICT REFRACTIVE INDICES AND ELECTRO- OR STRAIN-OPTIC COEFFICIENTS

M.D. Ewbank, P.R. Newman
Rockwell International Science Center
1049 Camino Dos Rios
Thousand Oaks, California 91360

and

W.A. Harrison
Department of Applied Physics
Stanford University
Stanford, California 94305

Introduction - Research and development of solid state optical devices has recently been increasing. Specific examples are tunable spectral filters, modulators and beam steerers (both acousto-optic (AO) and electro-optic (EO)). However, some devices exhibit unacceptable performance characteristics. This limitation is usually not device design but rather the relevant materials properties of the few selective compounds being utilized. One solution to this problem obviously is to find crystals which demonstrate superior materials properties. However, the experimental investigation (including growth, fabrication, and characterization) of random compounds which satisfy the necessary criteria is prohibitively expensive.

A more efficient approach entails theoretically estimating the virtues of candidate materials. Several authors[1-3] have addressed the issue of identifying promising compounds for both AO and EO applications. Other authors[4,5] have attempted to establish empirical "guidelines," which are based upon bulk macroscopic properties, for selecting new crystals. Our method, by contrast, is a "first principles" scheme that commences at the atomic level of the solid. The ultimate goal is to develop a completely general (based solely on elemental composition, atomic configuration, and crystal symmetry) theoretical predictive methodology for comparing materials properties of different compounds, to "prescreen" candidate materials, and subsequently to assist in the selection of optimal materials to be grown and characterized experimentally.

Approach - Initially, we have identified three relevant material parameters: 1) the refractive indices, 2) the electro-optic coefficients, and 3) the photoelastic constants. This selection is based, in part, on two "figures-of-merit" for EO[5] and AO[6] devices which are $F = n_i^7 r_{ij}^2/\varepsilon_j$ and $M_2 = n_i^3 n_j^3 p_{ij}^2/\rho v^3$, respectively, where n_i is the optical index of refraction, r_{ij} is the electro-optic coefficient, ε_j is the dielectric constant at the frequency of the external electric field, P_{ij} is the photoelastic component, ρ is the mass density and v is the acoustic velocity.

Briefly, the procedure for determining the refractive indices and the electro-optic or strain-optic tensors is as follows: 1) calculate the electronic susceptibility tensor and hence the refractive indices ($n_i = \sqrt{1 + 4\pi\chi_{ii}}$), using a "first principles" method discussed below, for the "unperturbed" crystal, 2) apply an external perturbation (an electric field for EO or a strain field for AO) and calculate the effects of this perturbation on the atomic configuration and/or chemical bonds, 3) recalculate the susceptibility for the "perturbed" crystal. The resulting change in the susceptibility tensor due to the external electric or strain field can be related to the electro-optic or strain-optic coefficients, respectively.[7]

The interaction between the electric field associated with light propagating in a material and its constituent electrons is manifest in the dynamic electronic susceptibility. Specifically, we are concerned with the spectral region above the lattice response modes (Reststrahl) and below the interband or interatomic transitions. A novel approach for the calculation of the principle (diagonalized) components of the electronic susceptibility has been put forth by Harrison[8] in terms of a modified LCAO theory as:

$$\chi_{ii} = (4e^2/v) \sum_{\alpha} \sum_{\beta} [V_{\alpha\beta}]^2 (\vec{d} \cdot \hat{E}_i)^2/(\varepsilon_\beta - \varepsilon_\alpha)^3 \qquad (1)$$

where $\sum_{\alpha}$ is a summation over occupied states in the unit cell, $\sum_{\beta}$ is a summation over coupled unoccupied states, e is the electronic charge, v is the volume per unit cell, $V_{\alpha\beta}$ represents the interatomic matrix element (overlap) between occupied state α and unoccupied state β, $\vec{d}$ is the vector distance between bonding atoms, $\hat{E}_i$ is the unit vector along the i-th principal crystal axis, ε_α is the energy of the occupied state α, and ε_β is the energy of the unoccupied state β. The factors v and $\vec{d}$ depend only on the crystal geometry. The interatomic matrix elements, $V_{\alpha\beta}$, can be quantitatively evaluated by using the Slater-Koster LCAO energy integral formulas[9] along with a parameterization by Harrison[10] for the two-center integrals. The energies, ε_α and ε_β, can be determined from band structure calculations which depend on elemental composition, crystal structure, and the same set of interatomic matrix elements, $V_{\alpha\beta}$.

Results - The above formalism has been applied to the change in the refractive indices due to variations in atomic positions, of the sulfosalt, Tl_3AsSe_3 (TAS). As one example, the variation of atomic positions caused by a longitudinal acoustic wave (uniaxial strain) leads to calculation of photoelastic constants. Another calculation involves the effects of thermal expansion on the refractive indices.[11]

The crystal structure of TAS at room temperature was determined by Hong, et al.[12] The perturbed structure is generated by incorporating a strain which is assumed to be anisotropic and microscopically inhomogeneous, with the As-Se, Se-Se and Tl-Tl interatomic distances remaining constant and the Se-Tl distances accommodating all of the strain. A detailed study of the atomic configuration makes this assumption plausible.

Following the procedure outlined above, the unperturbed refractive indices of TAS can be calculated. The ordinary index, n_o, is dominated by the As(p_z)-Se(p_z) π-bond since these two states constitute the bottom most conduction band and top most valence band, respectively, which results in a small energy difference $(\varepsilon_\beta - \varepsilon_\alpha)$.[13] However, since the As-Se bonds essentially lie in the $\underline{a}$ - $\underline{b}$ plane, they do not contribute to the extraordinary index, n_e. Consequently, the main contribution to n_e is from the Se-Tl p state interactions.

The change in the refractive indices, due to thermal contraction or strain (e.g. uniaxial contraction), can be understood by examining Eq. (1). Both n_o and n_e will experience the volume dependence; as contraction occurs, both refractive indices tend to increase. For n_o, this volume effect is the only contribution because n_o is dominated by the As-Se interaction whose interatomic distance remains constant despite contraction elsewhere in the lattice. Therefore, n_o increases with contraction. In contrast, n_e has several competing factors. Most are specified directly by the change in Se-Tl bond length. A significant contribution results from the change in the energy difference, $(\varepsilon_\beta - \varepsilon_\alpha)$, for the Se-Tl p state. As the interactomic distances contract, the wave function overlaps increase and the energy levels split apart. This variation in energy difference can be approximated by considering only <u>two coupled states</u>. Then the shift in $(\varepsilon_\beta - \varepsilon_\alpha)$ can be expressed as $\sqrt{(\varepsilon_1 - \varepsilon_2)^2 + 4V_{12}^2}$. In the case of TAS, ε_1 and ε_2 are the ionization energies of Se and Tl p states and V_{12} is the interatomic matrix element between the Se and Tl p states.

The seemingly anomalous experimental temperature dependences of the refractive indices for TAS are explained in the context of the above model, since the factor $(\varepsilon_\beta - \varepsilon_\alpha)$ dominates over the volume for n_e. A comparison between theory and experiment is shown in Figs. 1 and 2.

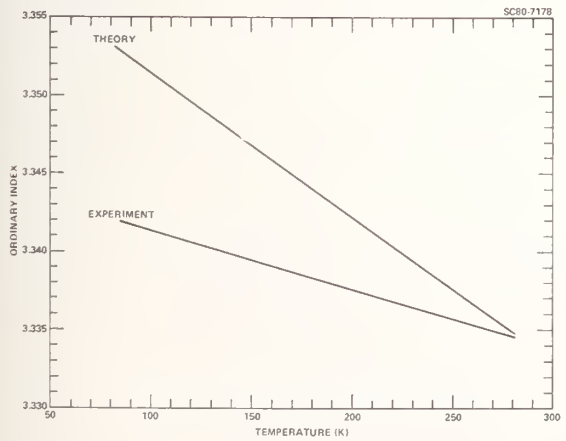

Fig. 1 Comparison of the predicted temperature dependence of the ordinary refractive index of Tl_3AsSe_3 with experiment.

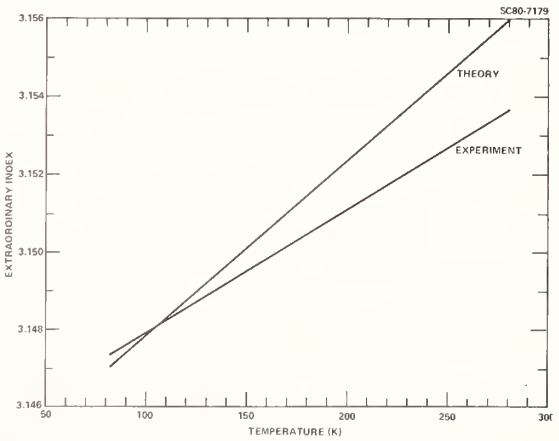

Fig. 2 Comparison of the predicted temperature dependence of the extraordinary refractive index of Tl_3AsSe_3 with experiment.

The strain-optic coefficients (P_{ijkl}) are defined in terms of the change in the dielectric impermeability tensor (B_{ij}) with respect to elastic strain (ε_{kl}):[7]

$$\Delta B_{ij} = \sum_{k,l} P_{ijkl}\, \varepsilon_{kl} \quad .$$

To examine the effect of a uniaxial strain in TAS along the optic axis, the lattice parameter, c, is modified as follows: $c' = (1 + \delta)c$ where δ is a small number. Then, since TAS has the point group 3m, $\Delta B_1 = \Delta B_2 = P_{13}\delta$ for ordinary polarized light and $\Delta B_3 = P_{33}\delta$ for extraordinary light, where we have used the standard contracted indices notation.[7] The strain-optic coefficients are then defined in terms of the refractive indices as:

$$P_{13} = \left[(n_o^{-2})_s - (n_o^{-2})_u\right]/\delta \quad \text{and} \quad P_{33} = \left[(n_e^{-2})_s - (n_e^{-2})_u\right]/\delta$$

where subscripts "s" and "u" refer to "strained" and "unstrained," respectively.

Conclusion - We have outlined a predictive methodology for calculating refractive indices and electro- or strain-optic coefficients. To test its fundamental basis, this theory was successfully employed in predicting the photoelastic constants and the temperature dependences of the refractive indices of Tl_3AsSe_3.

References

1. N. Uchida and N. Niizeki, Proc. of the IEEE 61, 1073 (1973).
2. R.W. Dixon, J. Appl. Phys. 38, 5149 (1967).
3. I.P. Kaminow and E.H. Turner, Proc. of the IEEE 54, 1374 (1966).
4. D.A. Pinnow, IEEE QE-6, 223 (1970).
5. I.P. Kaminow and E.H. Turner, in CRC Handbook of Lasers, p. 447 (1974).
6. I.C. Chang, IEEE SU-23, 2 (1976).
7. J.F. Nye, Physical Properties of Crystals, (Oxford Univ. Press, Oxford, 1976), p. 244.
8. W.A. Harrison, Electronic Structure and the Properties of Solids, (Freeman, San Francisco, 1980).
9. J.C. Slater and G.F. Koster, Phys. Rev. 94, 1498 (1954).
10. S. Froyen and W.A. Harrison, Phys. Rev. B20, 2420 (1979).
11. M.D. Ewbank, P.R. Newman, N.L. Mota, S.M. Lee, W.L. Wolfe, A.G. DeBell, and W.A. Harrison, to be published.
12. H. Y-P Hong, J.C. Mikkelsen and G.W. Roland, Mat. Res. Bull. 9, 365 (1974).
13. M.D. Ewbank, E.A. Kraut, S.P. Kowalczyk, W.A. Harrison, to be published.

DISPERSION OF THERMO-OPTIC COEFFICIENTS OF Nd LASER MATERIALS

K. E. Wilson and L. G. DeShazer
Hughes Research Laboratories
3011 Malibu Canyon Road
Malibu, CA 90625

We developed a double interferometer capable of measuring simultaneously both the coefficient of linear expansion α_ℓ and the thermo-optic coefficient α_n and also capable of measuring differences in dB/dT in anisotropic materials to better than 2%. The experimental technique consisted of having the sample in one arm of a Twyman-Green interferometer which formed the first interferometer and the second interferometer, a Fizeau type, was formed by the reflected beams from the front and back faces of the sample. The measured phase shifts in the Fizeau interferometer are caused by optical path length changes in the sample, while the phase shifts in the Twyman-Green are caused by path length changes between the two arms of the interferometer. The linear expansion and thermo-optic coefficients are therefore determined from the simultaneous solution of the equations for the phase shifts in the two interferometers.

The thermo-optic coefficients α_n and the thermal expanion coefficient α_ℓ were determined for seven laser materials: YAG, YALO, BeL, ruby ($Cr:Al_2O_3$), quartz, ED2 and Nd Kodak glasses using the double interferometer technique. For YAG and ED2 glass, the wavelength variation of the thermo-optic coefficient was fitted to a single resonance theoretical model from which the relative variation of the electronic resonance frequency with temperature $\omega_g^{-1}\, d\omega_g/dt$ was determined to be -1.73×10^{-5}/°C (undoped YAG), -1.77×10^{-5}/°C (Nd:YAG) and -1.39×10^{-5}/°C for ED2 glass. As a comparison, these values were determined for NaCl and quartz and are -2.03×10^{-5}/°C and -0.97×10^{-5}/°C respectively. Fig. 1 shows the wavelength dependence of the electronic resonance contribution to the thermo-optic coefficient.

In the course of our experiments, we discovered a new technique for precisely measuring the temperature dependence of the birefringence of anisotropic materials. We call this technique "fringe beating" which is the superposition of the interference fringes for the two orthogonal polarizations in the sample and is very sensitive for measuring small values of dB/dT, capable of measuring values of dB/dT on the order of 10^{-7}/°C. Figure 2 illustrates the beating for both Twyman-Green and Fizeau interferometer fringes with increasing sample temperature using ruby.

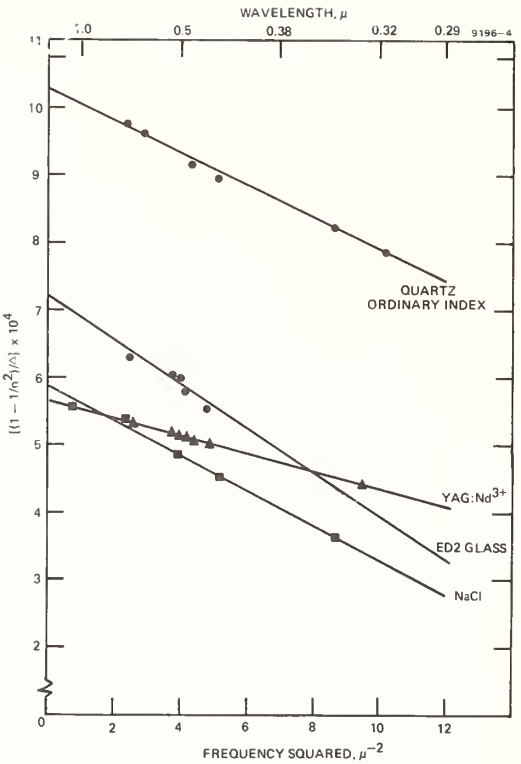

Figure 1. Plots of $(1-n^{-2})/\Delta$ vs. λ^{-2} where Δ is the electronic resonance part of the thermo-optic coefficients.

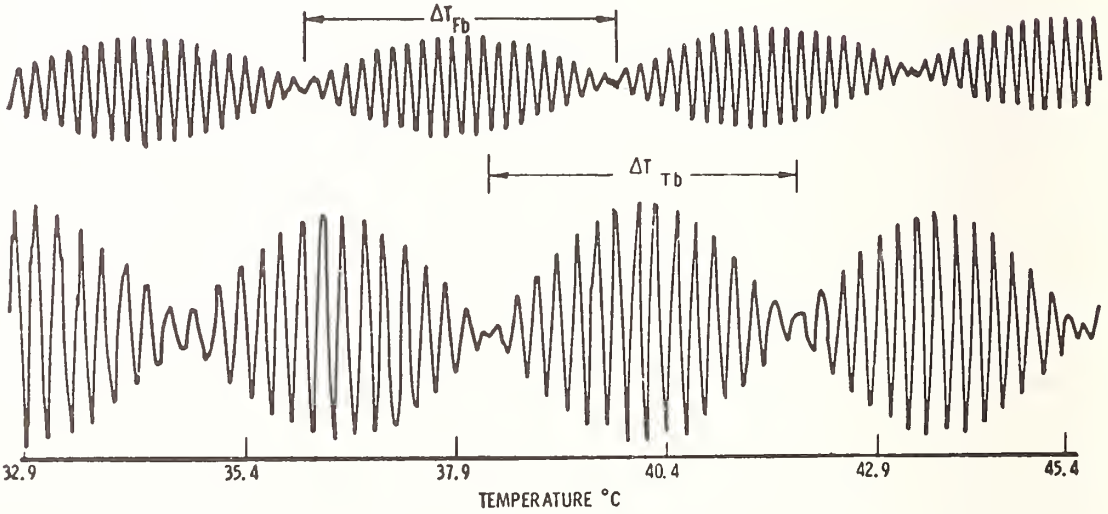

Figure 2. Beating of interferometer fringes for ruby (60° cut) for increasing T where top trace is Fizeau fringes and bottom, Tywman-Green.

TEMPERATURE DEPENDENCE OF THE OPTICAL PROPERTIES OF SOME METALS AT VISIBLE AND INFRARED WAVELENGTHS

D. L. Decker and V. A. Hodgkin
Michelson/Lauritsen Laboratories
Naval Weapons Center, China Lake, California 93555

This paper briefly describes experimental techniques and apparatus developed at the Naval Weapons Center for measuring temperature-dependent changes in the near-normal incidence reflectance (R) of a sample to a precision of a few parts in 10^5 [1]. Reflectance results obtained from this instrument are presented for Al, Cu, Ag, and Mo films and bulk material over the 0.6 to 10.0 μm wavelength range at temperatures from 80 to 450°K. The sample and reference surfaces were protected in ultrahigh vacuum for these measurements. These data (dR/dT) are analyzed by a differential Kramers-Kronig technique to yield the temperature dependence of the real and imaginary parts of the index of refraction and dielectric constants [2].

The infrared optical properties of a "good" metal are described classically by the simple Drude model [3]. The temperature dependence of the optical constants computed from this model primarily arises from the temperature dependence of the dc conductivity (σ) [4]. For the metals considered in this paper, at temperatures near room temperature and at wavelengths in the infrared, nearly wavelength and temperature independent values of dR/dT are computed from measured values of $\sigma(T)$. In the far infrared, the measured and computed values of dR/dT are in reasonable agreement and are on the order of -1×10^{-5}/°C. In detail, there are discrepancies which are both time and temperature dependent. Reflectance data taken with ascending and descending temperatures show hysteresis with very noticeable time dependence. Especially at elevated temperatures, permanent changes in reflectance do occur due to "annealing." Much of the time-dependent variation is very similar to that previously seen in heat capacity, thermal conductivity, and electrical resistivity and is broadly described under the title of "premelting effects" [5].

At shorter wavelengths in the visible and ultraviolet, these metals have an additional dispersion mechanism associated with electron interband transitions. This dispersion acts in addition to that provided by intraband electron transitions, which is accounted for by the Drude model. For example, in Al, a very pronounced dip occurs in reflectance with a minimum at about 0.83 μm, which has been identified with interband transitions near specific critical points in the Brillouin zone of this face centered cubic metal [6]. In this region, both the magnitude and sign of dR/dT fluctuate wildly, and at a given wavelength, dR/dT is

strongly temperature sensitive. This is especially true near 0.81 μm where $dR/dT \approx 0$. The detailed temperature dependence of the reflectance near the region of the interband transition is also strongly dependent upon the condition and method of preparation of the sample. Data are presented for both evaporated film and single-crystal samples. Another class of non-Drude effects has been discovered for Ag in the near infrared, which also causes a sign reversal in dR/dT. This effect occurs in a region where the reflectance is known to be very sensitive to surface roughness and may be associated with a surface plasmon-like excitation which is coupled to the incident light by very small slope, spatially uncorrelated surface roughness.

The data presented in this paper is of immediate engineering value in computing the performance of optical systems whose components necessarily operate at temperatures other than room temperature. It is also hoped that it will stimulate theoretical interest in examining some of the subtle and poorly understood dispersion effects such as those seen in the near infrared in silver.

References

[1] D. L. Decker, "Measurement of the Optical Constants of Thin Films of Silver and Other Metals at Temperatures Near Room Temperature," in *High Energy Laser Mirrors and Windows*, ARPA Semi-Annual Report #2, ARPA Order 2175 (Mar 1973), pp. 34-49.

[2] D. L. Decker, J. Opt. Soc. Am. 61, 679 (1971).

[3] H. E. Bennett and J. M. Bennett, "Validity of the Drude Theory for Silver, Gold, and Aluminum in the Infrared," *Optical Properties and Electronic Structure of Metals and Alloys*, ed. by F. Abelès (North Holland Publishing Co., Amsterdam, 1966), pp. 175-188.

[4] G. A. Boloshin, Opt. Spectrosc. 18, 423 (1965).

[5] G. Borelius, "The Changes in Energy Content, Volume and Resistivity With Temperature in the Simple Solids and Liquids," in *Solid State Physics*, Vol. 15, ed. by F. Seitz and D. Turnbull (Academic Press, New York, 1963), pp. 1-51.

[6] H. Ehrenreich, A. R. Philipp, and B. Segall, Phys. Rev. 132, 1918 (1963).

OPTICAL PROPERTIES OF Ti DIFFUSED $LiNbO_3$ WAVEGUIDES

W. K. Burns
Naval Research Laboratory
Washington, DC 20375

We will discuss measurements of the optical properties of $LiNbO_3$ which are pertinent to optical waveguiding applications. $LiNbO_3$, which is both electro-optic and piezoelectric, has many potential uses in integrated optic applications, including communications, signal processing, and spectrum analysis. Typically, optical waveguides are formed in $LiNbO_3$ by the diffusion of thin films of Ti at high temperatures, resulting in an increased index of refraction in a surface layer.[1] The waveguide is then characterized by the diffusion length and the surface index change. Since $LiNbO_3$ is uniaxial, the diffusion coefficients are anisotropic and the index change depends on optical polarization. The situation is complicated by the outdiffusion of Li which occurs simultaneously with the indiffusion of Ti, and causes a non-stoichiometric surface layer with a corresponding increase in the extraordinary index of refraction. Using a suitable dispersion theory to describe the graded-index waveguide, it is possible to obtain the index changes and diffusion coefficients from optical measurements of the effective indices (phase velocity) of the propagating modes.[2] By using a series of waveguides which vary in a known manner, a fairly complete description of the diffusion process can be obtained. Alternatively, using analyzing techniques such as secondary-ion mass spectrometry (SIMS), the Ti and Li concentration profiles can be observed directly. In channel waveguide devices, the extent of lateral diffusion from the channel is sometimes of interest. This effect has been successfully measured by the electron microprobe.

In integrated optical spectrum analyzer applications utilizing Ti diffused $LiNbO_3$ waveguides, it is desirable to induce absorption in various parts of the waveguide and substrate. This would improve the signal to noise ratio by reducing optical noise at the detector array. We will discuss the creation of optically absorbing layers which result from the implantation of H into bulk and Ti diffused $LiNbO_3$.

References

1) R. V. Schmidt and I. P. Kaminow, Appl. Phys. Lett. 25, 458 (1974).

2) W. K. Burns, P. H. Klein, E. J. West and L. E. Plew, J. Appl. Phys. 50, 6175 (1979).

OPTICAL PROPERTIES OF THIN FILMS BY GUIDED WAVES AND SURFACE POLARITONS

J. D. Swalen
IBM Research Laboratory
San Jose, California 95193

Guided optical waves, also called integrated optics, are optical waves which propagate in a thin layer, usually a few micrometers thick.[1] These parallel plate waveguides, as in the microwave case, have propagation characteristics which follow directly from a solution of Maxwell's equations matching the boundary conditions at each interface. The optical fields are highly localized within the film and the polarization of the light can be either s or p. Coupling is usually accomplished by high index half prisms[2] as illustrated in Fig. 1 or gratings.[3] The mode characteristics, the number of nodes in the optical field across the guide, their angle of propagation and their attenuation, can be analyzed to give detailed information about the film thickness and its refractive index, real and imaginary parts, or its related dielectric function.[4]

Surface polaritons are surface waves which propagate along an interface.[5] Like guided waves they are also highly localized but in this case decaying exponentially away from the surface. They exist only for p polarized light and require that the sum of the real parts of the two dielectric functions at the interface be less than zero. This can be accomplished either with a metal at energies below the bulk plasmon energy or with a strong absorber where the real part of the dielectric constant becomes sufficiently negative. For the case of a metal the surface wave is called a plasmon surface polariton and the polarization change at the interface of metal and dielectric comes from the oscillations of the pseudo-free electrons in the metal. For the case of a strong absorber the surface wave is called an exciton surface polariton when the absorption is from excitons and a phonon surface polariton when the absorption is from phonons. The dispersion curve is shown in the top of Fig. 2.

Coupling is again accomplished with high index prisms[6,7] or gratings[8] but since the propagation is for only a very short distance, a few micrometers in the visible region of the optical spectrum, the reflected instead of the propagated light is observed, see Fig. 1. In Fig. 2 a typical reflectivity curve is shown, θ_c being the critical angle for prism-air interface. Measurement of this reflectivity minimum gives a measure of dielectric function (and the thickness in

the Kretschmann scheme shown in the lower left of Fig. 1) of the metal or strongly absorbing layer. Overlayers of transparent or absorbing films shift the angle at which the reflectivity minimum occurs. This shift is a function of both the thickness and the refractive index (the real part) of the overlayer but from this measurement only one can be determined. Absorption has the added features of broadening and changing the depth of the reflectivity minimum. Detailed analysis of this exciton - plasmon surface polariton interaction has explained[9] this anomalous dispersion behavior which is orientationally dependent. Absorption, fluorescence,[10] Raman scattering,[11,12] lifetime, spatial and orientational dependency, and scattering from surface roughness[13] are some of the many observables which can be analyzed to characterized a film and the species within it. Recently thick liquid crystal cells next to metal electrodes have also been studied by surface polaritons as a function of applied electric field to determine the anchoring and reorientational characteristics.[14]

1. See for example D. Marcuse, Theory of Dielectric Optical Waveguides, (Academic, New York, 1974).
2. P. K.Tien, R. Ulrich, and R. J. Martin, Appl. Phys. Letters 14, 291 (1969).
3. M. K. Dakss, L. Kuhn, P. F. Heidrich and B. A. Scott, Appl. Phys. Letters 16, 523 (1970).
4. J. D. Swalen, J. Phys. Chem. 83, 1438 (1979).
5. E. Burstein, 'Introductory remarks on polaritons', Polaritons, Proceedings of the First Taormina Research Conference on the Structure of Matter, Edited by E. Burstein and F. de Martini, (Pergamon, New York, 1974).
6. A. Otto, Z. Physik 216, 398 (1968).
7. E. Kretschmann and H. Raether, Z. Naturforsch. 23a, 2135 (1968).
8. A. Girlando, M. R. Philpott, D. Heitmann, M. R. Philpott, J. D. Swalen and R. Santo J. Chem. Phys. (in press).
9. I. Pockrand, J. D. Swalen, J. G. Gordon II, and M. R. Philpott, J. Chem. Phys. 70, 3401 (1979).
10. W. H. Webber and C. F. Eagen, Optics Letters 4, 236Z(1979).
11. G. Burns, F. Dacol, J. C. Marinace, B. A. Scott and E. Burstein, Appl. Phys. Letters 22, 356 (1973).
12. J. F. Rabolt, R. Santo, and J. D. Swalen, J. Appl. Spectrosc. (in press).
13. I. Pockrand, Optics Commun. 13, 311 (1975).
14. J. D. Swalen and G. J. Sprokel, 'Liquid crystal - surface interactions by surface plasmons', Symposium on the Physics and Chemistry of Liquid Crystal Devices, IBM Symposium Series (Plenium Press, New York, 1979).

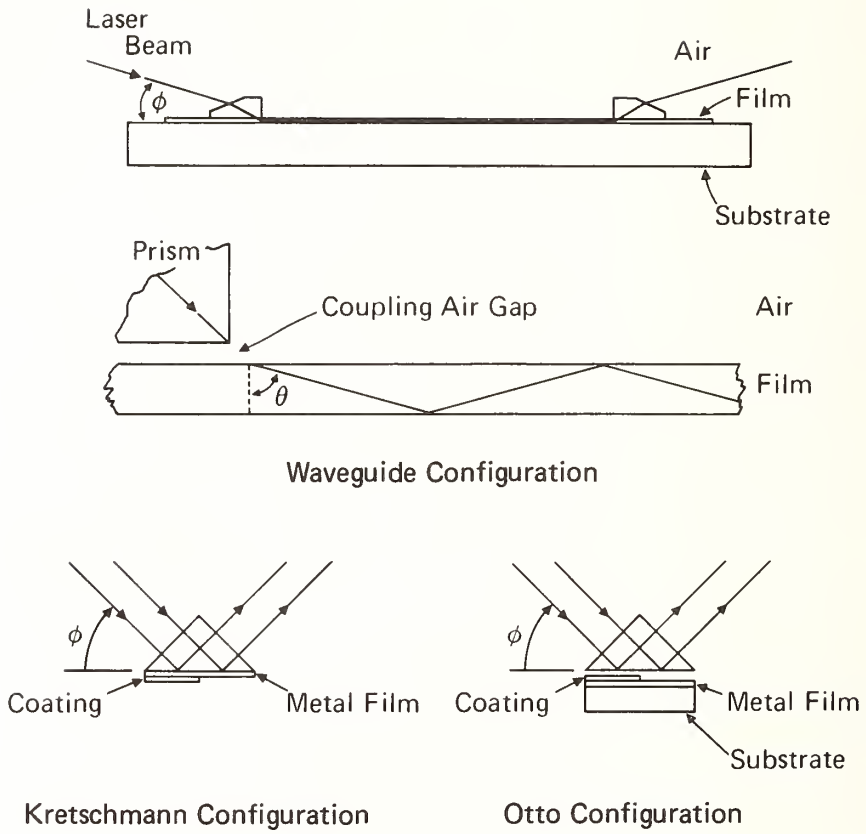

Fig. 1. The schematics for coupling light into guided waves and surface waves. In the top figure for waveguide coupling the film thickness is exaggerated and the angle ϕ is changed to couple to different modes. The middle figure is an enlargement showing the optical rays. The lower figures illustrate the two methods for coupling to surface waves. In the Kretschmann configuration the metal film must be thin enough for the evanescent wave to penetrate to the bottom side.

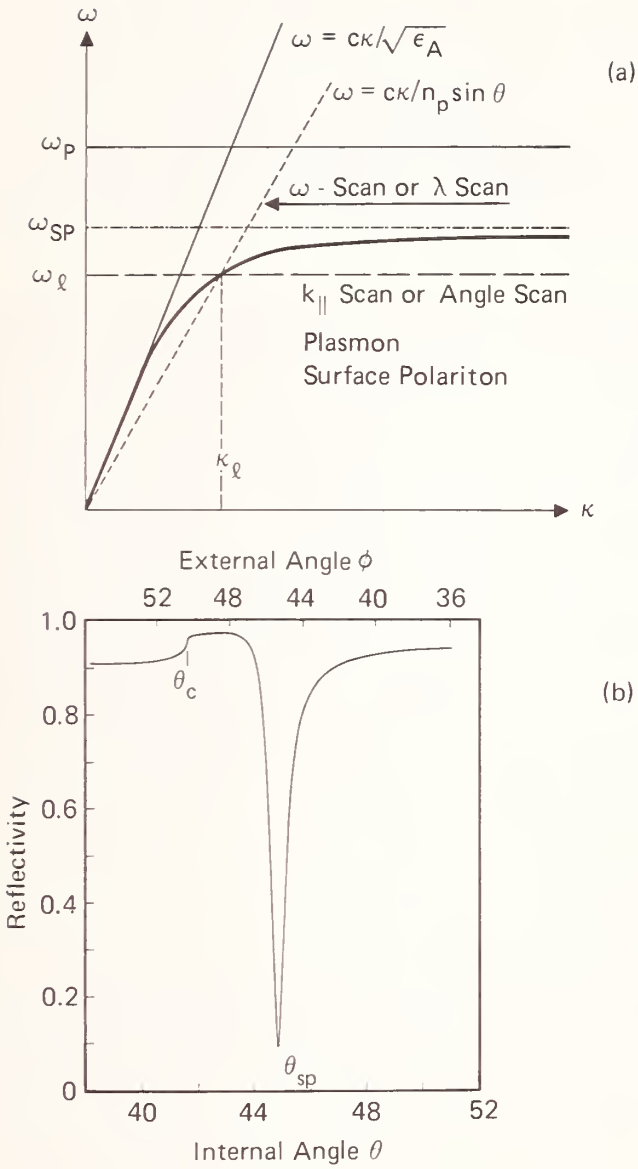

Fig. 2a The dispersion curve (ω vs. κ) for plasmon surface polaritons (SP) and its intersection with a laser frequency ω_ℓ and propagation vector κ_ℓ. The frequency ω_p is the bulk plasmon, ϵ_A is the dielectric function of the dielectric half space, and n_p is the refractive index of the coupling prism. 2b A typical reflectivity curve.

PROPERTIES OF LOW LOSS DIFFUSED OPTICAL WAVEGUIDES IN GLASS

T. Findakly, E. Garmire
Center for Laser Studies
University of Southern California
University Park, Los Angeles, California 90007

Graded index waveguides in glass are typically fabricated by ion exchange from a silver nitrate melt. Residual losses observed in such waveguides are from 0.5 to 2 dB/cm and are generally attributed to either scattering from surface irregularities or loss due to silver grains. In order to reduce the loss, and to investigate mechanisms for loss in glass waveguides, we have investigated other techniques of fabrication. In particular, we have employed a dry process, diffusing metallic silver into the glass substrates. In addition, we have investigated the effect of an electric field applied during diffusion. We have observed losses so low as to be unmeasurable (0.1 dB/cm), and have made both single mode waveguides and highly multimode waveguides with large numerical aperatures. We report measurements of mode-dependent losses in these waveguides at several wavelengths and also of absorption, measured calorimetrically. In addition, we report experiments on burying the waveguide below the surface.

Silver films several hundred angstroms thick were evaporated on soda-lime silicate glass slides and diffusion was carried out at 500°C in oxygen, for periods from 5 minutes to 7 hours forming waveguides at 6328Å of depths from 6 μm to 85 μm.

The waveguide losses of the thicker waveguides were lower than could be measured by monitoring the decrease in scattered light as a function distance along the waveguide, using the photomultiplier. This very low loss was due to a combination of relatively thick waveguides and a low concentration of silver, which reduced both absorption and scattering from any possible aggregates. The losses increased somewhat as the waveguides were made thinner, however. Figure 1 shows the loss as a function of the diffusion time, and would indicate that surface scattering is the dominant loss mechanism in this case (assuming an infinite diffusion source). Although they have very low loss, these waveguides have the advantage of having a very low index ($\Delta n \sim 0.002$). It is interesting to note that the ions may diffuse very far (85 μm), but with a very low solubility. This is in contrast to the high concentration of silver ions achieved with ion exchange.

In order to increase the index of the waveguides, we applied an electric field during diffusion. Diffusion was carried out at 300°C in air with an applied electric field of from 0 to 100 V/mm for periods ranging from a few minutes to one hour. The ionic current ranged from micro-

amperes to a few milliamperes and was monitored throughout. The refractive index profile for the multimode guides could be determined from the WKB method and is shown in Fig. 2. It can be seen that large refractive index increases can be obtained. The large index profiles obtained are very different from the erfc(x) profiles usually observed in ion exchange. These flatter distributions do not concentrate the light so close to the surface and should have a smaller loss contribution due to surface scattering than do those fabricated by ion exchange.

These studies show that by applying an electric field it is possible to drive as many silver ions into the glass as with ion exchange. We observed index changes as large as 0.03. A monitoring of the ionic current showed a decrease in exchange current as a function of time, which we attributed to a buildup of sodium on the gold cathode. In order to continue the diffusion for a long time and make deep waveguides, we have found it necessary to use $NaNO_3$ as the cathode.

These waveguides typically show more loss than those fabricated without an electric field. This appears to be due to the much larger silver content of the guides. The losses in these guides are $\sim$1 dB/cm and are comparable to those quoted in the literature for ion exchanged guides. The mode dependent loss was measured for a highly multimode waveguide and is shown in Fig. 3. The decrease in loss with increasing mode number differs from the independence observed in ion exchanged guides. The reasons for this difference will be discussed.

We have found that it is possible to reduce the loss below that shown in Fig. 2 by annealing after electro-diffusion. Reductions to less than 0.5 dB/cm for all modes was typical. Further reduction of the loss is possible by burying the waveguide below the surface. We fabricated an electro-thermally diffused waveguide, removed excess silver oxide, applied new electrodes and reintroduced the sample into the furnace. The loss was decreased by 70% and the fact that the guide was buried below the surface was confirmed by the substantial reduction in prism coupling efficiency.

In this paper we shall present detailed results on the losses for single mode guides and highly multimode guides. In addition, calorimetric absorption measurements and total loss measurements at other wavelengths are presently underway and will be presented at the conference.

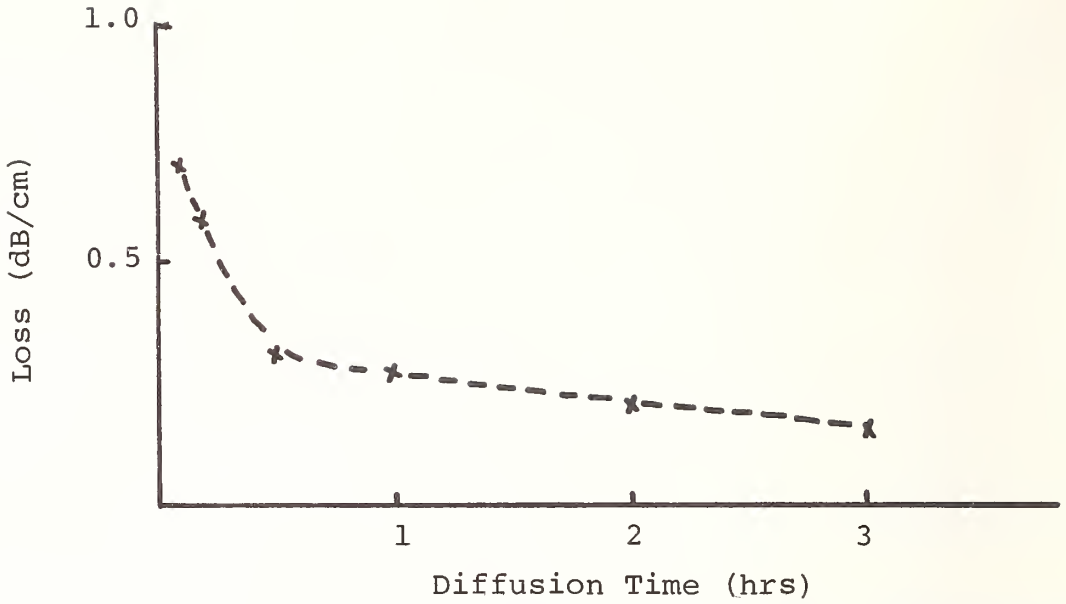

Fig. 1. Measured losses in waveguides fabricated by diffusion of evaporated silver at 500°C as a function of diffusion time.

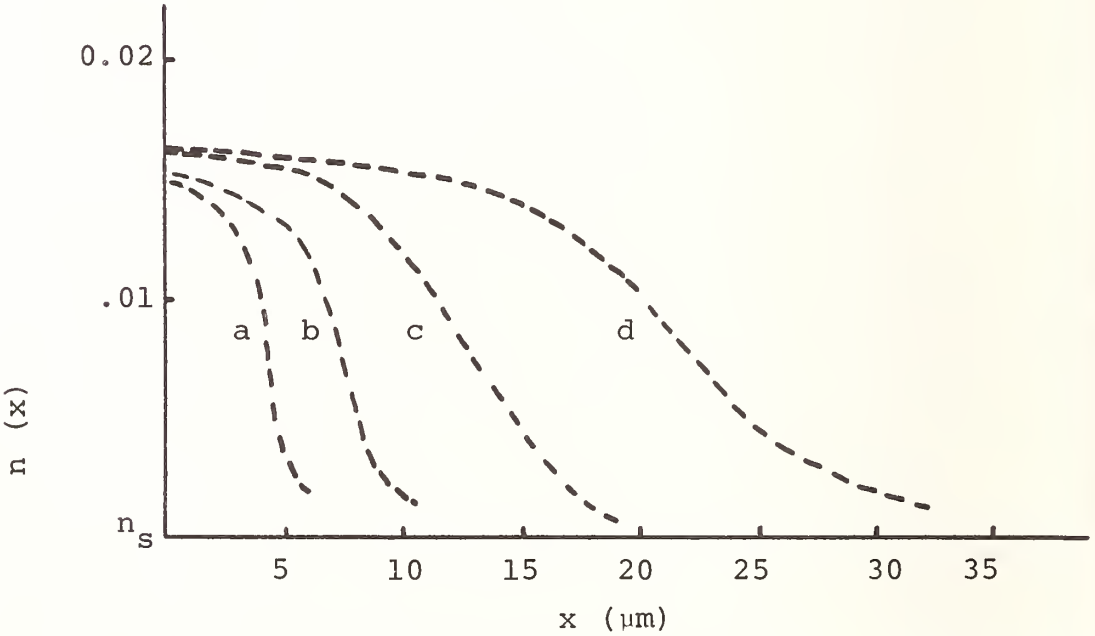

Fig. 2. Refractive index profiles for waveguides diffused in the presence of an electric field. (a) and (b) were at 60 V/mm with two metal electrodes for 15 and 60 min. respectively (c) and (d) were at 12 V/mm with a cathode of $NaNO_3$ for 1 and 2 hrs respectively.

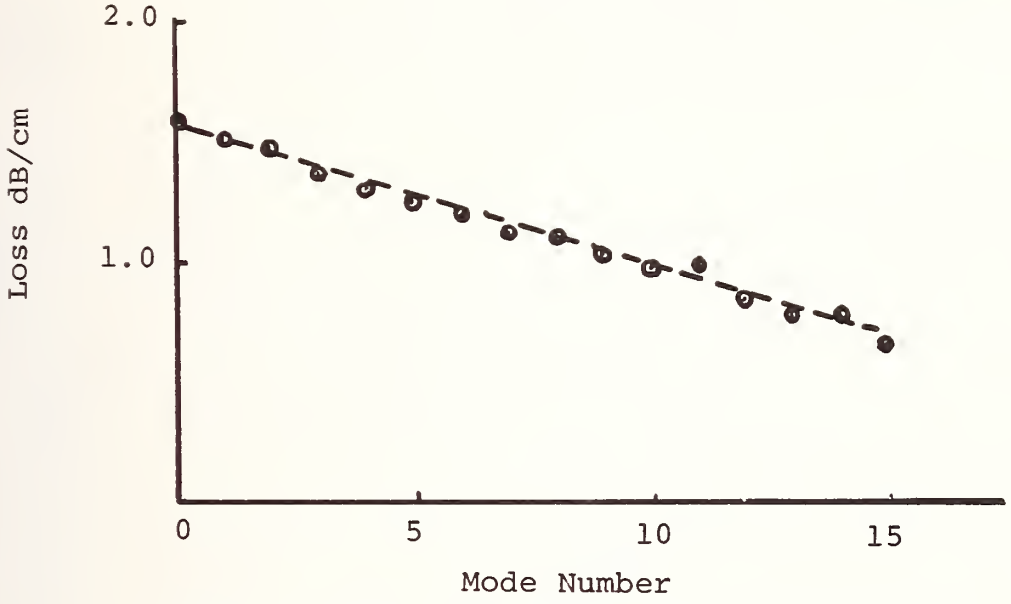

Fig. 3. Mode-dependent loss for a highly multi-mode waveguide

THICKNESS MEASUREMENT OF VERY THIN-FILMS BY OBSERVING ANOMALOUS LIGHT ABSORPTION

H. Kitajima†, K. Hieda† and Y. Suematsu††
† Kyushu Institute of Technology
Tobataku Kitakyushu, 804 Japan
†† Tokyo Institute of Technology
Ookayama Meguroku Tokyo, 152 Japan

1. Introduction

Rapid and accurate measurement of film thickness is important in many applications[1,2]. The prism coupler called m-line method[3], which is one of the most convenient methods, can not be used when a film is too thin or the refractive index of a film is too small to support a guided mode. We report here a powerful technique for measuring very thin-film thickness. The method is based on observing anomalous light absorptions in a metal-clad thin-film into which surface waves are excited through a prism[4]. A metal-clad thin-film, a transparent film coated on metal, can support the guided mode, number m=-1 of a TM wave, even the film is extremely thin[5,6]. Metal-clad films possess a quasi discrete spectrum of leaky modes[7] and a continuous spectrum of radiation modes. In contrast to the radiation modes which are observed by ellipsometry method[8], the leaky modes are obseved using a prism coupler. Therefore, the anomalous absorption characteristics strongly depend on the film thickness and the incident angle.

2. Theory

In the layered structure shown in Fig.1, the four media are denoted by subscripts j=1,2,3,4, respectively. Their refractive indices are n_j.

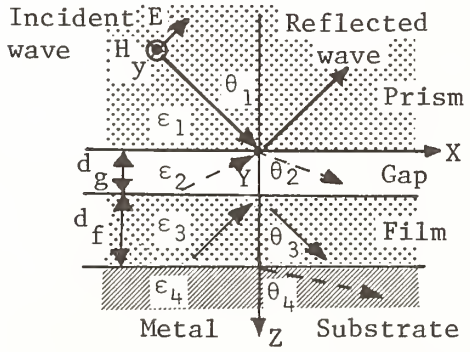

Fig.1. Prism-film coupling structure.

$$n_j = \sqrt{\varepsilon_j / \varepsilon_0} \quad (j=1,2,3)$$

$$n_4 = n_4' - i n_4'' = \sqrt{\varepsilon_4 / \varepsilon_0} \quad ,$$

$$\sqrt{\mu_j / \mu_0} = 1 \qquad (1)$$

$$k_0 = \omega \sqrt{\mu_0 \varepsilon_0} = 2\pi / \lambda_0$$

λ_0 : wavelength in vacuum space

$\exp[i\omega t]$: time convention

Let us assume that we are dealing with a plane wave which is impinging obliquely at the prism-gap boundary. The magnetic fields in each region are written as follows.

$$H_j = \exp[-i\beta x]\ (A_j \exp[-i\gamma_j z] + B_j \exp[i\gamma_j z]) \quad , \quad j=1,2,3,4 \quad , \tag{2}$$

where $A_1 = 1$ (incidence) , $B_4 = 0$,

$$\beta = k_0 n_j \sin\theta_j \tag{3}$$

$$\gamma_j = k_0 n_j \cos\theta_j \quad ; \quad \mathrm{Real}\{\gamma_j\} \geq 0 \quad , \quad \mathrm{Imag}\{\gamma_j\} \leq 0 \quad . \tag{4}$$

The reflection coefficient, B_1, at the prism-gap boundary is obtained

$$B_1 = \frac{\exp[i\phi_{12}] + B_2/A_2}{1 + \exp[i\phi_{12}]\cdot B_2/A_2} \quad , \quad \text{where} \tag{5}$$

$$\frac{B_2}{A_2} = \frac{-\exp[i\phi_{32}] + R_{34}\exp[i(\phi_{34}-2\phi_f)]}{1 - R_{34}\exp[i(\phi_{32}+\phi_{34}-2\phi_f)]} \cdot \exp[-2\alpha_g] \quad , \tag{6}$$

$$R_{jk} \exp[i\phi_{jk}] = \frac{\gamma_j/\varepsilon_j - \gamma_k/\varepsilon_k}{\gamma_j/\varepsilon_j + \gamma_k/\varepsilon_k} \quad , \tag{7}$$

$$R_{12} = R_{32} = 1 \quad , \quad R_{34} \neq 1 \quad , \quad \exp[i\phi_{jk}] = -\exp[i\phi_{kj}] \quad , \tag{8}$$

$$2\phi_f = 2\gamma_3 d_f \quad , \tag{9}$$

$$2\alpha_g = i2\gamma_2 d_g = 2|\gamma_2| d_g \quad . \tag{10}$$

The normalized film thickness (guided modes) :

$$\frac{d_f}{\lambda_0} = \frac{\phi_{32} + \phi_{34} + 2m\pi}{4\pi n_3 \cos\theta_3} \quad , \quad (m=-1,0,1,2,\cdots) \quad . \tag{11}$$

The no-reflection ($B_1=0$) conditions are given as

$$\Delta\phi_f \simeq \Delta\rho \tan\left(\frac{\pi}{2} - \phi_{12}\right) \quad , \quad \Delta(d_f/\lambda_0) = \frac{\Delta\rho \tan\left(\frac{\pi}{2} - \phi_{12}\right)}{4\pi n_3 \cos\theta_3} \quad ; \tag{12}$$

$$\frac{d_g}{\lambda_0} \simeq \frac{1}{4\pi|n_2\cos\theta_2|} \log\left\{\frac{2\sin\phi_{32}}{\sqrt{\Delta\rho^2 + \Delta\phi_f^2}}\right\} \quad , \quad \text{where} \tag{13}$$

$$\Delta\rho = 1 - R_{34} \quad , \tag{14}$$

$$\Delta\phi_f = \phi_{32} + \phi_{34} + 2m\pi - 2\phi_f \quad . \tag{15}$$

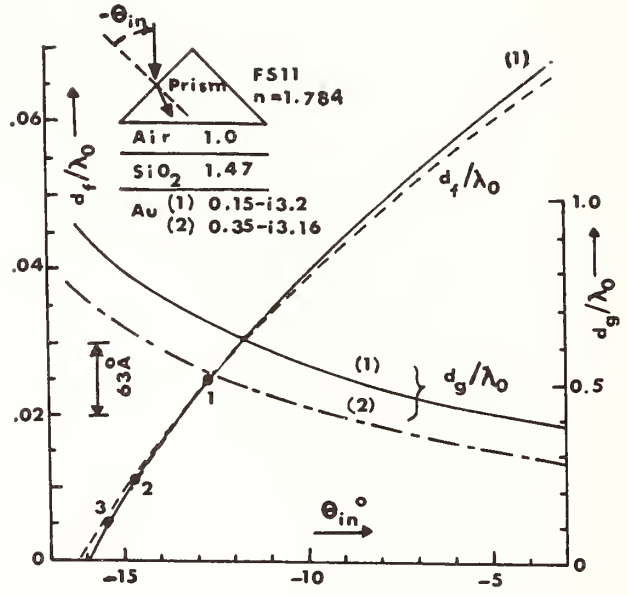

Fig.2. Film and gap thicknesses as functions of incident angles for the no-reflection. d_f/λ_0, d_g/λ_0 versus θ_{in}°. The broken line is corrected film thichness for the no reflection. The three dots (1,2,3) are experimental data.

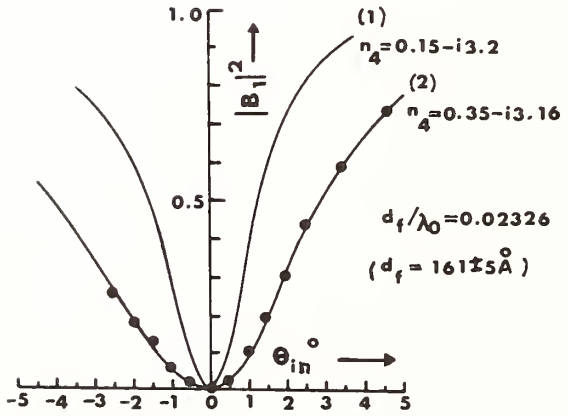

Fig.3. Light absorption characteristics as a function of incident angle. $|B_1|^2$ versus θ_{in}°. The plots are experimentally measured values.

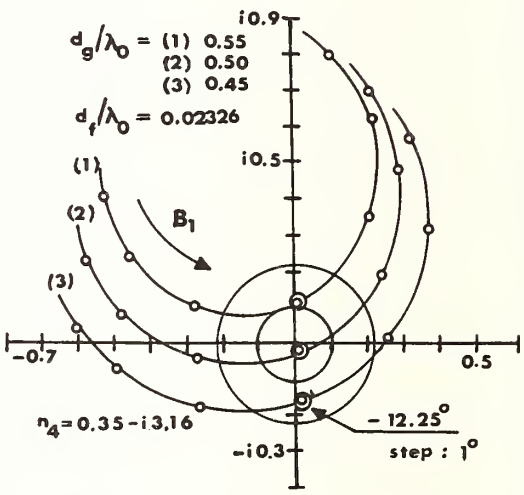

Fig.4. Vector trajectories of reflection coefficient showing resonant absorption. B_1 versus θ_{in}°. (◎ : guided mode point)

3. Experimental Results and Discussion

First, we determined the refractive index of sputtered silica films on gold films which support several guided modes.

Refractive index of sputtered SiO_2: 1.47 ± 0.002 at 6328Å

Next, we measured thickness of very thin silica films on gold, which is sputtered on glass substrates. Relation between the incident angles and the thickness are shown in Fig.2. According to Fig.3, the measured absorption characteristic fits in well with the calculated curve using the index of bulk gold. However, thickness differences between the bulk and evaporated gold are within 3Å for all samples. We did not deal with a serious matter here; the complex refractive index of the gold should have been measured.

From the vector trajectories shown in Fig.4, one can understand that when a trajectory crosses the origin, the reflection coefficient becomes zero. However, even when the reflection does not become zero completely, the incident angles at which the reflection becomes minimum are not so different from the angles which satisfy the guided mode. Therefore, rapid and accurate thickness measurement is possible.

Table 1. Measured samples.

Sample	Determined Thickness	Measured Thickness[Å]	
		Evaporated*	Bulk†
1	161±5	162.06	159.27
2	71±5	72.39	69.79
3	32±5	33.98	31.47
* $0.15-i3.2$, † $0.35-i3.16$ at λ_0=6328Å			

4. Conclusion

This work has demonstrated the feasibility of using anomalous light absorptions in metal-clad thin-film systems, as a thickness measurement method for very thin films. Complex refractive index of metal may also be measured in this way. Unlike ellipsometry, this technique need not to measure either the reflection ratio or the phase difference.

References

1. N. M. Bashara and D. W. Peterson, J. Opt. Soc. Am., 56, pp.1320-1331, 1966.
2. P. K. Tien, Rev. Mod. Phys., 42, 2, pp.361-420, 1977.
3. P. K. Tien, R. Ulrich and R. J. Martin, Appl. Phys. Lett., 10, 14, pp.291-294, 1969.
4. V. Shah and T. Tamir, Opt. Commun., 23, 10, pp.113-118, 1977.
5. A. Otto, Zeit Phys., 216, pp.398-410, 1968.
6. A. Otto and W. Sohler, Opt. Commun., 3, pp.254-258, 1971.
7. K. Furuya and Y. Suematsu, Trans. IECE Jpn., 57-c, 11, pp.411-418, 1974.
8. R. J. Archer, J. Opt. Soc. Am., 52, pp.970-977, 1962.

INTERFEROMETRIC WAVELENGTH MEASUREMENT OF INFRARED SURFACE WAVES

Z. Schlesinger and A. J. Sievers
Laboratory of Atomic and Solid State Physics
Ithaca, N. Y. 14853

We have developed an interferometric technique for accurately measuring the wavelength of surface electromagnetic waves (SEW's) on coated metal surfaces. A variable pathlength, two-beam interferometer is employed in which the beam separation and interference take place entirely on the coated surface. The SEW's comprise one arm of the interferometer and bulk waves traveling just above the surface the other. The observed interferograms are in good agreement with model predictions.

Consider the propagation of a SEW across a partially coated surface such that the coated region occupies an intermediate section of the SEW path. The interference phenomenon involves the inhomogeneous nature of the SEW in an essential way. The field amplitudes of a SEW decay exponentially with distance away from the surface. This distance is very sensitive to small changes in the SEW wavelength which, in turn, depends on the state of the surface. For example, at the free space wavelength λ_o = 10 microns, the SEW on a bare gold surface has a wavelength λ_s = 9.999 microns and extends 60 microns in the air above the surface, while the SEW on a gold surface with a 0.05 micron Ge overlayer has a wavelength λ_s = 9.992 microns and extends only 20 microns above the surface. This discrepancy in the SEW extent makes it impossible for the bound SEW to maintain its integrity when it traverses a boundary between coated and uncoated regions of surface. Specifically the electromagnetic boundary conditions require that the tangential E and H fields be continuous at the boundary between the coated and uncoated regions at all heights above the interface. When the SEW is incident at the first coating edge this condition can be satisfied only if bulk (unbound) radiation is produced in transmission in addition to the transmitted (bound) SEW. At the far edge of the overlayer the SEW and bulk wave packet both contribute to the transmission of a bare metal SEW; however, these two contributions will in general no longer be in phase. The total intensity of the resultant SEW is

$$I(\ell) = I_{SEW}(\ell) + I_B(\ell) + 2\sqrt{I_{SEW}(\ell) I_B(\ell)}\cos\left[\frac{2\pi}{\lambda_o}\left(\frac{\lambda_o}{\lambda_s} - 1\right)\ell\right] \qquad (1)$$

where $I_{SEW}(\ell)$ and $I_B(\ell)$ are the component intensities and ℓ is the length of the coated region across which the beam travels. From the third term in Equation (1), the spatial period of the interference is

$$\Delta\ell = \frac{\lambda_o}{\lambda_o/\lambda_s - 1} \quad .$$

Because $\lambda_o/\lambda_s - 1$ is small, large interference periods will be produced by relatively short wavelength radiation (e.g. $\Delta\ell \cong 3$ mm at $\lambda \cong 10\mu$).

To test these conclusions, evaporated Ag and Au films were deposited on KCl couplers.[1] Over part of these rectangularly shaped films thin Ge overlayers of a triangular shape were then deposited. Both the metal and Ge film evaporations were carried out at a pressure of 4×10^{-6} torr. The SEW was launched from a CO_2 laser beam at one edge of the metal film by means of the edge coupling technique.[1] The length, ℓ, of the overlayer region probed by the beam was continuously varied by translating the film assembly in the plane of the surface but perpendicular to the beam direction. The transmission was measured as a function of ℓ for fixed overlayer thicknesses, d, and CO_2 laser wavelength, λ_o.

Ge overlayers ranging in thickness from $0.1\mu \leq d \leq 0.7\mu$ were studied in this manner in the range $9.2\mu \leq \lambda_o \leq 10.8\mu$. In each case the observed transmission characteristics and interference period were in agreement with model predictions.

In conclusion the SEW interferometer provides a unique method for studying thin films on metal surfaces. Not only is the attenuation of the SEW obtained but also, of equal spectroscopic significance, the wavelength of the SEW is measured, an undetermined quantity in ordinary transmission measurements.

ACKNOWLEDGMENTS

The authors acknowledge valuable conversation with R. Warner and Y. Chabal.

Work supported by AFOSR under Grant #AFOSR-76-3684. Additional support was received from the National Science Foundation under Grant No. DMR-76-81083 A02 and technical report #4210, to the Cornell Materials Science Center.

REFERENCE

1. Y. Chabal and A. J. Sievers, Appl. Phys. Lett. 32, 90 (1978).

AUTHOR INDEX

☆ U.S. GOVERNMENT PRINTING OFFICE : 1980 O-311-046 (54)

NBS-114A (REV. 9-78)

U.S. DEPT. OF COMM. BIBLIOGRAPHIC DATA SHEET	1. PUBLICATION OR REPORT NO. SP 574	2. Gov't. Accession No.	3. Recipient's Accession No.

4. TITLE AND SUBTITLE
Basic Optical Properties of Materials, Summaries of Papers (Topical Conference on Basic Optical Properties of Materials)

5. Publication Date
May 1980

6. Performing Organization Code

7. AUTHOR(S)
Albert Feldman, Chairperson, Editorial Committee

8. Performing Organ. Report No.

9. PERFORMING ORGANIZATION NAME AND ADDRESS

NATIONAL BUREAU OF STANDARDS
DEPARTMENT OF COMMERCE
WASHINGTON, DC 20234

10. Project/Task/Work Unit No.

11. Contract/Grant No.

12. SPONSORING ORGANIZATION NAME AND COMPLETE ADDRESS *(Street, City, State, ZIP)*

National Bureau of Standards
Department of Commerce
Washington, DC 20234

Optical Society of America
1816 Jefferson Place NW
Washington, DC 20036

13. Type of Report & Period Covered

14. Sponsoring Agency Code

15. SUPPLEMENTARY NOTES

☐ Document describes a computer program; SF-185, FIPS Software Summary, is attached.

16. ABSTRACT *(A 200-word or less factual summary of most significant information. If document includes a significant bibliography or literature survey, mention it here.)*

This Special Publication contains summaries of papers to be presented at the Topical Conference on Basic Optical Properties of Materials to be held at the National Bureau of Standards in Gaithersburg, Maryland on May 5-7, 1980. The conference is sponsored by the National Bureau of Standards in cooperation with the Optical Society of America. This publication contains summaries of 62 papers which include 14 invited papers. The principal topical areas are: Nonlinear Optical Properties; Ultraviolet Properties; Infrared Properties; Graded Index Materials; Inhomogeneous Materials; Properties of Thin Films; Optical Fibers, Planar Optical Waveguides; External Influences - Piezo-optics, Thermo-optics, Magneto-optics.

The purpose of the conference is to discuss the state of the art in the measurement of the optical properties of optical materials. The emphasis is primarily on materials properties rather than on optical devices. The primary focus of the conference is on the measurement and theory of basic optical properties of materials in bulk, thin film and fiber form.

17. KEY WORDS *(six to twelve entries; alphabetical order; capitalize only the first letter of the first key word unless a proper name; separated by semicolons)*
Fiber optics; graded index materials; infrared; magneto-optics; nonlinear optics; piezo-optics; planar waveguides; thermo-optics; thin films; and ultraviolet.

18. AVAILABILITY ☒ Unlimited

☐ For Official Distribution. Do Not Release to NTIS

☒ Order From Sup. of Doc., U.S. Government Printing Office, Washington, DC 20402

☐ Order From National Technical Information Service (NTIS), Springfield, VA. 22161

19. SECURITY CLASS (THIS REPORT) UNCLASSIFIED

20. SECURITY CLASS (THIS PAGE) UNCLASSIFIED

21. NO. OF PRINTED PAG 252

22. Price $6.50

USCOMM-DC

NBS TECHNICAL PUBLICATIONS

PERIODICALS

JOURNAL OF RESEARCH—The Journal of Research of the National Bureau of Standards reports NBS research and development in those disciplines of the physical and engineering sciences in which the Bureau is active. These include physics, chemistry, engineering, mathematics, and computer sciences. Papers cover a broad range of subjects, with major emphasis on measurement methodology and the basic technology underlying standardization. Also included from time to time are survey articles on topics closely related to the Bureau's technical and scientific programs. As a special service to subscribers each issue contains complete citations to all recent Bureau publications in both NBS and non-NBS media. Issued six times a year. Annual subscription: domestic $17; foreign $21.25. Single copy, $3 domestic; $3.75 foreign.

NOTE: The Journal was formerly published in two sections: Section A "Physics and Chemistry" and Section B "Mathematical Sciences."

DIMENSIONS/NBS—This monthly magazine is published to inform scientists, engineers, business and industry leaders, teachers, students, and consumers of the latest advances in science and technology, with primary emphasis on work at NBS. The magazine highlights and reviews such issues as energy research, fire protection, building technology, metric conversion, pollution abatement, health and safety, and consumer product performance. In addition, it reports the results of Bureau programs in measurement standards and techniques, properties of matter and materials, engineering standards and services, instrumentation, and automatic data processing. Annual subscription: domestic $11; foreign $13.75.

NONPERIODICALS

Monographs—Major contributions to the technical literature on various subjects related to the Bureau's scientific and technical activities.

Handbooks—Recommended codes of engineering and industrial practice (including safety codes) developed in cooperation with interested industries, professional organizations, and regulatory bodies.

Special Publications—Include proceedings of conferences sponsored by NBS, NBS annual reports, and other special publications appropriate to this grouping such as wall charts, pocket cards, and bibliographies.

Applied Mathematics Series—Mathematical tables, manuals, and studies of special interest to physicists, engineers, chemists, biologists, mathematicians, computer programmers, and others engaged in scientific and technical work.

National Standard Reference Data Series—Provides quantitative data on the physical and chemical properties of materials, compiled from the world's literature and critically evaluated. Developed under a worldwide program coordinated by NBS under the authority of the National Standard Data Act (Public Law 90-396).

NOTE: The principal publication outlet for the foregoing data is the Journal of Physical and Chemical Reference Data (JPCRD) published quarterly for NBS by the American Chemical Society (ACS) and the American Institute of Physics (AIP). Subscriptions, reprints, and supplements available from ACS, 1155 Sixteenth St., NW, Washington, DC 20056.

Building Science Series—Disseminates technical information developed at the Bureau on building materials, components, systems, and whole structures. The series presents research results, test methods, and performance criteria related to the structural and environmental functions and the durability and safety characteristics of building elements and systems.

Technical Notes—Studies or reports which are complete in themselves but restrictive in their treatment of a subject. Analogous to monographs but not so comprehensive in scope or definitive in treatment of the subject area. Often serve as a vehicle for final reports of work performed at NBS under the sponsorship of other government agencies.

Voluntary Product Standards—Developed under procedures published by the Department of Commerce in Part 10, Title 15, of the Code of Federal Regulations. The standards establish nationally recognized requirements for products, and provide all concerned interests with a basis for common understanding of the characteristics of the products. NBS administers this program as a supplement to the activities of the private sector standardizing organizations.

Consumer Information Series—Practical information, based on NBS research and experience, covering areas of interest to the consumer. Easily understandable language and illustrations provide useful background knowledge for shopping in today's technological marketplace.

Order the **above** *NBS publications from: Superintendent of Documents, Government Printing Office, Washington, DC 20402.*

Order the **following** *NBS publications—FIPS and NBSIR's—from the National Technical Information Services, Springfield, VA 22161.*

Federal Information Processing Standards Publications (FIPS PUB)—Publications in this series collectively constitute the Federal Information Processing Standards Register. The Register serves as the official source of information in the Federal Government regarding standards issued by NBS pursuant to the Federal Property and Administrative Services Act of 1949 as amended, Public Law 89-306 (79 Stat. 1127), and as implemented by Executive Order 11717 (38 FR 12315, dated May 11, 1973) and Part 6 of Title 15 CFR (Code of Federal Regulations).

NBS Interagency Reports (NBSIR)—A special series of interim or final reports on work performed by NBS for outside sponsors (both government and non-government). In general, initial distribution is handled by the sponsor; public distribution is by the National Technical Information Services, Springfield, VA 22161, in paper copy or microfiche form.

BIBLIOGRAPHIC SUBSCRIPTION SERVICES

The following current-awareness and literature-survey bibliographies are issued periodically by the Bureau:

Cryogenic Data Center Current Awareness Service. A literature survey issued biweekly. Annual subscription: domestic $25; foreign $30.

Liquefied Natural Gas. A literature survey issued quarterly. Annual subscription: $20.

Superconducting Devices and Materials. A literature survey issued quarterly. Annual subscription: $30. Please send subscription orders and remittances for the preceding bibliographic services to the National Bureau of Standards, Cryogenic Data Center (736) Boulder, CO 80303.

U.S. DEPARTMENT OF COMMERCE
National Bureau of Standards
Washington, D.C. 20234

OFFICIAL BUSINESS

Penalty for Private Use, $300

POSTAGE AND FEES PAID
U.S. DEPARTMENT OF COMMERCE
COM-215

SPECIAL FOURTH-CLASS RATE
BOOK